

The Pennsylvania State University
The Graduate School
John and Willie Leone Family Department of Energy and Mineral Engineering

**PALLADIUM-COPPER BIMETALLIC CATALYSTS FOR
SELECTIVE CARBON DIOXIDE HYDROGENATION TO
METHANOL**

A Dissertation in
Energy and Mineral Engineering
by
Xiao Jiang

© 2015 Xiao Jiang

Submitted in Partial Fulfillment
of the Requirements
for the Degree of

Doctor of Philosophy
December 2015

The dissertation of Xiao Jiang was reviewed and approved* by the following:

Chunshan Song

Distinguished Professor of Fuel Science and Professor of Chemical Engineering
Director, EMS Energy Institute;
Associate Director, Penn State Institutes of Energy and the Environment
Dissertation Advisor
Chair of Committee

Sarma V. Pisupati

Professor of Energy and Mineral Engineering
Undergraduate Program Chair of Energy Engineering
Director of Online Education

Randy L. Vander Wal

Professor of Energy and Mineral Engineering and Materials Science and Engineering

Michael J. Janik

Professor of Chemical Engineering & John J. and Jean M. Brennan Clean Energy Early
Career Professor in the College of Engineering

Lius F. Ayala

Associate Professor of Petroleum and Natural Gas Engineering
Associate Department Head for Graduate Education of Energy and Mineral Engineering

*Signatures are on the file in the Graduate School

ABSTRACT

Catalytic CO₂ hydrogenation for synthesis of methanol has attracted significant attention recently as a way of recycling carbon dioxide as a resource. In the past decades, most prior works focused on Cu-based and supported Pd-based catalysts to hydrogenate CO₂ to CH₃OH. Cu and Pd were proposed to have different affinities towards the adsorption of CO₂ and H₂, respectively. However, little attention has been paid to the effect of Pd-Cu bimetallic catalysts on the methanol synthesis from CO₂ hydrogenation. Thus, this work aims at studying the effect of combining Pd and Cu on the activity and selectivity of methanol synthesis via CO₂ hydrogenation and developing a fundamental understanding on composition-structure-activity relationship. The Pd-Cu bimetallic catalysts with various compositions were prepared and examined in CO₂ hydrogenation at relatively mild reaction conditions (523 K and 4.1 MPa).

A strong synergistic effect was observed over Pd–Cu bimetallic catalysts supported on silica at specific compositions as evidenced from the superior methanol formation rate and selectivity in comparison to monometallic catalysts, and the optimal Pd/(Pd+Cu) atomic ratios lied in the range of 0.25-0.34. The methanol formation rate over Pd(8.7)-Cu(10)/SiO₂ was almost three times higher than the simple sum of those over monometallic Cu and Pd catalysts. To investigate the composition-structure-activity relationship, the Pd-Cu bimetallic catalysts were characterized by X-ray diffraction (XRD), transmission electron microscopy (TEM), scanning transmission electron microscopy coupled with energy dispersive X-ray spectroscopy (STEM/EDS), X-ray photoelectron spectroscopy (XPS), hydrogen temperature-programmed reduction (H₂-TPR), and temperature-programmed desorption (H₂-, CO₂-, & CO-TPD). Detailed characterization results demonstrated the importance of two well-dispersed Pd–Cu alloy particles (PdCu₃ and PdCu) for

the observed methanol promotion over Pd–Cu bimetallic catalysts. DRIFTS spectra revealed that the incorporation of Pd and Cu greatly improved the formation of formate and CO species during the CO₂ hydrogenation. CO-TPD profiles confirmed the existence of three forms of chemisorbed CO species, and the bonding strength increased in the following order: CO^L (linear) < CO^B (di-coordinated bridging) < CO^H (triple-coordinated bridging). Among them, chemisorbed CO^B was suggested as a potential intermediate for methanol synthesis because of its moderate bonding strength and desorption temperature range (proximity to reaction temperature). Quantitative analyses showed that the Pd-Cu could promote the chemisorbed CO^B at specific composition and thus gave rise to the possibility of methanol formation via the following hydrogenation.

The selectivity-conversion profile of the Pd–Cu/SiO₂ catalyst suggested that CO₂ was a primary carbon source for methanol synthesis at lower CO₂ conversion, and chemisorbed CO species contributed at higher CO₂ conversion within the conversion range examined.

TABLE OF CONTENTS

LISTS OF TABLES	x
LISTS OF FIGURES	xiii
ACKNOWLEDGMENTS	xxvii
Chapter 1 Introduction	1
1.1 Background of research.....	1
1.1.1 Issue of CO ₂ emission	1
1.1.2 Catalytic CO ₂ conversion	2
1.1.3 CH ₃ OH production in industry	4
1.1.4 CH ₃ OH synthesis via CO ₂ hydrogenation.....	5
1.2 Thermodynamic issues of catalytic CO ₂ conversion to methanol.....	6
1.3 Methanol synthesis activity over Pd-based catalysts	10
1.3.1 Activity performance over Pd-based catalysts via CO and CO ₂ HYD	10
1.3.2 Reaction mechanism over Pd series catalysts	11
1.3.3 Promoters effect.....	12
1.3.4 Support: Al ₂ O ₃ vs. SiO ₂	13
1.4 Methanol synthesis activity over Cu-based catalysts	14
1.4.1 Cu-based multicomponent catalyst.....	14
1.4.2 Reaction mechanism for both methanol synthesis and reverse water-gas shift	16
1.4.3 Cu-Zn alloy.....	19
1.4.4 Deactivation.....	20
1.5 Other approaches	20
1.5.1 Photocatalytic conversion.....	20
1.5.2 Electrochemical reduction	21
1.6 Motivations.....	22
1.7 Objectives, hypotheses, and dissertation outline.....	23
1.7.1 Objectives	23
1.7.2 Hypotheses	24
1.7.3 Dissertation outline.....	24
1.8 Reference.....	27

Chapter 2 The Effect of Combining Pd and Cu on Catalytic Properties for CO ₂ Hydrogenation to Methanol	33
Abstract	33
2.1 Introduction	35
2.2 Experimental	37
2.2.1 Preparation of catalysts.....	37
2.2.2 Catalytic test	39
2.2.3 Passivation of reduced/spent catalysts.....	41
2.2.4 Characterization of catalysts.....	41
2.3 Results and discussion.....	44
2.3.1 Synergetic effect of Pd and Cu on CO ₂ hydrogenation.....	44
2.3.2 Support effect on CH ₃ OH formation over Pd-Cu bimetallic catalysts.....	49
2.3.3 Comparison to Cu-Zn based catalysts	50
2.3.4 Physical properties of Pd-Cu catalysts	51
2.3.5 Crystallite structures of Pd-Cu catalysts.....	54
2.3.5.1 Amorphous silica supported Pd-Cu catalysts	54
2.3.5.2 Effect of support on Pd-Cu alloy formation	60
2.3.6 Morphological properties of Pd and Cu species and element distribution	61
2.3.7 Surface properties of reduced Pd-Cu catalysts	68
2.3.8 Importance of Pd-Cu alloy formation for bimetallic promotion	72
2.4 Conclusions	76
2.5 Acknowledgements	77
2.6 Reference.....	78
Chapter 3 The Effect of Pd and Cu Combination on Surface Chemical Properties in CO ₂ Hydrogenation to Methanol	83
Abstract	83
3.1 Introduction	85
3.2 Experimental	86
3.2.1 Preparation of catalysts.....	86
3.2.2 Catalytic test	87
3.2.3 Characterization of catalysts.....	88

3.2.3.1 Temperature-programmed reduction (H ₂ -TPR).....	88
3.2.3.2 Temperature-programmed desorption (H ₂ , CO ₂ , and CO-TPD)	89
3.2.3.3 Diffuse reflectance FT-IR	92
3.3 Results and discussion.....	95
3.3.1 Temperature-programmed reduction (TPR).....	95
3.3.2 H ₂ adsorption properties of Pd-Cu catalysts.....	100
3.3.3 CO ₂ adsorption properties of Pd-Cu catalysts	104
3.3.4 Diffuse reflectance FT-IR (DRIFTS)	107
3.3.4.1 Surface species & bands assignment	107
3.3.4.2 Effect of Pd and Cu combination on surface species.....	115
3.3.4.3 Effect of Pd loading on surface species	118
3.3.4.4 CO ₂ adsorption and formate formation.....	122
3.3.4.5 H ₂ /N ₂ purge after CO ₂ hydrogenation	124
3.3.4.6 Reactivity of CO	129
3.3.5 CO adsorption properties of Pd-Cu catalysts	132
3.3.6 Reaction pathway	135
3.3.7 Discussion.....	138
3.4 Conclusions	141
3.5 Acknowledgements	142
3.6 Reference.....	143
Chapter 4 Conclusions and Recommendations for Future Work.....	149
4.1 Summary	149
4.2 Conclusions	150
4.3 Recommendations for future work.....	151
4.3.1 Pd-Cu alloy effect with lower metal loadings	152
4.3.2 Effect of PdCu ₃ and PdCu alloys on methanol synthesis	152
4.3.3 Effect of ZnO on methanol synthesis activity over Pd-Cu bimetallic catalysts	153
4.4 Reference.....	155
Appendix A Preparation of Mesoporous Silicas	156
Appendix B Incipient Pore Volume	158
Appendix C X-ray Photoelectron Spectroscopy (XPS).....	159

Appendix D X-ray Diffraction (XRD).....	162
Appendix E Energy Dispersive Spectroscopy Mapping (STEM/EDS).....	167
Appendix F Temperature-Programmed Reduction (H ₂ -TPR)	170
Appendix G Hydrogen Temperature-Programmed Desorption (H ₂ -TPD)	174
Appendix H Carbon Dioxide Temperature-Programmed Desorption (CO ₂ -TPD).....	179
Appendix I Carbon Monoxide Temperature-Programmed Desorption (CO-TPD)	187
Appendix J Mass Transfer Limitation	190
J.I Bulk concentration of CO ₂ , C _s	191
J.2 Effective diffusivity	191
J.2.1 Mean free path estimation.....	191
J.2.2 Determine of effective diffusivity.....	192
Appendix K Effects of Mesoporous Silica Supports and Alkali/Alkaline Earth Metal Promoters on the Activity of Pd-based Catalysts in CO ₂ Hydrogenation for Methanol Synthesis.....	195
Abstract	195
K.1 Introduction	197
K.2 Experimental	200
K.2.1 Support materials	200
K.2.2 Preparation of Pd catalysts	200
K.2.3 Activity test.....	201
K.2.4 N ₂ physisorption	203
K.2.5 H ₂ chemisorption	204
K.2.6 Temperature programmed reduction (TPR)	205
K.2.7 In-situ Pd K-edge EXAFS	205
K.2.8 CO ₂ temperature programmed desorption (CO ₂ -TPD)	206
K.3 Results and discussions	208
K.3.1 Physical properties of Ca-promoted Pd catalysts	208
K.3.2 Coordination environment.....	215
K.3.3 Pd ⁰ dispersion	217
K.3.4 Temperature-programmed reduction (TPR).....	221
K.3.5 CO ₂ temperature programmed desorption (CO ₂ -TPD)	225
K.3.6 Effects of support (SBA-15 & amorphous SiO ₂) and promoters	227

K.3.7 Effect of Ca/Pd molar ratio on CH ₃ OH formation	230
K.3.8 Impact of pore diameter.....	236
K.4 Conclusions	240
K.5 Acknowledgements	242
K.6 Reference.....	243

LISTS OF TABLES

Table 1-1 Reactions in methanol synthesis from CO ₂ /H ₂	6
Table 2-1 CO ₂ hydrogenation activity and product selectivity over supported Pd-Cu and Cu-Zn catalysts ^{a, b)}	47
Table 2-2 Physical properties of supported Pd(X)-Cu(10) catalysts ^{a)}	52
Table 2-3 Crystallite phases, sizes and interplanar spacings for <i>reduced</i> Pd(X)-Cu(10)/SiO ₂ catalysts	54
Table 2-4 Quantitative analyses based on XRD patterns for Pd-Cu bimetallic catalysts with various Pd loadings	60
Table 2-5 Quantified phase compositions in Pd-Cu alloy nanoparticles from STEM/EDS maps a)	64
Table 2-6 Quantified phase compositions in Pd-Cu alloy nanoparticles from STEM/EDS maps a)	66
Table 2-7 Pd 3d XPS parameters of <i>reduced</i> Pd-Cu/SiO ₂ catalysts	68
Table 2-8 Cu 2p XPS parameters of <i>reduced</i> Pd-Cu/SiO ₂ catalysts	70
Table 2-9 Surface chemical compositions of <i>reduced</i> Pd-Cu/SiO ₂ catalysts determined by XPS	71
Table 3-1 Denotations of the background spectra used in DRIFTS analyses.....	94
Table 3-2 Summary of TPR data for Pd(X)-Cu(10)/SiO ₂ and monometallic catalysts ^{a)}	96
Table 3-3 Amount of H ₂ desorbed in H ₂ -TPD of Pd(X)-Cu(10)/SiO ₂ and monometallic catalysts ^{a)}	104
Table 3-4 Amount of CO ₂ desorbed in CO ₂ -TPD of Pd(X)-Cu(10)/SiO ₂ and monometallic catalysts ^{a)}	107

Table 3-5 Infrared peak assignment of the surface species observed during the CO ₂ hydrogenation at different temperatures and 0.1 MPa, and together with those of the methanol/formic acid adsorption at 373 K and 0.1 MPa over pre-reduced Pd(8.7)-Cu(10)/SiO ₂	114
Table 3-6 CO uptakes in CO-TPD of Pd(X)-Cu(10)/SiO ₂ and monometallic catalysts ^{a)}	134
Table 4-1 Activity performances on ZnO-promoted and unpromoted Pd-Cu catalysts ^{a-c)}	153
Table D-1 Summary of card data for potential phases	164
Table G-1 Amount of adsorbed H ₂ species over Pd(8.7)/SiO ₂	174
Table G-2 Amount of adsorbed H ₂ species over Pd(5.7)-Cu(10)/SiO ₂	175
Table G-3 Amount of adsorbed H ₂ species over Pd(8.7)-Cu(10)/SiO ₂	176
Table G-4 Amount of adsorbed H ₂ species over Pd(8.7)-Cu(10)/SiO ₂	177
Table H-1 Amount of adsorbed CO ₂ species over Pd(8.7)/SiO ₂	180
Table H-2 Amount of adsorbed CO ₂ species over Cu(10)/SiO ₂	181
Table H-3 Amount of adsorbed CO ₂ species over Pd(2.5)-Cu(10)/SiO ₂	182
Table H-4 Amount of adsorbed CO ₂ species over Pd(5.7)-Cu(10)/SiO ₂	183
Table H-5 Amount of adsorbed CO ₂ species over Pd(8.7)-Cu(10)/SiO ₂	184
Table H-6 Amount of adsorbed CO ₂ species over Pd(15.7)-Cu(10)/SiO ₂	185
Table H-7 Amount of adsorbed CO ₂ species over the bare support (amorphous silica)	186
Table J-1 Reaction conditions of CO ₂ hydrogenation to methanol over Pd(8.7)-Cu(10)/SiO ₂ ..	193
Table J-2 Parameter values in calculation of mass transfer effect.....	194
Table K-1 Physical properties of Ca(0.37)/Pd(5.7) catalysts and support materials ^{a,b)}	209
Table K-2 Structural parameters of Pd-Pd coordination shell for Pd catalysts prepared from aqueous Pd(NO ₃) ₂ solution	216

Table K-3 H ₂ chemisorption results for Ca-promoted and unpromoted Pd catalysts	218
Table K-4 Quantitative data based on CO ₂ -TPD measurements over promoted and unpromoted Pd catalysts supported on either SBA-15 or MSU-F (Pd loading = 5.7 wt%) ..	225
Table K-5 Point of zero charge (PZC) of SBA-15 and pH values for precursors	227
Table K-6 Support effect of SBA-15 on CO ₂ hydrogenation activity and selectivity over Pd and Cu-ZnO catalysts ^{a,b)}	229
Table K-7 CO ₂ hydrogenation activity and selectivity of Pd catalysts supported on mesoporous silica with different pore diameters ^{a-c)}	236

LISTS OF FIGURES

Figure 1-1 Monthly mean atmospheric carbon dioxide at Mauna Loa Observatory, Hawaii. The black curve represents the seasonally corrected data and the red one indicates the monthly corrected data. Trends in CO ₂ values given are dry air mole fractions expressed in parts per million (ppm). National Oceanic & Atmospheric Administration (NOAA).	2
Figure 1-2 Changes of equilibrium CO ₂ conversion % (A) and product yield % (B) as a function of temperature at pressures. (Calculated by HSC software).....	8
Figure 1-3 Changes of equilibrium CH ₃ OH yield as a function of H ₂ /CO ₂ ratios at pressures. Simulating temperature: 523 K. Data was obtained based on theoretical calculations [36]. The original data was reorganized by the author and plotted in this figure.	9
Figure 1-4 Rate enhancement for methanol formation in the hydrogenation of CO as a function of the electronegativity (EN) of the additive cation. Copied from the reference without further modification [42].....	13
Figure 1-5 Schematic diagram of a recycle reactor designed for the Cu-Zn-based multi-component catalyst in methanol synthesis via CO ₂ hydrogenation [19].....	15
Figure 1-6 Schematic illustrations for conversion of pure CO ₂ , pure CO, and CO ₂ +CO to methanol over Cu. The whole scheme was copied without modification, see Ref [76].	18
Figure 2-1 Schematic diagram of the fixed-bed flow reactor system for CO ₂ hydrogenation.	40
Figure 2-2 Changes in CO ₂ conversion and formation rate of products (CH ₃ OH and CO) over Pd(5.7)-Cu(Y)/SiO ₂ with a fixed Pd loading at 5.7wt% (A) and Pd(X)-Cu(10)/SiO ₂ with a fixed Cu loading at 10 wt% (B) as functions of Cu/(Pd+Cu) and Pd/(Pd+Cu) atomic ratios, respectively. CO ₂ hydrogenation conditions: 523 K, 4.1 MPa, 6.2 g-cat h mol ⁻¹	45

Figure 2-3 Stabilities of CO₂ conversion and products formation rates with time on stream over Pd(8.7)-Cu(10)/SiO₂. CO₂ hydrogenation conditions: 523 K, 4.1 MPa, 6.2 g-cat h mol⁻¹ 49

Figure 2-4 N₂ adsorption-desorption isotherms of Pd-Cu catalyst and bare support materials along with their BJH pore size distributions in the insets. (A) Bare amorphous silica (●) and the *calcined* Pd(5.7)-Cu(10)/SiO₂ (○), (B) SBA-15 (■) and the *calcined* Pd(5.7)-Cu(10)/SBA-15 (□). 53

Figure 2-5 XRD patterns of Pd(X)-Cu(Y)/SiO₂ catalysts with the thick lines indicating original patterns, while the thin lines indicating deconvoluted patterns. (a) *calcined* Pd(5.7)-Cu(10)/SiO₂, (b) *reduced* Cu(10)/SiO₂, (c) *reduced* Pd(5.7)/SiO₂, (d) *reduced* Pd(5.7)-Cu(10)/SiO₂, (e) *reduced* Pd(8.7)/Cu(10)/SiO₂ with the magnified pattern in the inset (2θ: 39-54 °). Bimetallic catalyst samples were prepared by coimpregnation method, while sample (e) by sequential impregnation method. For all Cu containing samples, the Cu loading was 10 wt%. Symbols assignment: ▲: Pd⁰; ▼: Cu⁰; ♦: PdCu₃; ■: CuPdO₂..... 55

Figure 2-6 XRD patterns of the *reduced* Pd(X)-Cu(10)/SiO₂ catalysts with magnified XRD patterns in the inset (2θ: 39-45 °). (a) Pd(2.5)-Cu(10)/SiO₂, (b) Pd(8.7)-Cu(10)/SiO₂, (c) Pd(15.7)-Cu(10)/SiO₂. Original patterns were highlighted with thick lines and patterns after deconvolution were featured with thin lines. For all samples, the Cu loading was 10 wt%. Symbols assignment: ▲: Pd⁰; ▼: Cu⁰; ♦: PdCu₃; ■: PdCu..... 56

Figure 2-7 XRD patterns of the *spent* Pd(5.7)-Cu(10) catalysts supported on (a) SBA-15, (b) MCM-41, and (c) MSU-F. Original patterns were highlighted with thick lines, while thin lines were patterns after deconvolution. Symbols assignment: ♦: PdCu₃; ■: PdCu..... 61

Figure 2-8 TEM images of <i>reduced</i> Pd(8.7)-Cu(10)/SiO ₂ with different magnifications (A-C).	
The lattice fringe pattern of ca. 0.2 nm is discernible in image (B). (D) represents the corresponding particle size distribution.	62
Figure 2-9 (A) HAADF STEM image of <i>reduced</i> Pd(8.7)-Cu(10)/SiO ₂ and its corresponding STEM/EDS overlap maps for Pd and Cu (B). A representative alloy particle was magnified in the inset showing clear fringe alignment.	63
Figure 2-10 (A) HAADF STEM image of <i>reduced</i> Pd(2.5)-Cu(10)/SiO ₂ and its corresponding STEM/EDS overlap maps for Pd and Cu (B). A representative alloy particle was magnified in the inset showing clear fringe alignment.	65
Figure 2-11 TEM Image (A) shows the characteristic pore structure of SBA-15. (B-C) are TEM images of <i>reduced</i> Pd(5.7)-Cu(10)/SBA-15 with different areas. (D) represents the corresponding particle size distribution.	67
Figure 2-12 Pd 3d XP spectra of (a) <i>reduced</i> Pd(8.7)-Cu(10)/SiO ₂ ; (b) <i>reduced</i> Pd(8.7)/SiO ₂ .	68
Figure 2-13 Cu 2p XP spectra of (a) <i>reduced</i> Pd(8.7)-Cu(10)/SiO ₂ ; (b) <i>reduced</i> Cu(10)/SiO ₂	69
Figure 2-14 Bimetallic promotion of CH ₃ OH formation over (A) amorphous silica-supported Pd(X)-Cu(10)/SiO ₂ and (B) its correlation with total alloy contents for Pd(X)-Cu(10)/SiO ₂ with various Pd loadings	74
Figure 2-15 Bimetallic promotion of CH ₃ OH formation over various mesoporous silica-supported Pd(5.7)-Cu(10)/support.	76
Figure 3-1 A schematic illustration for hydrogen temperature-programmed reduction (H ₂ -TPR) over monometallic and bimetallic Pd-Cu catalysts.	89
Figure 3-2 A schematic illustration for hydrogen temperature-programmed desorption (H ₂ -TPD) over monometallic and bimetallic Pd-Cu catalysts.	90

Figure 3-3 A schematic illustration for carbon dioxide temperature-programmed desorption (CO ₂ -TPD) over monometallic and bimetallic Pd-Cu catalysts.	91
Figure 3-4 A schematic illustration for carbon monoxide temperature-programmed desorption (CO-TPD) over monometallic and bimetallic catalysts.	92
Figure 3-5 TPR profiles for monometallic and bimetallic Pd-Cu catalysts with different metallic compositions. TPR conditions: 20 mL min ⁻¹ of 5 vol% H ₂ /Ar flow, 10 K min ⁻¹ of heating rate. (a) Pd(8.7); (b) Pd(2.5)-Cu(10); (c) Pd(5.7)-Cu(10); (d) Pd(8.7)-Cu(10); (e) Pd(15.7)-Cu(10); (f) Cu(10).	95
Figure 3-6 TPR profile of CuO (Sigma-Aldrich). The data was collected by mass spectrometer. TPR conditions: 20 mL min ⁻¹ of 5 vol% H ₂ /Ar flow with a heating rate of 10 K min ⁻¹	96
Figure 3-7 TPR profiles for (A) Pd(5.7)-Cu(10)/SiO ₂ and (B) Cu(10)/SiO ₂ at different heating rates. TPR conditions: 20 mL min ⁻¹ of 5 vol% H ₂ /Ar flow. (a) 2 K min ⁻¹ ; (b) 5 K min ⁻¹ ; (c) 10 K min ⁻¹ ; (d) 15 K min ⁻¹ ; (e) 20 K min ⁻¹	98
Figure 3-8 Kissinger plots of Pd(5.7)-Cu(10)/SiO ₂ and Cu(10)/SiO ₂	99
Figure 3-9 H ₂ -TPD profiles of pre-reduced monometallic and bimetallic catalysts. (a) Cu(10)/SiO ₂ , (b) Pd(8.7)/SiO ₂ , (c) Pd(8.7)-Cu(10)/SiO ₂ . (---) measured TPD profile, (–) deconvoluted peaks.	101
Figure 3-10 H ₂ -TPD profiles of Pd(X)-Cu(10)/SiO ₂ . (a) Pd(2.5)-Cu(10)/SiO ₂ , (b) Pd(5.7)-Cu(10)/SiO ₂ , (c) Pd(8.7)-Cu(10)/SiO ₂ , (d) Pd(15.7)-Cu(10)/SiO ₂ . (---) measured TPD profile, (–) deconvoluted peaks.	102

Figure 3-11 CO ₂ -TPD profiles of pre-reduced monometallic and bimetallic catalysts. (a) Cu(10)/SiO ₂ , (b) Pd(8.7)/SiO ₂ , (c) Pd(8.7)-Cu(10)/SiO ₂ . (---) measured TPD profile, (–) deconvoluted peaks.....	105
Figure 3-12 CO ₂ -TPD profiles of Pd(X)-Cu(10)/SiO ₂ . (a) Pd(2.5)-Cu(10)/SiO ₂ , (b) Pd(5.7)-Cu(10)/SiO ₂ , (c) Pd(8.7)-Cu(10)/SiO ₂ , (d) Pd(15.7)-Cu(10)/SiO ₂ . (---) measured TPD profile, (–) deconvoluted peaks.....	106
Figure 3-13 Diffuse reflectance FT-IR spectra of pre-reduced Pd(8.7)-Cu(10)/SiO ₂ in CO ₂ /H ₂ at temperatures. CO ₂ hydrogenation conditions: CO ₂ /H ₂ /Ar=24/72/4 (vol%), 0.1 MPa, ca. 30 mL min ⁻¹ . All spectra were processed by BG-1.....	109
Figure 3-14 Diffuse reflectance FT-IR spectra of pre-reduced Pd(8.7)-Cu(10)/SiO ₂ in CO ₂ /H ₂ at temperatures (a-d) and methanol/formic acid adsorption at 373 K (e-f). CO ₂ hydrogenation conditions: CO ₂ /H ₂ /Ar=24/72/4 (vol%), 0.1 MPa, ca. 30 mL min ⁻¹ . Methanol/formic acid adsorption conditions: N ₂ (30 mL min ⁻¹), 0.1 MPa, 373 K, 4.0 μL injection. (a-d) were processed by BG-1, while (e-f) were based on BG-0. CO ₂ hydrogenation at (a) 373 K, (b) 423 K, (c) 474 K, (d) 523 K, and adsorption at (e-f) 373 K.....	110
Figure 3-15 Diffuse reflectance FT-IR spectra of pre-reduced Pd(8.7)-Cu(10)/SiO ₂ in CO ₂ /H ₂ at temperatures (a-d) and methanol/formic acid adsorption at 373 K (e-f). CO ₂ hydrogenation conditions: CO ₂ /H ₂ /Ar=24/72/4 (vol%), 0.1 MPa, ca. 30 mL min ⁻¹ . Methanol/formic acid adsorption conditions: N ₂ (30 mL min ⁻¹), 0.1 MPa, 373 K, 4.0 μL injection. (a-d) were processed by BG-1, while (e-f) were based on BG-0. CO ₂ hydrogenation at (a) 373 K, (b) 423 K, (c) 474 K, (d) 523 K, and adsorption at (e-f) 373 K.....	111

Figure 3-16 Diffuse reflectance FT-IR spectra of pre-reduced monometallic and bimetallic catalysts in CO₂/H₂ at 373 K. CO₂ hydrogenation conditions: CO₂/H₂/Ar=24/72/4 (vol%), 0.1 MPa, ca. 30 mL min⁻¹. All spectra were processed by BG-1. (a) Cu(10)/SiO₂; (b) Pd(8.7)/SiO₂; (c) Pd(8.7)-Cu(10)/SiO₂ 116

Figure 3-17 Diffuse reflectance FT-IR spectra of pre-reduced monometallic and bimetallic catalysts in CO₂/H₂ at 523 K. CO₂ hydrogenation conditions: CO₂/H₂/Ar=24/72/4 (vol%), 0.1 MPa, ca. 30 mL min⁻¹. All spectra were processed by BG-1. (a) Cu(10)/SiO₂; (b) Pd(8.7)/SiO₂; (c) Pd(8.7)-Cu(10)/SiO₂ 117

Figure 3-18 Diffuse reflectance FT-IR spectra of pre-reduced bimetallic catalysts in CO₂/H₂ at 373 K. CO₂ hydrogenation conditions: CO₂/H₂/Ar=24/72/4 in vol%, 0.1 MPa, ca. 30 mL min⁻¹. All spectra were processed by BG-1. (a) Pd(2.5)-Cu(10)/SiO₂; (b) Pd(8.7)-Cu(10)/SiO₂; (c) Pd(15.7)-Cu(10)/SiO₂ 119

Figure 3-19 Changes of relative intensities for formate-relevant bands over pre-reduced monometallic and bimetallic catalysts in CO₂/H₂ at 373 K. The quantitative data was determined based on infrared spectra in Figs. 3-16 and 3-18, and the band at 3730 cm⁻¹ was used as an internal standard in the evaluation 120

Figure 3-20 Diffuse reflectance FT-IR spectra of pre-reduced bimetallic catalysts in CO₂/H₂ at 523 K. CO₂ hydrogenation conditions: CO₂/H₂/Ar=24/72/4 in vol%, 0.1 MPa, ca. 30 mL min⁻¹. All spectra were processed by BG-1. (a) Pd(2.5)-Cu(10)/SiO₂; (b) Pd(8.7)-Cu(10)/SiO₂; (c) Pd(15.7)-Cu(10)/SiO₂ 121

Figure 3-21 Changes of relative intensities for carious carbonyl bands over pre-reduced bimetallic catalysts in CO₂/H₂ at 523 K. The quantitative data was determined based on

infrared spectra in Figs. 3-17 and 3-20, and the band at 3730 cm ⁻¹ was used as an internal standard in the evaluation.....	122
Figure 3-22 Diffuse reflectance FT-IR spectra of pre-reduced bimetallic catalysts in CO ₂ /H ₂ at 373 K. CO ₂ hydrogenation conditions: CO ₂ /H ₂ /Ar=24/72/4 in vol%, 0.1 MPa, ca. 30 mL min ⁻¹ . All spectra were processed by BG-1. (a) Pd(2.5)-Cu(10)/SiO ₂ ; (b) Pd(8.7)-Cu(10)/SiO ₂ ; (c) Pd(15.7)-Cu(10)/SiO ₂	123
Figure 3-23 Changes of diffuse reflectance FT-IR spectra on pre-reduced Pd(8.7)-Cu(10)/SiO ₂ as a function of exposing time of hydrogen purge (30 mL min ⁻¹) after CO ₂ hydrogenation (1 h) at 373 K. CO ₂ hydrogenation conditions: CO ₂ /H ₂ /Ar=24/72/4 in vol%, 0.1 MPa, ca. 30 mL min ⁻¹ . All spectra were processed depending on BG-1.....	124
Figure 3-24 Changes of diffuse reflectance FT-IR spectra over pre-reduced Pd(8.7)-Cu(10)/SiO ₂ as a function of exposing time of hydrogen purge (30 mL min ⁻¹) after CO ₂ hydrogenation (1 h) at 373 K. CO ₂ hydrogenation conditions: CO ₂ /H ₂ /Ar=24/72/4 in vol%, 0.1 MPa, ca. 30 mL min ⁻¹ . The spectra were reprocessed by BG-2.....	125
Figure 3-25 Changes of diffuse reflectance FT-IR spectra over pre-reduced Pd(8.7)-Cu(10)/SiO ₂ as a function of exposing time of hydrogen purge (30 mL min ⁻¹) after CO ₂ hydrogenation (1 h) at 523 K. CO ₂ hydrogenation conditions: CO ₂ /H ₂ /Ar=24/72/4 in vol%, 0.1 MPa, ca. 30 mL min ⁻¹ . All spectra were processed depending on BG-1.	126
Figure 3-26 Changes of diffuse reflectance FT-IR spectra over pre-reduced Pd(8.7)-Cu(10)/SiO ₂ as a function of exposing time of nitrogen purge (30 mL min ⁻¹) after CO ₂ hydrogenation (1 h) at 373 K. CO ₂ hydrogenation conditions: CO ₂ /H ₂ /Ar=24/72/4 in vol%, 0.1 MPa, ca. 30 mL min ⁻¹ . All spectra were processed depending on BG-2.	127

Figure 3-27 Changes of diffuse reflectance FT-IR spectra over pre-reduced Pd(8.7)-Cu(10)/SiO ₂ as a function of exposing time of hydrogen purge (30 mL min ⁻¹) after CO ₂ hydrogenation (1 h) at 373 K. CO ₂ hydrogenation conditions: CO ₂ /H ₂ /Ar=24/72/4 in vol%, 0.1 MPa, ca. 30 mL min ⁻¹ . Spectra range: 3100-3600 cm ⁻¹ . The spectra were reprocessed based on BG-2.....	129
Figure 3-28 Diffuse reflectance FT-IR spectra of pre-reduced Pd(8.7)-Cu(10)/SiO ₂ in CO adsorption (1 h) at 523 K. CO adsorption: CO/Ar=10/90 in vol%, 0.1 MPa, ca. 30 mL min ⁻¹ . The spectrum was processed by BG-1.....	130
Figure 3-29 Changes of diffuse reflectance FT-IR spectra of pre-reduced Pd(8.7)-Cu(10)/SiO ₂ as a function of exposing time of hydrogen purge (30 mL min ⁻¹) after CO adsorption (1 h) at 523 K. CO adsorption: CO/Ar=10/90 in vol%, 0.1 MPa, ca. 30 mL min ⁻¹ . The spectra were reprocessed by BG-3.....	131
Figure 3-30 CO-TPD profiles of pre-reduced monometallic and bimetallic Pd-Cu catalysts. (a) Cu(10)/SiO ₂ ; (b) Pd(8.7)/SiO ₂ ; (c) Pd(2.5)-Cu(10)/SiO ₂ ; (d) Pd(8.7)-Cu(10)/SiO ₂ ; (e) Pd(15.7)-Cu(10)/SiO ₂ . CO adsorption was carried out at 523 K by using 5 vol% CO/He. TPD conditions: 5 K min ⁻¹ , Ar flow rate 30 mL min ⁻¹ . Solid lines: original desorption profiles; dash lines: fitting curves after deconvolution.....	132
Figure 3-31 Percentage of different carbonyl species desorbed from mono and bimetallic Pd-Cu catalysts. Quantitative data was determined based on CO-TPD profiles.....	135
Figure 3-32 Changes in products selectivity as a function of CO ₂ conversion over Pd(8.7)-Cu(10)/SiO ₂ (A) and Cu(10)/SiO ₂ (B). CO ₂ hydrogenation conditions: 523 K, 4.1 MPa, W/F=1.2-29.9 g-cat h mol ⁻¹ for (A) and 6.2-59.1 g-cat h mol ⁻¹ (B).....	138

Figure 3-33 The correlations of CH ₃ OH promotion with the amounts of weakly-bonded H ₂ (I+II) and CO ₂ (I+II) for Pd(X)-Cu(10)/SiO ₂ . Reaction conditions: 523 K, 4.1 MPa, 6.2 g h mol ⁻¹	140
Figure 4-1 Selectivities of products over Pd(8.7)-Cu(10)/SiO ₂ and Pd(8.7)-Cu(10)-ZnO(10)/SiO ₂ catalysts. Reaction conditions: 523 K, 4.1 MPa. W/Fs, from left to right, were 2.45 and 6.25 g h mol ⁻¹ , respectively.....	154
Figure B-1 Incipient pore volumes of different mesoporous silicas used in this work	158
Figure C-1 O 1s XP spectra of <i>reduced</i> Pd-Cu/SiO ₂ catalysts and together with support (amorphous silica). Pd loading was 8.7 wt% for Pd-containing samples and Cu loading was 10 wt% for Cu-containing samples. All samples were reduced first and then passivated....	160
Figure C-2 C 1s XP spectra of <i>reduced</i> Pd-Cu/SiO ₂ catalysts and together with support (amorphous silica). Pd loading was 8.7 wt% for Pd-containing samples and Cu loading was 10 wt% for Cu-containing samples. All samples were reduced first and then passivated....	160
Figure D-1 XRD patterns of Pd(X)-Cu(Y)/SiO ₂ catalysts with the thick lines indicating original patterns, while the thin lines indicating deconvoluted patterns. (a) <i>calcined</i> Pd(5.7)-Cu(10)/SiO ₂ , (b) <i>reduced</i> Cu(10)/SiO ₂ , (c) <i>reduced</i> Pd(5.7)/SiO ₂ , (d) <i>reduced</i> Pd(5.7)-Cu(10)/SiO ₂ , (e) <i>spent</i> Pd(5.7)-Cu(10)/SiO ₂ . Bimetallic catalysts were prepared by the coimpregnation method.....	162
Figure D-2 XRD pattern of <i>reduced</i> Cu(10)/Pd(8.7)/SiO ₂ catalyst with magnified XRD pattern in the inset (2θ: 39-45 °). Original pattern was highlighted with thick lines and patterns after deconvolution were featured with thin lines. Symbols assignment: ▼: Cu ⁰ and ♦: PdCu ₃	163

Figure D-3 X-ray diffraction patterns observed and calculated for <i>reduced</i> Pd(8.7)-Cu(10)/SiO ₂ . R=1.01 % and E=0.58 %.....	165
Figure D-4 X-ray diffraction patterns observed and calculated for <i>reduced</i> Pd(15.7)-Cu(10)/SiO ₂ . R=1.20 % and E=0.52 %.....	166
Figure E-1 STEM/EDS mapping of <i>reduced</i> Pd(8.7)-Cu(10)/SiO ₂ . (A): Oxygen (blue); (B): Palladium (yellow); (C): Silicon (green); (D): Copper (red).	167
Figure E-2 STEM/EDS overlap mapping of <i>reduced</i> Pd(8.7)-Cu(10)/SiO ₂ . Color assignment: Oxygen (blue); Palladium (yellow); Silicon (green); Copper (red).	168
Figure E-3 STEM/EDS mapping of <i>reduced</i> Pd(2.5)-Cu(10)/SiO ₂ . (A): Oxygen (blue); (B): Palladium (yellow); (C): Silicon (green); (D): Copper (red).	169
Figure F-1 TPR profile of standard sample AgO. Conditions: 20 mL min ⁻¹ of 5 vol% H ₂ /Ar with the heating rate of 10 K min ⁻¹	171
Figure F-2 TPR profile of Pd(8.7)/SiO ₂ . The sample was prepared by wet impregnation method in acetone solution of palladium (II) acetate. The H ₂ consumption rate was recorded by mass spectroscopy. TPR conditions: 20 mL min ⁻¹ of 5% H ₂ /Argon with a heating rate of 10 K min ⁻¹	172
Figure F-3 TPR profiles of Pd(5.7)-Cu(10)/SiO ₂ at different flow rates. TPR conditions: 5 vol% H ₂ /Ar flow, 10 K min ⁻¹ . (a) 20 mL min ⁻¹ ; (b) 40 mL min ⁻¹ ; (c) 40 mL min ⁻¹ (repeat); (d) 60 mL min ⁻¹	172
Figure G-1 Deconvolution of the H ₂ -TPD profile of the reduced Pd(8.7)/SiO ₂ . (---) measured TPD profile, (–) deconvoluted peaks, and red (–) cumulative fitting peaks.....	174
Figure G-2 Deconvolution of the H ₂ -TPD profile of the reduced Pd(5.7)-Cu(10)/SiO ₂ . (---) measured TPD profile, (–) deconvoluted peaks, and red (–) cumulative fitting peaks.....	175

Figure G-3 Deconvolution of the H ₂ -TPD profile of the reduced Pd(8.7)-Cu(10)/SiO ₂ . (---) measured TPD profile, (–) deconvoluted peaks, and red (–) cumulative fitting peaks.....	176
Figure G-4 Deconvolution of the H ₂ -TPD profile of the reduced Pd(15.7)-Cu(10)/SiO ₂ . (---) measured TPD profile, (–) deconvoluted peaks, and red (–) cumulative fitting peaks.....	177
Figure G-5 H ₂ -TPD profile of the bare support (amorphous silica).	178
Figure H-1 CO ₂ -TPD profiles of pre-reduced Pd(8.7)-Cu(10)/SiO ₂ . CO ₂ -TPD condition: 1 vol% Ar/He (30 mL min ⁻¹), 10 K min ⁻¹ of heating rate.....	179
Figure H-2 Deconvolution of the CO ₂ -TPD profile of the reduced Pd(8.7)/SiO ₂ . (---) measured TPD profile, (–) deconvoluted peaks, and red (–) cumulative fitting peaks.....	180
Figure H-3 Deconvolution of the CO ₂ -TPD profile of the reduced Cu(10)/SiO ₂ . (---) measured TPD profile, (–) deconvoluted peaks, and red (–) cumulative fitting peaks.....	181
Figure H-4 Deconvolution of the CO ₂ -TPD profile of the reduced Pd(2.5)-Cu(10)/SiO ₂ . (---) measured TPD profile, (–) deconvoluted peaks, and red (–) cumulative fitting peaks.....	182
Figure H-5 Deconvolution of the CO ₂ -TPD profile of the reduced Pd(5.7)-Cu(10)/SiO ₂ . (---) measured TPD profile, (–) deconvoluted peaks, and red (–) cumulative fitting peaks.....	183
Figure H-6 Deconvolution of the CO ₂ -TPD profile of the reduced Pd(8.7)-Cu(10)/SiO ₂ . (---) measured TPD profile, (–) deconvoluted peaks, and red (–) cumulative fitting peaks.....	184
Figure H-7 Deconvolution of the CO ₂ -TPD profile of the reduced Pd(15.7)-Cu(10)/SiO ₂ . (---) measured TPD profile, (–) deconvoluted peaks, and red (–) cumulative fitting peaks.....	185
Figure H-8 Deconvolution of the CO ₂ -TPD profile of the bare support (amorphous silica). (--) measured TPD profile, (–) deconvoluted peaks, and red (–) cumulative fitting peaks.....	186
Figure I-1 A schematic illustration for the pulse injection of 5 vol% CO/He in Ar (carrier gas) at 343 K.....	187

Figure I-2 Responses to 5 vol% CO/He pulses in Ar (carrier gas) at 343 K. Conditions: injection loop volume 0.518 mL (383 K), Ar flow rate 30 mL min ⁻¹	188
Figure I-3 A schematic illustration for the pulse injection of pure He in Ar (carrier gas) at 343 K.....	189
Figure I-4 Responses to pure He pulses in Ar (carrier gas) at 343 K. Conditions: injection loop volume 0.518 mL (383 K), Ar flow rate 30 mL min ⁻¹	189
Figure K-1 Schematic diagram of the fixed-bed flow reactor system for CO ₂ hydrogenation. .	202
Figure K-2 A schematic illustration for hydrogen temperature-programmed reduction (H ₂ - TPR) over promoted and unpromoted Pd catalysts.....	204
Figure K-3 A schematic illustration for hydrogen temperature-programmed reduction (H ₂ - TPR) promoted and unpromoted Pd catalysts.....	205
Figure K-4 A schematic illustration for carbon dioxide temperature-programmed desorption (CO ₂ -TPD) over promoted and unpromoted Pd catalysts.....	207
Figure K-5 A schematic illustration for the pulse injection of 1 vol% CO ₂ /He in He (carrier gas) at 343 K.	208
Figure K-6 Responses to 1 vol% CO ₂ /He pulses in He (carrier gas) at 343 K.....	208
Figure K-7 N ₂ adsorption isotherms (A-E) of support (solid symbol) and Ca-promoted Pd catalysts with a Ca/Pd molar ratio of 0.37 (open symbol): (A) MCM-48, (B) MCM-41, (C) SBA-15, (D) MSU-F, and (E) amorphous silica; (F) shows the isotherms of fresh (open symbol) and spent (solid symbol) Ca(0.37)/Pd(5.7)/SBA-15. Insets are BJH pore size distributions of corresponding supported Ca/Pd catalysts and pristine support materials....	215
Figure K-8 In-situ Pd K-edge FT-EXAFS of promoted and unpromoted Pd catalysts prepared from PN precursor solution, showing the formation of small Pd ⁰ nanoparticles on SBA-15	

after H ₂ reduction: (a) Pd foil, (b) Pd(4)/SiO ₂ , (c) Mg(0.5)/Pd(4)/SiO ₂ , (d)	
Ca(0.5)/Pd(4)/SiO ₂ , (e) Pd(4)/SBA-15, (f) Ca(0.5)/Pd(4)/SBA-15. H ₂ reduction conditions:	
673 K, 0.1 MPa	215
Figure K-9 TPR profiles of Ca-promoted and unpromoted Pd catalysts. The Pd loading for all	
samples was fixed at 5.7 wt% with PTAN as precursor, while Ca/Pd molar ratio ranged	
from 0.0 to 0.74 mol mol ⁻¹ . TPR conditions: 20 mL min ⁻¹ of 5 vol% H ₂ /Ar flow, 10 K min ⁻¹	
of heating rate. (a) Pd/SiO ₂ ; (b) Ca(0.37)/Pd/SiO ₂ ; (c) Ca(0.74)/Pd/SiO ₂ ; (d) Pd/SBA-15;	
(e) Ca(0.37)/Pd/SBA-15; (f) Ca(0.74)/Pd/SBA-15.....	221
Figure K-10 TPR profiles of Ca-promoted and unpromoted Pd catalysts and bare support. (a)	
Amorphous SiO ₂ ; (b) Ca(0.37)/SiO ₂ ; (c) Pd(5.7)/SiO ₂ ; (d) Ca(0.37)/Pd(5.7)/SiO ₂ . TPR	
conditions: 20 mL min ⁻¹ of 5 vol% H ₂ /Ar flow, 10 K min ⁻¹ of heating rate.	224
Figure K-11 Promoting effect of Ca on CH ₃ OH synthesis activity (Pd-time yield) for Pd	
catalysts supported on SiO ₂ and SBA-15. All catalysts in (A) were prepared by PN	
precursor, and the Pd loading was fixed at 4 wt%; all samples in (B) were prepared by	
PTAN precursor with a fixed Pd loading of 5.7 wt%. CO ₂ hydrogenation conditions: 523	
K, 4.1 MPa, W/F=6.2-6.3 g h mol ⁻¹	231
Figure K-12 Changes of CH ₃ OH formation rate in Pd-time yield and corresponding Pd ⁰	
dispersion as a function of Ca/Pd molar ratios. Reaction conditions: 523 K, 4.1 MPa,	
W/F=6.2 g h mol ⁻¹	234
Figure K-13 The stability test of CO ₂ conversion (open triangle) and formation rates of CO	
(closed circle) and CH ₃ OH (closed square) over PTAN-based Pd(5.7)/Ca(0.37)/SBA-15.	
CO ₂ hydrogenation conditions: 523 K, 4.1 MPa, 6.2 g h mol ⁻¹	235

Figure K-14 (A) Changes of CH₃OH formation rate over promoted and unpromoted Pd catalysts as a function of the average pore diameter of the support materials. (B) Dependencies of CH₃OH formation rate over Ca(0.37)/Pd(5.7) catalysts on averages pore diameter of the support materials. (C) Dependencies of CH₃OH formation rate over Ca(0.37)/Pd(5.7) catalysts on BET surface areas of the support materials. PTAN solution was used exclusively the preparation of catalysts. CO₂ hydrogenation conditions: 523 K, 4.1 MPa, 6.2-6.3 g h mol⁻¹ 238

ACKNOWLEDGMENTS

Over the past five years, I have received a lot of supports and encouragements from a number of people. I feel sincerely grateful to have such great opportunities to interact with them and learn from them, both of which, in return, help me make progress in my research and course studies. As I plan to move on, I would like to acknowledge those who have been always supportive by my side, and my dissertation cannot be completed without your enlightenments, inspiration, and kindness.

I wish to express my sincere gratitude to my advisor, Dr. Chunshan Song, for his guidance over the past five years. I would also like to thank Dr. Sarma Pisupati. Dr. Randy Vander Wal, and Dr. Michael Janik for their agreements on serving as my committee members and helpful discussions and invaluable advice during my studies. Although Dr. Yongsheng Chen and Dr. Donghai Wang are not available in my final dissertation defense due to the time conflict, their suggestion during my comprehensive examination is also acknowledged here.

I owe my deepest gratitude to my dissertation advisor, Dr. Chunshan Song, for his kindness and generosity to accept me at the beginning of my graduate study, his wisdom and passion to inspire me to confront the challenges and make research enjoyable while struggling, and also his profound philosophical knowledge to help construct my own significance of research and even life. He is the best advisor I could have wished for during my Ph. D. study. Dr. Song has his unique understandings of both teaching and researching arts as he always encourages me to think of every previous work critically, which has also been extended to my research as well. Besides, his idea of shifting the Ph. D. work into a three dimensional coordinate system impresses me, including working (x), thinking (y), and creating (z). These novel and characteristic ideas really prompt me

to think outside the box and open my mind. Besides, I also cherish those philosophical discussions on various aspects of research and life. Lastly, I know that updating myself from a linear or two-dimensional world to the advanced three-dimensional space would be my own energy barrier for further improvement, I will always bear the following most promising suggestions from Dr. Song through all my life: (i) in research, always stick to and focus on what you have observed based on your own data and always keep my mind open for other possibilities and new observations; (ii) in normal life, family is always the source and motivation for our improvement, depending upon which we can upgrade ourself and even contribute the human society to our best.

Another person who had a significant role to play during my graduate study is Dr. Naoto Koizumi. He taught me lots of fundamentals in the catalysis area at the beginning of my research in lab, which greatly helped me to adapt the laboratory and get knowing my own research topic as soon as possible. I especially appreciate his honest feedback, helpful discussion, and invaluable suggestions on every aspect of my work.

I would like to thank Dr. Xiaoxing Wang and Dr. Dongxiang Wang for their helpful discussions and suggestions during my research, especially when I was stuck. I would also like to thank the students from the Dr. Song's group for their support, feedback and friendship. Special mentions have to be made for Dr. Jiahua Guo and Dr. Chao Xie who were extremely helpful at the very beginning of my life in State College, and Sukanya Thepwatee and Pawnprapa Pitakjakpipop who have been always supportive during my struggles in experiments. Last but not least, special gratitude was also given to Michael Omelchenko who helped to correct and polish the language throughout this dissertation.

I extend my gratitude to the staff from both Energy Institute and the Department of Energy and Mineral Engineering. Cindy Anders, Angel Johnson, and Kelly Rhoades for helping me

process orders, reimbursement, room reservations, and schedule appointment; Miss Jaime Harter for being patient to answer all of my questions regarding course learning, examination arrangements, and graduation formalities.

In addition, I would also like to thank my master degree advisor, Dr. Xinwen Guo, from Dalian University of Technology, China, who first brought me into the world of research and science. I hope that I can finally appreciate his devotion by returning him with my doctoral degree and more endeavor in future.

Most importantly, I would like to show my sincere gratitude and endless love for my parents and family. For my parents, no words can explain how grateful I feel for you for binging me into this world and raising me up with all of your care, strength, and inspiration, and also giving me such great family to grow up with, my heroic grandfathers, kind-heated grandmothers, uncles, aunts, and parents in law. This dissertation would not have been possible without your care and support. Last but not least, I would like to thank my wife, Wenying Quan, for always being tender, kind, patient, and supportive by my side. Thank you for taking me out of the quagmire and making my life more shiny, colorful, and delightful.

I greatly appreciate the support provided by the Pennsylvania State University for supporting CO₂ conversion through the Penn State Institute of Energy and the Environment and providing the requisite facilities for the completion of my doctoral dissertation. Finally, the financial support from Chinese Scholarship Council (CSC) is gratefully acknowledged.

Chapter 1 Introduction

1.1 Background of research

1.1.1 Issue of CO₂ emission

CO₂, a main component of the greenhouse gases (e.g., 9-26%), can bring both advantages and disadvantages side by side. For example, the existence of CO₂, together with other greenhouse gases, is beneficial for creating a warm environment for living creatures on the earth, while the burning of fossil fuels causes the great rise of CO₂ concentration in the atmosphere (e.g., 20% increase in the last 50 years), generally leading to the substantial changes of the world's climate [1-3]. Nowadays, the rapid development of industry consumes a great amount of fossil fuel, which considerably increases the CO₂ emission. In 2005, approximately 28 Gt of CO₂ were produced and emitted by fossil fuel consuming processes [4]. Fig. 1-1 shows the changes in the global atmospheric CO₂ concentration for recent ca. 50 years, and the data was based on actual analyses in Hawaii (see notations below the figure). Clearly, the CO₂ concentration grows monotonically, and the very latest concentration has already broken 400 ppm level. Ongoing discussions at governmental levels worldwide are attempting to maintain and reduce the CO₂ concentrations in the atmosphere in following steps under a legal, conductive, economic, and efficient framework in the next couple of years [4].

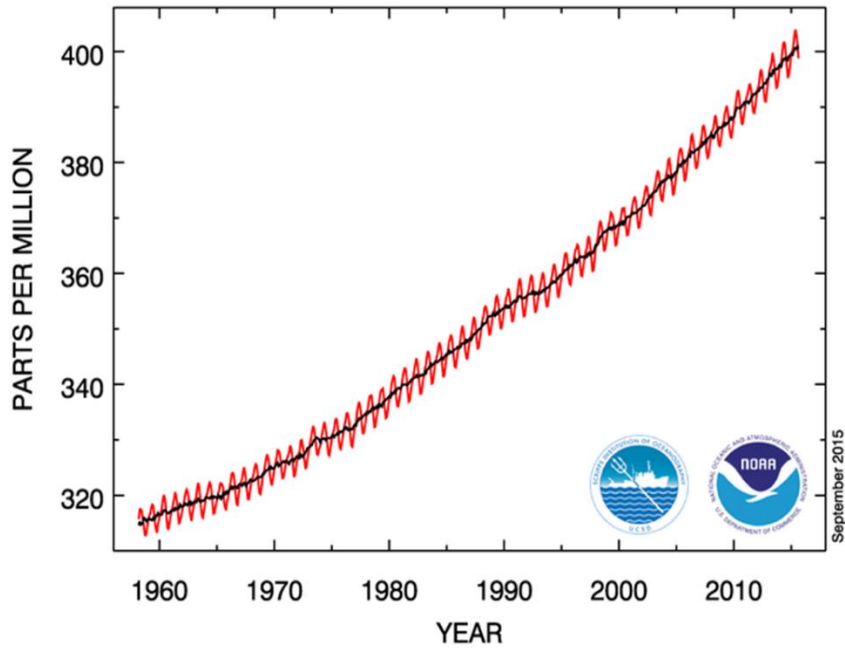


Figure 1-1 Monthly mean atmospheric carbon dioxide at Mauna Loa Observatory, Hawaii. The black curve represents the seasonally corrected data and the red one indicates the monthly corrected data. Trends in CO₂ values given are dry air mole fractions expressed in parts per million (ppm). National Oceanic & Atmospheric Administration (NOAA).

1.1.2 Catalytic CO₂ conversion

Although the influence of CO₂ emission is still in debate, many options have been figured out to control the CO₂ emission in the last decades. Developing and applying more energy efficient technologies can help to limit and control the CO₂ emission [4, 5]. However, it would be more promising to recycle such carbon source in the atmosphere with a sustainable chemical production, therefore, CO₂ needs to be captured and then reused as feedstocks.

In this context, the utilization of CO₂ as a carbon source for synthesizing chemical feedstocks and transportation fuels (e.g., heterogeneous, homogeneous, electrochemical, and photochemical conversion) has recently attracted great attention worldwide [5-14] because a major advance in energy-efficient catalytic CO₂ conversion using renewable energy could reduce both greenhouse-gas emissions and dependence on nonrenewable resources such as petroleum. The

synthesis of oxygenates and hydrocarbons from CO₂ hydrogenation using hydrogen produced with renewable energy such as solar energy, is one of the promising approaches for the environmentally-friendly synthesis of sustainable chemical feedstocks and fuels.

Methanol (CH₃OH) is an important chemical feedstocks [4] and can also be used as a fuel for internal combustion engines and fuel cells [15]. Industrially, methanol is produced from mixing feed gases (CO₂+CO)/H₂ (i.e., synthesis gas + CO₂) over a Cu/ZnO/Al₂O₃ catalyst, and typical reactions are operated at ~573 K and 7-12 MPa, such as the new ground-breaking Lurgi MegaMethanol® process for plants with 5000 tonnes of methanol per day [4]. The feed gas can be produced from steam reforming (i.e., CH₄ + H₂O = CO + 3H₂). An alternative route to produce synthesis gas (syngas), named dry reforming, has been proposed as well, which involves the reaction between CH₄ and CO₂, two inexpensive carbon-containing sources [16]. Based on early industrial applications of some technologies, Aresta and coworkers [17] roughly estimated the reduction amount of CO₂ in the short-medium period, and the value was 300Mt/year. Among them, the syngas hydrogenation (CO+CO₂+H₂) contributed 5-10 Mt/year, yet this did not include the contribution from direct CO₂ hydrogenation processes, such as NITE/RITE process in Japan [18, 19]. Thus, the methanol synthesis via CO₂ hydrogenation possesses immense potential to mitigate the CO₂ emission and facilitate the production of other useful chemicals in the downstream, such as dimethyl ether and formaldehyde.

Noteworthy, as long as the production of H₂ is relying upon fossil fuels, the benefits of the CO₂ hydrogenation to methanol will be mitigated or limited. If wind power, photovoltaic cells or excess nuclear power were applied to produce hydrogen via electrolysis, the whole process would be more sustainable [4, 20-23]. On the other hand, various processes and efficient adsorbents have been proposed to capture CO₂, including oxycombustion in pure oxygen [4], integrated

gasification combined cycle (IGCCs) [4, 24], and molecular-basket sorbent (MBS) [25, 26]. The applications of these processes can benefit the methanol synthesis via CO₂ hydrogenation by providing CO₂-rich or even pure CO₂ in the feed gases.

1.1.3 CH₃OH production in industry

Methanol, also known as wood alcohol, is largely considered as a candidate medium for energy storage because it can produce other useful chemicals in a value chain as feedstocks, such as formaldehyde (36 %), methyl tertiary-butyl ether/tertiary-amylmethylether (MTBE/TAME; 13 %), and acetic acid (9 %); moreover, a large variety of products could be produced via methanol-derived derivatives, e.g., olefins and acetate esters [27]. According to the Global Methanol Supply & Demand Estimates, the annual consumption of methanol is nowadays around 53 million tonnes in 2011, and it has become one of the most important and valuable commodities of the chemical industry.

In 19th century, the commercial CH₃OH production was produced by the destructive distillation of wood [27]. In 1920s, syngas, mainly CO and H₂, was introduced as feed gases to produce methanol, and the first industrial plant was built by BASF in 1923 [27]. In this process, ZnO/Cr₂O₃ was used as catalyst, and the reaction was operated at 573 K and 20 MPa. This process is also known as high-pressure methanol synthesis [16, 27, 28]. Most recently, a number of efforts have been devoted to improving the methanol synthesis activity based on early processes, and the predominant technology nowadays is a low-pressure process. In this process, Cu-Zn-Al₂O₃ is used as catalyst, and the reaction is usually operated at ca. 553 K and P < 10 MPa [4, 16, 29]. The feedstock, syngas, is obtainable by catalytic steam reforming (CH₄ + H₂O = CO + 3H₂) or non-catalytic partial oxidation of hydrocarbons or coal [4, 16]. CO₂ is introduced into the syngas to adjust the C/H ratio. At present stage, several companies could offer commercial technology

solutions to produce methanol based on this process, e.g., Lurgi [4, 27] and Mitsubishi [27]. For instance, the Lurgi MegaMethanol® plant started up in fall 2004 and possessed the ability to produce 5000 tonnes of methanol per day. Nevertheless, ongoing studies regarding the kinetics and the reaction mechanism are still carrying on to further improve the activity of methanol synthesis.

1.1.4 CH₃OH synthesis via CO₂ hydrogenation

CO hydrogenation to methanol had attracted great attentions in the last decades, and the mixing feed gases, namely CO+CO₂+H₂, were widely used in the methanol synthesis in industry [27, 28]. The addition of CO₂ (small concentration) in the syngas is to balance the C/H ratio to approximate the stoichiometry of CO hydrogenation to methanol. In order to clarify the role of CO₂ in the methanol synthesis on Cu-Zn-based catalyst, Liu and coworkers [30, 31] carried out a series of labeling studies. From the ¹⁸O labeling experiments, it was found that four parallel reactions were primarily involved on the catalyst, namely CO₂ dissociation to CO, reverse water-gas shift, CO hydrogenation, and CO₂ hydrogenation. More importantly, the ¹⁴C labeling experiment demonstrated that CO₂ was the source for methanol synthesis in feed gases. Later, similar conclusions were drawn by others [32, 33]. Thus, CO₂ hydrogenation started to attract attentions since mid-90s because it would be promising to recycle CO₂ as feedstocks and thus have great potential to control the CO₂ emission in medium-long term.

Preliminary results from CO₂ hydrogenation to methanol exhibited simple product distribution (mainly CO and CH₃OH as carbon-containing products) [16, 18]. Moreover, the selectivity towards methanol synthesis could be significantly improved by the catalysts even with higher purity than the commercial produced methanol [34]. In addition, the application of such CO₂-based methanol synthesis process may also facilitate the production of some methanol-

derived chemicals in the downstream, such as dimethyl ether (DME) [4, 35, 36]. Hence, various methods have been carried out in the past decades regarding the CO₂ conversion to methanol, such as heterogeneous [9] and homogeneous hydrogenation [37], electrochemical conversion [38], and photocatalytic conversion [39].

In following sections, the previous work regarding CO₂-based methanol synthesis is categorized and introduced concisely, particularly for Cu- and Pd-based catalysts in heterogeneous hydrogenation, which are relevant to the work in this dissertation. Other approaches for CO₂ conversion/reduction to methanol are also included and summarized briefly.

1.2 Thermodynamic issues of catalytic CO₂ conversion to methanol

As known, CO₂ is a highly stable molecule compared to CO, which makes it harder to be activated and converted subsequently. Thus, effective reaction conditions and active catalyst are necessary for the catalytic conversion of CO₂. Thermodynamically, the reaction would be energy-demanding if CO₂ were the single reagent; however, the energy demand could be reduced substantially if another substance with higher Gibbs free energy, e.g., H₂, were introduced as co-reagent [5].

Table 1-1 Reactions in methanol synthesis from CO₂/H₂.

Reactions	Chemical reaction	$\Delta H^0_{(T = 298 \text{ K})} / \text{kJ mol}^{-1}$
CO ₂ hydrogenation (HYD)	CO ₂ + 3H ₂ = CH ₃ OH + H ₂ O	-49.0
Reverse water-gas shift (RWGS)	CO ₂ + H ₂ = CO + H ₂ O	41.0
CO hydrogenation (HYD)	CO + 2H ₂ = CH ₃ OH	-90.4

Generally, three reactions are possibly involved in the methanol synthesis from CO₂/H₂, as tabulated in Table 1-1, including CO₂, CO hydrogenation, and reverse water-gas shift (RWGS) [2, 40-42]. Thermodynamically, the methanol formation, through either CO₂ or CO hydrogenation, is exothermic reaction, while the RWGS is endothermic reaction. Therefore, in order to remove the heat produced from the reaction, a fixed-bed reactor is appropriate for the exothermic reactions in lab-scale activity tests.

Additionally, changes of equilibrium CO₂ conversion and equilibrium CH₃OH yield as a function of temperature were calculated by software HSC 6.0 and plotted in Fig. 1-2 at different pressures, and the curve for CO hydrogenation at 4.0 MPa is also included for comparison. Clearly, the methanol synthesis via CO₂/H₂ favors lower temperature and higher pressure. Compared to CO hydrogenation, CO₂ hydrogenation to methanol is not thermodynamically favored at the same reaction conditions. Nevertheless, the CO₂ hydrogenation only produces CH₃OH and CO as carbon-containing components, which are far less than the syngas-based processes in industry (e.g., methanol, higher alcohol, dimethyl ether, and hydrocarbons, etc.). Moreover, as illustrated in Fig. 1-2B, higher reaction temperatures (e.g., > 535 K) favor the production of CO more than the methanol because the reverse water-gas shift reaction is an endothermic reaction. Thus, the design and development of catalyst with better activity at relatively mild reaction temperatures (ca. < 535 K) would become an important issue in this research field. In this context, considering the thermodynamic issues and maintaining the reaction kinetics, the reaction conditions are set at relatively mild conditions, namely 523 K and 4 MPa.

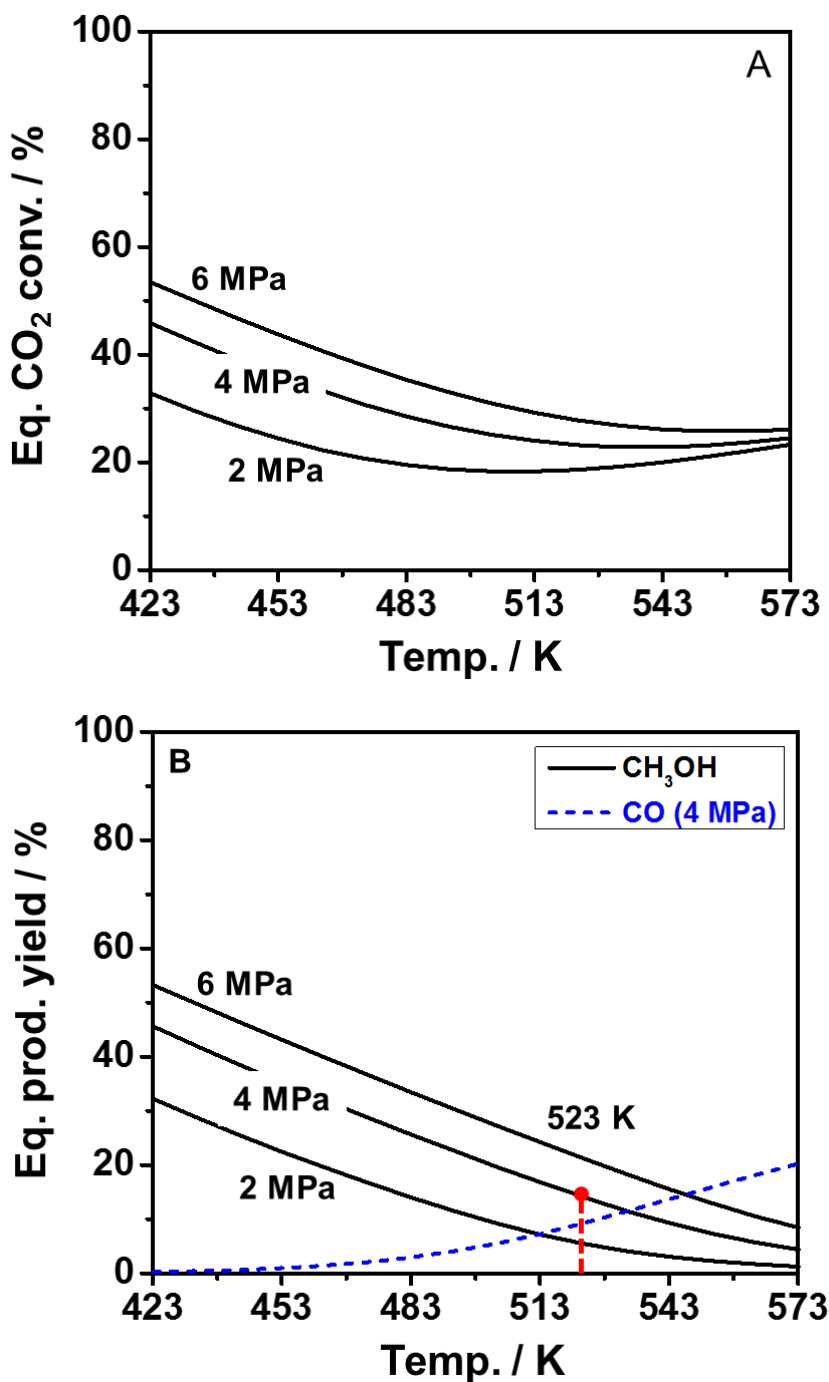


Figure 1-2 Changes of equilibrium CO₂ conversion % (A) and product yield % (B) as a function of temperature at pressures. (Calculated by HSC software).

Shen *et al.* [36] theoretically studied the effect of H₂/CO₂ ratios in feed gases on methanol synthesis activity via CO₂ hydrogenation, and corresponding results were reorganized and plotted

in Fig. 1-3. Clearly, at each pressure, higher H_2/CO_2 ratios facilitated the methanol yield. Similar simulation results were drawn by Skrzypek *et al.* [43]. Practically, Fan *et al.* [44] studied the H_2/CO_2 ratio effect on the methanol selectivity over Pd-based catalysts at ca. 3 MPa and found that the methanol selectivity was not affected significantly. Thus, it could be considered that the H_2/CO_2 had limited impact on the methanol yield and selectivity when the pressure is no greater than 5 MPa. Besides, the actual ratio must be adjusted for the economic viability. Therefore, the stoichiometric ratio, namely $\text{CO}_2/\text{H}_2=1/3$, is widely used in the investigation of CO_2 hydrogenation to methanol.

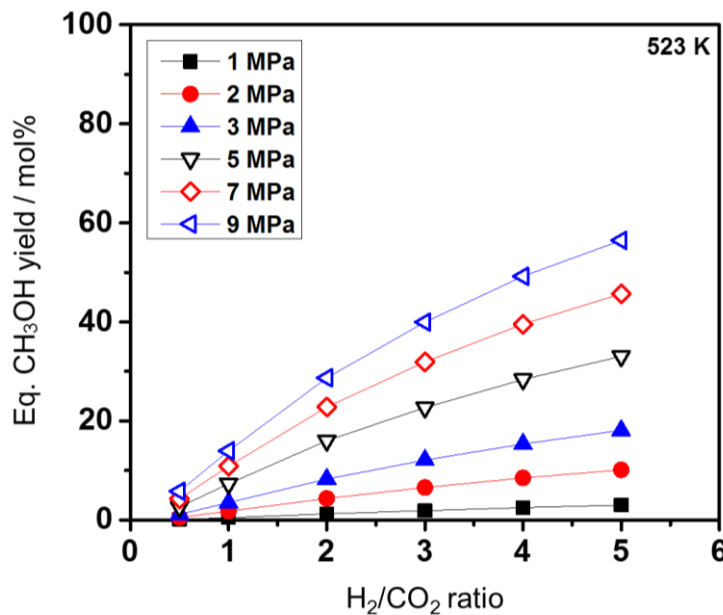


Figure 1-3 Changes of equilibrium CH_3OH yield as a function of H_2/CO_2 ratios at pressures. Simulating temperature: 523 K. Data was obtained based on theoretical calculations [36]. The original data was reorganized by the author and plotted in this figure.

1.3 Methanol synthesis activity over Pd-based catalysts

1.3.1 Activity performance over Pd-based catalysts via CO and CO₂ HYD

Supported Pd catalysts have been reported to be effective for CH₃OH formation from syngas (CO/H₂) at low temperatures [45]. Pd catalysts supported on La₂O₃ [46], Nd₂O₅ [46], and CeO₂ [47] can selectively hydrogenate CO into CH₃OH. Alkali and alkaline earth metals are also known as effective promoters for enhancing the CH₃OH synthesis activity of Pd/SiO₂ [42, 48]. Furthermore, Matsumura *et al.* [47] demonstrated that Pd/CeO₂ yielded 300 g kg-cat⁻¹ h⁻¹ of CH₃OH from syngas at 443 K and 3.0 MPa, whereas the Cu-ZnO catalyst required more severe reaction conditions, e.g., 503 K and 3.0 MPa, to yield comparable amounts of CH₃OH from syngas containing CO₂. Therefore, the Pd catalysts would be a potential candidate for the low-temperature CH₃OH synthesis catalyst via CO₂/H₂ as well as syngas. Thus, an improvement of their CH₃OH synthesis activity in CO₂ hydrogenation is an important challenge.

The investigations of Pd-based catalyst on methanol synthesis via CO₂ hydrogenation had started since 1990s. Fan and coworkers [44] prepared ceria-supported Pd catalysts (e.g., Pd = 4 wt% on support weight basis) and applied them in the activity test at 503 K and 3 MPa which were relatively milder than the Cu-Zn-based tests. Although the CO₂ conversion was only ca. 3%, the methanol selectivity reached 90 % with good durability. In addition, the H₂/CO₂ ratio in the feed gases were also studied, and the ratio was varied from 2-9. The results indicated that the ratio did not have significant impact on the production distribution. Thus, the stoichiometric ratio was suggested for the CO₂ hydrogenation if the cost of hydrogen consumption was considered. Considering the reported surface species from FT-IR spectra over the same catalysts [49, 50], the author inferred that the addition of Pd clearly improved the uptake of CO₂ as formate species which was proposed as an important intermediate during the methanol synthesis. Subsequently, the

metal-support interaction was studied, and the author proposed that new active sites were created on the metal-oxide interface, which played a critical role in CO₂ dissociation to CO [51]. As a result, the activated CO hydrogenation pathway was suggested to be responsible for the observed high methanol selectivity.

1.3.2 Reaction mechanism over Pd series catalysts

In an early study, Solymosi *et al.* [49] studied the methanol formation via CO₂/H₂ over Pd/SiO₂ catalysts by virtue of FT-IR technique. Formate and various carbonyl species were observed from the spectra. The former species was suggested to be adsorbed primarily on the support, which could undergo the fixation of CO₂ as carbonate species and then be hydrogenated to formate; the latter was adsorbed strongly on Pd through well-known π -back donation. More importantly, the production of CO may develop from either formate decomposition or CO₂ dissociation, or both.

Soon after, Erdohelyi and coworkers [50] confirmed the existence of both formate and carbonyl species from FT-IR spectra as well in CO₂ hydrogenation over similar monometallic Pd/SiO₂. Quantitatively, the amount of surface adsorbed formate species and the number of surface Pd atoms were found unmatched. Consequently, the support was believed to be responsible for the fixation of CO₂ as formate. Furthermore, the author suggested that the formate species was a potential intermediate for methanol formation because it was very sensitive to the reaction conditions. On the other hand, the CO₂ dissociation to CO was again confirmed to occur on Pd site, which was in harmony with others' observations [44, 51, 52]. Moreover, the methanol was possibly formed through CO hydrogenation pathway as well.

Noteworthy, the SiO₂-supported monometallic Pd catalysts exhibited very weak or even negligible absorption signals in the fingerprint region of carbonate species [49, 50]. As suggested,

CO_2 may initially be adsorbed on support as carbonate species and further fixated as formate species by the active hydrogen from Pd spilling over onto the support.

To sum up, in the CO_2 hydrogenation to methanol over Pd/SiO₂, four reactions might be involved, including CO_2 dissociation, reverse water-gas shift, formate-derived methanol formation, and adsorbed carbonyl-derived methanol formation. Thus, the formate species, CO_2 dissociation, and reactivity of carbonyl to methanol deserve great attention in this work.

1.3.3 Promoters effect

As reported by Prins *et al.* [42], the degree of rate enhancement of the doped Pd catalysts for the methanol formation varied as a function of the electronegativity (EN) of the additive cations, as shown in Fig. 1-4. As analyzed, basic (nucleophilic) OH groups presented on the oxide surface were responsible for the formation of formate species, and the hydrogenation rates of these intermediates were also correlated to the acid-base properties of additives. Metal oxides with low EN enhanced the surface concentration of formate, but their strong basic nature caused an excessive stabilization of formate. Consequently, the hydrogenation of formate to methanol was reduced by the weaker electrophilic character of the carbonyl carbon. On the other side, metal oxide with Lewis acid properties could increase the rate of formate hydrogenation potentially, however, the formation of adsorbed formate was limited by the lack of nucleophilic sites (OH group) on the surface. Therefore, the additives with moderate basicity would benefit the methanol formation to a large degree, such as CaO and MgO.

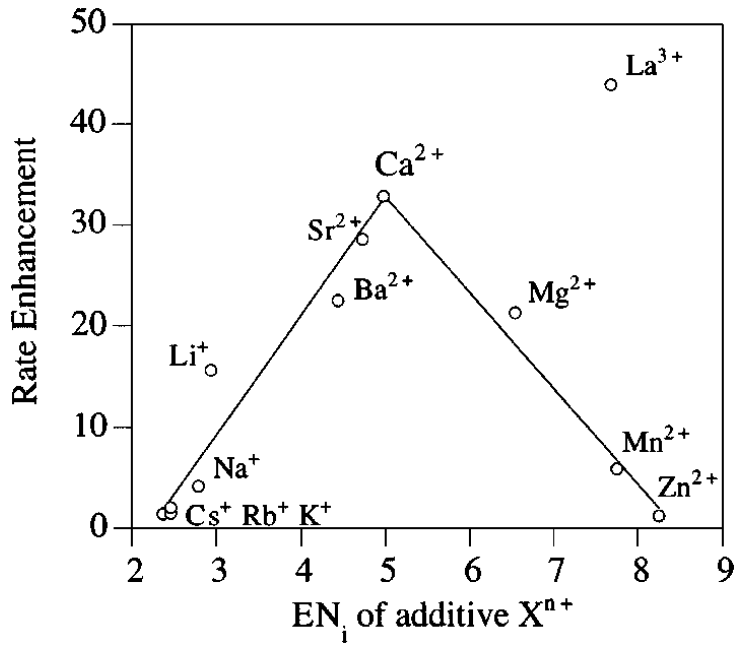


Figure 1-4 Rate enhancement for methanol formation in the hydrogenation of CO as a function of the electronegativity (EN) of the additive cation. Copied from the reference without further modification [42].

1.3.4 Support: Al_2O_3 vs. SiO_2

Although the amphoteric oxides, such as Al_2O_3 , possessed both acidic and basic sites, it had a negative impact on methanol formation. As reported, the Ca oxides interacted strongly with the acid sites on the surface of Al_2O_3 , which inhibited the bi-functional mechanism of Pd and CaO in the SiO_2 supported catalysts [42]. Moreover, Al_2O_3 was considered to be more active for hydrocarbons synthesis than oxygenates because of its strong acid sites as evidenced from literature as well [53, 54]. Therefore, the SiO_2 support was suggested to be more appropriate for methanol synthesis rather than Al_2O_3 . Mesoporous silicas, as support materials, attracted large attentions as a result of their ordered channel structures, narrow pore size distribution, high surface area, and pore volume [55]. MCM-type and SBA-serials mesoporous silica were characteristic in this big family and were widely used in preparations of different materials in different aspects, such as desulfurization [56], CO_2 capture [25], etc.. In particular, uniform pore structures of these

mesoporous materials may provide nano-sized, uniform reaction environments which enable the stabilization of small metal nanoparticles inside mesopores [57]. Thus, the mesoporous silica would be introduced as support material in this work, such as the traditional amorphous silica.

1.4 Methanol synthesis activity over Cu-based catalysts

1.4.1 Cu-based multicomponent catalyst

National Institute for Resources and Environment (NIRE) and Research Institute for Innovative Technology for the Earth (RITE), both from Japan, were pioneers to start the research project regarding CO₂ hydrogenation over Cu-Zn-based catalysts in both experimental scale and practical application in large scale. For a practical methanol synthesis process, it greatly requires an active catalyst with high and stable performance. In this context, NIRE and RITE had been jointly implicated in the development of Cu-Zn-based catalysts since 1990, and the developing progress can be traced from literature primarily reported by M. Saito and coworkers.

Initially, they started by testing the activity performances of Zn-deposited copper model catalyst in the methanol synthesis via CO₂ hydrogenation [58]. The results showed that the reactivity towards methanol formation depended upon the Zn coverage and revealed a volcano-like curve. Through the XPS analyses, the main role of the ZnO in Cu-Zn-based catalysts was to adjust the ratio of Cu⁰/Cu⁺ which was considered as active sites. In their following study, various metal oxides were introduced as additives to prepare a series of Cu-Zn-based catalysts [59]. Based on the screening tests, the key roles of these new additives could be classified into two categories: Al₂O₃/ZrO₂ was responsible for the improvement of Cu dispersion (i.e., surface area of metallic Cu⁰), while Ga₂O₃/Cr₂O₃ possessed the character to optimize the active sites (ratio of Cu⁰/Cu⁺) on the surface. Relying upon these preliminary results, the work was further extended to the tests of

Cu-Zn-based multi-component catalysts in the methanol synthesis [34]. In order to optimize the roles of different metal oxides, a four and a five-component catalysts were prepared by incorporating different metal oxides based on their categorized characters, namely Cu/ZnO/ZrO₂/Al₂O₃ and Cu/ZnO/ZrO₂/Al₂O₃/Ga₂O₃. Both of them showed markedly better performance compared to the ternary catalysts. More importantly, the activities were confirmed to be stable with the time on stream more than 2000 h in the lab-scale test, and the purity of produced crude methanol (ca. 99.96%) was comparable to that of the commercially synthesized crude methanol from syngas and even slightly higher (ca. 99.95%). Additionally, a type of recycle reactor, designed based on the multi-component catalysts, was employed in the activity test in order to reuse the unreacted reagents, mostly CO₂ and H₂. The schematic diagram is illustrated in Fig. 1-5. Since CH₃OH was produced selectively over these catalysts, the concentration of CO in the recycling gas was much lower. Consequently, such low CO concentration in the feed gases could largely limit the production of other byproducts, such as hydrocarbons.

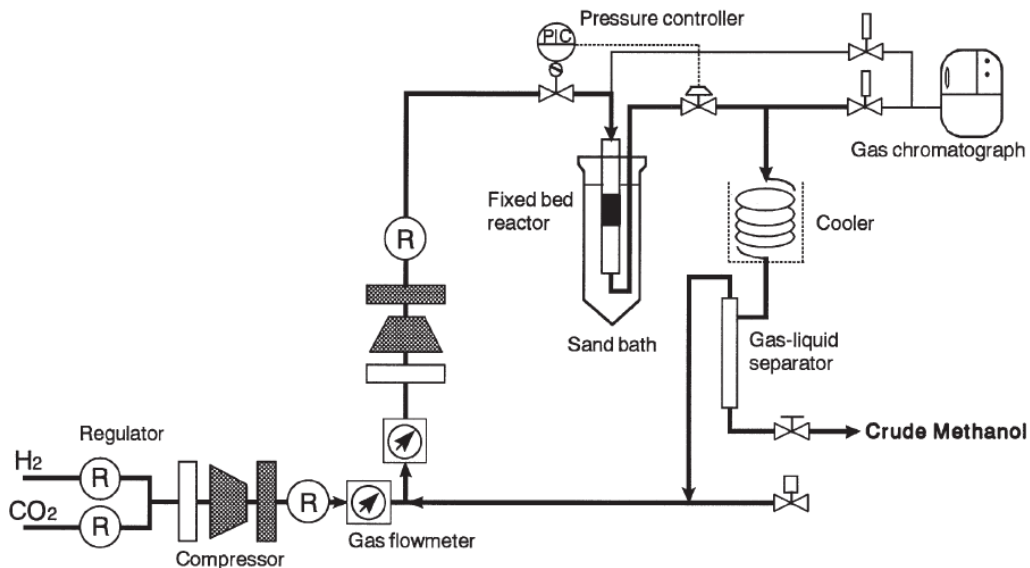


Figure 1-5 Schematic diagram of a recycle reactor designed for the Cu-Zn-based multi-component catalyst in methanol synthesis via CO₂ hydrogenation [19].

In their following study, the pilot-scale process was also designed and constructed for real application based on the multi-component catalysts. After a long-time test, the methanol formation was found to be stable with the time on stream [18, 19, 60-62]. In the meantime, the lab-scale research continued with more challenges to further improve their reactivity and stability, such as the influence of preparation method [63] and the introduction of Raney copper catalysts [64]. On the other hand, the exothermic property of the methanol synthesis can produce heat during the process, which could lead to the sintering of the Cu-Zn-based catalysts. To overcome this issue, the liquid phase methanol synthesis via CO₂ hydrogenation was designed and carried out as well, which focused on resolving two key issues: recycling of solvent and separation of products and solvent [19, 65].

Apart from Cu-Zn-based catalysts, the noble metal catalysts also drew their attention, such as Pd-based catalysts [19, 58]. Preliminary screening results showed that the Pd/Ga₂O₃ catalyst revealed better activity in both CO₂ conversion and turnover frequency (TOF) than other tested Pd-based catalysts, such as Al₂O₃, Cr₂O₃, Ga₂O₃, TiO₂, ZnO, and ZrO₂. Particularly, the Pd/Ga₂O₃ revealed more advanced activity than the conventional Cu-Zn-based catalyst by factors of 2 in yield and 20 in TOF. Such better activity performance can be ascribed to the influence of Ga₂O₃ which acted to optimize the amount of Pdⁿ⁺ over the catalyst surface.

In summary, their systematic work brought a great insight to the practical application of CO₂ hydrogenation in industrial to mitigate the CO₂ emission issue globally in short-medium term.

1.4.2 Reaction mechanism for both methanol synthesis and reverse water-gas shift

In the past decades, great efforts had been devoted to studying the mechanism of methanol synthesis via CO₂ hydrogenation over Cu-based catalysts. Although still in dispute, formate species was widely considered as an important intermediate in the methanol synthesis because the

formate adsorption and its subsequent hydrogenation to methoxy species were observed from FT-IR spectra [66-72]. In addition, since the Cu is also active for water gas shift (WGS) and reverse water-gas shift, the relevant intermediates and reaction pathways were investigated as well along with the methanol synthesis from CO₂/H₂ [73-75].

Most recently, Yang and coworkers [70, 76-78] studied the reaction mechanism and the water effect in the methanol synthesis via CO₂ hydrogenation, and a CO₂-containing syngas was also involved. Initially, depending upon the isotopic experiment and FT-IR technique (hydrogen titration), they observed that methanol could be produced from surface formate species on Cu/SiO₂ surface via CO₂ hydrogenation. Subsequently, a comprehensive scheme was proposed consisting of all possible reactions deriving from either pure CO₂/CO or mixed CO₂+CO hydrogenations, as shown in Fig. 1-6. In CO₂ hydrogenation, the methanol synthesis mainly underwent the left column, namely formate hydrogenation pathway, while the produced CO, from reverse water-gas shift, possessed the possibility to be further hydrogenated to formyl and ultimately to methanol through CO hydrogenation pathway. If the feed gases consisted of CO and CO₂, the carboxyl reaction pathway, the newly proposed one, was more favored due to its lower energy barrier, and the formate species, although still formed on the surface, became a stable spectator. However, the carboxyl formation was not evidenced from FT-IR spectra. Notably, the effect of water and reaction mechanism in both pure CO₂ and CO₂+CO (mixture) hydrogenations were studied by means of computational and experimental methods. The results showed that water and water-derived species acted as critical reactants and co-reactants in both reverse water-gas shift and methanol formation on copper surface.

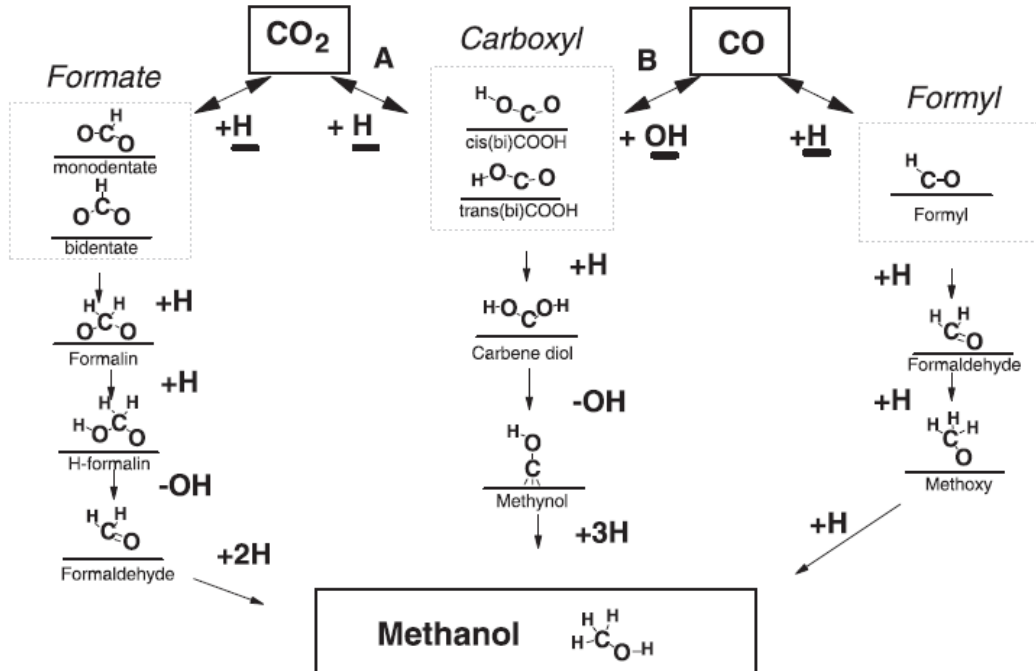


Figure 1-6 Schematic illustrations for conversion of pure CO_2 , pure CO, and CO_2+CO to methanol over Cu. The whole scheme was copied without modification, see Ref [76].

In addition, other surface species and surface reactions were also reported from literature, e.g., carbonate species and CO_2 dissociation. Clarke *et al.* [67] observed carbonate species on the metallic surface of Cu/SiO₂ and considered it as the precursor for the formation of formate species. On the other hand, Hadden *et al.* [79] studied the interaction between CO_2 and polycrystalline copper via radiolabeling techniques using ¹⁴CO₂ and temperature-programmed desorption (TPD). They found that CO₂ was weakly-adsorbed at the clean metallic surface, which could behave as the precursor to produce adsorbed CO and surface oxygen through dissociation and, hence, initiate the oxidation of the metallic surface. Such oxidized metallic surface could adsorb CO₂ more strongly, thus yielding a state which could be hydrogenated further to formate and, thereafter, to methanol.

To sum up, several important intermediates were proposed for the methanol synthesis from CO₂/H₂, including formate, carbonate, formyl, and carboxyl. Some of them are observable from

FT-IR spectra, some are not due to their poor stability or fast conversion. Therefore, these proposed potential intermediates would be instructive for the mechanism study in this work.

1.4.3 Cu-Zn alloy

In an early study, a synergetic effect was observed methanol synthesis via CO+CO₂ hydrogenation over Cu-ZnO-based catalysts [80]. Characterization results suggested that ZnO could behave as a reservoir for spillover hydrogen, thereby leading to methanol promotion. Soon after, Nitta *et al.* [81] studied the roles of ZnO in the Cu-Zr-based catalysts on methanol synthesis activity and selectivity via CO₂/H₂. The variations in activity performances between with and without ZnO addition indicated that the interface between Cu and ZrO₂ were more essential for methanol promotion. On the other hand, the primary role of ZnO was to increase the surface area of metallic Cu⁰ and its dispersion.

Fujitani and Nakamura and coworkers had comprehensively studied the reactivity of Cu/ZnO on methanol synthesis via CO₂ hydrogenation and the roles of ZnO in the methanol promotion in a series of literature [59, 82-86]. According to the established relationship between ZnO contents in catalysts and corresponding activity performances, the methanol formation was promoted with an appropriate amount of Zn doping; however, an excessive Zn doping caused the coverage of metallic Cu⁰ particles. In addition, the Zn-doped Cu catalysts showed a promoting methanol synthesis activity with the elevation of reduction temperature, which was not observed over the monometallic Cu catalysts, demonstrating that the new active sites might be created upon the high-temperature reduction program. The subsequent characterization results revealed the migration of the Zn species from ZnO to Cu in a physical mixture of Cu/SiO₂ and ZnO/SiO₂ upon reduction in H₂, and, thereby, new active sites, Cu-Zn alloy, were created for methanol synthesis. Combining the observations from in-situ FT-IR measurements, the author comprehensively

summarized the roles of ZnO: (i) the Cu⁰ dispersion could be improved with the doping of Zn; (ii) a novel active site, Cu-Zn alloy, could increase the surface coverage of formate species and facilitate its subsequent hydrogenation to methoxy. Besides, the changes of TOFs over Zn-doped Cu(111) surface varied as a function of Zn coverage, while the other two doped surfaces, namely Zn/Cu(110) and Zn/Cu(100), hardly revealed promotional effect with respect to Zn coverage. Thus, the methanol synthesis over Cu/ZnO catalysts was structure sensitive. During the experiment, the Cu-Zn alloy was found to retain metallic state basically, which further confirmed that Cu⁰, instead of Cu^{δ+}, was the active site for methanol formation. In the following step, for the purpose of providing a better environment for Cu-Zn alloy formation, the author also studied the effect of different Zn precursors, and aurichalcite (Cu, Zn)₅(CO₃)₂(OH)₆ was found to be an excellent potential precursor because the Cu and Zn ions were atomically mixed in the compound.

1.4.4 Deactivation

Wu *et al.* [87] investigated the effect of water on the stability of Cu/ZnO-based catalysts in the methanol synthesis activity. They found that the CO₂-rich feed (CO₂+CO) accelerated the crystallization of Cu and ZnO, which thereby led to the deactivation of the catalyst. Therefore, designing a water-tolerable catalyst is promising.

1.5 Other approaches

1.5.1 Photocatalytic conversion

He *et al.* [39] studied the catalytic behavior of ZnO/g-C₃N₄ (graphitic carbon nitride, with moderate band gap and high stability) in the efficiency conversion of CO₂ to fuels (CH₃OH, etc.) via photocatalysis (simulated sunlight irradiation). The characterization results showed that the

ZnO and g-C₃N₄ were uniformly combined, and the deposition of ZnO on g-C₃N₄ exhibited nearly no effect on its light-absorption performance. However, the two components promoted the formation of a hetero-junction structure in the composite, which inhibited the recombination of electron-hole pairs and, hence, enhanced the photocatalytic performance. The activity performance towards CO₂ conversion rate was 45.6 μmol g-cat⁻¹ h⁻¹ (ca. 0.01 μmol g-cat⁻¹ s⁻¹). This work provides promising insight in the CO₂ conversion to fuel using cost-efficient materials, and more efforts are still carrying on in this area [88, 89].

1.5.2 Electrochemical reduction

Perez-Rodriguez and coworkers [38] employed different novel carbon materials in the electroreduction of CO₂ to high-added value products, including CH₃OH. Carbon nanocoils (CNCs), carbon nanofibers (CNFs) and ordered mesoporous carbon materials (OMCs) had been studied as supports of the Pd-based catalysts. Various characterization techniques revealed that support presented different morphologies and structures. Specifically, CNFs and CNCs exhibited a crystalline structure with well-aligned graphitic layers, while OMCs possessed a hexagonal ordered structure composed of not crystalline carbon. These differences did not have significant impact on the average Pd crystallite size, even though the dispersion was found depending upon the carbon materials. In practical reaction, catalysts displayed different responses to hydrogen adsorption/absorption, evolution and oxidation processes, and such variations can reflect on the CO₂ electroreduction reactivity. Additionally, the textual properties of the support materials conditioned the diffusion hindrance of hydrogen which could be partially retained into the structure of carbon as absorbed species H_{ab}, apart from H_{ad}. On the other hand, the thin Rh, Pt, and Cu films were employed into the electrochemical promotion of the CO₂ reduction as well [90].

1.6 Motivations

As concisely introduced in sections 1.3 and 1.4, the industrial methanol synthesis was usually operated at relatively harsh conditions by using Cu-Zn-based catalysts (ca. 573 K and 7–12 MPa), where the methanol formation is not thermodynamically favored. Consequently, there is still a demand in developing the catalysts which are active at relatively mild temperatures (e.g., < 535 K). In mid-90s, noble metal catalysts, particularly Pd-based catalysts, started to attract attentions because of their superior activity at relatively mild temperatures towards methanol synthesis from CO₂/H₂, such as 443–503 K [44, 47, 51]. We have recently shown that nanostructured Pd catalysts with enhanced activities for CO₂ hydrogenation to CH₃OH can be prepared by combining uniform mesoporous supports and basic promoters [57]. The mesoporous silica could confine the growth of Pd⁰ nanoparticles, thereby providing more active hydrogen for the methanol synthesis. On the other side, Cu-Zn-based catalysts have been extensively studied in the past in methanol synthesis from CO₂, and Cu⁰ sites were proposed as the active sites to stabilize CO₂ on the surface as formate species with the promotional effect of ZnO. However, to our knowledge, little work has been reported on the catalytic properties of Pd-Cu bimetallic catalysts on the methanol synthesis activity via CO₂ hydrogenation. Thus, the Pd and Cu have different affinities towards different reagents in the CO₂ hydrogenation to methanol.

Most recently, our group reported that the Pd-Cu/CeO₂ bimetallic catalysts exhibited good activities in the oxygen-enhanced water-gas shift reaction [73–75]. The bimetallic catalyst with specific composition formed Pd-Cu alloy with highly dispersed metals as evidenced from EXAFS and XPS spectra. The alloy played an important role in the enhanced activity.

Consequently, due to different adsorptive properties of Pd and Cu towards the reagents and the potential of forming characteristic Pd-Cu alloy structure, it would be of great interest to study

whether the combination of Pd and Cu could synergetically promote methanol formation from CO₂ hydrogenation, not only for exploring new CH₃OH synthesis catalysts, but also for understanding the chemistry in methanol formation on the bimetallic surface.

As reported, the catalytic properties of bimetallic catalysts can be largely determined by the preparation methods, such as the solvent used during Pd precursor impregnation and the times of calcination [91-94]. In a recent work from our group, a coimpregnation method was used to prepare the desired bimetallic catalysts which showed alloy formation with specific composition [73-75]. Therefore, such preparation method is instructive and adoptable in this work.

1.7 Objectives, hypotheses, and dissertation outline

1.7.1 Objectives

The present work aims at clarifying the effect of combining Pd and Cu on the activity and selectivity towards methanol synthesis from CO₂ hydrogenation and developing a fundamental understanding on composition-structure-activity relationship. The specific objectives are:

Obj. 1: explore the effect of Pd and Cu composition on the activity and selectivity of methanol synthesis.

Obj. 2: investigate the influence of Pd loading on the structure of the bimetallic catalysts and its correlation with catalytic performance.

Obj. 3: clarify the effect of combining Pd and Cu on the surface chemical properties in CO₂ hydrogenation.

1.7.2 Hypotheses

Hypo. 1: The combination of Pd and Cu shows a synergetic effect on methanol formation from CO₂ hydrogenation.

Hypo. 2: Pd and Cu can form alloy that is catalytically more active for methanol formation than Pd and Cu alone.

Hypo. 3: The combination of Pd and Cu enhances the amount of CO₂ and H₂ on the surface.

1.7.3 Dissertation outline

Chapter 2: The effect of combining Pd and Cu on catalytic properties for CO₂ hydrogenation to methanol

Question 1: How do Pd and Cu compositions affect methanol SYN and how about the comparison to the catalytic performances over monometallic catalysts ?

- Activity test: Pd(X)-Cu(Y)/SiO₂, Cu/SiO₂, and Pd/SiO₂.
- Activity test: Impact of impregnation method and sequence on methanol synthesis activity.
- Stability test over bimetallic catalysts with the optimal metal composition.

Question 2: What is the effect of Pd loading on the crystalline structure of bimetallic catalysts?

- Physical properties: N₂ adsorption desorption
- Crystalline structure and crystallite size: XRD.
- Morphological properties: TEM & HAADF images.
- Metallic phase composition: STEM-EDS.
- Surface properties: XPS.

Question 3: What are the bimetallic catalyst composition-structure-catalytic performance relationships on methanol synthesis?

Question 4: What are the catalytic properties of Pd-Cu bimetallic catalysts supported on other mesoporous silicas (SBA-15, MCM-41, and MSU-F)?

- Activity test: Comparison of the activity performances among SBA-15, MCM-41, amorphous silica, and MSU-F-supported Pd-Cu bimetallic catalyst.

Question 5: What is the effect of mesoporous silicas with uniform pore structure on crystalline structure in bimetallic catalysts?

- Crystalline structure and crystallite size: XRD.
- Morphological properties: TEM.

Chapter 3: The effect of Pd and Cu combination on surface chemical properties in CO₂ hydrogenation to methanol

Question 1: What is the interaction between Pd and Cu in the bimetallic catalysts?

- Reducibility : H₂-TPR.
- Surface properties: XPS, discussed mainly in Chapter 2.

Question 2: What is the effect of Pd and Cu combination on the CO₂ and H₂ adsorption?

- H₂ adsorption properties: H₂-TPD.
- CO₂ adsorption properties: CO₂-TPD.

Question 3: What is the effect of Pd and Cu combination on the formation of surface species during the CO₂ hydrogenation?

- Surface species in reaction: DRIFTS.
- CO adsorption properties: CO-TPD.

Question 4: What is the possible reaction pathway?

- Activity test (effect of contact time): The impact of contact time will be investigated over the bimetallic catalysts with the optimal composition, and the resultant activity and

selectivity will be plotted in the selectivity-conversion form, wherein it shows the changes of production selectivity as a function CO₂ conversion.

1.8 Reference

- [1] C.D. Keeling, T.P. Whorf, Atmospheric CO₂ records from sites in the SiO air sampling network, in: Trends: A Compendium of Data on Global Change. Carbon Doxide Information Anlysis Center, Oak Ridge National Laboratory, U.S. Department of Energy, Oak Rdge, TN, USA, 2005.
- [2] Y. Borodko, G.A. Somorjai, Appl. Catal., A-Gen, 186 (1999) 355-362.
- [3] G.A. Florides, P. Christodoulides, Environ Int, 35 (2009) 390-401.
- [4] F. Pontzen, W. Liebner, V. Gronemann, M. Rothaemel, B. Ahlers, Catal. Today, 171 (2011) 242-250.
- [5] C. Song, Catal. Today, 115 (2006) 2-32.
- [6] M.B. Ansari, S.-E. Park, Energy & Environmental Science, 5 (2012) 9419-9437.
- [7] R.W. Dorner, D.R. Hardy, F.W. Williams, H.D. Willauer, Energy & Environmental Science, 3 (2010) 884-890.
- [8] P. Markewitz, W. Kuckshinrichs, W. Leitner, J. Linssen, P. Zapp, R. Bongartz, A. Schreiber, T.E. Müller, Energy & Environmental Science, 5 (2012) 7281-7305.
- [9] W. Wang, S. Wang, X. Ma, J. Gong, Chem. Soc. Rev., 40 (2011) 3703-3727.
- [10] M. Mikkelsen, M. Jørgensen, F.C. Krebs, Energy & Environmental Science, 3 (2010) 43-81.
- [11] Y. Li, S.H. Chan, Q. Sun, Nanoscale, 7 (2015) 8663-8683.
- [12] A. Le Valant, C. Comminges, C. Tisseraud, C. Canaff, L. Pinard, Y. Pouilloux, J. Catal., 324 (2015) 41-49.
- [13] E.V. Kondratenko, G. Mul, J. Baltrusaitis, G.O. Larraz ábal, J. Pérez-Ram íez, Energy & Environmental Science, 6 (2013) 3112-3135.
- [14] M. Drees, M. Cokoja, F.E. K ihn, ChemCatChem, 4 (2012) 1703-1712.

- [15] H. Arakawa, M. Aresta, J.N. Armor, M.A. Bartea, E.J. Beckman, A.T. Bell, J.E. Bercaw, C. Creutz, E. Dinjus, D.A. Dixon, K. Domen, D.W. Goodman, J. Keller, G.J. Kubas, H.H. Kung, J.E. Lyons, L.E. Manzer, J. Rostrup-Nielson, W.M.H. Sachtler, L.D. Schmidt, A. Sen, G.A. Somorjai, P.C. Stair, B.R. Stults, W. Tumas, *Chem. Rev.*, 101 (2001) 953-996.
- [16] R. Raudaskoski, E. Turpeinen, R. Lenkkeri, E. Pongrácz, R.L. Keiski, *Catal. Today*, 144 (2009) 318-323.
- [17] M. Aresta, A. Dibenedetto, *Catal. Today*, 98 (2004) 455-462.
- [18] J. Toyir, R. Miloua, N.E. Elkadri, M. Nawdali, H. Toufik, F. Miloua, M. Saito, *Phys. Procedia*, 2 (2009) 1075-1079.
- [19] M. Saito, *Catalysis Surveys from Japan*, 2 (1998) 175-184.
- [20] P. Galindo Cifre, O. Badr, *Energy Convers. Manage.*, 48 (2007) 519-527.
- [21] P. Galindo, O. Badr, *Energy Convers. Manage.*, 48 (2007) 519-527.
- [22] D. Mignard, M. Sahibzada, J.M. Duthie, H.W. Whittington, *Int. J. Hydrogen Energy*, 28 (2003) 455-464.
- [23] K. Liu, C. Song, V. Subramani, *Hydrogen and Syngas Production and Purification Technologies*, A John Wiley & Sons, Inc., New Jersey, 2010.
- [24] D. Mahajan, A.N. Goland, *Catal. Today*, 84 (2003) 71-81.
- [25] X. Ma, X. Wang, C. Song, *J. Am. Chem. Soc.*, 131 (2009) 5777-5783.
- [26] X. Wang, V. Schwartz, J.C. Clark, X. Ma, S.H. Overbury, X. Xu, C. Song, *J. Phys. Chem. C*, 113 (2009) 7260-7268.
- [27] M. Bertau, H. Offermanns, L. Plass, F. Schmidt, H.-J. Wernicke, *Methanol The Basic Chemical and Energy Feedstock of the Future*, Springer-Verlag Berlin Heidelberg, Berlin Heidelberg, 2014.

- [28] G.A. Olah, A. Goepert, G.K.S. Prakash, *Beyond Oil and Gas: The Methanol Economy*, WILEY-VCH Verlag GmbH & Co. KGaA, Weinheim, 2009.
- [29] Methanol Institutes, <http://www.methanol.org/>.
- [30] G. Liu, D. Willcox, M. Garland, H.H. Kung, *J. Catal.*, 90 (1984) 139-146.
- [31] G. Liu, D. Willcox, M. Garland, H.H. Kung, *J. Catal.*, 96 (1985) 251-260.
- [32] A. Coteron, A.N. Hayhurst, *Chem. Eng. Sci.*, 49 (1994) 209-221.
- [33] J.A.B. Bourzutschky, H. Homs, A.T. Bell, *J. Catal.*, 124 (1990) 73-85.
- [34] M. Saito, T. Fujitani, I. Takahara, T. Watanabe, M. Takeuchi, Y. Kanai, K. Moriya, T. Kakumoto, *Energy Convers. Manage.*, 36 (1995) 577-580.
- [35] L.C. Grabow, M. Marvrikakis, *ACS Catal.*, 1 (2011) 365-384.
- [36] W. Shen, K. Jun, H. Choi, K. Lee, *Korean J. Chem. Eng.*, 17 (2000) 210-216.
- [37] P.G. Jessop, F. Jo ó, C.-C. Tai, *Coord. Chem. Rev.*, 248 (2004) 2425-2442.
- [38] S. Pérez-Rodríguez, N. Rillo, M.J. Lázaro, E. Pastor, *Appl. Catal., B-Environ.*, 163 (2015) 83-95.
- [39] Y. He, Y. Wang, L. Zhang, B. Teng, M. Fan, *Appl. Catal., B-Environ.*, 168-169 (2015) 1-8.
- [40] J. Ma, N. Sun, X. Zhang, N. Zhao, F. Xiao, W. Wei, Y. Sun, *Catal. Today*, 148 (2009) 221-231.
- [41] A. Xu, S. Indala, T.A. Hertwig, R.W. Pike, F.C. Knopf, C.L. Yaws, J.R. Hopper, *Clean Techn. Environ. Policy*, 7 (2005) 97-115.
- [42] A. Gotti, R. Prins, *J. Catal.*, 175 (1998) 302-311.
- [43] J. Skrzypek, M. Lachowska, D. Serafin, *Chem. Eng. Sci.*, 45 (1990) 89-96.
- [44] L. Fan, K. Fujimoto, *Appl. Catal., A-Gen*, 106 (1993) L1-L7.
- [45] M.L. Poutsma, L.F. Elek, P.A. Ibarbia, A.P. Risch, J.A. Rabo, *J. Catal.*, 52 (1978) 157-168.

- [46] M. Ichikawa, K. Shikakura, *Shokubai*, 21 (1979) 253-255.
- [47] Y. Matsumura, W.-J. Shen, Y. Ichihashi, M. Okumura, *J. Catal.*, 197 (2001) 267-272.
- [48] Y. Kikuzono, S. Kagami, S. Naito, T. Onishi, K. Tamaru, *Faraday Discuss. Chem. Soc.*, 72 (1981) 135-143.
- [49] F. Solymosi, A. Erdohelyi, M. Lancz, *J. Catal.*, 95 (1985) 567-577.
- [50] A. Erdohelyi, M. Pasztor, F. Solymosi, *J. Catal.*, 98 (1986) 166-177.
- [51] L. Fan, K. Fujimoto, *Energy Convers. Manage.*, 36 (1995) 633-636.
- [52] L.F. Liotta, G.A. Martin, G. Deganello, *J. Catal.*, 164 (1996) 322-333.
- [53] R. Satthawong, N. Koizumi, C. Song, P. Prasassarakich, *J. CO₂ Util.*, 3-4 (2013) 102-106.
- [54] R. Satthawong, N. Koizumi, C. Song, P. Prasassarakich, *Top. Catal.*, 57 (2013) 588-594.
- [55] D. Zhao, J. Feng, Q. Huo, N. Melosh, G.H. Fredrickson, B.F. Chmelka, G.D. Stucky, *Sci.*, 279 (1998) 548-552.
- [56] C. Song, K.M. Reddy, *Appl. Catal., A-Gen*, 176 (1999) 1-10.
- [57] N. Koizumi, X. Jiang, J. Kugai, C. Song, *Catal. Today*, 194 (2012) 16-24.
- [58] T. Fujitani, M. Saito, Y. Kanai, T. Watanabe, J. Nakamura, T. Uchijima, *Appl. Catal., A-Gen*, 125 (1995) L199-L202.
- [59] J. Nakamura, I. Nakamura, T. Uchijima, Y. Kanai, T. Watanabe, M. Saito, T. Fujitani, *Catal. Lett.*, 31 (1995) 325-331.
- [60] M. Saito, M. Takeuchi, T. Watanabe, J. Toyir, S. Luo, J. Wu, *Energy Convers. Manage.*, 38 (1997) 403-408.
- [61] M. Saito, M. Takeuchi, T. Fujitani, J. Toyir, S. Luo, J. Wu, H. Mabuse, K. Ushikoshi, K. Mori, T. Watanabe, *Appl. Organomet. Chem.*, 14 (2000) 763-772.
- [62] M. Saito, K. Murata, *Catal. Surv. Asia*, 8 (2004) 285-294.

- [63] J. Wu, S. Luo, J. Toyir, M. Saito, M. Takeuchi, T. Watanabe, *Catal. Today*, 45 (1998) 215-220.
- [64] J. Toyir, M. Saito, I. Yamauchi, S. Luo, J. Wu, I. Takahara, M. Takeuchi, *Catal. Today*, 45 (1998) 245-250.
- [65] K. Hagihara, H. Mabuse, T. Watanabe, M. Saito, *Catal. Today*, 36 (1997) 33-37.
- [66] N. Nomura, T. Tagawa, S. Goto, *Appl. Catal., A-Gen*, 166 (1998) 321-326.
- [67] D.B. Clarke, A.T. Bell, *J. Catal.*, 154 (1995) 314-328.
- [68] J. Yoshihara, C.T. Campbell, *J. Catal.*, 161 (1996) 776-782.
- [69] F. Arena, G. Italiano, K. Barbera, S. Bordiga, G. Bonura, L. Spadaro, F. Frusteri, *Appl. Catal., A-Gen*, 350 (2008) 16-23.
- [70] Y. Yang, C.A. Mims, R.S. Disselkamp, D. Mei, J.-H. Kwak, J. Szanyi, C.H.F. Peden, C.T. Campbell, *Catal. Lett.*, 125 (2008) 201-208.
- [71] F.L. Peltier, P. Chaumette, J. Saussey, M.M. Bettahar, J.C. Lavalley, *J. Mol. Catal. A: Chem.*, 132 (1998) 91-100.
- [72] Z.-M. Hu, K. Takahashi, H. Nakatsuji, *Surf. Sci.*, 442 (1999) 90-106.
- [73] J. Kugai, E.B. Fox, C. Song, *Appl. Catal., A-Gen*, 497 (2015) 31-41.
- [74] J. Kugai, J.T. Miller, N. Guo, C. Song, *J. Catal.*, 277 (2011) 46-53.
- [75] J. Kugai, J.T. Miller, N. Guo, C. Song, *Appl. Catal., B-Environ.*, 105 (2011) 306-316.
- [76] Y. Yang, C.A. Mims, D.H. Mei, C.H.F. Peden, C.T. Campbell, *J. Catal.*, 298 (2013) 10-17.
- [77] Y.-F. Zhao, Y. Yang, C. Mims, C.H.F. Peden, J. Li, D. Mei, *J. Catal.*, 281 (2011) 199-211.
- [78] Y. Yang, C.A. Mims, R.S. Disselkamp, J.-H. Kwak, C.H.F. Peden, C.T. Campbell, *J. Phys. Chem. C*, 114 (2010) 17205-17211.
- [79] R.A. Hadden, H.D. Vandervell, K.C. Waugh, G. Webb, *Catal. Lett.*, 1 (1988) 27-34.

- [80] R. Burch, S.E. Golunski, M.S. Spencer, J. Chem. Soc., Faraday Trans., 86 (1990) 2683-2691.
- [81] Y. Nitta, O. Suwata, Y. Ikeda, Y. Okamoto, T. Imanaka, Catal. Lett., 26 (1994) 345-354.
- [82] J. Nakamura, T. Uchijima, Y. Kanai, T. Fujitani, Catal. Today, 28 (1996) 223-230.
- [83] T. Fujitani, I. Nakamura, S. Ueno, T. Uchijima, J. Nakamura, Appl. Surf. Sci., 121/122 (1997) 583-586.
- [84] T. Fujitani, I. Nakamura, T. Uchijima, J. Nakamura, Surf. Sci., 383 (1997) 285-298.
- [85] I. Nakamura, H. Nakano, T. Fujitani, T. Uchijima, J. Nakamura, Surf. Sci., 402-404 (1998) 92-95.
- [86] T. Fujitani, J. Nakamura, Appl. Catal., A-Gen, 191 (2000) 111-129.
- [87] J. Wu, M. Saito, M. Takeuchi, T. Watanabe, Appl. Catal., A-Gen, 218 (2001) 235-240.
- [88] T. Ohno, T. Higo, N. Murakami, H. Saito, Q. Zhang, Y. Yang, T. Tsubota, Appl. Catal., B-Environ, 152-153 (2014) 309-316.
- [89] Y. Lee, S. Kim, J.K. Kang, S.M. Cohen, Chem. Commun., 51 (2015) 5735-5738.
- [90] E.I. Papaioannou, S. Souentie, A. Hammad, C.G. Vayenas, Catal. Today, 146 (2009) 336-344.
- [91] I. Melian-Cabrera, M.L. Granados, P. Terreros, J.L.G. Fierro, Catal. Today, 45 (1998) 251-256.
- [92] I. Melian-Cabrera, M.L. Granados, J.L.G. Fierro, Catal. Lett., 79 (2002) 165-170.
- [93] I. Melian-Cabrera, M.L. Granados, J.L.G. Fierro, J. Catal., 210 (2002) 273-284.
- [94] I. Melian-Cabrera, M.L. Granados, J.L.G. Fierro, J. Catal., 210 (2002) 285-294.

Chapter 2 The Effect of Combining Pd and Cu on Catalytic Properties for CO₂ Hydrogenation to Methanol

This chapter was published in Applied Catalysis B: Environmental, volume 170, pages 173-185 in 2015 and was authored by Xiao Jiang, Naoto Koizumi, Xinwen Guo, and Chunshan Song*. Most parts of the original version were reorganized and rephrased by the author Xiao Jiang, and some complementary figures, tables, and discussions were also included.

Abstract

This paper reports on novel Pd-Cu bimetallic catalysts for selective CO₂ hydrogenation to methanol. A strong synergistic effect on promoting methanol formation was observed over amorphous silica supported Pd-Cu bimetallic catalysts when the Pd/(Pd+Cu) atomic ratios lied in the range of 0.25-0.34 (i.e., 5.7-8.7 wt% Pd loading). The methanol formation rate over Pd(5.7)-Cu(10)/SiO₂ was two times higher than the simple sum of those over monometallic Cu and Pd catalysts. The Pd-Cu bimetallic catalysts were characterized by X-ray diffraction, transmission electron microscopy, scanning transmission electron microscopy coupled with energy dispersive X-ray spectroscopy, and X-ray photoelectron spectroscopy. Detailed characterization results demonstrated the catalyst with the optimal metal composition only showed the coexistence of uniform and nano-sized Pd-Cu alloy particles with two different stoichiometric ratios, namely PdCu₃ and PdCu, which was correlated to the superior synergistic effect on catalytic performance. A similar bimetallic promotion was also observed for other mesoporous silica supported Pd-Cu catalysts, and MCM-41 and SBA-15 supported Pd(5.7)-Cu(10) catalysts showed a better synergistic effect than other mesoporous silicas supported counterpart. This can be attributed to their smaller pore diameter and/or surface chemical nature.

Keywords: CO₂ hydrogenation, Pd-Cu bimetallic catalyst, Methanol, Pd-Cu alloy formation, Support effect

2.1 Introduction

Utilization of CO₂ as a carbon source for synthesizing chemical feedstocks and transportation fuels has recently attracted great attention worldwide [1-13] because a major advance in energy-efficient catalytic CO₂ conversion using renewable energy could reduce both the greenhouse-gas emissions and the dependence on nonrenewable resources such as petroleum. The synthesis of oxygenates and hydrocarbons from CO₂ hydrogenation using hydrogen produced with renewable energy such as solar energy, is one of the promising approaches for the environmentally-friendly synthesis of sustainable chemical feedstocks and fuels.

Methanol (CH₃OH) is an important chemical feedstock and can also be used as a fuel for internal combustion engines and fuel cells. Over the past two decades, significant efforts have been devoted to developing effective catalysts for CO₂ hydrogenation to CH₃OH. These previous studies focused mainly on improving the activity and selectivity of Cu-Zn based catalysts by, e.g., exploring effective promoters and supports, or developing new preparation methods [14-26]. For the Cu-Zn system, Zn is well known as an effective promoter. Nakamura *et al.* [27] studied mechanistic aspects of the role of the Zn promoter using a Zn doped Cu(111) model catalyst, demonstrating that the addition of Zn to the Cu surface formed Cu-Zn alloy that decreased the stability of adsorbed formate species, which the authors considered as a crucial intermediate for CH₃OH formation. However, Cu-Zn based catalysts require higher temperatures for CO₂ hydrogenation at adequate rates, while hydrogenation to CH₃OH is favorable thermodynamically at lower temperatures. At the typical reaction condition for the Cu-Zn catalyst (573 K and 4.1 MPa), the equilibrium yield of CH₃OH is only 14%.

Several researchers have reported that Pd nanoparticles supported on metal oxides possess the ability to hydrogenate CO₂ to CH₃OH [28-35]. Supported Pd nanoparticles have been reported

to be active for CH₃OH formation from CO hydrogenation [36-39]. CeO₂ supported Pd catalysts showed excellent activities for CO hydrogenation to CH₃OH even at low temperatures where Cu-ZnO based catalysts did not work well [37]. We have recently shown that nano-structured Pd catalysts with enhanced activities for CO₂ hydrogenation to CH₃OH can be prepared by combining two different strategies, namely incorporation of uniform mesoporous supports such as MCM-41 and SBA-15 leading to small Pd nanoparticles inside nano-sized pore channels, and promotion by alkali/alkaline earth metal additives [40]. K(Ca)-promoted Pd supported on SBA-15 yielded 2-5 times more methanol than a conventional amorphous silica supported Pd catalyst. However, current Pd catalysts yield much smaller amounts of CH₃OH from CO₂ hydrogenation compared to the Cu-Zn based catalysts [32], although the Pd catalysts would be a potential candidate for low-temperature CH₃OH synthesis using CO₂.

In addition to Cu-based and Pd-based catalysts, it has been reported that the metallic Cu-Ni alloy surface is active for CO/CO₂ hydrogenation to CH₃OH [41, 42]. In this context, it is interesting to clarify if the combination of Pd and Cu could result in more active catalysts for CO₂ hydrogenation to methanol. It is known that Pd and Cu can form stable alloy after the reduction [43, 44]. Moreover, compared to Cu-Zn alloy, Pd-Cu alloy may promote CH₃OH with different active sites. Therefore, it would be of great interest to see if the Pd-Cu alloys with different compositions promote CO₂ hydrogenation, not only for exploring new CH₃OH synthesis catalysts, but also for understanding the chemistry in CH₃OH formation on the metallic alloy surface. Previous work showed that Pd-Cu bimetallic catalysts were active for hydrogenation of unsaturated organic compounds [45-47] and oxygen-enhanced water-gas shift reaction [48, 49]. However, to our knowledge, little has been reported on the Pd-Cu bimetallic catalyst for CO₂ hydrogenation to CH₃OH.

The aim of this work is to explore the catalytic properties of Pd-Cu bimetallic catalysts for CO₂ hydrogenation to methanol. A series of supported Pd-Cu catalysts with a wide range of Pd and Cu loadings were prepared using amorphous silica and uniform mesoporous silica (SBA-15, MCM-41, and MSU-F) as supports. CO₂ hydrogenation activity and selectivity over these bimetallic catalysts were investigated under pressurized conditions and also were compared to those over Cu-ZnO counterparts. In order to examine the structure-activity relationships for Pd-Cu catalysts, these catalysts were also characterized by powder X-ray diffraction (XRD), transmission electron microscopy (TEM), scanning transmission electron microscopy/energy dispersive X-ray spectroscopy (STEM/EDS), X-ray photoelectron spectroscopy (XPS), and temperature programmed desorption of hydrogen (H₂-TPD).

2.2 Experimental

2.2.1 Preparation of catalysts

Amorphous silica (Davisil Grade 62, particle size=75-250 × 10⁻⁶ m) was used as support. MCM-41 and SBA-15 were prepared according to the procedures reported previously [50-52], and the detailed preparation method is referring to Appendix A. MSU-F is a mesoporous silica (purchased from Aldrich) with a hexagonal and cellular foam-like structure containing large pores and well cross-lined framework walls.

Amorphous silica supported Pd-Cu bimetallic catalysts were prepared mainly by two methods: the stepwise incipient wetness impregnation in aqueous solution and the coimpregnation in acetone solution. The former one used Pd(NH₃)₄(NO₃)₂ (Alfa Aesar, Pd=3.162 wt%, density=2.01 g cm⁻³) and Cu(NO₃)₂·2.5H₂O (Alfa Aesar, ≥ 98 %) as precursors, and the catalyst was prepared stepwise in an aqueous solution. This catalyst was only calcined once in an electric

furnace at 723 K for 5 h under flowing dry air (ca. 100 mL (NTP) min⁻¹). The latter Pd-Cu bimetallic catalysts were prepared by coimpregnation method using an acetone solution of Pd(CH₃COO)₂ (Aldrich, > 99.9%) and Cu(NO₃)₂·2.5H₂O (Alfa Aesar, ≥ 98 %) [53]. The impregnated samples were dried at ambient temperature and calcined in an electric furnace by using a similar temperature program. The Cu/(Pd+Cu) atomic ratios were varied in the range of 0.0 to 0.94 (i.e., 0-50 wt% of Cu loading), and Pd/(Pd+Cu) atomic ratios ranged from 0.0 to 0.60 (i.e., 0-15.7 wt% of Pd loading). The coimpregnation method was also carried out for preparing uniform mesoporous silicas supported Pd-Cu bimetallic catalysts (e.g., SBA-15, MCM-41, and MSU-F). Note that different mesoporous silica supported monometallic catalysts were also prepared using the impregnation method in an acetone solution, and Pd acetate was employed exclusively as precursor for Pd-containing catalysts.

For comparison, Pd-Cu bimetallic catalysts were also prepared by the sequential impregnation onto the amorphous silica using an acetone solution of the same precursors with different impregnation sequences, and the composition of the catalysts was maintained identical to the coimpregnated sample. The precursor for Pd (or Cu) was impregnated first and dried at ambient temperature followed by the impregnation of the Cu (or Pd) precursor without an intermediate calcination. The sequentially impregnated Pd-Cu samples were calcined at the same conditions as those for coimpregnated samples.

Additionally, amorphous silica supported Cu-Zn catalysts and commercial Cu-ZnO-Al₂O₃ catalyst (MDC-3, Süd-Chemie, 40 wt% Cu, 20-32 meshes) were also tested. Amorphous silica supported Cu-Zn bimetallic catalysts were prepared using Zn(NO₃)₂·6H₂O (Alfa Aesar, 99.998 %) as the Zn source, and the Cu loading was fixed at 10 wt% (support weight basis). The Zn/(Zn+Cu) atomic ratio ranged from 0.0 to 0.80.

The bimetallic catalysts, prepared by the coimpregnation method, are denoted as Pd(X)-Cu(Y)/support and Cu-ZnO(Z)/SiO₂, where X, Y, and Z represent Pd loading (support basis), Cu loading (support basis), and Zn/(Zn+Cu) atomic ratios, respectively. Monometallic catalysts are denoted as Pd/support and Cu/support, and the metal loadings of Pd and Cu are 5.7 wt% and 10 wt%, respectively, unless otherwise noted. Generally, the catalysts, denoted with a hyphen (-) in between two metals, are prepared by the coimpregnation method, while the sequential method prepared samples are marked with a slash (/) in between metals. The metal next to the support in the denotation is impregnated first.

2.2.2 Catalytic test

The prepared catalysts were tested at 4.1 MPa using a fixed bed reactor system consisting of a stainless steel tube with an internal diameter of 6 mm placed in an electrically heated oven. The reaction system was illustrated in Fig. 2-1. The gases, H₂ (99.995 %) and CO₂/H₂/Ar (24/72/4, vol%, 99.995 %) were used without further purification. The flow rate and pressure of these gases were regulated with mass flow controllers and a backpressure regulator, respectively. The amount of catalyst used in a typical run was 0.20 g. The amorphous silica supported catalysts were diluted by inert amorphous silica particles (ca. 0.42 g) of the same size to attain an aspect ratio of approximately 6.0, while other mesoporous silica supported catalysts with lower densities (e.g., SBA-15, MCM-41, and MSU-F) were not diluted. In the catalyst pretreatment, the catalyst bed was heated up to 573 K in a stream of H₂ at a ramp rate of 2.3 K min⁻¹ and then maintained isothermally at this temperature for 2 h. After H₂ reduction, the temperature was reduced to the ambient temperature. The feed gas CO₂/H₂/Ar was then employed to pressurize the system to 4.1 MPa (GHSV=3600 mL(STP) g-cat⁻¹ h⁻¹), and the reactor system was heated up to 523 K at a ramp rate of 1.9 K min⁻¹ for the catalytic reaction.

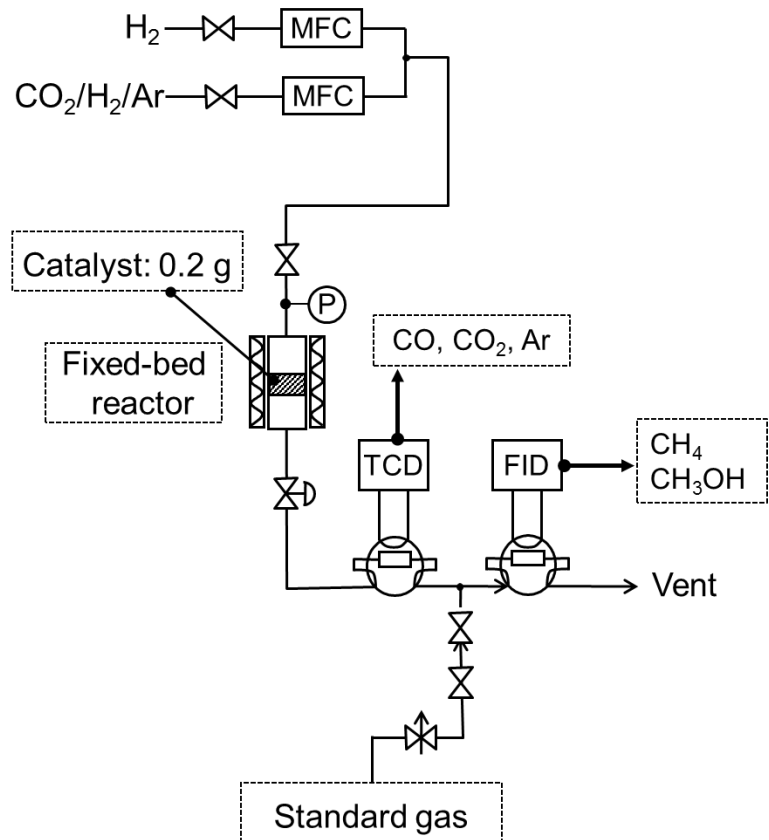


Figure 2-1 Schematic diagram of the fixed-bed flow reactor system for CO_2 hydrogenation.

Gaseous products were periodically sampled with computer-controlled gas samplers and analyzed by two online GCs (SRI 8610C). The online GC/TCD was used to analyze Ar, CO and CO_2 , while the other online GC/FID was for CH_3OH and CH_4 . Ar was an internal standard to estimate the CO_2 conversion, and CH_4 was employed as an external standard for measuring the methanol formation rate.

The activity and selectivity of the catalysts were evaluated by the values obtained at about 12 h on-stream. The carbon balance was estimated according to the ratio between the simple summation of CO and CH_3OH formation rates and CO_2 conversion rate. All data published in this work lie within a reasonable range close to 100 mol%. In the investigation of the effect of Pd-Cu bimetallic catalysts, Pd(8.7)-Cu(10)/ SiO_2 showed the maximum CH_3OH formation rate, and the

repeatability was ensured by five separate runs. The standard deviations for CO₂ conversion, CH₃OH formation rate, and CO formation rate over this sample were 0.2 %, 0.02 μmol g-cat⁻¹ s⁻¹, and 0.01 μmol g-cat⁻¹ s⁻¹, respectively. The general deviations for CO₂ conversion, CH₃OH formation rate, and CO formation rate varied from 0.1-0.3 %, 0.01-0.03 μmol g-cat⁻¹ s⁻¹, and 0.01-0.03 μmol g-cat⁻¹ s⁻¹, respectively.

2.2.3 Passivation of reduced/spent catalysts

In order to preserve the alloy phase after the reduction or reaction for further characterization, the reduced and spent catalysts were passivated in O₂/He (0.97/99.03, vol%, 99.995%) at ambient temperature for 4 h. The flow rate was set at ca.20 mL (STP) min⁻¹. The catalysts were then collected and hereafter simply denoted with an italic prefix of *reduced* or *spent* in front of the catalysts.

2.2.4 Characterization of catalysts

The N₂ adsorption–desorption isotherms for the catalysts in the calcined form and corresponding pristine mesoporous materials were measured in a Micromeritics ASAP 2020 instrument. The samples (ca. 60 mg) were degassed at 523 K for nearly 12 h prior to analyses. Specific surface areas were estimated by using the B.E.T. approach. Pore size distributions were obtained by applying the B.J.H. formalism to the desorption branches of the isotherms.

XRD patterns of the catalysts were collected using a PANalytical Empyrean X-Ray Diffractometer with Cu Kα ($\lambda=0.154059$ nm) radiation, and fixed slit incidence (0.25° divergence, 0.5° anti-scatter, specimen length 10 mm) and diffracted (0.25° anti-scatter, 0.02 mm nickel filter) optics. Samples were prepared by the back-loading method in which a powder sample is pressed into the cavity of a quartz zero-background support. Data was collected at 45 kV and 40 mA from

30-90° (2θ) using a PIXcel detector in scanning mode and 255 active channels for a duration time of ~20 min. Resulting patterns were corrected for both 2θ position and instrumental peak broadening using NIST (National Institute of Standards and Technology) 640c silicon and analyzed with Jade 2010 software by MDI of Livermore, CA. All of the XRD patterns were replotted after background subtraction and curve fitting. The crystal sizes of different metal phases in the samples were determined from the full width at half maximum (FWHM) of the (111) peaks using Scherrer equation,

$$D = \frac{K \cdot \lambda}{\beta * \cos\theta} \quad \text{Eq. 2-1}$$

where the K is a dimensionless shape factor, with a value close to unity, λ is the X-ray wavelength (0.154059 nm), θ is the Bragg angle, D is the mean size of ordered crystalline domains, and β is the FWHM in radians after correction. The composition of each phases were also quantified by the semi-quantitative method using Jade 2010, and detailed procedure is described in Appendix D.

The *reduced* Pd-Cu bimetallic catalysts were analyzed by the transmission electron microscopy (TEM, Tecnai G220 S-Twin, 200 kV, FEI Company). Reduced samples were first collected after the passivation and then ultrasonicated in ethanol. A few droplets of ethanol suspension were dripped onto a carbon-coated copper grid followed by drying at ambient temperature. Typically about 30 micrographs were taken for each sample. Alloy Pd-Cu particle size histograms were generated by counting at least 150 particles.

The morphological properties and elemental distribution of *reduced* Pd-Cu bimetallic catalysts were also studied by the scanning transmission electron microscopy in conjunction with the energy-dispersive X-ray spectroscopy (STEM/EDS) using a FEI Titan G2 TEM equipped with a spherical aberration corrector on the probe-forming lens at an accelerating voltage of 300 kV.

EDS maps were acquired in the Titan using ChemiSTEM quad detectors at a current of 0.12 nA for 10 minutes. Standardless Cliff-Lorimer quantification was done on the deconvoluted EDS line intensity data using the Bruker Esprit software. The sample preparation procedure was very similar to TEM samples. Noteworthy, a carbon-coated molybdenum grid was applied to avoid the interference from Cu in both mapping and quantifying.

X-ray photoelectron spectra (XPS) were acquired on a Kratos Axis Ultra using monochromatic Al-K α radiation (1486.6 eV). The anode voltage and current were 14 keV and 20 mA, respectively. Analytical chamber pressures were in the low 10^{-8} torr range during data acquisition. All spectra were acquired in hybrid slot mode, with the charge-neutralizer on. The neutralizer filament current was set at 2.2 amps, while the charge balance and filament bias settings were 1 volt and 3 volts, respectively. High resolution spectra were acquired at a pass energy of 40 eV, with a step size of 0.2 eV. A dwell time of 2500 ms was used for the Cu 2p, C 1s, and Pd 3d peaks. The dwell times for the O 1s and Si 2p peaks were 800 and 1500 ms, respectively. Survey spectra were acquired at a pass energy of 80 eV, with 0.5 eV steps, and a 150 ms dwell time. All spectra were acquired in one sweep. The analysis area was roughly 1 mm in diameter. Transmission function corrections were provided by the Kratos software, and all data were processed with CASA XPS, using the following RSF values: Pd 3d (5.323), Cu 2p $3/2$ (3.134), Si 2p (0.303), C 1s (0.297), and O 1s (0.703). The BE scale was calibrated using the BEs of Au 4f $7/2$, Ag 3d $5/2$, and Cu 2p $3/2$ at 83.96, 368.21, and 932.62 eV, respectively. All spectra were charge corrected to Si 2p at 103.5 eV (see Appendix C). All samples, including the bare support silica, were reduced under the same conditions, with subsequent passivation. Surface carbon was detected in all samples and included in the calculation of surface composition. The atomic concentrations of palladium, copper, silicon, carbon, and oxygen were calculated from peak areas obtained from the high-resolution spectra,

using a Shirley background subtraction.

2.3 Results and discussion

2.3.1 Synergetic effect of Pd and Cu on CO₂ hydrogenation

To identify the effect of Cu and Pd loadings, two series of amorphous silica supported Pd-Cu bimetallic catalysts with different metal loadings, Pd(X)-Cu(Y)/SiO₂, were prepared and tested for CO₂ hydrogenation under pressurized reaction conditions. For comparison, the reaction conditions were maintained the same to our recent work over Ca-promoted Pd catalysts, namely at 523 K and 4.1 MPa [40]. These bimetallic catalysts yielded only CO and CH₃OH as carbon-containing products. Both CO₂ conversion and products formation rates were practically constant from 5 h to 20 h on stream. Thus, the activity and selectivity of the bimetallic catalysts reported here were collected at 10-12 h on stream.

Fig. 2-2A illustrates the changes of both CO₂ conversion and product formation rates over Pd(5.7)-Cu(Y)/SiO₂ catalysts as a function of the Cu/(Pd+Cu) atomic ratio, and the activity performances of monometallic catalysts are included as well. The ratio was varied by changing the Cu loading from 0 to 50 wt%, and the Pd loading was initially fixed at 5.7 wt% based on our recent work [40]. In Fig. 2-2A, the CO₂ conversion of Pd/SiO₂ is 3 %. Only a small amount of CH₃OH is obtained in the product stream, and CO is produced selectively. On the other hand, the CO₂ conversion increases gradually with the increment of Cu loading and maximizes at the Cu/(Pd+Cu) ratio of 0.9. The formation rate of CO changes in a similar way. Differently, the CH₃OH formation rate maximizes at a slightly lower Cu/(Pd+Cu) atomic ratio, namely 0.75 (i.e., Cu loading=10 wt%). Since the optimal CH₃OH formation rate was obtainable at 10 wt% Cu loading, this value would be fixed in the following activity tests of Pd loading.

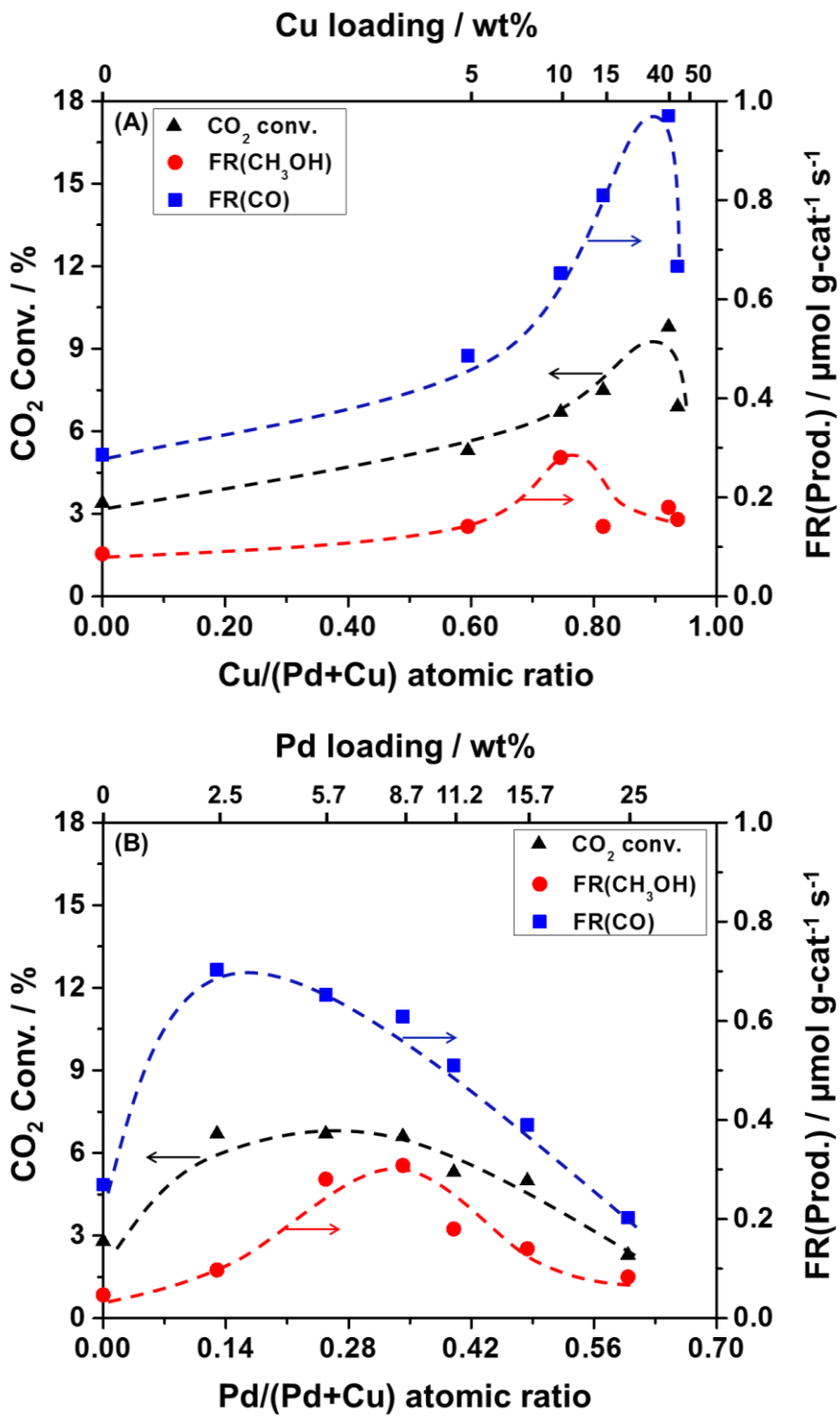


Figure 2-2 Changes in CO₂ conversion and formation rate of products (CH₃OH and CO) over Pd(5.7)-Cu(Y)/SiO₂ with a fixed Pd loading at 5.7wt% (A) and Pd(X)-Cu(10)/SiO₂ with a fixed Cu loading at 10 wt% (B) as functions of Cu/(Pd+Cu) and Pd/(Pd+Cu) atomic ratios, respectively. CO₂ hydrogenation conditions: 523 K, 4.1 MPa, 6.2 g-cat h mol⁻¹.

The effect of combining Pd and Cu was also investigated with different Pd/(Pd+Cu) atomic ratios while keeping Cu loading constant at 10 wt%. As illustrated in Fig. 2-2B, the trends of both CO and CH₃OH formation rates exhibit a volcano-like shape with the rise of Pd/(Pd+Cu) atomic ratio, and the CH₃OH maximizes in the range of 0.25-0.34 (i.e., Pd loading 5.7-8.7 wt%). Within this range, the CH₃OH space time yield (STY) over Pd(8.7)-Cu(10)/SiO₂ is 0.31 μmol g-cat⁻¹ s⁻¹. This yields almost 6 times more CH₃OH than the monometallic Cu/SiO₂ with the same Cu loading, and the CH₃OH selectivity is also doubled from 15 to 34 mol%. Thus, the optimal Pd/(Pd+Cu) atomic ratio appears to be 0.34, which corresponds to the metal loadings of 8.7 wt% Pd and 10 wt% Cu in the bimetallic catalyst. Table 2-1 summarizes both CO₂ hydrogenation activity and product selectivity over Pd(5.7)-Cu(10)/SiO₂ in comparison to those of monometallic Pd(5.7)/SiO₂ and Cu(10)/SiO₂ catalysts. The formation rate of CH₃OH on the bimetallic catalyst is 2 times as much as the simple sum of those over monometallic catalysts, indicating a significant synergetic promotion on CH₃OH formation.

In addition, it is noticeable that the maximum STYs of CO and CH₃OH formation rates appear at different atomic ratios, implying that CO may also contribute to the methanol formation through CO hydrogenation other than direct CO₂ hydrogenation. The possible reaction pathways involved in this work will be discussed in Chapter 3.

Table 2-1 CO₂ hydrogenation activity and product selectivity over supported Pd-Cu and Cu-Zn catalysts ^{a, b)}

Support	Composition	CO ₂ conv. / %	Prod. selec. / mol%		Formation rate / $\mu\text{mol g-cat}^{-1} \text{s}^{-1}$	
			CO	CH ₃ OH	CO	CH ₃ OH
SiO ₂	Pd _{5.7}	3.0 ± 0.1	77	23	0.29 ± 0.01	0.09 ± 0.02
	Cu	2.8 ± 0.1	85	15	0.27 ± 0.01	0.05 ± 0.01
	Pd _{5.7} -Cu	6.7 ± 0.3	70	30	0.65 ± 0.03	0.28 ± 0.01
	Pd _{8.7} -Cu	6.6 ± 0.2	66	34	0.61 ± 0.01	0.31 ± 0.02
	Pd _{5.7} /Cu-I ^{c)}	4.0	80	20	0.41	0.10
	Pd _{8.7} /Cu-II ^{d)}	5.0	77	23	0.50	0.16
	Cu/Pd _{8.7} -II ^{d)}	4.9	76	24	0.50	0.15
MCM-41	Pd _{5.7}	< 1	--	--	0.02	< 0.01
	Cu	< 1	60	40	0.03	0.02
	Pd _{5.7} -Cu	6.2	77	23	0.61	0.18
SBA-15	Pd _{5.7}	< 1	--	--	0.01	< 0.01
	Cu	1.5	88	12	0.21	0.03
	Pd _{5.7} -Cu	6.5	77	23	0.67	0.20
MSU-F	Pd _{5.7}	< 1	86	14	0.11	0.02
	Cu	< 1	82	18	0.13	0.03
	Pd _{5.7} -Cu	5.3	82	18	0.50	0.11
Cu-Zn(0.50)/SiO ₂ ^{e)}		1.7	61	39	0.11	0.07
Cu-Zn(0.67)/SiO ₂ ^{e)}		2.2	50	50	0.12	0.12
Cu-Zn(0.80)/SiO ₂ ^{e)}		2.2	54	36	0.13	0.11
Cu-ZnO-Al ₂ O ₃ ^{f)}		18.4	73	27	1.26	0.48

^{a)} Reaction conditions: 523 K, 4.1 MPa, GHSV=3600 mL(STP) g-cat⁻¹ h⁻¹. General deviations for CO₂ conversion, CH₃OH formation rate, and CO formation rate varied from 0.1-0.3 %, 0.01-0.03 $\mu\text{mol g-cat}^{-1} \text{s}^{-1}$, and 0.01-0.03 $\mu\text{mol g-cat}^{-1} \text{s}^{-1}$, respectively.

^{b)} Most catalysts were prepared by coimpregnation method, unless specially noted. The Pd loading was subscripted next to Pd symbol. The Cu loading for all Cu-containing catalysts was fixed at 10 wt%.

^{c)} Catalyst was prepared by stepwise incipient wetness impregnation method in an aqueous solution.

^{d)} Catalysts were prepared by sequential impregnation method in an acetone solution.

^{e)} Catalysts were prepared by coimpregnation method in acetone solution. Cu loading was 10 wt%.

^{f)} MDC-3 commercial catalyst (Cu loading=40 wt%), 20-32 meshes.

For comparison, the Pd-Cu bimetallic catalysts were also prepared by the stepwise incipient wetness impregnation method (Method I) and the sequential-wet impregnation method (IWI,

Method II). The former method used aqueous solutions of $\text{Pd}(\text{NH}_3)_4(\text{NO}_3)_2$ and $\text{Cu}(\text{NO}_3)_2$, while the latter one employed acetone solutions of $\text{Pd}(\text{CH}_3\text{COO})_2$ and $\text{Cu}(\text{NO}_3)_2$, and the activity performances are compared in Table 2-1. Actually, the coimpregnation of $\text{Pd}(\text{CH}_3\text{COO})_2$ and $\text{Cu}(\text{NO}_3)_2$ precursors in an aqueous solution was attempted as well in the beginning; however, these two precursors were found to be immiscible. Thus, the stepwise IWI was used instead. The bimetallic catalyst prepared by Method-I barely show any advances in either conversion, product formation, or selectivity, and the CH_3OH STY is only 1/3 of the catalyst prepared by the coimpregnation method. On the other hand, sequentially impregnated bimetallic catalysts, $\text{Pd}_{5.7}/\text{Cu-II}$ and $\text{Cu/Pd}_{5.7}\text{-II}$, show almost similar activities, and both are more active than the $\text{Pd}_{5.7}/\text{Cu-I}$ and monometallic catalysts. Nevertheless, neither of them reveals a comparable methanol formation rate nor selectivity compared to coimpregnated samples with the same metal loadings. In fact, XRD results demonstrate that the formation of alloy phases is sensitive to the impregnation method and, thereby, influential to activity performances. It is found that the specific order of the sequential impregnation has little impact on the formation of alloy phases, thus leading to identical activity of the two catalysts. The correlation between the alloy formation and preparation methods will be discussed in a later section. Due to the observed superior activity toward methanol synthesis, the coimpregnation method in an acetone solution of $\text{Pd}(\text{CH}_3\text{COO})_2$ and $\text{Cu}(\text{NO}_3)_2$ was used exclusively throughout this work.

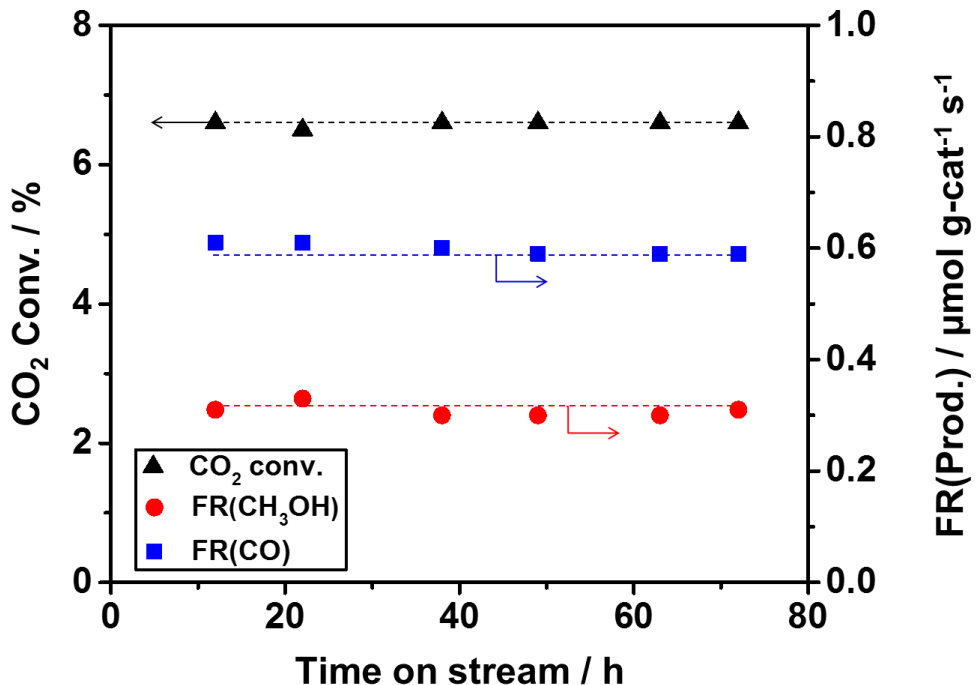


Figure 2-3 Stabilities of CO₂ conversion and products formation rates with time on stream over Pd(8.7)-Cu(10)/SiO₂. CO₂ hydrogenation conditions: 523 K, 4.1 MPa, 6.2 g-cat h mol⁻¹.

Fig. 2-3 demonstrates the good stabilities of CO₂ conversion and product formation rates over Pd(8.7)-Cu(10)/SiO₂. Both CO₂ conversion and product formation rates remain constant with the time on stream more than 70 h, and no deactivation of the CH₃OH synthesis activity is observed.

2.3.2 Support effect on CH₃OH formation over Pd-Cu bimetallic catalysts

Most recently, we have incorporated the mesoporous silicas, such as MCM-type materials, SBA-15, and MSU-F, into the preparation of nano-structured Pd catalysts, and their impacts on methanol synthesis activity were investigated [40]. In this context, it would be of great interest to examine the effect of these mesoporous silicas on the CH₃OH synthesis activity over Pd-Cu bimetallic catalysts. Thus, MCM-41, SBA-15, and MSU-F supported Pd-Cu bimetallic catalysts and corresponding monometallic catalysts were prepared, and the activity tests were also carried out over these catalysts, as summarized in Table 2-1. Pd and Cu loadings were fixed at 5.7 wt%

and 10 wt%, respectively, where the Pd loading was maintained similar as the Ca-promoted Pd catalysts deliberately for comparison [40].

Table 2-1 reveals that the formation rate of CH₃OH over supported Pd-Cu catalysts decreases in the following order: amorphous silica > SBA-15 ~ MCM-41 > MSU-F. The amorphous silica supported Pd-Cu catalyst showed the highest CH₃OH selectivity (ca. 30 mol%) among the bimetallic catalysts. It is also worth mentioning that the CH₃OH formation rates over MCM-41, SBA-15, and MSU-F supported bimetallic catalysts are all greater than the simple summation of those obtained over corresponding monometallic catalysts. Thus, the bimetallic synergistic effect on CH₃OH promotion is observed for these mesoporous silicas supported Pd-Cu catalysts as well. In fact, XRD patterns (Figs. 2-5 and 2-6) confirm the formation of nano-sized alloy particles over these bimetallic catalysts, which are responsible for such significant synergistic effect on methanol promotion compared to corresponding monometallic catalysts.

Most recently, the effect of mesoporous silica supports on CH₃OH synthesis activity over a series of Ca-promoted Pd catalysts was studied by our group [40]. The formation rate of CH₃OH varied as a function of the average pore diameters of mesoporous silica supports; the maximum CH₃OH formation rate was obtained over Ca promoted Pd(5.7 wt%)/MCM-41, which yielded 0.22 μmol g-cat⁻¹ s⁻¹ under the same reaction conditions. In contrast, the bimetallic catalyst, Pd(5.7)-Cu(10)/SiO₂, yields 0.28 μmol g-cat⁻¹ s⁻¹, which further improves the methanol formation rate by 27 %.

2.3.3 Comparison to Cu-Zn based catalysts

Cu-Zn(Z)/SiO₂ catalysts were prepared similarly as Pd-Cu catalysts, and their CO₂ hydrogenation activity and product selectivity over a representative sample are shown in Table 2-1. The reaction was conducted at the same conditions as well. Cu loading was fixed at 10 wt%,

while the Zn/(Zn+Cu) atomic ratio was adjusted by changing Zn loading. Within the Zn atomic ratio range (ca. 0 to 0.80) tested, the CH₃OH formation rate is enhanced slightly from 0.05 (Cu/SiO₂) to 0.12 μmol g-cat⁻¹ s⁻¹ when gradually doping Zn into Cu/SiO₂. Apparently, the improvement is not as significant as the Pd-Cu bimetallic catalysts, nor is the CO₂ conversion. In addition, the maximum CH₃OH formation is obtained over Cu-Zn(0.67)/SiO₂; however, it is not comparable to the result over Pd(5.7)-Cu(10)/SiO₂ with the same Cu loading (e.g., 0.12 < 0.28 μmol g-cat⁻¹ s⁻¹). Therefore, the novel Pd-Cu bimetallic catalyst shows a better activity performance than the Cu-ZnO-based catalysts prepared by the coimpregnation method.

A commercial Cu-Zn-Al₂O₃ catalyst (MDC-3, Süd-Chemie, 40 wt% Cu) was also tested as reference. As tabulated in Table 3-1, MDC-3 and Pd(5.7)-Cu(10)/SiO₂ show identical product selectivities, whereas the CH₃OH formation rate over Pd(5.7)-Cu(10)/SiO₂ accounts for ca. 60 % of that over MDC-3. The different metal loadings may cause such variation. Thus, the metal efficiency was introduced to evaluate their activities in the form of metal time yield (MTY) which was calculated by normalizing the CH₃OH formation rate to the total amount of metal loadings in the catalyst. The metal time yields are 0.16 mmol mol-(Pd+Cu)⁻¹ s⁻¹ and 0.08 mmol mol-Cu⁻¹ s⁻¹ for Pd(5.7)-Cu(10)/SiO₂ and MDC-3, respectively, implying that the bimetallic Pd-Cu/SiO₂ exhibits a better metal efficiency for CH₃OH synthesis than the MDC-3, even without considering the metal loading of Zn.

2.3.4 Physical properties of Pd-Cu catalysts

Physical properties of both *calcined* Pd-Cu bimetallic catalysts with different Pd/(Pd+Cu) atomic ratios and bare support materials were examined by N₂ adsorption-desorption measurements, and the resultant physical parameters are summarized in Table 2-2. The isotherms of two representative bimetallic catalysts in the calcined form, namely Pd(5.7)-Cu(10)/SiO₂ and

Pd(5.7)-Cu(10)/SBA-15, and corresponding pristine support materials are also depicted in the Fig. 2-4, along with their pore size distribution (PSD) charts in the insets.

Table 2-2 Physical properties of supported Pd(X)-Cu(10) catalysts ^{a)}

Catalyst ^{b)}	BET surface area /m ² g-cat ⁻¹	Pore volume ^{c)} /mL g-cat ⁻¹	Average pore ^{d)} diameter / nm
Pd _{2.5} -Cu/SiO ₂	304 (315)	0.9 (1.1)	9.9 (11.0)
Pd _{5.7} -Cu/SiO ₂	305	0.9	9.4
Pd _{8.7} -Cu/SiO ₂	309	0.8	9.3
Pd _{15.7} -Cu/SiO ₂	292	0.8	8.9
Pd _{5.7} -Cu/MCM-41	950 (1102)	1.1 (1.4)	3.6 (3.6)
Pd _{5.7} -Cu/SBA-15	553 (719)	0.9 (1.2)	6.1 (6.3)
Pd _{5.7} -Cu/MSU-F	457 (611)	1.6 (2.5)	12.0 (13.0)

^{a)} Values in parentheses are for corresponding pristine support materials.

^{b)} Cu loading was 10 wt% for all samples in the table.

^{c)} BJH desorption cumulative pore volume.

^{d)} BJH desorption average pore diameter.

As illustrated from Fig. 2-4A, the isotherm of Pd(5.7)-Cu(10)/SiO₂ in the calcined form is consistent with that of the amorphous silica in the whole range of relative pressure, implying that the mesopores are preserved during the catalyst preparation. Besides, both BET surface area and pore volume of *calcined* Pd(X)-Cu(10)/SiO₂ catalysts noticeably declined after the catalyst preparation in comparison to those of bare amorphous silica, especially in the case of higher Pd metal loading. Such differences can be ascribed to the incorporation of active metals inside the mesopores of the support. On the other hand, the isotherm of SBA-15 supported Pd(5.7)-Cu(10) also shows a resemblance as that of SBA-15 (Fig. 2-4B), again indicating the preservation of mesoporous structure after the preparation. Besides, as tabulated in Table 2-2, both BET surface area and pore volume for other mesoporous silica supported bimetallic catalysts reduce evidently

after the metal loadings. The average pore diameters of the MSU-F and SBA-15 supported Pd(5.7)-Cu(10) catalysts decrease by 1 nm and 0.2 nm, respectively, which can be attributed to the incorporation of Pd and Cu species into the mesopores of the support materials. Contrarily, such reduction is not observed for the MCM-41 supported counterparts. A possible explanation is that the average pore diameter of MCM-41 is too small to incorporate two metal oxides inside the pores in the meantime. Instead, only a small amount of metallic particles is incorporated inside the pores or plugged in the pore mouth, which causes the significant reductions in both surface area and pore volume.

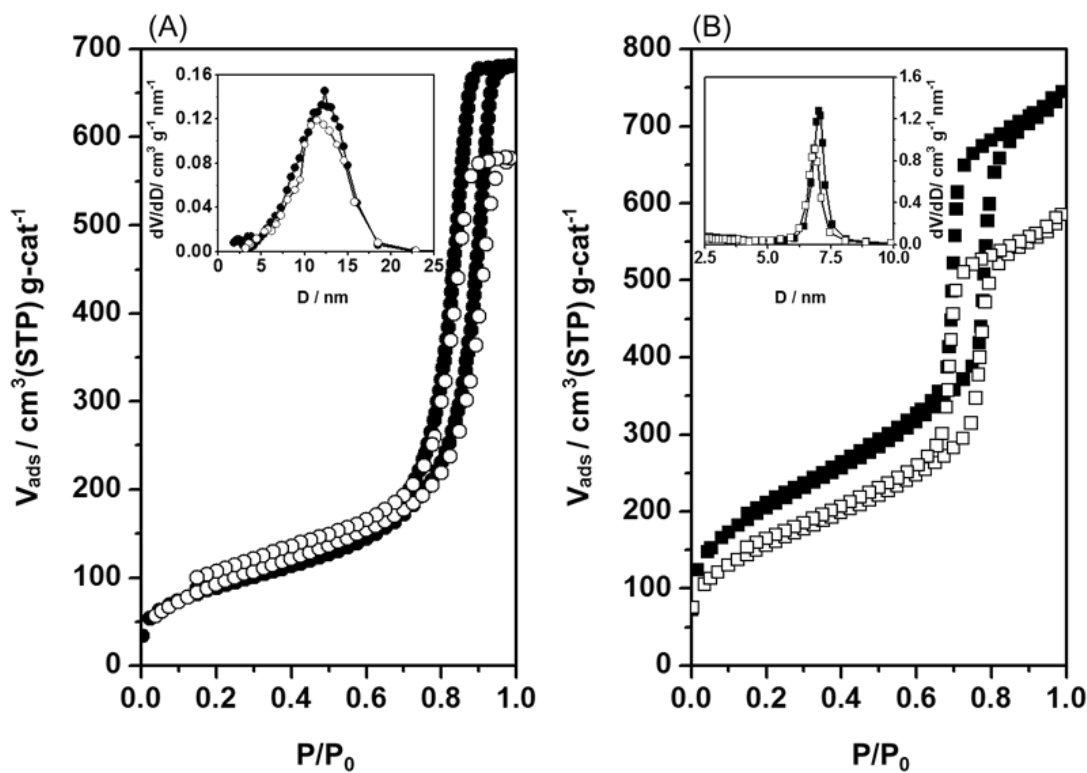


Figure 2-4 N₂ adsorption-desorption isotherms of Pd-Cu catalyst and bare support materials along with their BJH pore size distributions in the insets. (A) Bare amorphous silica (●) and the *calcined* Pd(5.7)-Cu(10)/SiO₂ (○), (B) SBA-15 (■) and the *calcined* Pd(5.7)-Cu(10)/SBA-15 (□).

2.3.5 Crystallite structures of Pd-Cu catalysts

2.3.5.1 Amorphous silica supported Pd-Cu catalysts

The crystalline structures of the *calcined* and *reduced* Pd(X)-Cu(Y)/SiO₂ catalysts were evaluated by X-ray diffraction measurements, and the resultant patterns are illustrated in Figs. 2-5 and 2-6. The average crystallite sizes were determined by the Scherrer equation and are summarized in Table 2-3.

Table 2-3 Crystallite phases, sizes and interplanar spacings for *reduced* Pd(X)-Cu(10)/SiO₂ catalysts

Catalyst ^{a)}	Metal Phase	$2\theta_{(111)}$ / °	Size ^{b)} / nm	d-spacing ^{c)} / nm
Cu	Cu ⁰	43.2	43	---
Pd _{2.5} -Cu	PdCu ₃	42.7	5	0.21
	Cu ⁰	43.3	53	---
Pd _{5.7} -Cu	PdCu ₃	42.6	4	0.21
Pd _{8.7} -Cu	PdCu	41.4	4	0.22
	PdCu ₃	42.5	5	0.21
Pd _{15.7} -Cu	Pd ⁰	40.5	23	---
	PdCu	41.5	3	0.22
	PdCu ₃	42.7	6	0.21
Pd _{5.7}	Pd ⁰	40.5	3	---

^{a)} Cu loading was fixed at 10 wt% for all Cu containing samples.

^{b)} Crystallite sizes determined from Scherrer equation (Eq. 2-1) for (111) peak.

^{c)} Spacing between (111) planes in PdCu and PdCu₃ structure.

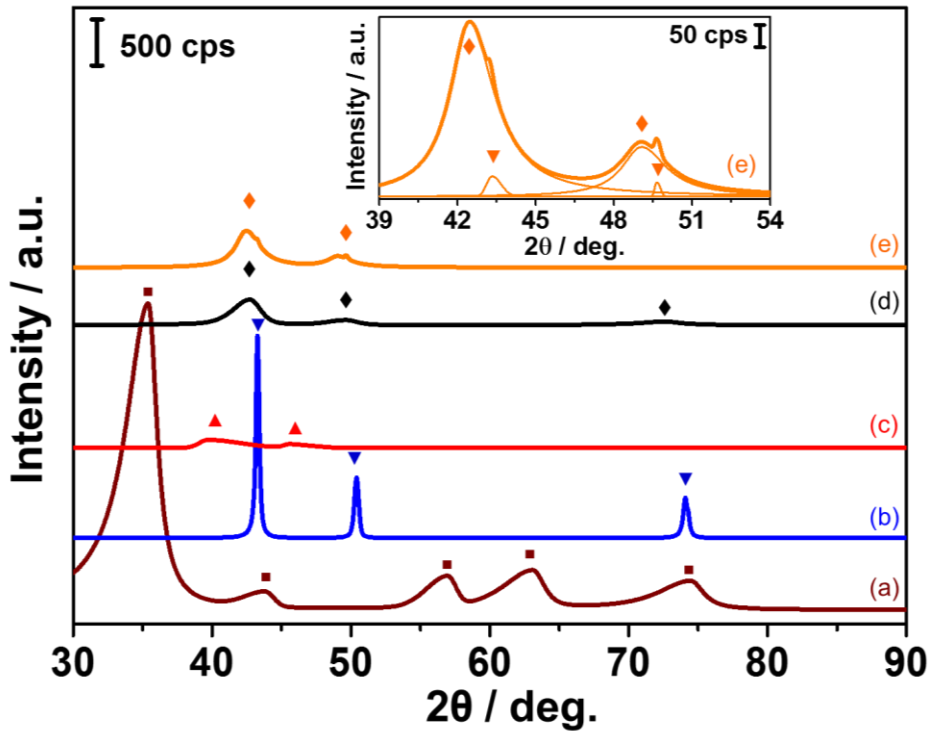


Figure 2-5 XRD patterns of Pd(X)-Cu(Y)/SiO₂ catalysts with the thick lines indicating original patterns, while the thin lines indicating deconvoluted patterns. (a) *calcined* Pd(5.7)-Cu(10)/SiO₂, (b) *reduced* Cu(10)/SiO₂, (c) *reduced* Pd(5.7)/SiO₂, (d) *reduced* Pd(5.7)-Cu(10)/SiO₂, (e) *reduced* Pd(8.7)/Cu(10)/SiO₂ with the magnified pattern in the inset (2θ : 39-54 °). Bimetallic catalyst samples were prepared by coimpregnation method, while sample (e) by sequential impregnation method. For all Cu containing samples, the Cu loading was 10 wt%. Symbols assignment: ▲: Pd⁰; ▼: Cu⁰; ♦: PdCu₃; ■: CuPdO₂.

In Fig. 2-5a, CuPdO₂ is observed for the *calcined* Pd(5.7)-Cu(10)/SiO₂ instead of separate metal oxides, implying a mutual diffusion into each other's crystal structure and the formation of a homogeneous oxides after the calcination. On the other hand, typical diffraction peaks of single metal phases (Cu⁰ and Pd⁰) are revealed in the XRD patterns of corresponding *reduced* Cu/SiO₂ (Fig. 2-5b) and Pd/SiO₂ (Fig. 2-5c) catalysts. Noticeably, the Cu⁰ diffraction peaks are much sharper than Pd⁰, implying a larger Cu⁰ crystallite size in comparison to Pd⁰. Quantitative analyses, determined by Scherrer equation, demonstrate that the average crystallite size of Cu⁰ (e.g., 43 nm) is considerably larger than that of Pd⁰ (e.g., 3 nm), as shown in Table 2-3. This is indicative of a better dispersion for nano-sized Pd⁰ particles than Cu⁰ particles. Interestingly, when Pd and Cu

were combined together (Fig. 2-5d), a major peak appears at $2\theta=42.6^\circ$, which is centered in between $\text{Pd}_{(111)}$ ($2\theta=40.5^\circ$) and $\text{Cu}_{(111)}$ ($2\theta=43.2^\circ$). Such distinct peak can be assigned to the diffraction of alloy phase $\text{PdCu}_3_{(111)}$ with face-centered cubic (FCC) structure. Besides, another two diffractions appear at $2\theta=49^\circ$ and 73° as well, corresponding to $\text{PdCu}_3_{(200)}$ and $\text{PdCu}_3_{(220)}$, respectively [54, 55]. Therefore, the XRD pattern of this *reduced* bimetallic catalyst evidently confirms the formation of Pd-Cu alloy. It is also worth noting that the XRD pattern of the *spent* $\text{Pd}(5.7)\text{-Cu}(10)/\text{SiO}_2$ catalyst resembles the fresh *reduced* catalyst, demonstrating the preservation of PdCu_3 alloy phase during the pressurized CO_2 hydrogenation reaction (see Fig. D-1, Appendix D).

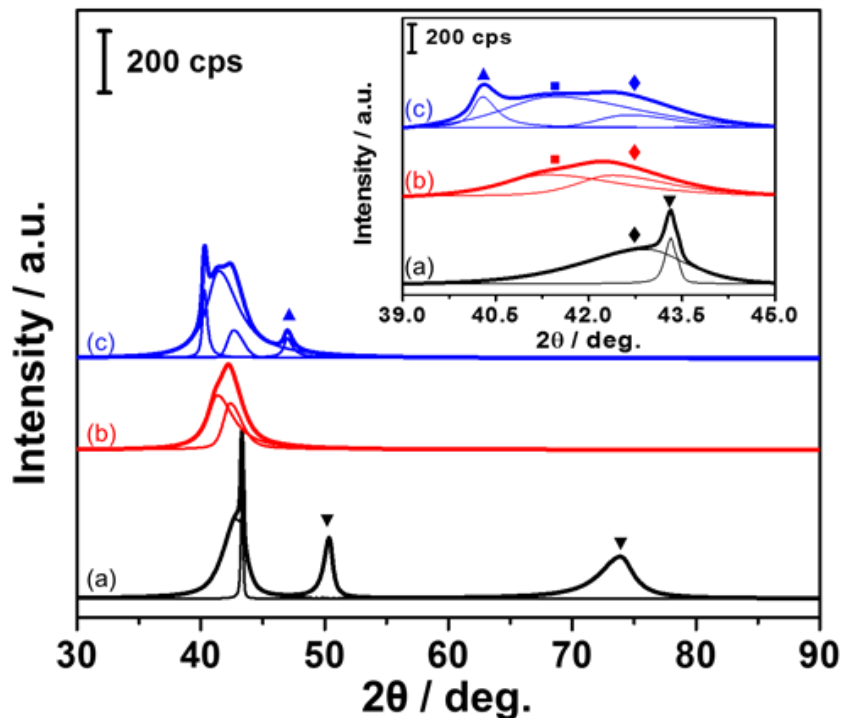


Figure 2-6 XRD patterns of the *reduced* $\text{Pd}(X)\text{-Cu}(10)/\text{SiO}_2$ catalysts with magnified XRD patterns in the inset ($2\theta: 39\text{-}45^\circ$). (a) $\text{Pd}(2.5)\text{-Cu}(10)/\text{SiO}_2$, (b) $\text{Pd}(8.7)\text{-Cu}(10)/\text{SiO}_2$, (c) $\text{Pd}(15.7)\text{-Cu}(10)/\text{SiO}_2$. Original patterns were highlighted with thick lines and patterns after deconvolution were featured with thin lines. For all samples, the Cu loading was 10 wt%. Symbols assignment: ▲: Pd^0 ; ▼: Cu^0 ; ♦: PdCu_3 ; ■: PdCu .

In order to identify the dependency of metallic/alloy phase on the Pd composition, three representative *reduced* Pd(X)-Cu(10)/SiO₂ catalysts with different Pd loadings (e.g., 2.5, 8.7 and 15.7) were examined by XRD measurements. The resultant patterns are displayed in Fig. 2-6, together with an amplified inset showing the patterns after the deconvolution. The crystallite structure information is summarized in Table 2-3. Fig. 2-6a shows the XRD pattern of Pd(2.5)-Cu(10)/SiO₂, wherein Cu is a relatively rich component in the total metallic loadings. Clearly, multiple peaks superimpose in the range between $2\theta=40^\circ$ and 45° , which turn out to be PdCu₃(111) ($2\theta=42.7^\circ$) and Cu⁰₍₁₁₁₎ ($2\theta=43.3^\circ$) after the deconvolution. Typically, the other two diffractions with higher Bragg angles correspond to Cu⁰₍₂₀₀₎ ($2\theta=50^\circ$) and Cu⁰₍₂₂₀₎ ($2\theta=74^\circ$). The crystallite sizes of PdCu₃ and Cu⁰ are estimated to be 5 nm and 53 nm, respectively, implying the agglomeration of Cu⁰ due to the Cu-rich environment under this composition. As illustrated in Fig. 2-6b, when the Pd loading was increased to 8.7 wt%, those intense Cu⁰ diffractions disappear; instead, the XRD pattern only presents a major diffraction, which is also a superimposed one as evidenced by its asymmetric peak shape. After the deconvolution, it consists of the alloy PdCu₃(111) ($2\theta=42.5^\circ$, FCC) and the alloy PdCu₍₁₁₁₎ ($2\theta=41.4^\circ$) with body-centered cubic (BCC) structure, and the estimated average crystallite sizes for PdCu₃ and PdCu are 5 nm and 4 nm, respectively. Clearly, the absence of intense unalloyed Cu⁰ diffractions indicates that an appropriate amount of Pd doping enables a substantial reduction of Cu⁰ particle size in the form of nano-sized Pd-Cu alloy particles. Fig. 2-6c illustrates the XRD pattern of the catalyst with a greater Pd loading of 15.7 wt%, and multiple diffractions are seen in the region of 40-42°. After the careful deconvolution, three different phases are found to coexist, namely Pd⁰₍₁₁₁₎ ($2\theta=40.5^\circ$), alloy PdCu₍₁₁₁₎ ($2\theta=41.5^\circ$, BCC) and alloy PdCu₃(111) ($2\theta=42.7^\circ$, FCC), and the corresponding crystallite sizes are 23 nm, 3 nm, and 6 nm, respectively. Evidently, it is noted that an excessive Pd loading

leads to the formation of larger Pd⁰ particles. Consequently, the metallic phases formed in the *reduced* bimetallic catalysts strongly depend upon the metallic composition, and the addition of Pd in the bimetallic catalysts significantly decreased the Cu particle size due to the alloy formation. An excessive loading of one component results in its agglomeration after the reduction, while an appropriate loading of each component can lead to the formation of alloy phases alone.

Additionally, the *reduced* Pd(8.7)/Cu(10)/SiO₂, prepared by the sequential impregnation method, was also examined by XRD measurement, as shown in Fig. 2-5e along with an amplified inset showing the region with superimposed diffractions. Unlike the coimpregnated sample with the same metal loadings (Fig. 2-6b), sequentially prepared Pd/Cu/SiO₂ shows PdCu₃ alloy ($2\theta=42.6^\circ$) and Cu⁰ diffraction (ca. $2\theta=43.2^\circ$) instead of PdCu₃ and PdCu alloy phases. Similar diffractions are also observed for the *reduced* Cu/Pd/SiO₂ prepared by the reverse order (see Fig. D-2, Appendix D). Note that the sequentially impregnated samples were prepared without intermediate calcination, which may preserve the first impregnated metal salt in the second step. Therefore, it provides an opportunity for at least a part of the first impregnated metal salt to redissolve into the solution and thus mix with the second metal salt. This is evidenced by the color variation during the second impregnation. Generally, the precursor solution changes from its original color (orange for Pd acetate and blue for Cu nitrate) to green during the second impregnation, which is characteristic when dissolving Pd and Cu salts together. However, the proposed redissolution process is inadequate for mixing Pd and Cu in the solution in comparison to the coimpregnation method, thereby resulting in the presence of the unalloyed metallic Cu⁰ phase. Besides, the similar tendency to greenish solution during the second impregnation suggests identical chemical states of metal salts regardless of the preparation order, and, thus, one would expect similar crystallite structures as observed from XRD patterns for Pd/Cu and Cu/Pd catalysts.

Therefore, based on the discussion above, the variation of alloy phases between coimpregnated and sequentially impregnated samples indicates the significance of preparation method on Pd-Cu alloy formation. In other words, the coimpregnation method could benefit the formation of alloy phases by forming a homogeneous solution.

The total content of alloy phase was also determined for the bimetallic catalysts with various Pd loadings by corresponding deconvoluted XRD patterns, and the resultant data is tabulated in Table 2-4. Noteworthy, both Pd(2.5)-Cu(10)/SiO₂ and Pd(5.7)-Cu(10)/SiO₂ exhibit a single alloy phase, thus the content of alloy phase was calculated based on the Pd loading in the catalyst as it is considered to be fully consumed in the alloy formation. The phase composition for the rest two catalysts with two alloy phases were determined by the semi-quantitative method using the software Jade 2010, and the detailed data processing method could be referred to Appendix D. Note that the estimated Pd/Cu ratios of these two catalysts match the theoretical values very well (see Table 2-4), thus, the diffraction peaks assignment is reasonable and the semi-quantitative analysis is convincing.

The total content of alloy phase increases with the increase of Pd loading and reaches the maximum value at the composition of Pd=8.7 wt%. Clearly, in comparison to the bimetallic catalysts with less Pd loadings (i.e., Pd=2.5 and 5.7 wt%), such observed maximum for this particular catalyst appears to be correlate with the coexistence of PdCu₃ and PdCu. On the other hand, although an excessive loading of Pd (ca. 15.7 wt%) could result in the coexistence of PdCu₃ and PdCu, the content of alloy phase decreases slightly and along with a large amount of unalloyed Pd⁰ phase. Consequently, the Pd loading not only affects the formation of metal and alloy phases in the bimetallic catalysts but also reflects on the quantity of alloy phase, and the maximum content could be obtained at specific composition.

Table 2-4 Quantitative analyses based on XRD patterns for Pd-Cu bimetallic catalysts with various Pd loadings

Catalyst ^{a)}	Pd/Cu ratio ^{b)}	Metal Phase	Wt. percent / wt%	Phase content / $\mu\text{mol g}^{-1}$	Est. Pd/Cu ratio ^{f)}
Pd _{2.5} -Cu	0.15	PdCu ₃	---	203.1 ^{e)}	---
Pd _{5.7} -Cu	0.34	PdCu ₃	---	450.6 ^{e)}	---
Pd _{8.7} -Cu	0.51	PdCu ₃	63.4 ^{c)}	653.2	0.50
		PdCu	36.6 ^{c)}		
Pd _{15.7} -Cu	0.94	PdCu ₃	48.4 ^{d)}	558.8	0.92
		PdCu	21.9 ^{d)}		
		Pd ⁰	29.7 ^{d)}	534.5	

^{a)} Cu loading for all samples is 10 wt%.

^{b)} Determined by the metal loadings.

^{c)} Determined by semi-quantitative analysis using Jade 2010 software. R% = 1.01, E% = 0.58.

^{d)} Determined by semi-quantitative analysis using Jade 2010 software. R% = 1.20, E% = 0.52.

^{e)} Estimated based on the observations that Pd had been fully consumed in the alloy formation.

^{f)} Estimated based on semi-quantitative analysis from XRD patterns.

2.3.5.2 Effect of support on Pd-Cu alloy formation

Likewise, the effect of support on Pd-Cu alloy formation was also evaluated by XRD measurements over *spent* Pd-Cu catalysts, and the resultant XRD patterns are illustrated in Fig. 2-7, where the Pd and Cu loading were kept at 5.7 and 10 wt%, respectively. In Fig. 2-7a and 2-7b, a major peak, centered at $2\theta=42^\circ$, is observed for both SBA-15 and MCM-41 supported bimetallic catalysts. Deconvolution over these superimposed diffractions show the coexistence of two alloy phases PdCu and PdCu₃, which disagrees with the observation of a single alloy (PdCu₃) in the amorphous silica supported counterparts with the same composition (see Fig. 2-5d). On the other hand, MSU-F supported Pd-Cu catalyst (Fig. 2-7c) explicitly reveals an identical alloy phase (e.g., PdCu₃) as the amorphous silica supported sample (Fig. 2-5d). These results suggest that unique pore structures with smaller pore sizes and/or surface chemical natures of MCM-41 and SBA-15

have a crucial impact on the formation of Pd-Cu alloy phases. In other words, with the composition of Pd(5.7)-Cu(10), a smaller pore size (e.g., < 6 nm) favors the mixture of different alloy phases, while a larger pore diameter results in the formation of a single alloy phase. Noteworthy, the estimated crystallite sizes of PdCu and PdCu₃ in these supported catalysts are quite similar, primarily ranging from 3 to 6 nm, as tabulated in Table 2-3.

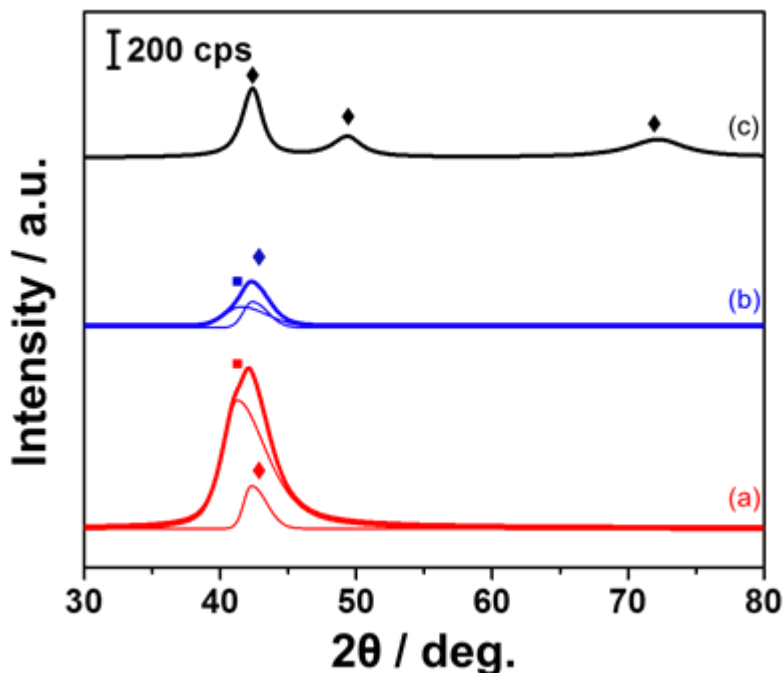


Figure 2-7 XRD patterns of the *spent* Pd(5.7)-Cu(10) catalysts supported on (a) SBA-15, (b) MCM-41, and (c) MSU-F. Original patterns were highlighted with thick lines, while thin lines were patterns after deconvolution. Symbols assignment: ♦: PdCu₃; ■: PdCu.

2.3.6 Morphological properties of Pd and Cu species and element distribution

Fig. 2-8 shows the typical TEM images of a *reduced* Pd(8.7)-Cu(10)/SiO₂ which contains both PdCu and PdCu₃ alloy phases in the *reduced* form. As illustrated from Figs. 2-8A and 2-8B, it is noticed that the particles are widely dispersed over the support. Fig. 2-8C is an amplified image concentrating on a few particles with a high resolution, and the lattice fringes align clearly

parallel to each other. The lattice space is measured to be ~ 0.20 nm on average, which agrees with the observed d-spacing of Pd-Cu alloys estimated from XRD patterns (see Table 2-3). Afterwards, approximately 150 particles were counted to estimate the particle size distribution, and the result is shown in Fig. 2-8D. Clearly, the average particle size mainly lies in the range of 4-7 nm, which evidently is in line with the XRD results (4-5 nm, Table 2-3). Therefore, it is suggested that these observed nano-sized particles from TEM images represent the Pd-Cu alloy particles. It is also worth noting that d-spacing value is quite similar among these alloy particles, which makes it impossible to distinguish the PdCu from the PdCu₃ only depending upon the TEM technique.

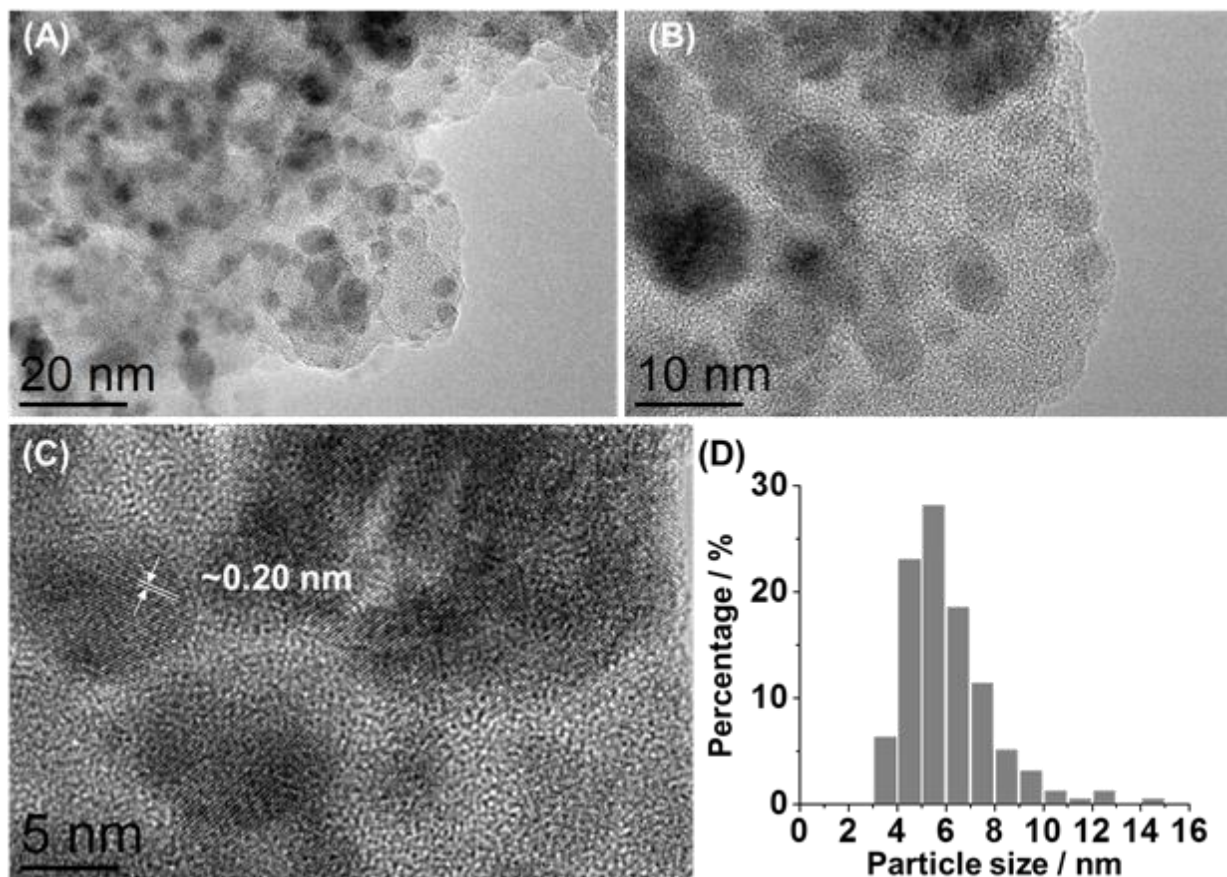


Figure 2-8 TEM images of *reduced* Pd(8.7)-Cu(10)/SiO₂ with different magnifications (A-C). The lattice fringe pattern of ca. 0.2 nm is discernible in image (B). (D) represents the corresponding particle size distribution.

The presence of Pd-Cu alloy particles was also evidenced by Z-contrast high-angle annular dark-field images (HAADF) of *reduced* Pd(8.7)-Cu(10)/SiO₂, as depicted in Fig. 2-9A. Evidently, all particles are nano-sized and widely-dispersed, which is similar to the observations from TEM images. The magnified inset shows a representative particle with relatively clear lattice fringe alignment. The measured average d-spacing is ca. 0.21 nm, which is in accordance with the results from both TEM images and XRD patterns. Thus, these particles are representative alloy particles. In order to further differentiate the alloy particles, the same area in the HAADF image was scanned by the energy-dispersive X-ray spectroscopy mapping technique in STEM mode (STEM/EDS). This cutting-edge technique allows us to identify the elemental compositions of individual alloy nanoparticles. It is worth noting that a carbon-coated molybdenum grid was applied instead of the copper grid, attempting to avoid its interference in both mapping and quantifying.

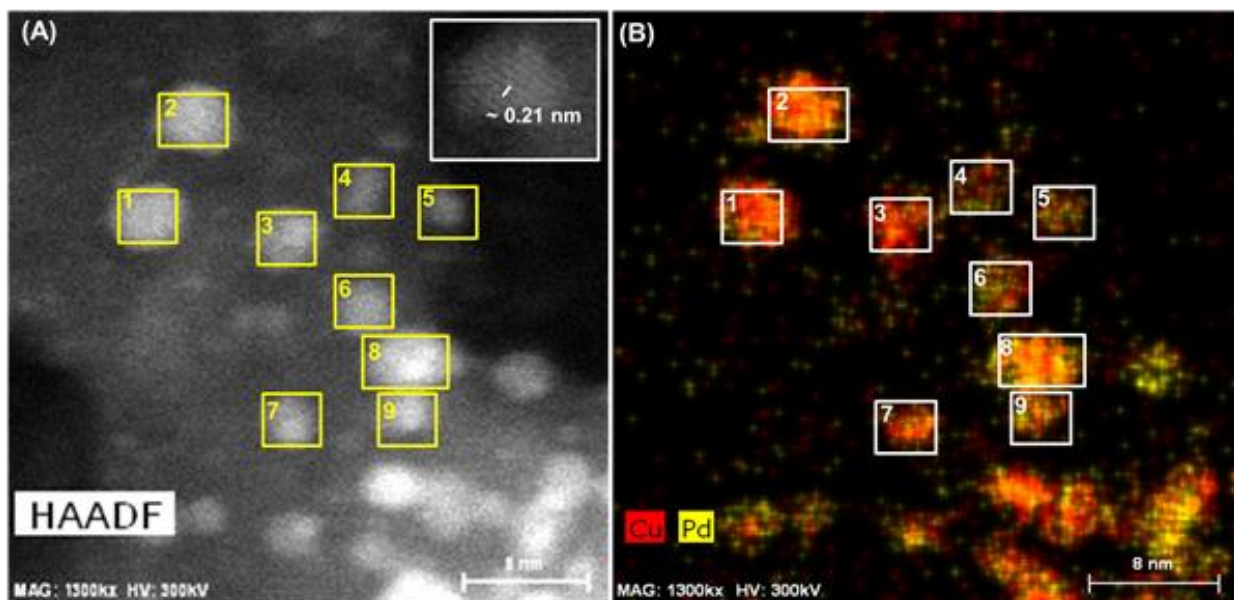


Figure 2-9 (A) HAADF STEM image of *reduced* Pd(8.7)-Cu(10)/SiO₂ and its corresponding STEM/EDS overlap maps for Pd and Cu (B). A representative alloy particle was magnified in the inset showing clear fringe alignment.

Table 2-5 Quantified phase compositions in Pd-Cu alloy nanoparticles from STEM/EDS maps ^{a)}

Particle #	Analyzed composition / at.% ^{b)}		Cu/Pd ratio / at. at ⁻¹ ^{c)}
	Cu-K	Pd-L	
1	23.22	15.91	PdCu _{1.5}
2	16.37	9.24	PdCu _{1.8}
3	11.03	4.14	PdCu _{2.7}
4	3.93	3.77	PdCu _{1.0}
5	29.10	34.89	PdCu _{0.8}
6	5.68	4.23	PdCu _{1.3}
7	8.57	3.01	PdCu _{2.8}
8	13.10	15.42	PdCu _{0.8}
9	4.96	6.57	PdCu _{0.8}

^{a)}Catalyst: *reduced* Pd(8.7)-Cu(10)/SiO₂.

^{b)} Uncertainty of each element in quantitative analysis: O (1.11 at.%); Si (0.60 at.%); Cu (0.31 at.%); Pd (0.38 at.%).

^{c)} Values in subscript were Cu/Pd ratios (at. at.⁻¹).

Generally, the EDS mappings reveal that both Si and O species distribute uniformly across the sample island (see Fig. E-1, Appendix E), while Pd and Cu species exist in close proximity but at different relative concentrations. In order to quantify the composition of the alloy particles, overlapping EDS maps were generated subsequently including two-element (Fig. 2-9B) and four-element overlapping maps (see Fig. E-2, Appendix E). Interestingly, the distributions of Pd and Cu species coincide perfectly with each other in location. When comparing those circled Pd-Cu clusters in Fig. 2-9B with corresponding particles in HAADF image (Fig. 2-9A), it is apparent that Pd and Cu distribute uniformly within the range of bimetallic particles, and thus these are the Pd-Cu alloy particles. On the other hand, those circled particles, which are discernible in shape from HAADF image, were selectively chosen for quantification, and the composition is listed in Table 2-5. Generally, the Cu/Pd ratios are in the range of 1.0-3.0, which evidently confirms the coexistence of alloy phases PdCu and PdCu₃. Therefore, these observations demonstrate a uniform

distribution of Pd and Cu in the nano-sized alloy particles after reduction and the coexistence of alloy phases with two stoichiometric ratios, namely PdCu_3 and PdCu , which strongly supports the XRD results over the same sample (Fig. 2-6b).

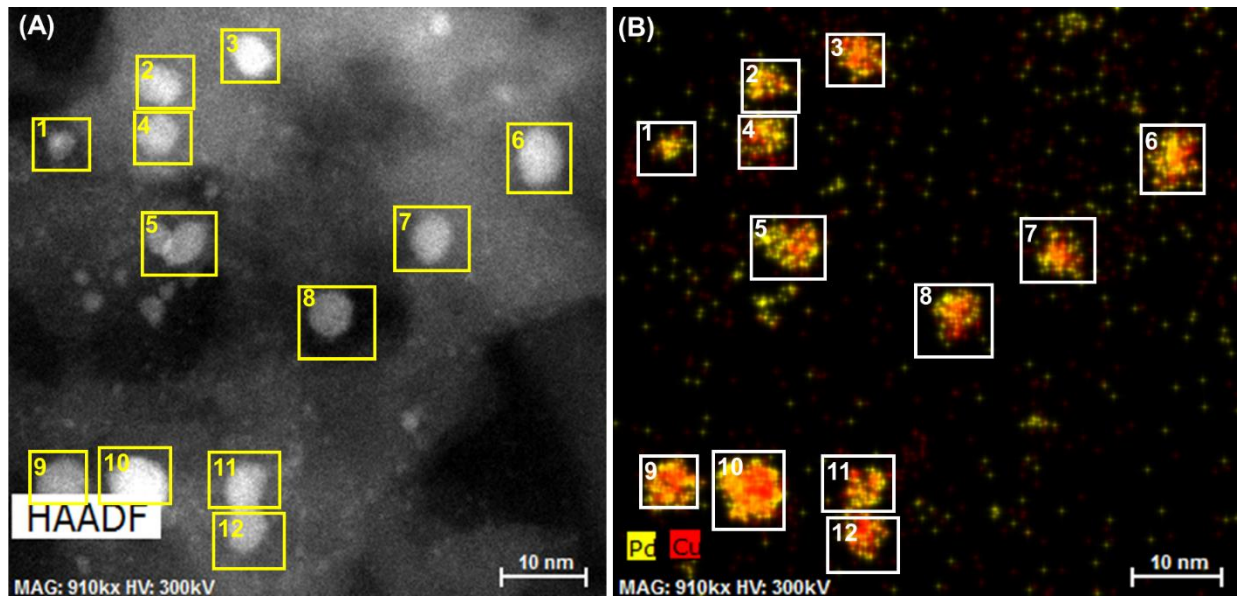


Figure 2-10 (A) HAADF STEM image of *reduced* $\text{Pd}(2.5)\text{-Cu}(10)/\text{SiO}_2$ and its corresponding STEM/EDS overlap maps for Pd and Cu (B). A representative alloy particle was magnified in the inset showing clear fringe alignment.

The STEM/EDS measurement was also conducted over the *reduced* $\text{Pd}(2.5)\text{-Cu}(10)/\text{SiO}_2$ catalyst. Likewise, the EDS mappings also show uniform distributions of Si and O species, while Pd species distributes in a close vicinity to Cu species within each particle perimeter (Fig. E-3, Appendix E). The HAADF image of this sample and its 2-element overlapping mapping are illustrated in Figs. 2-10A and 2-10B, respectively. The particle size is ca. 5 nm which agrees well with the XRD results over the same sample (Table 2-3). In addition, the compositions of the nano-sized particles were also quantified based on the same selection rule, and the quantitative data is tabulated in Table 2-6. The Cu/Pd ratio mainly falls into the range of 1.5-3.0 (ca. > 70%), implying the dominant existence of the Cu-rich alloy phase PdCu_3 . Such observation is in line with the

resolved XRD pattern over the same sample as well.

Table 2-6 Quantified phase compositions in Pd-Cu alloy nanoparticles from STEM/EDS maps ^{a)}

Particle #	Analyzed composition / at.% ^{b)}		Cu/Pd ratio / at. at ⁻¹ ^{c)}
	Cu-K	Pd-L	
1	5.87	6.54	PdCu _{0.9}
2	2.42	1.62	PdCu _{1.5}
3	5.15	2.71	PdCu _{1.9}
4	3.08	2.37	PdCu _{1.3}
5	7.37	7.23	PdCu _{1.0}
6	5.43	3.71	PdCu _{1.5}
7	4.80	2.94	PdCu _{1.6}
8	12.27	6.84	PdCu _{1.8}
9	12.41	7.00	PdCu _{1.8}
10	8.98	5.26	PdCu _{1.7}
11	4.71	3.18	PdCu _{1.5}
12	7.89	3.08	PdCu _{2.6}

^{a)}Catalyst: *reduced* Pd(2.5)-Cu(10)/SiO₂.

^{b)} Uncertainty of each element in quantitative analysis: O (1.19 at.%); Si (0.55 at.%); Cu (0.13 at.%); Pd (0.14 at.%).

^{c)} Values in subscript were Cu/Pd ratios (at. at.⁻¹).

Fig. 2-11 shows the typical TEM images of *reduced* Pd(5.7)-Cu(10)/SBA-15, for which both of the two Pd-Cu alloy phases are observed from the resolved XRD pattern (Fig. 2-7a). Fig. 2-11A reveals a characteristic image of 2D arrays of 1D channels of SBA-15. Fig. 2-11B and 2-11C exhibit an interesting dispersion of Pd-Cu alloy particles which align along with the 1D channels. The reason for such uniform and regular dispersion of Pd-Cu alloy particles can be attributed to the confinement of the unique pore structure of SBA-15. Fig. 2-11D illustrates the distribution of particle sizes, which were determined by measuring ca. 150 particles. Particle sizes mainly distribute in the range of 5-8 nm, which is reasonable as compared to the average value estimated from XRD patterns (e.g., ~6 nm).

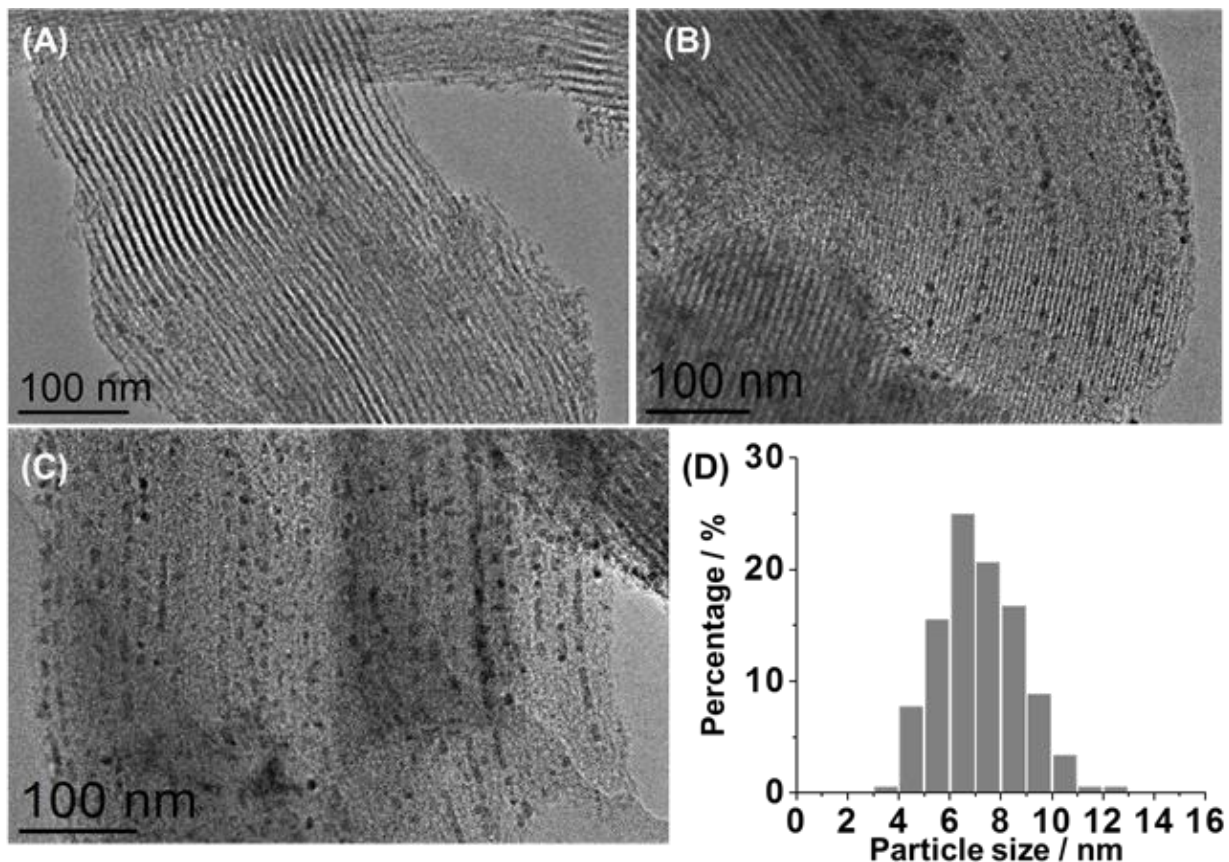


Figure 2-11 TEM Image (A) shows the characteristic pore structure of SBA-15. (B-C) are TEM images of *reduced* Pd(5.7)-Cu(10)/SBA-15 with different areas. (D) represents the corresponding particle size distribution.

2.3.7 Surface properties of reduced Pd-Cu catalysts

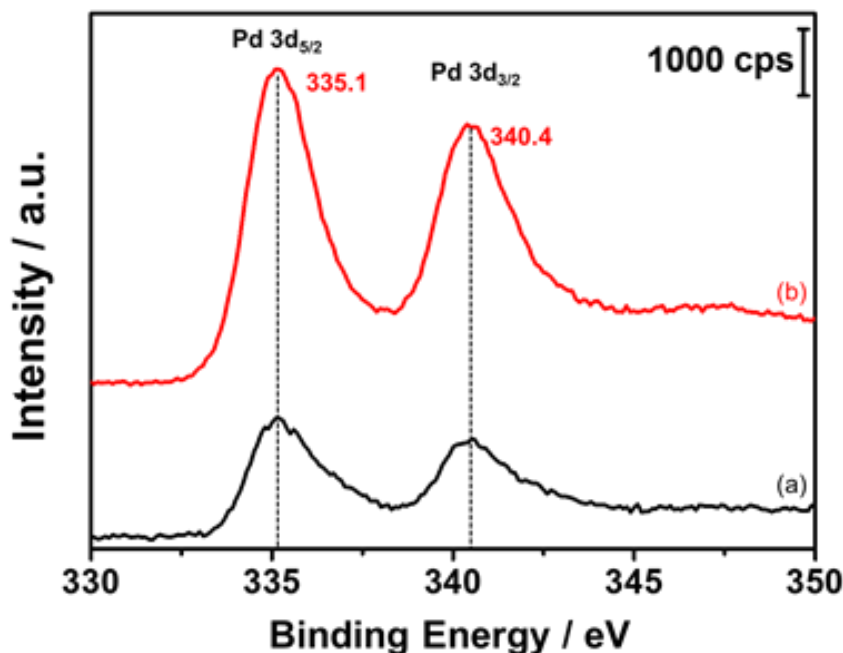


Figure 2-12 Pd 3d XP spectra of (a) *reduced* Pd(8.7)-Cu(10)/SiO₂; (b) *reduced* Pd(8.7)/SiO₂.

Table 2-7 Pd 3d XPS parameters of *reduced* Pd-Cu/SiO₂ catalysts

Catalyst	Pd 3d _{5/2}	Pd 3d _{3/2}	ΔE / eV
	BE / eV	BE / eV	
Pd _{8.7}	335.1	340.4	5.3
Pd _{8.7} -Cu ^{a)}	335.2	341.6	5.4
Pd-Cu/pumice ^{b)}	334.8	---	---
Pd-Cu/CeO ₂ ^{c)}	335.3	340.3	5.0
PdO ^{d)}	336.3	---	---
PdO ₂ ^{e)}	337.9	---	---
Pd metal ^{d)}	335.0	---	---

^{a)} Cu loading was 10 wt%.

^{b)} Data was acquired by *in situ* method over reduced samples, see ref. [56].

^{c)} Data was acquired by “*pseudo in situ*” method over reduced samples, see ref. [57].

^{d)} Ref. [58, 59].

^{e)} Ref. [60].

To investigate the surface chemical nature of Pd and Cu, the XPS measurements were conducted over *reduced* Pd-Cu bimetallic and monometallic catalysts. Fig. 2-12 depicts the XPS

spectra in the Pd 3d region for Pd(8.7)/SiO₂ and Pd(8.7)-Cu(10)/SiO₂, and the corresponding XPS parameters are summarized in Table 2-7. The *reduced* Pd(8.7)/SiO₂ exhibits an intense doublet centering at 335.1 and 340.4 eV, assigned to Pd 3d_{5/2} and Pd 3d_{3/2}, respectively, with a spin-orbit coupling energy of 5.3 eV. The observed BEs closely match with Pd metal in Table 2-7, which implies the existence of metallic Pd⁰. However, a fraction of Pd oxide may be contained as the peaks are slightly asymmetric. The doublet for *reduced* Pd(8.7)-Cu(10)/SiO₂ appears with similar BEs. In a previous study, Pd 3d doublet of bulky Pd-Cu alloy did not show apparent peak shift with respect to the pure metal [61]. Similarly, Venezia *et al.* [56] observed an identical result over the pumice supported Pd-Cu sample in the reduced state as compared to the monometallic catalyst. Therefore, Pd⁰ is suggested to be the dominant state in the *reduced* bimetallic catalyst. On the other hand, it is noticeable that the intensities of doublet decline in the bimetallic sample. Such reduction is due to a decreasing surface concentration of Pd in the alloy compared to the monometallic Pd/SiO₂, as tabulated in Table 2-9.

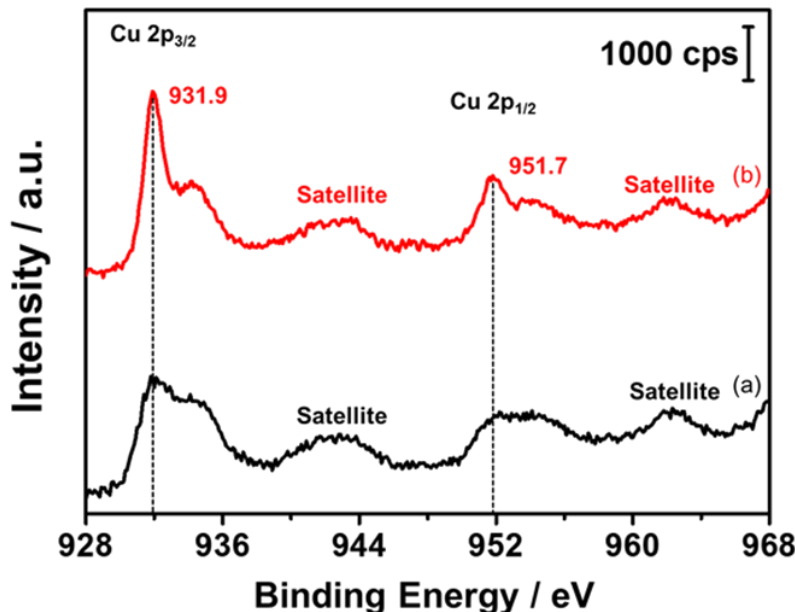


Figure 2-13 Cu 2p XP spectra of (a) *reduced* Pd(8.7)-Cu(10)/SiO₂; (b) *reduced* Cu(10)/SiO₂.

Table 2-8 Cu 2p XPS parameters of *reduced* Pd-Cu/SiO₂ catalysts

Catalyst	Cu 2p _{3/2}	Cu 2p _{1/2}	$\Delta E / \text{eV}$
	BE / eV	BE / eV	
Cu ^{a)}	931.9	951.7	19.8
Pd _{8.7} -Cu ^{a)}	932.0	951.8	19.8
Pd-Cu/pumice ^{b)}	931.9	---	---
PdCu/CeO ₂ ^{c)}	932.0	951.6	19.6
CuO ^{d)}	934.6	---	---
Cu ₂ O ^{d)}	932.8	---	---
Cu metal ^{d)}	932.8	---	---

^{a)} Cu loading was 10 wt%.

^{b)} Data was acquired by *in situ* method over reduced samples, see ref. [56].

^{c)} Data was acquired by “*pseudo in situ*” method over reduced samples, see ref. [57].

^{d)} Ref. [62].

The Cu 2p core level XP spectra for both *reduced* Cu(10)/SiO₂ and Pd(8.7)-Cu(10)/SiO₂ are shown in Fig. 2-13, and the XPS parameters are gathered in Table 2-8. Cu(10)/SiO₂ exhibits a linear superposition of distinct spectra in the typical BE ranges of both Cu 2p_{3/2} and 2p_{1/2}. Considering the relevant BEs of copper oxides, copper metal, and copper in alloys in Table 2-8, the spectrum primarily contains two components, one due to Cu metal as a sharp and intense peak at 931.9 eV and the other to CuO which is a shoulder peak around 934 eV and shake-up satellites above the main photoelectron transition. Such assignment can be applied to the spectrum of the *reduced* Pd(8.7)-Cu(10)/SiO₂ as well. Venezia *et al.* [56] acquired XPS data over the bimetallic sample by an *in situ* method in H₂ and found that the Cu 2p peaks of Pd-Cu catalyst shifted ca. 0.5 eV below the BE of monometallic Cu sample as a result of Pd-Cu alloy formation. An alloy-induced negative peak shift (ca. 0.4 eV) was also reported in another work by a “*pseudo in situ*” method [57]. However, such shift was not observed in this work. Unlike the *in situ* or “*pseudo in situ*” measurement, our samples were slowly passivated after the reduction to protect the alloy structure, through which the photoelectron of CuO was inevitable. Thus, the passivation may hinder us from observing the alloy-induced subtle peak shift of Cu⁰ species. Nevertheless, the intensity of the

characteristic peak for *reduced* Cu(10)/SiO₂, centered at 931.9 eV, decreases dramatically in the *reduced* bimetallic sample, suggesting the detection of more copper oxides over the surface. In a previous work, Pd EXAFS showed the evidence of Pd-Cu alloy formation, and Pd had about 4 Cu atoms in the neighboring coordination environment, which lowered the surface concentration of Pd [57]. Moreover, resolved XRD patterns in this work reveal that the Cu particle size decreases substantially with the alloy formation (Table 2-3), and distributions of Pd and Cu coincide well with each other in location as observed from EDS maps (Fig. 2-9). These characterization results suggest that the strong interaction between Pd and Cu is critical in improving the dispersion of Cu over the surface to form fine alloy particles with Pd. These Cu-containing fine particles are more easily oxidized compared to larger monometallic Cu particles. Therefore, more surface oxides appear over the surface as evidenced by the decreasing relative intensity of Cu 2p_{3/2} peak.

Table 2-9 Surface chemical compositions of *reduced* Pd-Cu/SiO₂ catalysts determined by XPS

Catalyst ^{a)}	Composition / at.%				
	Cu	Pd	Si	C	O
Cu/SiO ₂	0.63	---	31.97	3.09	64.31
Pd _{8.7} /SiO ₂	---	1.12	31.06	2.63	65.19
Pd _{8.7} -Cu/SiO ₂	0.92	0.44	31.22	3.27	64.15
SiO ₂ ^{b)}	---	---	32.31	2.84	64.85

^{a)} Cu loading was 10 wt% for all Cu-containing samples.

^{b)} The bare support material was also reduced *in situ* and passivated under the same conditions.

The estimated surface composition based on XPS is presented in Table 2-9. For clarity, the compositions of Si, C, and O are also included in the table, the compositions of which are practically stable for all samples and agree well with the bare support material. Thus, the fluctuation from these elements can be excluded in the following analyses. As a result of the alloy formation, the Pd surface concentration appears to be lower than Cu in the bimetallic sample, which also implies that Pd is mainly surrounded by Cu on the surface [48, 63]. The Pd/Cu ratio on the surface was

estimated to be 0.48 which approximates the theoretical value in total (ca. 0.51), further implying the uniform distribution of Pd and Cu in the bimetallic catalysts with this composition. Consequently, these observations demonstrate a strong interaction between Pd and Cu in alloyed particles.

2.3.8 Importance of Pd-Cu alloy formation for bimetallic promotion

As discussed in section 2.3.1, notable bimetallic promotions of CH₃OH formation appear over supported Pd(5.7)-Cu(10) bimetallic catalysts. Characterization results demonstrate that the strong interaction between Pd and Cu leads to the formation of Pd-Cu alloys, the phases of which are dependent on the Pd composition. In order to identify the correlation between the Pd-Cu alloy formation and the bimetallic CH₃OH promotion, an extent of “CH₃OH promotion” was defined as a ratio of CH₃OH formation rate over bimetallic catalyst (numerator) to the simple summation of CH₃OH formation rates over corresponding monometallic catalysts (denominator), as shown in Eq. 2-2.

$$CH_3OH \text{ promotion} = \frac{FR(CH_3OH)_{Pd-Cu}}{FR(CH_3OH)_{Pd} + FR(CH_3OH)_{Cu}} \quad \text{Eq. 2-2}$$

Fig. 2-14A shows the CH₃OH promotion level plotted as a function Pd loading. Similar to CH₃OH formation rate, CH₃OH promotion level exhibits a volcano-like curve in the whole range of Pd/(Pd+Cu) atomic ratio and maximizes at 8.7 (i.e., Pd atomic ratio=0.34), where the absolute CH₃OH formation rate is optimized as well. Based on characterization results, this particular catalyst, Pd(8.7)-Cu(10)/SiO₂, forms uniform and nano-sized alloy particles with two stoichiometric ratios (i.e., PdCu₃ and PdCu) after the reduction at 573 K. In contrast, other bimetallic catalysts contain either single alloy phase (e.g., Pd=5.7 wt%) or single metallic phase

(e.g., Pd=2.5 or 15.7 wt%) with considerably large particle size. Furthermore, the changes of both CH₃OH promotion and content of alloy phase are plotted as a function of Pd loading as well in Fig. 2-14B. Clearly, the trend of CH₃OH promotion appears to correlate with the content of alloy phases in the bimetallic catalysts with various Pd loadings and both maximize at Pd=8.7 wt%. Again, this can be attributed to the alloy structure and the accompanying strong interaction between metal components at this composition. Notably, Pd(15.7)-Cu(10)/SiO₂ only exhibits a slight drop of alloy content in comparison to the optimal composition and contains both PdCu₃ and PdCu phases, however, the loss in CH₃OH promotion is significant. Probably, the existence of large Pd⁰ particles at this Pd loading cause at least partial coverages of active alloy sites, which inhibits the adsorption towards reagents and methanol formation. The effect of metal loadings on the adsorption properties will be discussed in the next chapter. Therefore, the presence of Pd-Cu alloys is primarily responsible for the observed methanol promotion over Pd(X)-Cu(10)/SiO₂ catalysts; moreover, such enhancement occurs particularly in the condition of coexisted PdCu and PdCu₃ without unalloyed metals.

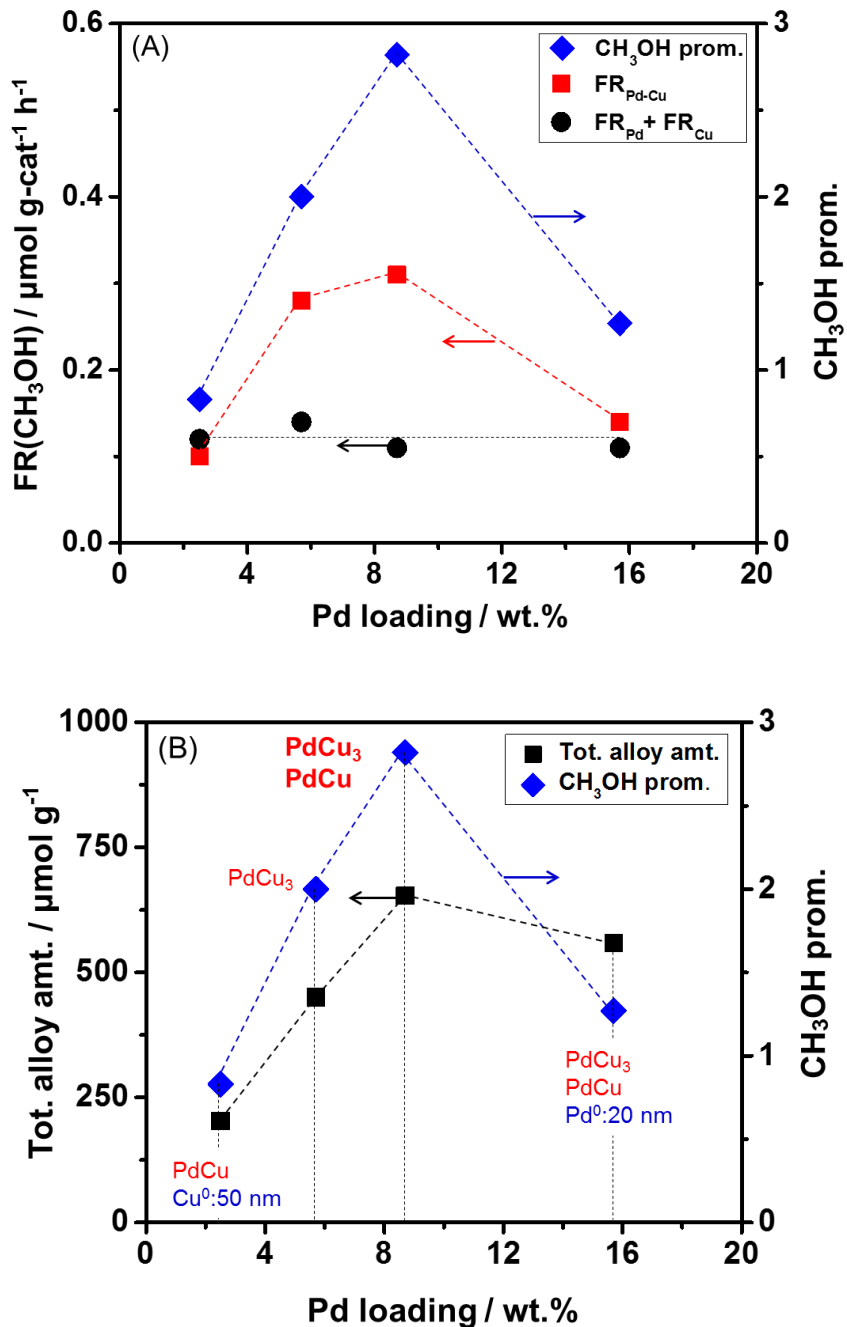


Figure 2-14 Bimetallic promotion of CH_3OH formation over (A) amorphous silica-supported $\text{Pd}(X)\text{-Cu}(10)/\text{SiO}_2$ and (B) its correlation with total alloy contents for $\text{Pd}(X)\text{-Cu}(10)/\text{SiO}_2$ with various Pd loadings

For Cu-Zn based catalysts, the mechanism of methanol synthesis has been proposed to proceed via the initiation of CO_2 to surface formate species which is then hydrogenated to

methoxide through propagation and ultimately to methanol as termination [64]. Nakamura *et al.* [27] reported that the Cu-Zn alloy could improve the surface coverage of formate species and promote its hydrogenation to methoxide, which was considered as the rate determining step (RDS). Similarly, it is suggested that the formation of Pd-Cu alloy can also benefit the formation of formate species and hydrogenation of the adsorbed intermediate species by providing more active sites, namely nano-sized and well-dispersed alloy particles, and hence leading to the pronounced CH₃OH promotion.

The significance of Pd-Cu alloy phases can also be considered as an important factor to explain the lower activity of sequentially impregnated samples compared to the coimpregnated one. Recalling that the sequentially loaded catalysts (i.e., Pd/Cu/SiO₂ and Cu/Pd/SiO₂) show PdCu₃ alloy alone and along with Cu⁰ regardless of impregnation sequence, and such variation can be attributed to the effect of preparation method. Therefore, in comparison to the sequential impregnation, coimpregnation method assists the alloy formation by means of forming a homogeneous precursor solution and thereby benefitting the CH₃OH promotion.

CH₃OH promotion level was plotted for Pd-Cu bimetallic catalysts on uniform mesoporous silicas as a function of pore diameter of support materials in Fig. 2-15 as well. MCM-41 and SBA-15 supported Pd-Cu catalysts with two alloy phases (PdCu₃ and PdCu) show stronger synergetic effects on CH₃OH than other catalysts with a single alloy phase. As suggested in 2.3.5.2, the special features of MCM-41 and SBA-15, such as the unique pore structure with relatively smaller pore diameter and/or surface chemical nature, may play an important role in the formation of two well-mixed alloyed phases, therefore resulting in a better performance in the CH₃OH promotion.

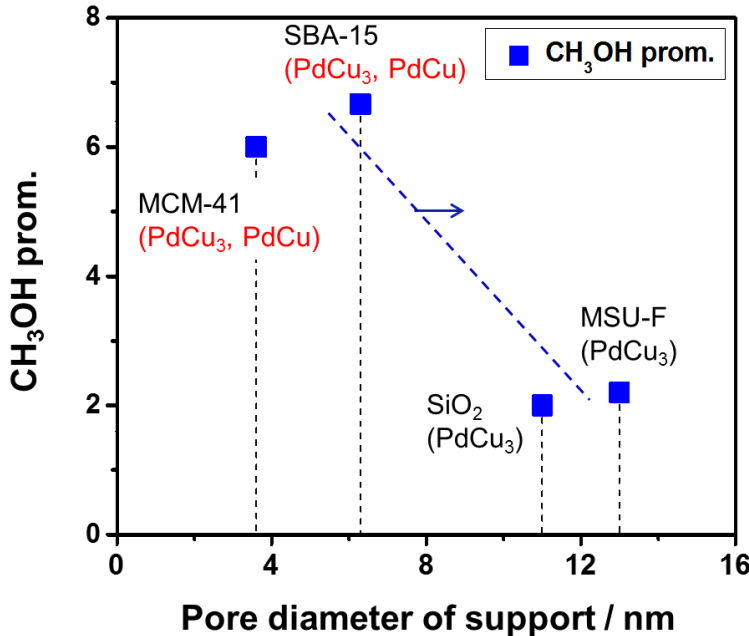


Figure 2-15 Bimetallic promotion of CH_3OH formation over various mesoporous silica-supported Pd(5.7)-Cu(10)/support.

2.4 Conclusions

In the present work, Pd-Cu bimetallic catalysts were prepared and studied in the CO_2 hydrogenation for methanol synthesis. The effects of Pd-Cu composition and types of mesoporous silica supports were also examined. Important results are summarized below.

- (1) The combination of Cu and Pd led to a strong synergistic promotion of CH_3OH formation rate when the Pd/(Pd+Cu) atomic ratios were within 0.25-0.34 (e.g., 5.7-8.7 wt% Pd loading) for amorphous silica supported Pd-Cu catalysts. Similar promotional effects were observed over other catalysts loaded on uniform mesoporous silicas, such as SBA-15, MCM-41, and MSU-F.
- (2) Pd(8.7)-Cu(10)/ SiO_2 showed the maximum CH_3OH formation rate among all bimetallic catalysts tested. Its catalytic performance was stable and no apparent deactivation was observed over 70 h on stream.
- (3) XRD results demonstrated that the metallic and alloy phases and corresponding phase

quantifies appeared to correlate with the Pd content in bimetallic catalysts. The addition of Pd significantly decreased the particle size of Cu in bimetallic catalysts. Uniform and nano-sized alloy particles (3-6 nm) were observed from high-resolution TEM images. STEM/EDS maps revealed the elemental compositions of individual Pd-Cu nanoparticles on the support surface and confirmed the existence of PdCu and PdCu₃ alloy phases based on quantitative analyses. XPS data further confirmed the strong interaction between Pd and Cu due to the alloy formation.

(4) Detailed characterization results demonstrated that the catalyst with the optimal composition, namely Pd(8.7)-Cu(10)/SiO₂, showed the coexisted PdCu₃ and PdCu alloy phases with uniform and nano-sized alloy particles and exhibited the maximum content of alloy phase, which could be correlated to the superior synergetic effect in catalytic performance.

2.5 Acknowledgements

This work was supported in part by the Pennsylvania State University through the Penn State Institute of Energy and the Environment. The XRD, STEM/EDS and XPS measurements were performed at the Materials Characterization Laboratory of the Penn State Materials Research Institute, for which the assistance of Nichole Wonderling, Jennifer Gray, and Vincent Bojan is gratefully acknowledged. The author (Xiao Jiang) also acknowledges the financial support from Chinese Scholarship Council (CSC).

2.6 Reference

- [1] M.B. Ansari, S.-E. Park, Energy & Environmental Science, 5 (2012) 9419-9437.
- [2] R.W. Dorner, D.R. Hardy, F.W. Williams, H.D. Willauer, Energy & Environmental Science, 3 (2010) 884-890.
- [3] P. Markewitz, W. Kuckshinrichs, W. Leitner, J. Linssen, P. Zapp, R. Bongartz, A. Schreiber, T.E. Müller, Energy & Environmental Science, 5 (2012) 7281-7305.
- [4] W. Wang, S. Wang, X. Ma, J. Gong, Chem. Soc. Rev., 40 (2011) 3703-3727.
- [5] Z. Jiang, T. Xiao, V.L. Kuznetsov, P.P. Edwards, Philosophical transactions. Series A, Mathematical, physical, and engineering sciences, 368 (2010) 3343-3364.
- [6] C. Song, A.F. Gaffney, K. Fujimoto, in: C. Song, A.F. Gaffney, K. Fujimoto (Eds.) CO₂ Conversion and Utilization, American Chemical Society, Washington D.C., 2002, pp. 2-30.
- [7] C. Song, Catal. Today, 115 (2006) 2-32.
- [8] M. Mikkelsen, M. Jørgensen, F.C. Krebs, Energy & Environmental Science, 3 (2010) 43-81.
- [9] H. Arakawa, M. Aresta, J.N. Armor, M.A. Barreau, E.J. Beckman, A.T. Bell, J.E. Bercaw, C. Creutz, E. Dinjus, D.A. Dixon, K. Domen, D.W. Goodman, J. Keller, G.J. Kubas, H.H. Kung, J.E. Lyons, L.E. Manzer, J. Rostrup-Nielson, W.M.H. Sachtler, L.D. Schmidt, A. Sen, G.A. Somorjai, P.C. Stair, B.R. Stults, W. Tumas, Chem. Rev., 101 (2001) 953-996.
- [10] M. Aresta, A. Dibenedetto, Catal. Today, 98 (2004) 455-462.
- [11] M. Aresta, Carbon Dioxide as Chemical Feedstock, Wiley-VCH Verlag GmbH & Co. KGaA, Weinheim, 2010.
- [12] G. Centi, S. Perathoner, Z.S. Rak, Appl. Catal., B-Environ, 41 (2003) 143-155.
- [13] G. Centi, S. Perathoner, Catal. Today, 148 (2009) 191-205.
- [14] H. Arakawa, J.-L. Dubois, K. Sayama, Energy Convers. Manage., 33 (1992) 521-528.

- [15] M. Saito, T. Fujitani, I. Takahara, T. Watanabe, M. Takeuchi, Y. Kanai, K. Moriya, T. Kakumoto, *Energy Convers. Manage.*, 36 (1995) 577-580.
- [16] M. Saito, T. Fujitani, M. Takeuchi, T. Watanabe, *Appl. Catal., A-Gen*, 138 (1996) 311-318.
- [17] T. Inui, H. Hara, T. Takeguchi, J.-B. Kim, *Catal. Today*, 36 (1997) 25-32.
- [18] J. Toyir, P.R.d.l. Piscina, J.L.G. Fierro, N. Homs, *Appl. Catal., B-Environ*, 29 (2001) 207-215.
- [19] J. Słoczyński, R. Grabowski, P. Olszewski, A. Kozłowska, J. Stoch, M. Lachowska, J. Skrzypek, *Appl. Catal., A-Gen*, 310 (2006) 127-137.
- [20] Y. Ma, Q. Sun, D. Wu, W.-H. Fan, Y.-L. Zhang, J.-F. Deng, *Appl. Catal., A-Gen*, 171 (1998) 45-55.
- [21] J. Słoczyński, R. Grabowski, A. Kozłowska, P. Olszewski, J. Stoch, J. Skrzypek, M. Lachowska, *Appl. Catal., A-Gen*, 278 (2004) 11-23.
- [22] F. Arena, K. Barbera, G. Italiano, G. Bonura, L. Spadaro, F. Frusteri, *J. Catal.*, 249 (2007) 185-194.
- [23] R. Yang, Y. Fu, Y. Zhang, N. Tsubaki, *J. Catal.*, 228 (2004) 23-35.
- [24] R. Yang, Y. Zhang, Y. Iwama, N. Tsubaki, *Appl. Catal., A-Gen*, 288 (2005) 126-133.
- [25] R. Yang, X. Yu, Y. Zhang, W. Li, N. Tsubaki, *Fuel*, 87 (2008) 443-450.
- [26] G. Bonura, M. Cordaro, C. Cannilla, F. Arena, F. Frusteri, *Appl. Catal., B-Environ*, 152-153 (2014) 152-161.
- [27] T. Fujitani, J. Nakamura, *Appl. Catal., A-Gen*, 191 (2000) 111-129.
- [28] L. Fan, K. Fujimoto, *Appl. Catal., A-Gen*, 106 (1993) L1-L7.
- [29] T. Fujitani, M. Saito, Y. Kanai, T. Watanabe, J. Nakamura, T. Uchijima, *Appl. Catal., A-Gen*, 125 (1995) L199-L202.

- [30] C. Shao, L. Fan, K. Fujimoto, Y. Iwasawa, *Appl. Catal., A-Gen*, 128 (1995) L1-L6.
- [31] L. Fan, K. Fujimoto, *Energy Convers. Manage.*, 36 (1995) 633-636.
- [32] T. Fujitani, I. Nakamura, *Bull. Chem. Soc. Jpn.*, 75 (2002) 1393-1398.
- [33] S.E. Collins, D.L. Chiavassa, A.L. Bonivardi, M.A. Baltanas, *Catal. Lett.*, 103 (2005) 83-88.
- [34] D.L. Chiavassa, J. Barrandeguy, A.L. Bonivardi, M.A. Baltanás, *Catal. Today*, 133-135 (2008) 780-786.
- [35] X.-L. Liang, X. Dong, G.-D. Lin, H.-B. Zhang, *Appl. Catal., B-Environ.*, 88 (2009) 315-322.
- [36] M.L. Poutsma, L.F. Elek, P.A. Ibarbia, A.P. Risch, J.A. Rabo, *J. Catal.*, 52 (1978) 157-168.
- [37] Y. Matsumura, W.-J. Shen, Y. Ichihashi, M. Okumura, *J. Catal.*, 197 (2001) 267-272.
- [38] Y. Kikuzono, S. Kagami, S. Naito, T. Onishi, K. Tamaru, *Faraday Discuss. Chem. Soc.*, 72 (1981) 135-143.
- [39] A. Gotti, R. Prins, *J. Catal.*, 175 (1998) 302-311.
- [40] N. Koizumi, X. Jiang, J. Kugai, C. Song, *Catal. Today*, 194 (2012) 16-24.
- [41] J. Nerlov, I. Chorkendorff, *Catal. Lett.*, 54 (1998) 171-176.
- [42] J. Nerlov, I. Chorkendorff, *J. Catal.*, 181 (1999) 271-279.
- [43] P.R. Subramanian, D.E. Laughlin, *J. Phase Equilib.*, 12 (1991) 231-243.
- [44] P. Huang, S. Menon, D.d. Fontaine, *J. Phase Equilib.*, 12 (1991) 3-5.
- [45] L. Lianos, Y. Debauge, J. Massardier, Y. Jugnet, J.C. Bertolini, *Catal. Lett.*, 44 (1997) 211-216.
- [46] L. Constant, P. Ruiz, M. Abel, Y. Robach, L. Porte, J.C. Bertolini, *Top. Catal.*, 14 (2001) 125-129.
- [47] S. Sitthisa, T. Pham, T. Prasomsri, T. Sooknoi, R.G. Mallinson, D.E. Resasco, *J. Catal.*, 280 (2011) 17-27.

- [48] J. Kugai, J.T. Miller, N. Guo, C. Song, *Appl. Catal., B-Environ.*, 105 (2011) 306-316.
- [49] J. Kugai, J.T. Miller, N. Guo, C. Song, *J. Catal.*, 277 (2011) 46-53.
- [50] X. Xu, C. Song, J.M. Andresen, B.G. Miller, A.W. Scaroni, *Energy Fuels*, 16 (2002) 1463-1469.
- [51] X. Wang, V. Schwartz, J.C. Clark, X. Ma, S.H. Overbury, X. Xu, C. Song, *J. Phys. Chem. C*, 113 (2009) 7260-7268.
- [52] X. Ma, X. Wang, C. Song, *J. Am. Chem. Soc.*, 131 (2009) 5777-5783.
- [53] J. Kugai, E.B. Fox, C. Song, *Appl. Catal., A-Gen*, 497 (2015) 31-41.
- [54] M.-W. Hsieh, T.-J. Whang, *Appl. Surf. Sci.*, 270 (2013) 252-259.
- [55] X. Zhang, W. Wang, J. Liu, S. Sheng, G. Xiong, W. Yang, *Thin Solid Films*, 516 (2008) 1849-1856.
- [56] A.M. Venezia, L.F. Liotta, G. Deganello, Z. Schay, L. Guczi, *J. Catal.*, 182 (1999) 449-455.
- [57] E.B. Fox, S. Velu, M.H. Engelhard, Y.-H. Chin, J.T. Miller, J. Kropf, C. Song, *J. Catal.*, 260 (2008) 358-370.
- [58] W.-J. Shen, Y. Matsumura, *Phys. Chem. Chem. Phys.*, 2 (2000) 1519-1522.
- [59] R. Gopinath, N. Lingaiah, B. Sreedhar, I. Suryanarayana, P.S. Sai Prasad, A. Obuchi, *Appl. Catal., B-Environ.*, 46 (2003) 587-594.
- [60] D. Briggs, M.P. Seah, *Practical Surface Analysis: Auger and X-Ray Photoelectron Spectroscopy*, John Wiley and Sons Ltd, Chichester, 1990.
- [61] A. Rochefort, M. Abon, P. Delichere, J.C. Bertolini, *Surf. Sci.*, 294 (1993) 43-52.
- [62] J. Batista, A. Pintar, D. Mandrino, M. Jenko, V. Martin, *Appl. Catal., A-Gen*, 206 (2001) 113-124.

[63] V. Sanchez-Escribano, L. Arrighi, P. Riani, R. Marazza, G. Busca, Langmuir, 22 (2006) 9214-9219.

[64] L.C. Grabow, M. Marvrikakis, ACS Catal., 1 (2011) 365-384.

Chapter 3 The Effect of Pd and Cu Combination on Surface Chemical Properties in CO₂ Hydrogenation to Methanol

This chapter will appear in the form of a journal article in a referred journal and is authored by Xiao Jiang, Xiaoxing Wang, Naoto Koizumi, and Chunshan Song*.

Abstract

The SiO₂-supported Pd-Cu bimetallic catalyst showed a strong synergetic effect on methanol synthesis at specific composition, which had been attributed to the alloy structure and the accompanying strong interaction between metal components. For the purpose of clarifying the effect of combining Pd and Cu on the surface chemical properties in CO₂ hydrogenation, the bimetallic catalysts with various Pd loadings were measured by H₂ temperature-programmed reduction (H₂-TPR), H₂/CO₂/CO temperature-programmed desorption (H₂/CO₂/CO-TPD), and diffuse reflectance FT-IR (DRIFTS). TPR profiles of bimetallic catalysts clearly showed the structuring procedure of alloy formation which considerably improved the reducibility of CuO. From H₂/CO₂-TPD, the combination of Pd and Cu promoted the adsorption towards weakly-bonded H₂ and CO₂ around reaction temperatures at specific composition, which appeared to correlate to the observed methanol promotion of bimetallic catalysts. DRIFTS spectra revealed that the formation of Pd-Cu alloy greatly improved the formation of intermediates formate and CO species. CO-TPD profiles confirmed the existence of three forms of chemisorbed CO species, and the bonding strength increased in the following order: CO^L (linear) < CO^B (di-coordinated bridging) < CO^H (triple-coordinated bridging). Among them, CO^B was suggested as a potential intermediate for methanol synthesis because of its moderate bonding strength and desorption temperature range

(proximity to reaction temperature). Quantitative analyses showed that the combination of Pd and Cu could promote the proportion towards CO^B adsorption at specific composition and thus gave rise to the possibility of methanol promotion via the following hydrogenation. Such pathway was further confirmed by the selectivity-conversion plot of Pd(8.7)-Cu(10)/SiO₂.

Keywords: CO₂ hydrogenation, Pd-Cu bimetallic catalyst, Methanol synthesis, Pd-Cu alloy, H₂ adsorption, CO₂ adsorption, CO adsorption, Formate species, Carbonyl species, Reaction pathway,

3.1 Introduction

Utilization of CO₂ as a carbon source for synthesizing chemical feedstocks and transportation fuels has recently attracted great attentions worldwide because a major advance in energy-efficient catalytic CO₂ conversion using renewable energy possesses great potentials to both control the CO₂ emission and mitigate the dependence on non-renewable fossil fuels [1-15]. CO₂ is a highly stable molecule, the conversion of which would be energy demanding if one were to use CO₂ as a single reactant; however, the CO₂ conversion would become thermodynamically easier if another substance with higher free Gibbs energy could be introduced as a co-reactant, such as hydrogen [7]. Thus, the synthesis of oxygenates and hydrocarbons via CO₂ hydrogenation is one of the promising approaches for the production of sustainable chemical feedstocks and fuels. If renewable energies, such as wind power, photovoltaic cells, and solar power, were used in replacement of fossil fuels to produce hydrogen, the whole synthesis would become more environmentally friendly [15].

Methanol (CH₃OH) is an important chemical feedstocks as well as an energy storage medium. Over the past two decades, significant efforts have been devoted to developing Cu-Zn-based catalysts for CO₂ hydrogenation to CH₃OH [16-20]. On the other hand, noble metal-based catalysts, particularly Pd-based series, gained attentions since mid-90s because of its superior reactivity towards methanol synthesis at relatively mild temperatures in CO hydrogenation [21-24] where Cu-ZnO based catalysts did not work well [22]. Several researchers have reported that Pd nanoparticles supported on metal oxides possess the ability to hydrogenate CO₂ to CH₃OH [25-32]. We have recently shown that nano-structured Pd catalysts with enhanced activities for CO₂ hydrogenation to CH₃OH can be prepared by combining two different strategies, namely incorporation of uniform mesoporous supports such as MCM-41 and SBA-15 leading to small Pd

nanoparticles inside nano-sized pore channels, and promotion by alkali/alkaline earth metal additives [33].

Most recently, motivated by the interest to explore the catalytic performance of Pd-Cu bimetallic catalysts in CO₂ conversion to methanol from various compositions, a series of bimetallic catalysts were prepared [34]. Compared to monometallic catalysts, a strong synergetic effect towards methanol formation was observed over the bimetallic catalysts with the metallic compositions at Pd=8.7 and Cu=10 wt%. The observed methanol promotion of Pd-Cu bimetallic catalysts at specific composition had been attributed to the alloy structure and the accompanying strong interaction between metal components. However, there is still a lack of fundamental understanding towards the composition-chemical properties relationship. In this context, the present work aims at clarifying the effect of Pd-Cu combination on surface chemical properties for CO₂ hydrogenation to methanol. For this purpose, the monometallic catalysts and bimetallic catalysts with various Pd loadings were characterized by H₂ temperature-programmed reduction (TPR), H₂ temperature-programmed desorption (H₂-TPD), CO₂ temperature-programmed desorption (CO₂-TPD), CO temperature-programmed desorption (CO-TPD), and diffuse reflectance FT-IR (DRIFTS). In the meantime, the reaction pathway was also proposed based on the selectivity-conversion plot where the CO₂ conversion was adjusted by the contact time W/F (W: Weight of catalyst, F: Flow rate).

3.2 Experimental

3.2.1 Preparation of catalysts

Amorphous silica was used as the support (Davisil Grade 62, particle size=75-250 × 10⁻⁶ m). The Pd-Cu bimetallic catalysts were prepared by the coimpregnation method using an acetone

solution of $\text{Pd}(\text{CH}_3\text{COO})_2$ (Aldrich, > 99.9%) and $\text{Cu}(\text{NO}_3)_2 \cdot 2.5\text{H}_2\text{O}$ (Alfa Aesar, $\geq 98\%$) [35]. The coimpregnated samples were dried at ambient temperature and calcined in an electric furnace at 723 K for 5 h under flowing dry air (ca. 100 mL (NTP) min⁻¹). The Pd/(Pd+Cu) atomic ratios were varied in the range of ca. 0.0 to 0.60 (i.e., 0-15.7 wt% of Pd loading). For comparison, supported monometallic Pd and Cu catalysts were prepared as well by using the same method.

The bimetallic catalysts, prepared by the coimpregnation method, are denoted as $\text{Pd}(X)\text{-Cu}(Y)/\text{SiO}_2$, where X and Y represent Pd loading (support basis) and Cu loading (support basis), respectively. Monometallic catalysts are denoted as Pd/support and Cu/support.

3.2.2 Catalytic test

The prepared catalysts were tested using a fixed bed reactor system consisting of a stainless steel tube with an internal diameter of 6 mm placed in an electrically heated oven. The reactor system and activity tests can be referred to section 2.2.2 from Chapter 2. The reaction temperature and pressure were maintained stable at 523 K and 4.1 MPa, respectively, unless otherwise noticed. The effect of contact time over $\text{Pd}(8.7)\text{-Cu}(10)/\text{SiO}_2$, exhibiting the maximum methanol formation rate, was investigated by varying the contact time (W/F, W, weight; F, flow rate) which ranged within 1.2-29.9 g-cat h mol⁻¹. For comparison, this series of experiments was also conducted on $\text{Cu}(10)/\text{SiO}_2$, wherein the W/F was adjusted within 6.2-59.1 g-cat h mol⁻¹ in order to obtain a comparable CO_2 conversion as $\text{Pd}(8.7)\text{-Cu}(10)/\text{SiO}_2$.

Gaseous products were periodically sampled with computer-controlled gas samplers and analyzed by two online GCs (SRI 8610C). The online GC/TCD was used to analyze Ar, CO and CO_2 , while the online GC/FID was for CH_3OH and CH_4 . Ar was an internal standard to estimate the CO_2 conversion, and CH_4 was employed as an external standard for measuring the methanol formation rate. The catalysts in this work yielded only CO and CH_3OH as carbon-containing

products, and the carbon balance was estimated according to the ratio between the simple summation of CO and CH₃OH formation rates and CO₂ conversion rate. All data published in this work lie within a reasonable range close to 100 mol%.

The mass transfer limitations were ruled out using the method recommended in literature [36], specifically “Weisz-Prater criterion”[37]. Depending upon these, it can be safely assumed that the reaction over Pd(8.7)-Cu(10)/SiO₂, which was mainly studied in this chapter, took place in a fully kinetic regime at 523 K and 4.1 MPa and free from mass transfer limitation (see Appendix H).

3.2.3 Characterization of catalysts

3.2.3.1 Temperature-programmed reduction (H₂-TPR)

The temperature programmed reduction (H₂-TPR) was conducted on the Micromeritics Autochem 2910 TPD/TPR equipped with a TCD. About 50 mg of sample was charged into the U-tube for every test. A representative temperature program process is illustrated in Fig. 3-1, and a typical process used 20 mL min⁻¹ of 5% H₂/Ar as the reduction gas with the heating rate of 10 K min⁻¹. The selection of operational parameters is described in Appendix F. The TPR profiles were characterized by three factors: the temperature at the maximum H₂ consumption (T_M), the full width at half maximum of the H₂ consumption, and the ratio between reducible metal species and actual hydrogen consumptions (i.e., M/H₂ ratio). In order to quantify the H₂ uptake, the silver oxide (II) was introduced as the standard (Micromeritics). This standard sample has been tested twice, and the average maximum reduction peak shows at 457.7 K (Fig. F-1, Appendix F). In addition, the copper oxide (II, Aldrich) was measured as well as benchmark.

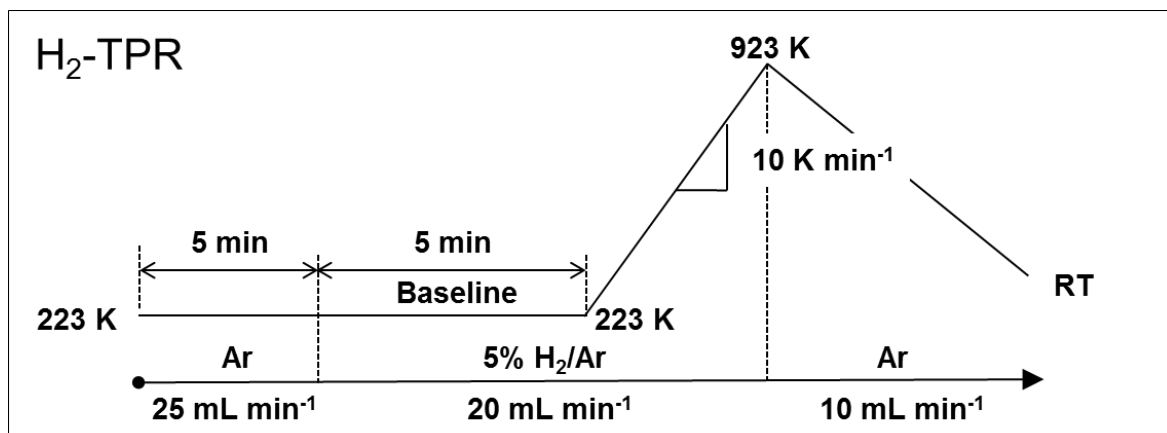


Figure 3-1 A schematic illustration for hydrogen temperature-programmed reduction (H₂-TPR) over monometallic and bimetallic Pd-Cu catalysts.

3.2.3.2 Temperature-programmed desorption (H₂, CO₂, and CO-TPD)

The hydrogen temperature-programmed desorption (H₂-TPD) was also carried out on the Autochem 2910 TPD/TPR. Ametek Dycor Dymaxion mass spectrometer DM200M was employed for monitoring the real-time concentration of desorbed hydrogen. The calcined catalyst (~150 mg) was charged and reduced in H₂ at 573 K for 2 h and then allowed to cool down to 303 K followed by flushing the catalyst bed with 1 vol% Ar/He (30 mL min⁻¹) at ambient temperature until the signal of H₂ ($m/z=2$) in MS was stable. The temperature elevation program was then initiated by heating up to 1173 K at a ramp rate of 10 K min⁻¹. A representative temperature program is illustrated in Fig. 3-2.

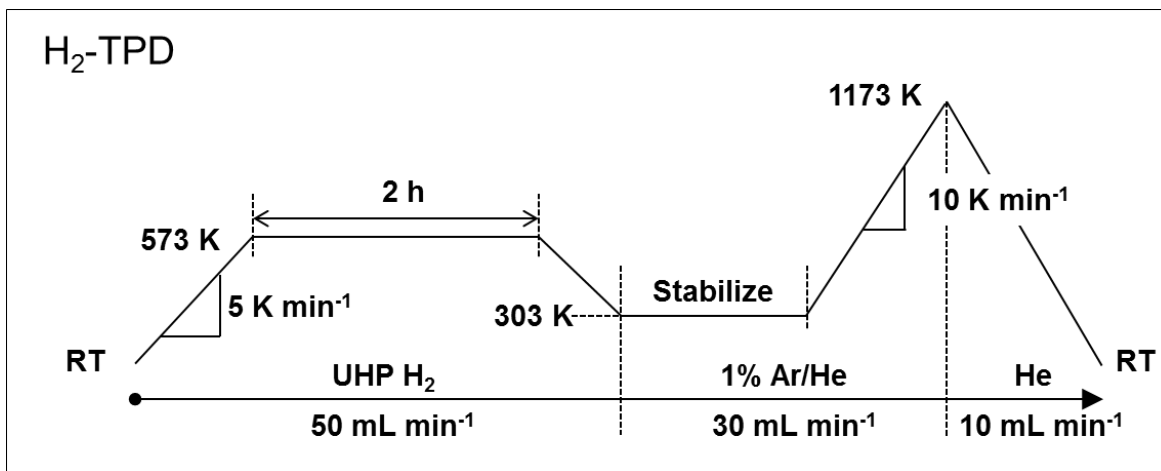


Figure 3-2 A schematic illustration for hydrogen temperature-programmed desorption (H₂-TPD) over monometallic and bimetallic Pd-Cu catalysts.

The carbon dioxide temperature-programmed desorption (CO₂-TPD) was also carried out on the Autochem 2910 TPD/TPR. Ametek Dycor Dymaxion mass spectrometer DM200M was employed for monitoring the real-time concentration of desorbed hydrogen. The calcined catalyst (~150 mg) was charged and reduced *in situ* in H₂ at 573 K for 2 h and then allowed to cool down to 523 K, followed by flushing the catalyst bed with 1 vol% Ar/99 vol% He (30 mL min⁻¹) for 30 min to remove adsorbed hydrogen. At this temperature, CO₂ chemisorption was carried out by flowing 15 vol% CO₂/He with a flow rate of 30 mL min⁻¹ for 1 hour. Then, the catalyst sample was allowed to cool down to room temperature and followed by flushing with 1 vol% Ar/He for 14–20 min. The temperature elevation program was then initiated with heating up to 1173 K at a ramp rate of 10 K min⁻¹. A representative temperature program is illustrated in Fig. 3-3.

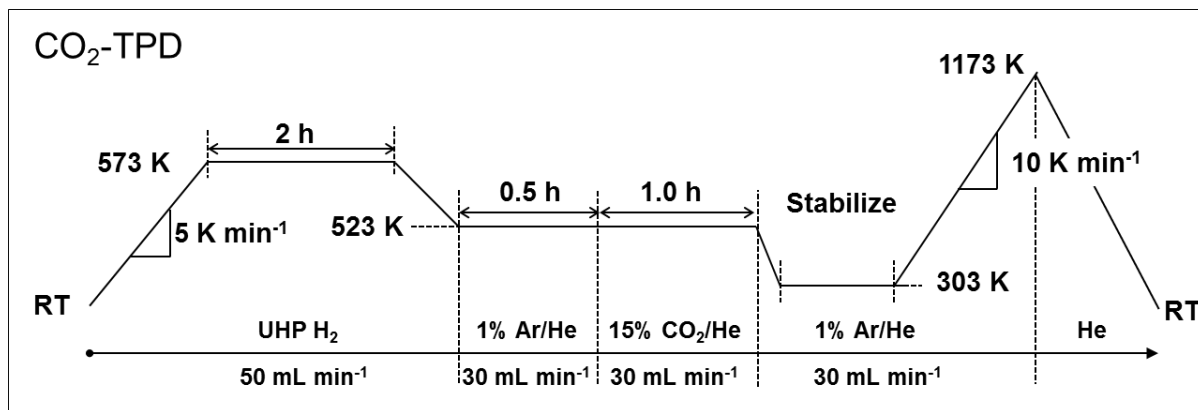


Figure 3-3 A schematic illustration for carbon dioxide temperature-programmed desorption (CO₂-TPD) over monometallic and bimetallic Pd-Cu catalysts.

The carbon monoxide temperature-programmed desorption (CO-TPD) was carried out on an Autochem 2920 TPD/TPR equipped with a TCD at the Materials Characterization Laboratory of the Penn State Materials Research Institute. The calcined catalyst (ca. 100 mg) was charged and reduced in situ in H₂ at 573 K for 1 h and then allowed to cool down to 523 K followed by flushing the catalyst bed with Ar (30 mL min⁻¹) for 1 h to remove the adsorbed hydrogen. At the same temperature, CO adsorption was carried out by switching to 5 vol% CO/He with a flow rate of 30 mL min⁻¹ for 1 h. Then, the catalyst sample was allowed to cool down to 323 K and flushed with Ar in the meantime (30 mL min⁻¹) for 20 min. When the baseline was stable, the temperature elevation program was initiated by heating up to 873 K at a ramp rate of 5 K min⁻¹. A representative temperature program is illustrated in Fig. 3-4. The CO uptake was determined quantitatively, and detailed procedure was described in Appendix G.

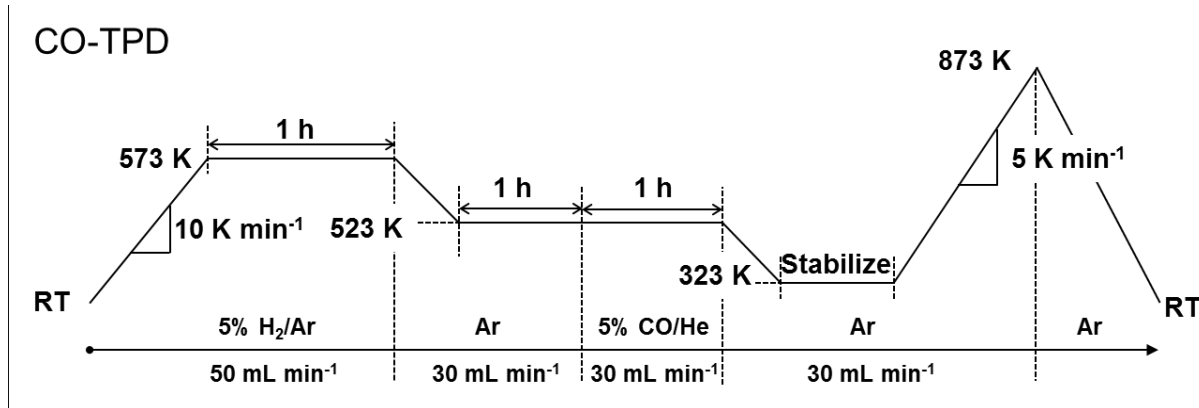


Figure 3-4 A schematic illustration for carbon monoxide temperature-programmed desorption (CO-TPD) over monometallic and bimetallic catalysts.

3.2.3.3 Diffuse reflectance FT-IR

The adsorbed surface species during the CO₂ hydrogenation over various mono and bimetallic catalysts was analyzed by the in situ diffuse reflectance Fourier Transform Infrared Spectroscopy (DRIFTS) using a Nexus 470 spectrometer with a Smart Collector environmental chamber. About 20 mg of sample was mounted on the chamber for each measurement. A resolution of 4 cm⁻¹ was used throughout investigations, and every spectrum was acquired by 128 scans. OMNIC ver. 7 was used for the data collection and processing. As benchmark, the methanol and formic acid adsorption experiments were also performed at temperatures. Methanol was purchased from VWR (ACS Grade \geq 99.8%), while formic acid (Grade \geq 95%) was from Sigma-Aldrich. In the methanol and formic acid adsorption experiments, the sample was initially purged by N₂ (e.g., 30 mL min⁻¹) for 1 h at 373 K followed by the reduction at 573 K for 1 h under a H₂ flow and then allowed to cool down to room temperature. Prior to the injection, N₂ (UHP) was allowed to flush the system for 30 min followed by collecting the background, hereafter denoted as BG-0. The interferogram was collected right after the injection of 4.0 μ L of methanol or formic acid. Then the chamber was elevated to the target temperature and allowed to stabilize for \sim 15 min

before acquiring the corresponding interferograms. All resultant interferograms were processed by the BG-0.

In the in situ CO₂ hydrogenation over pre-reduced mono and bimetallic Pd-Cu catalysts, the sample was initially purged by N₂ at 373 K for 1 hour followed by the reduction in a H₂ flow (UHP, 30 mL min⁻¹) at 573 K for 1 hour. The reduced sample was allowed to cool down to 373 K and maintained for 30 min for stabilization. The background interferogram was collected at this condition and hereafter denoted as BG-1. Then, the in situ CO₂ hydrogenation was performed by using CO₂/H₂/Ar (24/72/4, vol%) as feed gases at a flow rate of ~ 30 mL min⁻¹ (NTP). The spectra at different temperatures were acquired at steady state (e.g., after 30 min stabilization) and were processed based on BG-1.

The conversion of adsorbed surface species over pre-reduced Pd(8.7)-Cu(10)/SiO₂ was performed by switching to H₂ (UHP) with a rate of 30 mL min⁻¹ after one-hour CO₂ hydrogenation or CO adsorption at temperatures (e.g., 373 or 523 K). The spectra were collected at regular intervals. BG-1 was used as the background during the data process. For clarity, the spectra were further reprocessed based on the first spectrum collected after the gas switch, which can be marked as BG-2 and BG-3, standing for the first spectrum at 373 K and 523 K, respectively. For comparison, N₂ (UHP, 30 mL min⁻¹) purge was also carried out after the one-hour reaction at 373 K. Likewise, similar methods were applied to process the resultant spectra. For clarity, the notations of each background spectrum are summarized in Table 3-1.

Table 3-1 Denotations of the background spectra used in DRIFTS analyses

Background #	Description
Background-0 (BG-0)	<ul style="list-style-type: none"> • N₂ purge at 373 K for 1 h; • H₂ reduction at 573 K for 1 h; • N₂ purge at room temperature (RT) for 0.5 h; <p>➤ <i>Used exclusively for methanol and formic acid adsorptions</i></p>
Background-1 (BG-1)	<ul style="list-style-type: none"> • N₂ purge at 373 K for 1 h; • H₂ reduction at 573 K for 1 h followed by cooling down to 373 K and stabilizing for 0.5 h; <p>➤ <i>For in situ CO₂ HYD and H₂ purge after CO₂ HYD at different temperatures</i></p>
Background-2 (BG-2)	<ul style="list-style-type: none"> • N₂ purge at 373 K for 1 h; • H₂ reduction at 573 K for 1 h followed by cooling down to 373 K and stabilizing for 0.5 h; • The spectrum was collected after 1 h CO₂ HYD at 373 K prior to the initiation of H₂ or N₂ purge; <p>➤ <i>For H₂/N₂ purge after CO₂ HYD at 373 K</i></p>
Background-3 (BG-3)	<ul style="list-style-type: none"> • N₂ purge at 373 K for 1 h; • H₂ reduction at 573 K for 1 h followed by cooling down to 523 K and stabilizing for 0.5 h; • The spectrum was collected after 1 h CO adsorption at 523 K prior to the initiation of H₂ purge; <p>➤ <i>For H₂ purge after CO adsorption at 523 K</i></p>

It is noted that this series of experiments is designed to observe the formed and adsorbed species during the reaction and their change/conversion in the conditions of H₂/N₂ purge. For this purpose, the interferogram of the sample itself was used as background instead of KBr.

3.3 Results and discussion

3.3.1 Temperature-programmed reduction (TPR)

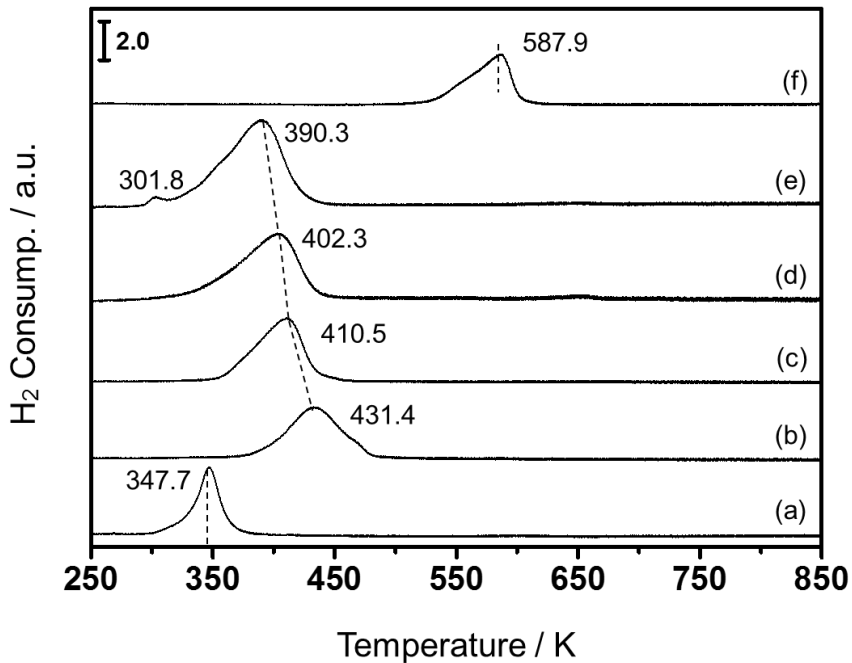


Figure 3-5 TPR profiles for monometallic and bimetallic Pd-Cu catalysts with different metallic compositions. TPR conditions: 20 mL min⁻¹ of 5 vol% H₂/Ar flow, 10 K min⁻¹ of heating rate. (a) Pd(8.7); (b) Pd(2.5)-Cu(10); (c) Pd(5.7)-Cu(10); (d) Pd(8.7)-Cu(10); (e) Pd(15.7)-Cu(10); (f) Cu(10).

The TPR profiles of the mono and bimetallic catalysts with different compositions are shown in Fig. 3-5, and the corresponding parameters are tabulated in Table 3-2. All samples were cooled down to cryogenic temperatures (ca. 223 K) before the elevation of the temperature program because Pd is susceptible to hydrogen and can be reduced even at ambient temperature. Fig. 3-5a shows the TPR profile of Pd(8.7)/SiO₂, and the maximum reduction peak is symmetric and centered at 347.7 K. The TPR profile of Cu(10)/SiO₂ (Fig. 3-5f) reveals an asymmetric peak centered at 587.9 K, which resembles the TPR profile of pure CuO, as shown in Fig. 3-6. Such superimposed peak is indicative of a stepwise reduction of crystalline CuO from Cu²⁺ to Cu⁺ at

relatively lower temperature (ca. 573 K), and closely followed by the reduction from Cu⁺ to metallic Cu⁰ at relatively higher temperature (ca. 587.9 K). A similar procedure has been proposed in literature [38, 39].

Table 3-2 Summary of TPR data for Pd(X)-Cu(10)/SiO₂ and monometallic catalysts ^{a)}

Catalyst	T_M / K	H ₂ /M ratio ^{b)}
Pd _{8.7}	347.7	1.3
Cu ₁₀	587.9 ± 2.7	1.0 ± 0.1
Pd _{2.5} -Cu ₁₀	431.4 ± 2.2	1.1 ± 0.2
Pd _{5.7} -Cu ₁₀	410.5	1.2
Pd _{8.7} -Cu ₁₀	402.3 ± 2.2	1.2 ± 0.1
Pd _{15.7} -Cu ₁₀	390.3	1.3

^{a)} Some of the reported data were ensured by at least 3 separated measurements, and corresponding errors were shown as well.

^{b)} Ratio between the amounts of hydrogen consumed and the reducible species in mole.

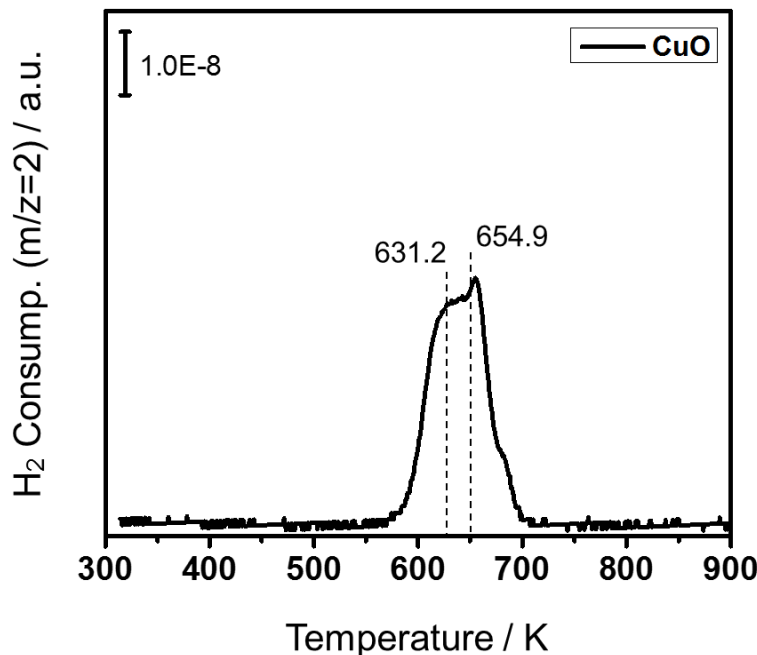


Figure 3-6 TPR profile of CuO (Sigma-Aldrich). The data was collected by mass spectrometer. TPR conditions: 20 mL min⁻¹ of 5 vol% H₂/Ar flow with a heating rate of 10 K min⁻¹.

Interestingly, when Pd is doped into the catalyst (e.g., 2.5 to 15.7 wt%), a distinctive-single reduction peak is shown in the whole temperature range, particularly in between the maximum reduction peaks of monometallic Cu/SiO₂ and Pd/SiO₂ (see Fig. 3-5b to 3-5e). Moreover, the single peak gradually shifts towards lower temperatures with the stepwise increment of Pd loading. These observations indicate that PdO reduction is retarded, while CuO reducibility is significantly improved with the addition of palladium; more importantly, the reduction of metal oxides occurs simultaneously instead of separately. Recall that the XRD pattern of Pd(5.7)-Cu(10)/SiO₂ in the calcined form reveals typical diffractions of CuPdO₂ rather than isolated PdO and CuO [34]. Therefore, the reduction of CuO is facilitated by the formation of such well-mixed oxides, while the reduction of PdO was retarded due to the mutual diffusion into each lattice. Noticeably, the reduction peaks for both Pd(8.7)-Cu(10)/SiO₂ (Fig. 3-5d) and Pd(15.7)-Cu(10)/SiO₂ (Fig. 3-5e) show a tail in low-temperature side, which may be indicative of the alloy restructuring during the reduction [39]. It is also worth mentioning that the TPR profile of Pd(15.7)-Cu(10)/SiO₂ (Fig. 3-5e) exhibits a small peak at lower temperature (ca. 301.8 K), which can be assigned to the reduction of isolated PdO due to excessive Pd loading. In fact, the XRD pattern of the same sample clearly shows distinguishable diffractions of unalloyed Pd⁰ with considerable larger particle size (Fig. 2-6c, Chapter 2). Thus, the TPR profile agrees well with the XRD results.

Additionally, the improvement of CuO reducibility suggests the promoting effect of palladium, which may involve a decrease in activation energy and/or an increase in the pre-exponential term according to Arrhenius equation. In order to understand this aspect in more detail, the activation energy of the reduction was determined by means of Kissinger method which correlates the variation of the temperature at maximum reduction T_M with the heating rate (β) [40]. The relevant mathematical expression is shown in Eq. 3-1,

$$\ln\left(\frac{\beta}{T_M}\right) = -\frac{E_a}{R} \cdot \frac{1}{T_M} + \ln[H_2]_m + \text{Const.} \quad \text{Eq. 3-1}$$

where β : heating rate, K min⁻¹; T_M : temperature at maximum rate, K; R : gas constant, kJ mol⁻¹; E_a : apparent activation energy; $[H_2]_m$: hydrogen concentration at T_M . For comparison, the bimetallic catalyst Pd(5.7)-Cu(10)/SiO₂ and the monometallic Cu(10)/SiO₂ were measured, and the heating rates were varied from 2 K min⁻¹ to 20 K min⁻¹. The TPR profiles are shown in Fig. 3-7, and corresponding Kissinger plot is illustrated in Fig. 3-8. Note that the test for diffusion effect has been carried out prior to the TPR kinetic analysis over Pd(5.7)-Cu(10)/SiO₂, and the profiles show that both peak shape and FWHM remain unchanged and are independent of the flow rate (see Fig. F-3, Appendix F). Therefore, the measurement is free from diffusion effects [41].

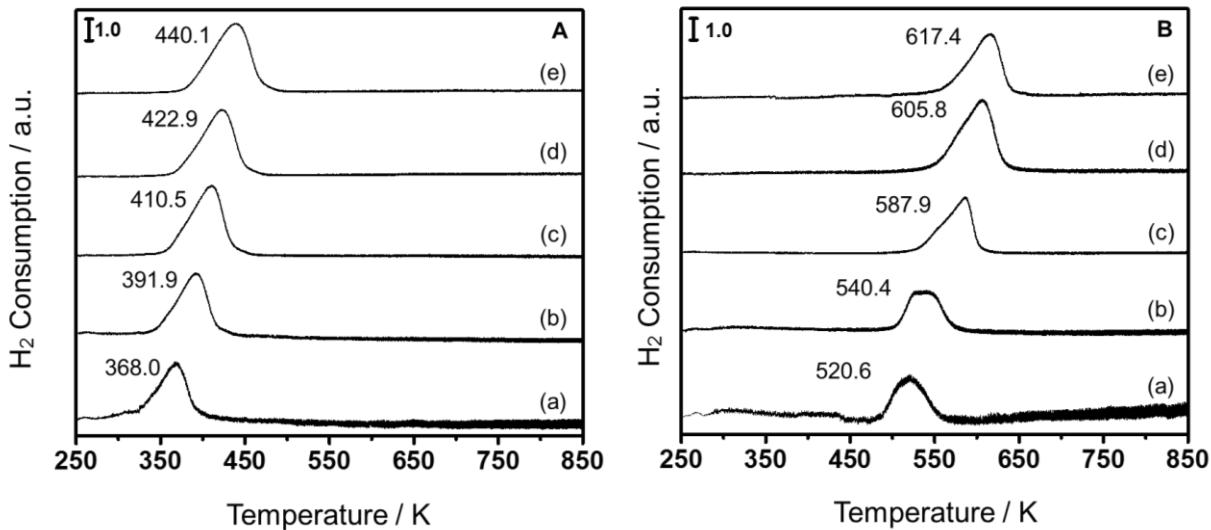


Figure 3-7 TPR profiles for (A) Pd(5.7)-Cu(10)/SiO₂ and (B) Cu(10)/SiO₂ at different heating rates. TPR conditions: 20 mL min⁻¹ of 5 vol% H₂/Ar flow. (a) 2 K min⁻¹; (b) 5 K min⁻¹; (c) 10 K min⁻¹; (d) 15 K min⁻¹; (e) 20 K min⁻¹.

As shown in Fig. 3-8, the activation energies obtained for monometallic and bimetallic catalysts are 48.5 and 37.5 kJ mol⁻¹, respectively. Clearly, the addition of Pd in the bimetallic catalysts causes a slight decline of the activation energy. On the other hand, Melian-Cabrera *et al.*

[42] proposed that Pd may provide a high concentration of active hydrogen that is susceptible for the use in CuO reduction. This explanation may still be valid in this work because the H₂/M ratio slightly increases with the increment of Pd loadings as tabulated in Table 3-2. Therefore, an intimate contact between Pd and Cu in bimetallic catalysts is observed as evidenced by the observation of a single reducing peak on bimetallic catalysts with various compositions. The reduction of PdO has been retarded in the bimetallic catalysts, while the addition of Pd greatly improves the reducibility of CuO by reducing the activation energy and providing concentrated hydrogen during the reduction.

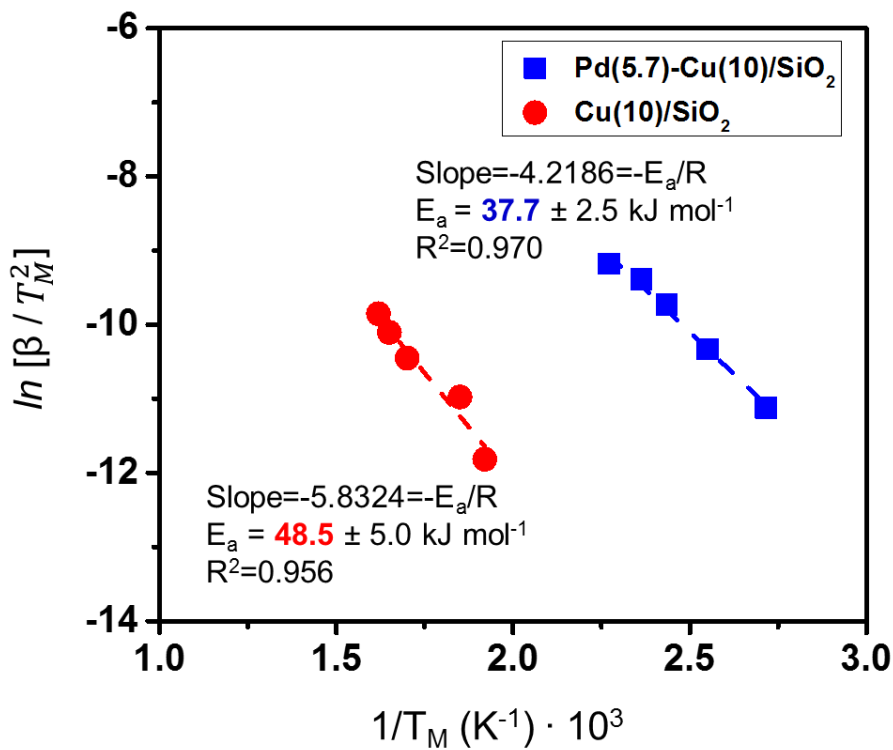


Figure 3-8 Kissinger plots of Pd(5.7)-Cu(10)/SiO₂ and Cu(10)/SiO₂.

The ratio of the amount of hydrogen consumption relative to that of reducible species (ca. Pd²⁺ and/or Cu²⁺) is determined quantitatively and summarized in Table 3-2. For accuracy, some of the experiments had been repeated at least three times, and the average data was listed along

with the errors. It is clear that the experimental and stoichiometric values do not vary substantially. Notably, the ratio of Pd(15.7)-Cu(10)/SiO₂, H₂/M=1.3, is higher than the stoichiometric unity. The exceeding ratio could be attributed to the existence of large-isolated PdO as evidenced by the peak at 301.8 K (Fig. 3-5e), which dissociates more hydrogen at relatively lower temperature. Hence, the additional adsorbed hydrogen leads to a higher hydrogen consumption. Such higher ratio over Pd-doped catalysts is also known in literature [42].

3.3.2 H₂ adsorption properties of Pd-Cu catalysts

The effect of Pd and Cu combination on H₂ adsorption properties was studied by H₂-TPD. Fig. 3-9 presents H₂-TPD profiles of Pd(8.7)-Cu(10)/SiO₂ and monometallic catalysts with corresponding metal loadings. As illustrated in Fig. 3-9a, Cu(10)/SiO₂ barely shows any desorption peaks. It is suggested that Cu/SiO₂ has a negligible hydrogen chemisorption capacity, or hydrogen atoms are adsorbed so weakly on Cu⁰ surface that they are removed easily during the He flushing prior to the desorption program. Pd(8.7)/SiO₂ exhibits multiple desorption peaks in the whole temperature range (Fig. 3-9c), specifically centered at ca. 400 K, 550-700 K, and 850 K, which correspond to weak, medium, and strong adsorptive forms of hydrogen, respectively [43]. On the other hand, the Pd(8.7)-Cu(10)/SiO₂ (Fig. 3-9b) shows a distinct hydrogen desorption peak, centered at 380-400 K, indicating the presence of weakly-bonded hydrogen atoms on the surface [44]. Apparently, the peaks for medium and strong adsorptive species become weaker over the bimetallic catalyst than Pd alone, while the adsorption towards weakly-bonded hydrogen is more concentrated. For this particular sample, XPS results demonstrate that the Cu disperses the Pd on the surface of alloy particles as evidenced by the decline of Pd surface concentration, which could be correlated to such characteristic adsorption property towards weakly-bonded hydrogen. In other words, the uniform and nano-sized alloy particles, with highly dispersed metals, play a critical role

in the selective adsorption of weakly-bonded hydrogen.

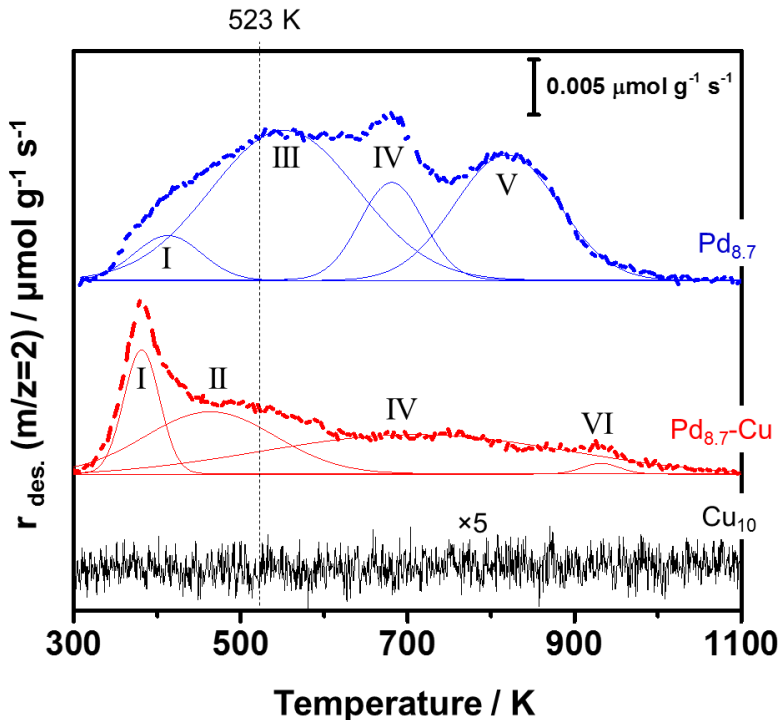


Figure 3-9 H₂-TPD profiles of pre-reduced monometallic and bimetallic catalysts. (a) Cu(10)/SiO₂, (b) Pd(8.7)/SiO₂, (c) Pd(8.7)-Cu(10)/SiO₂. (---) measured TPD profile, (—) deconvoluted peaks.

Fig. 3-10 presents H₂-TPD profiles of Pd-Cu catalysts with various Pd loadings, and the Cu loading was fixed at 10 wt% for all. For comparison, the profile of Pd(8.7)-Cu(10)/SiO₂ is also included (Fig. 3-10c). For Pd(2.5)-Cu(10)/SiO₂ (Fig. 3-10a), the hydrogen desorption curve is generally similar to that for Cu(10)/SiO₂ in the whole temperature range, except a weak peak appears at lower temperature (ca. < 400 K), indicating the existence of a small amount of weakly-adsorbed hydrogen atoms due to the addition of less Pd. As confirmed from our recent work, this sample presents PdCu₃ and Cu⁰ phases in XRD pattern (Fig. 2-6a, Chapter 2) and shows the existence of PdCu₃ alloy particles in a local area from a STEM/EDS image (Fig. 2-10, Chapter 2) [34]. Hence, the resemblance of TPD profiles is indicative of a Cu⁰-dominant surface, which might

even cause a partial coverage of PdCu₃ alloy particles. Fig. 3-10d is the TPD profile for Pd(5.7)-Cu(10)/SiO₂. Similarly to the profile of Pd(8.7)-Cu(10)/SiO₂ (Fig. 3-10c), a distinct hydrogen desorption peak, centered at 380-400 K, is observed, indicating the presence of concentrated weakly-bonded hydrogen atoms on the surface. Likewise, this could be attributed to the uniform and nano-sized alloy particles for this catalyst. Fig. 3-10d depicts the TPD profile of a Pd-rich bimetallic catalyst, namely Pd(15.7)-Cu(10)/SiO₂, and it reveals an analogous desorption profile as Pd(8.7)/SiO₂ in the whole temperature range. Note that the excessive Pd loading leads to the unalloyed Pd⁰ particles with considerably large size, apart from alloy particles (Fig. 2-6c, Chapter 2) [34]. Thus, the surface is dominated by Pd⁰ particles, and the partial coverage of alloy particles may also occur.

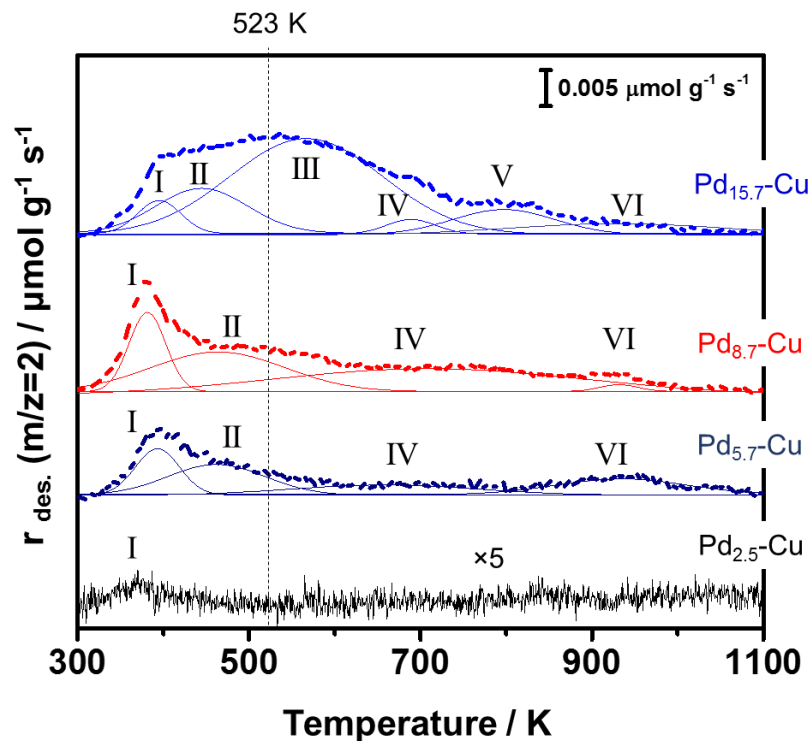


Figure 3-10 H₂-TPD profiles of Pd(X)-Cu(10)/SiO₂. (a) Pd(2.5)-Cu(10)/SiO₂, (b) Pd(5.7)-Cu(10)/SiO₂, (c) Pd(8.7)-Cu(10)/SiO₂, (d) Pd(15.7)-Cu(10)/SiO₂. (---) measured TPD profile, (–) deconvoluted peaks.

In addition, the superimposed peaks in the H₂-TPD profiles of Pd(8.7)/SiO₂ and Pd(X)-Cu(10)/SiO₂ were deconvoluted using Gaussian functions, and these peaks are hereafter denoted I-V from low to high temperatures (see Appendix G). Noteworthy, the H₂-TPD measurement was also conducted on the bare support amorphous silica by using the same procedure, and it barely shows any desorption peak throughout the whole temperature range (see Appendix G). In comparison to Pd alone, the bimetallic catalysts, with Pd loading varying from 2.5 to 8.7 wt% (Fig. 3-10a-c), exhibit a selective adsorption tendency towards type I and II, and such trend is growing stronger with the increase of Pd loading. Moreover, the type I and II desorb below 523 K which is the reaction temperature. Thus, they are potentially active for the methanol synthesis from CO₂ hydrogenation. The quantities of type I and II adsorbed hydrogen were also determined by integrating these Gaussian peaks and presented in Table 3-3. Generally, the total H₂ uptake of Pd(X)-Cu(10)/SiO₂ catalysts enhances monotonically with the increasing Pd loading from 2.5 to 15.7 wt%. In contrast, the amount of weakly-bonded hydrogen (I+II) increases initially and then decreases after reaching the maximum at Pd=8.7 wt% (e.g., 10.0 μmol g-cat⁻¹). When correlating with its featured alloy phases, it is clear that the alloy formation plays a critical role in the selective adsorption towards weakly-bonded hydrogen atoms compared to the monometallic Pd catalyst, particularly when PdCu₃ and PdCu coexisted without unalloyed metallic phases. Although Pd(15.7)-Cu(10)/SiO₂ shows the coexistence of PdCu₃ and PdCu as well from XRD pattern, the large and unalloyed Pd⁰ particles may dominate the surface and cause partial coverage of the alloy phases, which inhibits the adsorption of weakly-bonded hydrogen as Pd alone.

Table 3-3 Amount of H₂ desorbed in H₂-TPD of Pd(X)-Cu(10)/SiO₂ and monometallic catalysts ^{a)}

Catalyst	Amount of desorbed H ₂ / μmol g-cat ⁻¹	
	Total	I+II ^{b)}
Cu ₁₀	1.1	0.2
Pd _{8.7}	35.5	2.4
Pd _{2.5} -Cu ₁₀	2.4	0.9
Pd _{5.7} -Cu ₁₀	11.0	6.2
Pd _{8.7} -Cu ₁₀	19.7	10.0
Pd _{15.7} -Cu ₁₀	31.9	7.4

^{a)} TPD conditions: 1 vol% Ar/He (30 mL min⁻¹), 10 K min⁻¹ of heating rate.

^{b)} Total amount of type I and II desorbed H₂ below 523 K.

Consequently, the hydrogen adsorption properties appear to correlate with the Pd contents in the bimetallic catalysts. Pd(8.7)-Cu(10)/SiO₂ presents a selective adsorption towards weakly-bonded hydrogen (I+II) below the reaction temperature (523 K), which could be attributed to the coexisted PdCu₃ and PdCu alloy phases with uniform and nano-sized particles. Therefore, the combination of Pd and Cu could provide more active hydrogen around reaction temperatures with specific composition, and the correlation of these weakly-adsorbed hydrogen with CH₃OH promotion will be discussed in section 3.3.7.

3.3.3 CO₂ adsorption properties of Pd-Cu catalysts

The effect of combining Pd and Cu on CO₂ adsorption properties was studied by CO₂-TPD. Fig. 3-11 illustrates the TPD profiles of Pd(8.7)-Cu(10)/SiO₂ and monometallic catalysts with corresponding metal loadings. Generally, CO₂ mainly desorbs at 310-465 K and ca. 775 K for both mono and bimetallic catalysts. A deconvolution processing (Gaussian function) was also applied

in these superimposed peaks, which is also referred to the desorbed CO₂ species observed from the CO₂-TPD profile of the bare support amorphous silica (see Appendix H). Two types of weakly-bonded CO₂ are observed below 523 K, which are denoted as type I-II from low to high temperatures. In comparison to monometallic catalysts (Figs. 3-11a and 3-11c), the combination of Pd and Cu (Fig. 3-11b) leads to an improvement of these two weakly-bonded species as evidenced from the more intense peaks .

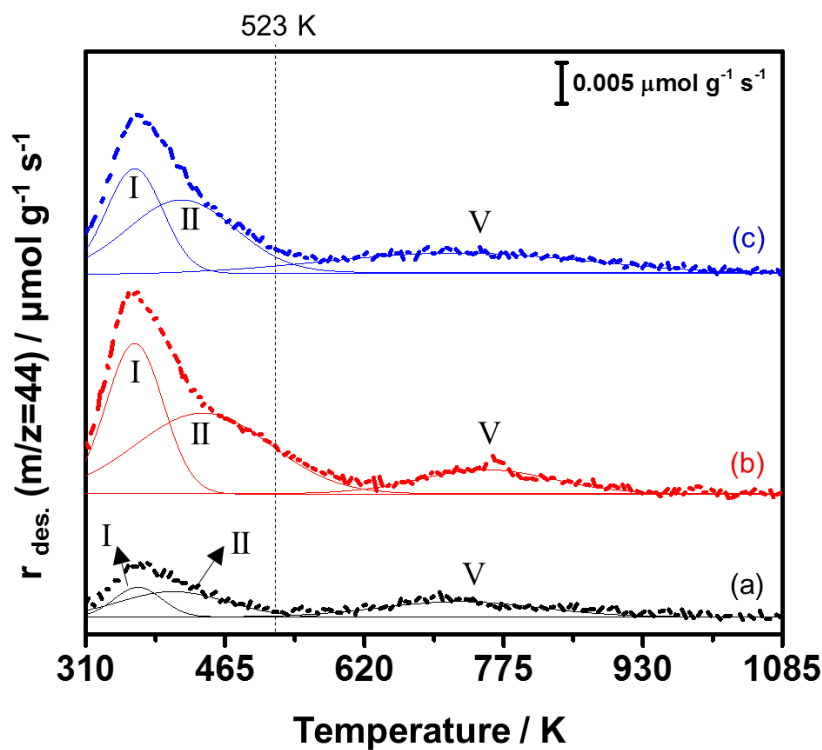


Figure 3-11 CO₂-TPD profiles of pre-reduced monometallic and bimetallic catalysts. (a) Cu(10)/SiO₂, (b) Pd(8.7)/SiO₂, (c) Pd(8.7)-Cu(10)/SiO₂. (---) measured TPD profile, (–) deconvoluted peaks.

Fig. 3-12 depicts the CO₂-TPD profiles of Pd(X)-Cu(10)/SiO₂ with various Pd loadings, and the superimposed peaks were also deconvoluted by using a similar processing method. When the Pd loading is varied from 2.5 to 8.7 wt% (Fig. 3-11a-c), weakly-bonded CO₂ with the assigned number type I and II are observed for all catalysts below 523 K, and the peak intensities appear to

increase with the increase of Pd loading. On the other hand, when loading excessive amount of Pd, the peak intensities of those weakly-bonded CO₂ decrease slightly, instead, more moderately-bonded CO₂ appears in the range of 555-700 K.

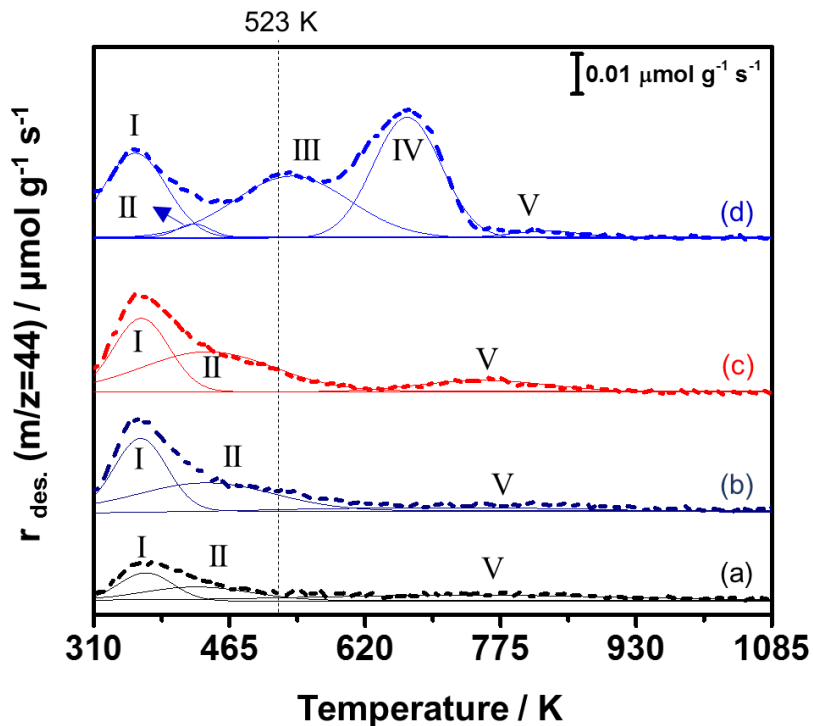


Figure 3-12 CO₂-TPD profiles of Pd(X)-Cu(10)/SiO₂. (a) Pd(2.5)-Cu(10)/SiO₂, (b) Pd(5.7)-Cu(10)/SiO₂, (c) Pd(8.7)-Cu(10)/SiO₂, (d) Pd(15.7)-Cu(10)/SiO₂. (---) measured TPD profile, (–) deconvoluted peaks.

The quantities of desorbed CO₂ were also determined by integrating these Gaussian peaks and presented in Table 3-4. Clearly, the total amount of desorbed CO₂ increases with the increase of Pd loading, while the weakly-bonded CO₂ increases with increasing Pd loading initially and followed by a decline after reaching the maximum value at Pd=8.7 wt%. Again, such characteristic adsorption property could be attributed to the uniform and nano-sized alloy particles for this particular bimetallic catalyst. Therefore, the combination of Pd and Cu could provide more active CO₂ around reaction temperatures with specific composition, and the correlation of these weakly-

adsorbed CO₂ with CH₃OH promotion will be discussed in section 3.3.7 along with the correlation of the amount of weakly-bonded H₂.

Table 3-4 Amount of CO₂ desorbed in CO₂-TPD of Pd(X)-Cu(10)/SiO₂ and monometallic catalysts ^{a)}

Catalyst	Amount of desorbed CO ₂ / $\mu\text{mol g-cat}^{-1}$	
	Total	I+II ^{b)}
Cu ₁₀	6.5	4.0
Pd _{8.7}	19.0	13.2
Pd _{2.5} -Cu ₁₀	9.3	6.2
Pd _{5.7} -Cu ₁₀	19.4	15.4
Pd _{8.7} -Cu ₁₀	22.0	18.8
Pd _{15.7} -Cu ₁₀	44.6	11.2

^{a)} TPD conditions: 1 vol% Ar/He (30 mL min⁻¹), 10 K min⁻¹ of heating rate.

^{b)} Total amount of type I and II desorbed CO₂ below 523 K.

3.3.4 Diffuse reflectance FT-IR (DRIFTS)

3.3.4.1 Surface species & bands assignment

To investigate the surface species on bimetallic catalysts, diffuse reflectance FT-IR measurements were conducted in CO₂/H₂ atmospheres at different temperatures (e.g., 373-523 K). Pd(8.7)-Cu(10)/SiO₂ was selectively chosen due to its superior performance in methanol synthesis and characteristic crystal structure featured with uniform and nano-sized alloy particles (3-6 nm). For clarity, the interferograms are shown in three separated ranges, as illustrated from Figs. 3-13 to 3-15. The absorbance intensity, corresponding to the symmetric stretching vibration of CO₂ (g) (e.g., 2349 cm⁻¹), is too strong to deduce any information in that region; therefore, we omit it for

clarification. As reference, the methanol and formic acid adsorption measurements were also performed at 373 K, and the resulting spectra were included in some figures. Noteworthy, the data processing method for methanol/formic acid adsorption is based on BG-0, while the spectra acquired in CO₂ hydrogenation were processed by BG-1 (see Table 3-1).

3000-4000 cm⁻¹: Fig. 3-13 depicts the FT-IR spectra (3000-4000 cm⁻¹) collected in CO₂/H₂ over pre-reduced Pd(8.7)-Cu(10)/SiO₂ at temperatures. Evidently, four bands are observed in this region, centered at 3730, 3703, 3627, and 3597 cm⁻¹. As known, gaseous CO₂ is a linear triatomic molecule with three fundamental vibrations, including ν_1 (1388 cm⁻¹, symmetric stretching vibration, IR inactive), ν_2 (667 cm⁻¹, degenerate bending vibration), and ν_3 (2349 cm⁻¹, symmetric stretching vibration). Since two fundamental vibrations of CO₂ (g) can be excited simultaneously, some combinational bands, also known as rovibrational bands, would appear in the 3000-4000 cm⁻¹ region. Therefore, the observed quartet peaks can be assigned to combinational bands of CO₂ (g). Specifically, 3730 (R branch) and 3703 cm⁻¹ (P branch) are the combinational bands of $\nu_1+\nu_3$, while 3627 (R branch) and 3597 cm⁻¹ (P branch) are the combinational bands of $2\nu_2+\nu_3$ [45]. It is worth stating that these combinational bands are observed for all samples, and both intensity and peak shape are independent of either temperature or metallic compositions. Besides, the CO₂ conversion is very low at ambient pressure (e.g., < 2 %). Thus, the intensities of the quartet, particularly the distinct band at 3730 cm⁻¹, can be employed as internal references, through which the relative intensities of other surface species can be measured and compared among different samples. Additionally, the temperature elevation also results in a negative peak centered at 3747 cm⁻¹, and it becomes sharp gradually. This signifies the consumption of isolated silanol groups at higher temperatures [46].

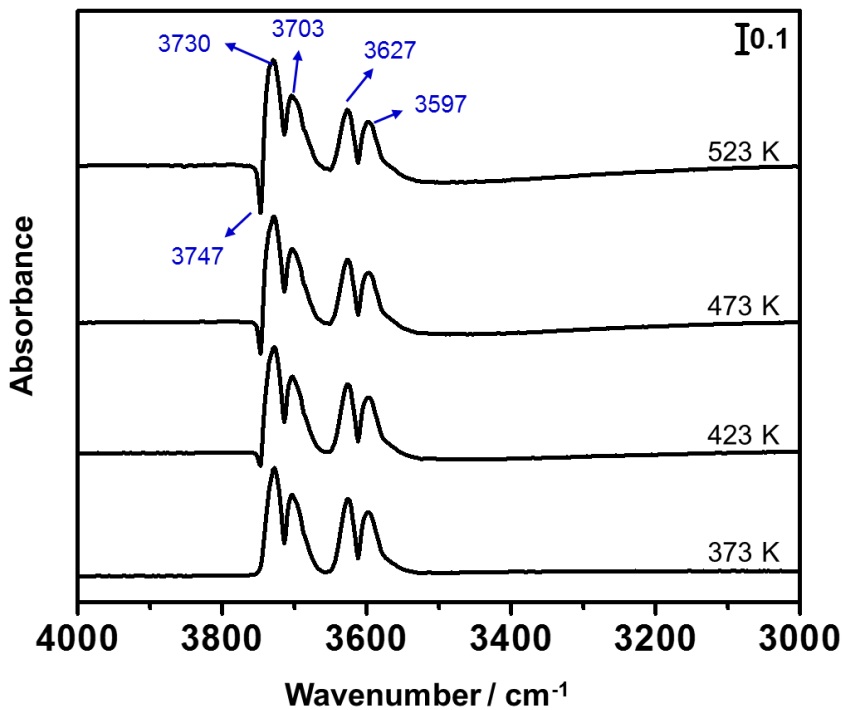


Figure 3-13 Diffuse reflectance FT-IR spectra of pre-reduced Pd(8.7)-Cu(10)/SiO₂ in CO₂/H₂ at temperatures. CO₂ hydrogenation conditions: CO₂/H₂/Ar=24/72/4 (vol%), 0.1 MPa, ca. 30 mL min⁻¹. All spectra were processed by BG-1.

2600-3000 cm⁻¹: Fig. 3-14 shows the FT-IR spectra collected from the same measurement within 2600-3000 cm⁻¹ (Fig. 3-14a to 3-14d), along with the spectra of methanol and formic acid adsorption over the same pre-reduced sample at 373 K (Fig. 3-14e to 3-14f). In Fig. 3-14a, a doublet, centered at 2935 and 2854 cm⁻¹, presents and exhibits similar relative intensities and frequencies as the doublet in Fig. 3-14f, which represents the interferogram of formic acid adsorption at the same temperature. Thus, this doublet can be assigned to the adsorbed formate species on the surface. Specifically, 2935 cm⁻¹ is the combinational bands of $\nu_{as}(OCO) + \delta_{(CH)}$, while 2854 cm⁻¹ is the vibration of $\nu_{(CH)}$ [46-48]. Additionally, the absorption peak, centered at 2694-2697 cm⁻¹, is also a characteristic band for formate species, corresponding to the overtone of $\nu_s(OCO)$ [48]. In Fig. 3-14e, a pair of doublet peaks with similar intensities, centered at 2960 and 2858 cm⁻¹

¹, appears as well in the methanol adsorption at 373 K and can be assigned to $\nu_{\text{as}(\text{CH})}$ and $\nu_{\text{s}(\text{CH})}$ of methoxy species, respectively [46]. Note that the $\nu_{\text{s}(\text{CH})}$ of methoxy species (e.g., 2858 cm^{-1}) locates in proximity to $\nu_{(\text{CH})}$ of formate species (2854 cm^{-1}), however, these bands are discernible by referring to their own paired bands in the higher frequency: the doublet of methoxy species exhibits similar peak intensity, while clearly distinctive for the doublet of formate species. Such difference would be promising in the purge experiments which were designed to observe the changes of surface species after CO_2 hydrogenation.

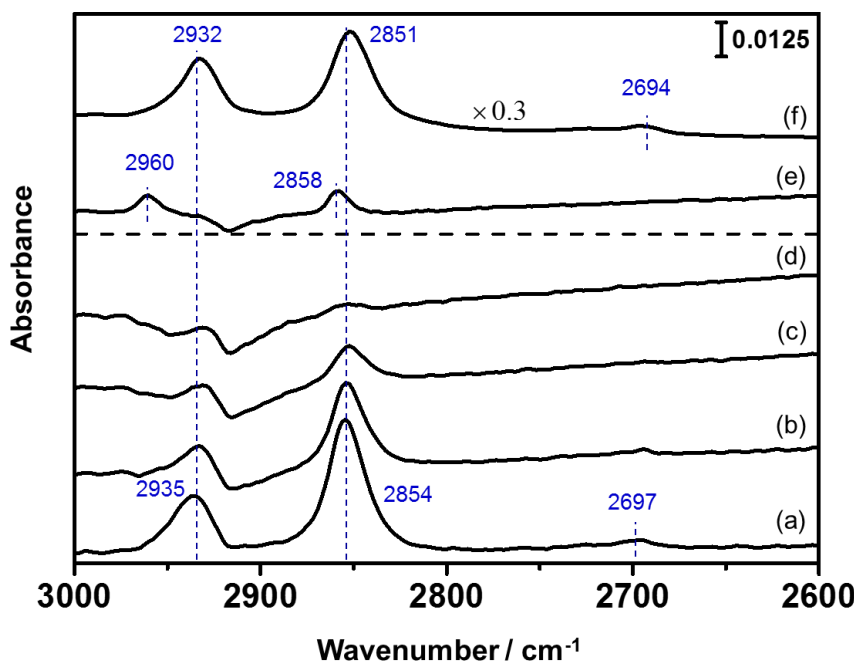


Figure 3-14 Diffuse reflectance FT-IR spectra of pre-reduced Pd(8.7)-Cu(10)/ SiO_2 in CO_2/H_2 at temperatures (a-d) and methanol/formic acid adsorption at 373 K (e-f). CO_2 hydrogenation conditions: $\text{CO}_2/\text{H}_2/\text{Ar}=24/72/4$ (vol%), 0.1 MPa, ca. 30 mL min^{-1} . Methanol/formic acid adsorption conditions: N_2 (30 mL min^{-1}), 0.1 MPa, 373 K, 4.0 μL injection. (a-d) were processed by BG-1, while (e-f) were based on BG-0. CO_2 hydrogenation at (a) 373 K, (b) 423 K, (c) 474 K, (d) 523 K, and adsorption at (e-f) 373 K.

1200-2200 cm^{-1} : Fig. 3-15 shows the frequency range of 1200-2200 cm^{-1} , which is the fingerprint area for carbonyl bands (i.e., chemisorbed CO species), carboxylate bands (i.e.,

symmetric and asymmetric O-C-O stretching vibrations of formate species), and carbonate species (i.e., O-C-O vibrations of CO_3^{2-} species).

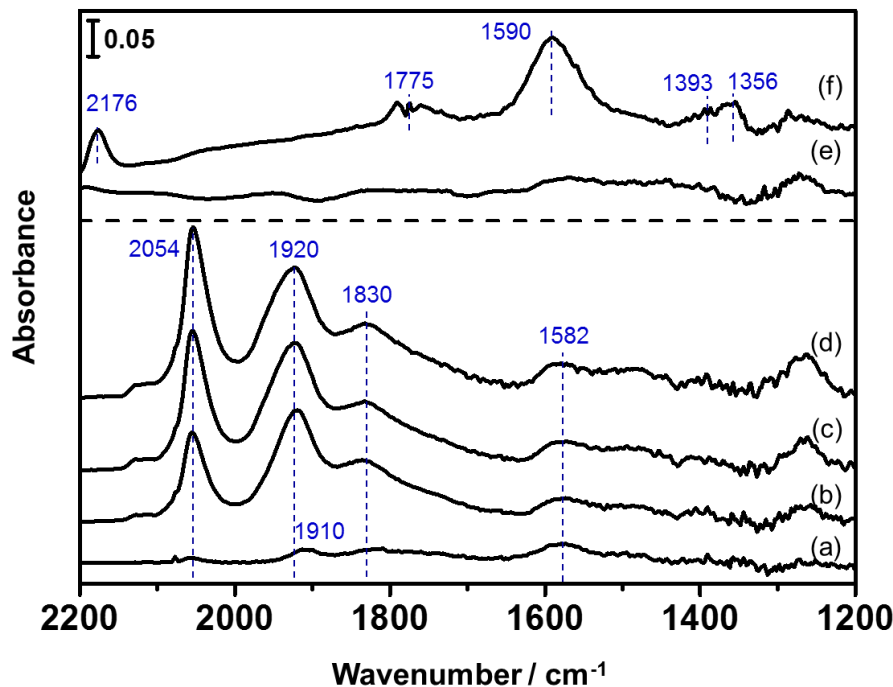


Figure 3-15 Diffuse reflectance FT-IR spectra of pre-reduced Pd(8.7)-Cu(10)/SiO₂ in CO₂/H₂ at temperatures (a-d) and methanol/formic acid adsorption at 373 K (e-f). CO₂ hydrogenation conditions: CO₂/H₂/Ar=24/72/4 (vol%), 0.1 MPa, ca. 30 mL min⁻¹. Methanol/formic acid adsorption conditions: N₂ (30 mL min⁻¹), 0.1 MPa, 373 K, 4.0 μL injection. (a-d) were processed by BG-1, while (e-f) were based on BG-0. CO₂ hydrogenation at (a) 373 K, (b) 423 K, (c) 474 K, (d) 523 K, and adsorption at (e-f) 373 K.

1800-2000 cm⁻¹ is the fingerprint region for carbonyl species, and three primary absorbance peaks are discernible, implying that three forms of chemisorbed CO species coexist over the surface during the CO₂ hydrogenation. Generally, two well-reported types of chemisorbed CO on either copper or palladium have been identified [46, 48-51]. The band above 2000 cm⁻¹ can be attributed to the terminal and monocoordinated/linearly bonded CO species, denoted as CO^L, while the multiple bands within 1800-2000 cm⁻¹ can be assigned to the multicoordinated-bridging CO species. The latter group could be precisely categorized into two subgroups: (i) the band slightly

lower than 2000 cm⁻¹ corresponds to the di-coordinated bridging CO species (denoted as CO^{B1}) adsorbed on structurally open crystal planes, e.g., (100); (ii) the band lies between CO^{B1} and 1900 cm⁻¹ relates to the other di-coordinated bridging CO species inside the lattice, e.g., (111) (denoted as CO^{B2}) [51]. Another band, around 1830 cm⁻¹, can be attributed to the triply-bridging CO species on “hollow” sites in the lattice (herein, denoted as CO^H) [51]. Accordingly, the assignments of the bands observed from Fig. 3-15 in a similar region become straightforward: 2054, 1923, and 1830 cm⁻¹ correspond to linear chemisorbed CO^L, bi-coordinated bridging CO^{B2}, and triply chemisorbed CO^H. Since the CO^{B2} is dominant in the di-coordinated bridging CO species on the surface, the CO^{B2} is mostly considered in the following discussion and simply denoted as CO^B henceforth, unless otherwise noted. Most recently, carboxyl species (COOH) was proposed as an intermediate for the CO formation via reverse water-gas shift [52]; however, we fail to see any relevant bands from FT-IR spectra. Probably, this species is not stable or the surface reaction undergoes fast, which inhibits us from observing [53].

The bands of formate species, such as $\nu_{(OCO)} + \delta_{(CH)}$ and $\nu_{(CH)}$, have been clarified in the region of 2600-3000 cm⁻¹, and the corresponding fingerprint region for O-C-O vibrations lies within 1300-1600 cm⁻¹. According to the FT-IR spectrum of formic acid adsorption (Fig. 3-15f), two absorption peaks are observed, centered at 1590 and 1356 cm⁻¹, corresponding to the asymmetric ($\nu_{(OCO)as}$) and symmetric ($\nu_{(OCO)s}$) vibrations of O-C-O bond, respectively [46-48, 54]. The shoulder band, centered at 1393 cm⁻¹, can be assigned to the deformation vibration of C-H bond of formate species (denoted as $\delta_{(CH)}$) [30, 47]. In contrast, the interferograms of CO₂ hydrogenation only exhibit a clear band of $\nu_{(OCO)as}$ (ca. 1582 cm⁻¹), and the band of $\nu_{(OCO)s}$ (ca. 1350 cm⁻¹) is weak. Such indiscernible $\nu_{(OCO)s}$ band probably results from a lower surface coverage of formate species than the formic acid adsorption as evidenced by the difference in the relative

intensities. Besides, the orientation of the adsorbed formate species is another possible explanation. As reported, the existence of $\nu_{\text{OCO}}^{\text{as}}$ implies that a proportion of the formate species is oriented at an angle to the normal direction of the metal surface [47], thus resulting in the activation of C-H deformation vibration (ca. 1390 cm^{-1}), its corresponding overtone (ca. 2697 cm^{-1}), and even the enhancement of the combinational band at ca. 2935 cm^{-1} . Nearly all of these characteristic bands can be evidenced from Fig. 3-14. Therefore, the formate species is adsorbed dominantly inclining towards the alloy surface with an angle, and such orientation explicates the weak band of $\nu_{\text{s(OCO)}}$. Additionally, $1300\text{-}1700 \text{ cm}^{-1}$ is also the fingerprint region for carbonate species, and the characteristic bands of carbonate species in CO_2 adsorption are asymmetric and symmetric vibrations of O-C-O bond at ca. 1640 and 1420 cm^{-1} , respectively [30, 47, 48, 55-57]. However, these bands are barely seen in Fig. 3-15 except for a very weak plateau at ca. 1470 cm^{-1} . Probably, the carbonate species is in a quite low surface coverage or readily converted to other more stable species immediately under the environment of hydrogen, such as formate species [56]. Therefore, the bands of carbonate species are not abundant. The bands below 1300 cm^{-1} are unresolved because this area can be interfered by the Si-O-Si stretching vibrations.

Overall, the dominant intermediates over Pd(8.7)-Cu(10)/ SiO_2 in CO_2 hydrogenation is formate species and CO species. It is worth mentioning that those are also widely proposed as important intermediates in CO_2 hydrogenation over Pd or Cu-based catalysts [52, 58-60]. For clarity, all relevant bands are summarized in Table 3-5, together with some bands that are not mentioned but emerged in FT-IR spectra.

Table 3-5 Infrared peak assignment of the surface species observed during the CO₂ hydrogenation at different temperatures and 0.1 MPa, and together with those of the methanol/formic acid adsorption at 373 K and 0.1 MPa over pre-reduced Pd(8.7)-Cu(10)/SiO₂

Frequency / cm ⁻¹	Species	Experiment	Ref.
3730, 3703	CO ₂ / $\nu_1+\nu_3$ (R & P branch)	CO ₂ HYD	[45]
3627, 3597	CO ₂ /2 $\nu_2+\nu_3$ (R & P branch)	CO ₂ HYD	[45]
2960	Methoxy/ $\nu_{as(CH)}$	CH ₃ OH ads.	[46]
2935	Formate/ $\nu_{as(OCO)}+\delta_{(CH)}$	CO ₂ HYD	[46-48]
2932	Formate/ $\nu_{as(OCO)}+\delta_{(CH)}$	HCOOH ads.	[46]
2858	Methoxy/ $\nu_{s(CH)}$	CH ₃ OH ads.	[46]
2854	Formate/ $\nu_{(CH)}$	CO ₂ HYD	[46-48]
2851	Formate/ $\nu_{(CH)}$	Formic acid ads.	[46]
2697	Formate/ $\nu_{as(OCO)}\times 2$	CO ₂ HYD	[48]
2694	Formate/ $\nu_{as(OCO)}\times 2$	Formic acid ads.	[46]
2176	CO(g)	HCOOH ads.	[46, 48]
2120	CO (Cu)	CO ads.	[48, 61]
2054	CO/CO ^L (linear, Pd ⁰)	CO ₂ HYD	[46, 48-51]
1995	CO/CO ^{B1} (di-coordinated bridging, Pd ⁰)	CO ads.	[46, 51]
1923-1940	CO/CO ^{B2} (di-coordinated bridging, Pd ⁰)	CO ₂ HYD	[46, 48-51]
1830	CO/CO ^H (triply bridging, Pd ⁰)	CO ₂ HYD	[46, 48-51]
1791, 1775, 1760	HCOOH(g)/ $\nu_{s(C=O)}$ (R, Q, and P branch)	HCOOH ads.	[46, 62]
1590	Formate/ $\nu_{as(OCO)}$	HCOOH ads.	[46-48, 54]
1582	Formate/ $\nu_{as(OCO)}$	CO ₂ HYD	[46-48, 54]
1393	Formate/ $\delta_{(CH)}$	HCOOH ads.	[46-48, 54]
1356	Formate/ $\nu_{s(OCO)}$	HCOOH ads.	[46-48, 54]

Noteworthy, in Fig. 3-14a-d, the intensities of the bands corresponding to the formate species decrease considerably as the temperature elevation. Besides, the formate species can decompose to CO₂, and H₂ at high temperatures (ca. 450-570 K) or is more likely to be hydrogenated to methoxy species or even methanol when exposed to hydrogen [54, 63-67]. On the other hand, Fig. 3-15a-d shows that CO^L, CO^{B2}, and CO^H become abundant as the temperature ascends gradually. Such variation can be assigned to the enhancement of reverse water-gas shift reaction (RWGS) which favors higher temperatures thermodynamically (endothermic reaction) [68, 69]. Clearly, both formate and chemisorbed CO species are very sensitive to the reaction conditions, which requires different temperature ranges for a clear observation. Accordingly, 373 K is proper for the formate species in the region of 2600-3000 cm⁻¹, while 523 K is suitable for chemisorbed CO species in the region of 1800-2000 cm⁻¹.

3.3.4.2 Effect of Pd and Cu combination on surface species

In order to clarify the effect of alloy on the formation of surface species, the diffuse reflectance FT-IR experiments were performed over mono and bimetallic catalysts at different temperatures (e.g., 373 and 523 K). The resultant spectra are compared in Figs. 3-16 and 3-17, and all interferograms were processed based on BG-1.

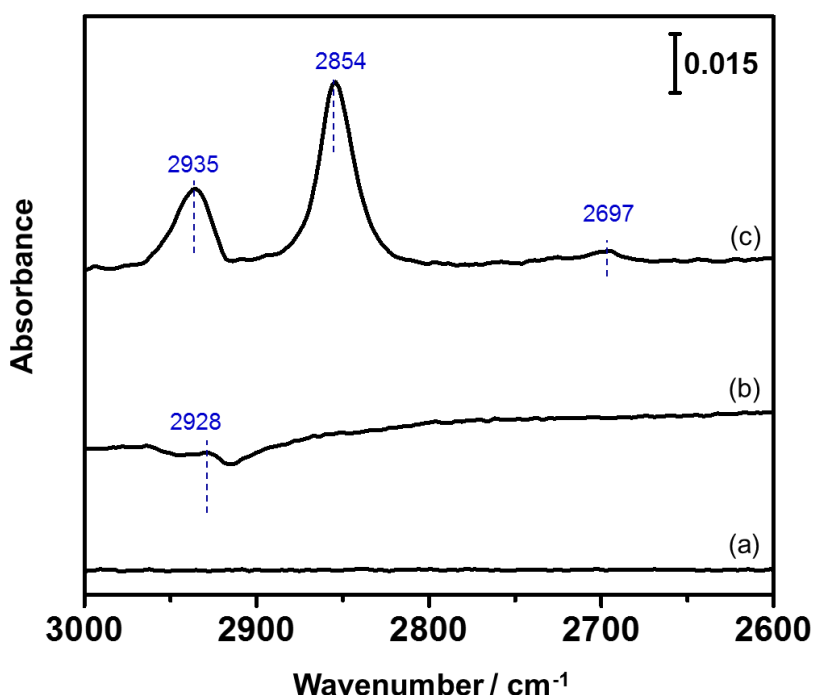


Figure 3-16 Diffuse reflectance FT-IR spectra of pre-reduced monometallic and bimetallic catalysts in CO₂/H₂ at 373 K. CO₂ hydrogenation conditions: CO₂/H₂/Ar=24/72/4 (vol%), 0.1 MPa, ca. 30 mL min⁻¹. All spectra were processed by BG-1. (a) Cu(10)/SiO₂; (b) Pd(8.7)/SiO₂; (c) Pd(8.7)-Cu(10)/SiO₂.

Fig. 3-16 depicts the region of 2600–3000 cm⁻¹ for formate species over pre-reduced monometallic and bimetallic catalysts at 373 K. As shown in Fig. 3-16a, the formate species is not formed on the surface of Cu/SiO₂, which can be ascribed to the low activity of Cu/SiO₂ at ambient pressure [48, 56, 70]. Differently, the formation of adsorbed formate species is observed over Pd/SiO₂ (Fig. 3-16b), although the intensities are weak [30, 55, 71, 72]. In contrast to monometallic catalysts, Pd(8.7)-Cu(10)/SiO₂ not only exhibits distinguishable bands of adsorbed formate species but with considerably stronger intensities. Considering the uniform and nano-sized alloy particles for this bimetallic catalyst, it is suggested that the alloy formation could greatly improve the formation of formate species over the surface in comparison to monometallic catalysts.

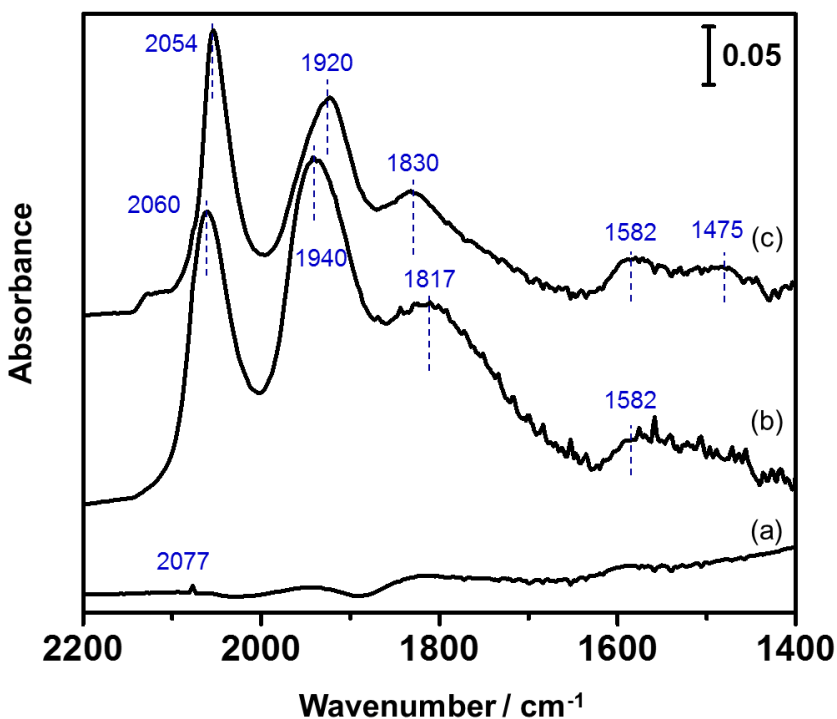


Figure 3-17 Diffuse reflectance FT-IR spectra of pre-reduced monometallic and bimetallic catalysts in CO_2/H_2 at 523 K. CO_2 hydrogenation conditions: $\text{CO}_2/\text{H}_2/\text{Ar}=24/72/4$ (vol%), 0.1 MPa, ca. 30 mL min⁻¹. All spectra were processed by BG-1. (a) $\text{Cu}(10)/\text{SiO}_2$; (b) $\text{Pd}(8.7)/\text{SiO}_2$; (c) $\text{Pd}(8.7)\text{-}\text{Cu}(10)/\text{SiO}_2$.

Fig. 3-17 illustrates the region of 1800–2000 cm⁻¹ over the same samples at 523 K in CO_2 hydrogenation. The infrared spectrum of Cu/SiO_2 (Fig. 3-17a) only exhibits weak bands in the fingerprint region of carbonyl species. On the contrary, the spectrum of Pd/SiO_2 (Fig. 3-17b) exhibits more intense bands of chemisorbed CO species, reflecting a better surface coverage of CO than Cu/SiO_2 under the same reaction conditions. Such difference may derive from the ability of electron donation because Pd binds CO much stronger than Cu via π -back donation [58, 73]. In addition, Pd/SiO_2 reveals a stronger intensity of CO^B than that of CO^L , implying that CO^B is more favorable on palladium alone [74]. The spectrum of $\text{Pd}(8.7)\text{-}\text{Cu}(10)/\text{SiO}_2$ (Fig. 3-17c) exhibits all types of adsorptive CO species which resemble those of Pd/SiO_2 , suggesting the primary role of Pd component in the alloy particles for CO stabilization as an intermediate during the CO_2

hydrogenation. The difference between the spectra of Pd alone and Pd-Cu is observed in two aspects: band shift and relative CO^L/CO^B ratio. Usually, a higher surface coverage of CO leads to a blue shift [74]; however, the bands in this work do not shift unidirectionally. This can be attributed to a combinational effect of both surface coverage and alloy formation [75]. The latter aspect is that bimetallic catalyst exhibits a higher CO^L/CO^B ratio than Pd/SiO₂. As reported, a relatively higher CO^L/CO^B ratio correlates to smaller Pd⁰ particles because smaller particles can expose a larger proportion of low-coordinated and/or surface atoms than larger particles, if all other factors remain equal [51, 74, 76]. Therefore, it is clear that the Pd⁰ dispersion in the alloy particles is improved in comparison to the Pd⁰ alone in the monometallic catalyst, and such characteristic Pd⁰ distribution could be evidenced from the STEM/EDS mappings as well [34].

3.3.4.3 Effect of Pd loading on surface species

Since the alloy and metallic phases in the bimetallic catalysts are dependent on Pd contents, it would be of great interest to investigate the effect of Pd loading on surface species during the CO₂ hydrogenation [34]. Thus, the FT-IR measurements were carried out over the Pd-Cu bimetallic catalysts with various Pd loadings (e.g., 2.5 to 15.7 wt%), and the resultant spectra are depicted in Figs. 3-18 and 3-20. The intensities of different species were also determined quantitatively by referring to the intensity of the band at 3730 cm⁻¹ (see Table 3-5), and the quantified data was illustrated in Figs. 3-19 and 3-21, corresponding to Figs. 3-18 and 3-20, respectively. All interferograms were processed by BG-1.

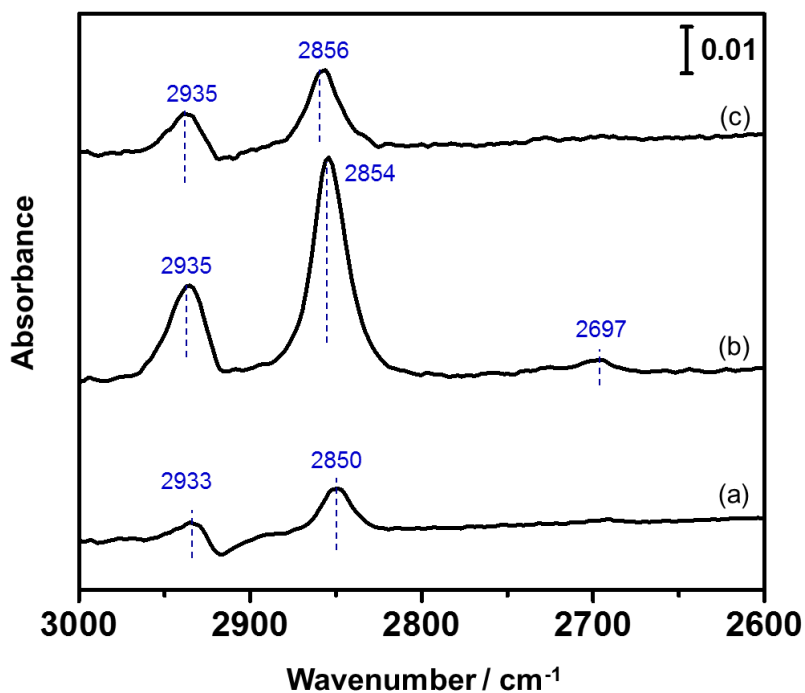


Figure 3-18 Diffuse reflectance FT-IR spectra of pre-reduced bimetallic catalysts in CO_2/H_2 at 373 K. CO_2 hydrogenation conditions: $\text{CO}_2/\text{H}_2/\text{Ar}=24/72/4$ in vol%, 0.1 MPa, ca. 30 mL min^{-1} . All spectra were processed by BG-1. (a) Pd(2.5)-Cu(10)/ SiO_2 ; (b) Pd(8.7)-Cu(10)/ SiO_2 ; (c) Pd(15.7)-Cu(10)/ SiO_2 .

Fig. 3-18 demonstrates the effect of Pd loading on the formed and adsorbed formate species (373 K), and relative peak intensities are illustrated in Fig. 3-19, along with the information of monometallic catalysts. As depicted in Fig. 3-18, all three bimetallic catalysts show characteristic bands of formate species within $2600\text{-}3000 \text{ cm}^{-1}$, while Pd(8.7)-Cu(10)/ SiO_2 (i.e., Pd atomic ratio=0.34) exhibits the most intense absorption peaks (Fig. 3-18b). Besides, Fig. 3-19 confirms that the relative intensities of adsorbed formate species maximize at Pd = 0.34 at., implying a better surface coverage of formate species over this catalyst. As discussed in Chapter 2, the same sample only reveals alloy diffractions in XRD pattern, while the rest (i.e., Pd=2.5 and 15.7 wt%) clearly contains unalloyed metallic diffractions [34]. Consequently, the enhanced surface coverage of formate species appears to correlate with the alloy phases, particularly when PdCu_3 and PdCu

coexist with uniform and nano-sized alloy particles.

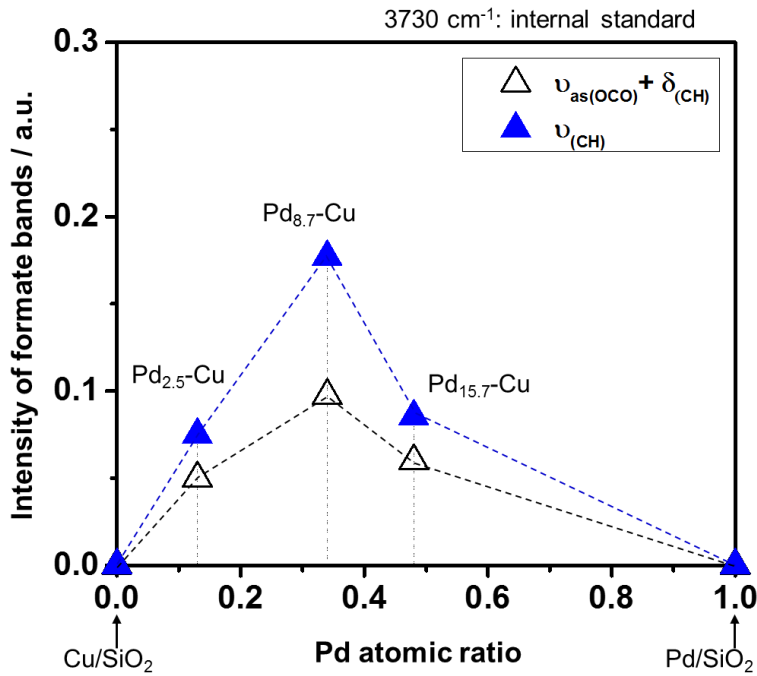


Figure 3-19 Changes of relative intensities for formate-relevant bands over pre-reduced monometallic and bimetallic catalysts in CO_2/H_2 at 373 K. The quantitative data was determined based on infrared spectra in Figs. 3-16 and 3-18, and the band at 3730 cm^{-1} was used as an internal standard in the evaluation.

Fig. 3-20 depicts the fingerprint region of carbonyl species (523 K), and the relative intensities of different forms of chemisorbed CO were also measured by referring to that of the same band at 3730 cm^{-1} , as depicted in Fig. 3-21. In Fig. 3-20, with the addition of Pd into Cu, the bands belonging to different CO species become more intense, particularly when the Pd loading exceeds 8.7 wt%. On the other hand, the relative intensities of CO^{B} and CO^{H} increase monotonically with the increment of Pd content, while the relative intensity of CO^{L} maximizes at $\text{Pd}=0.34$ at. (i.e., Pd=8.7 wt%), as shown in Fig. 3-21. Again, such maximized CO^{L} can be attributed to the uniform and nano-sized alloy particles with a large proportion of low-coordinated surface and corner/edge Pd^0 atoms [49]; while the monotonic increases of CO^{B} and CO^{H} are

anticipated because of the increment of Pd content which improves the chemisorbed CO species in the terrace of crystal structure [74].

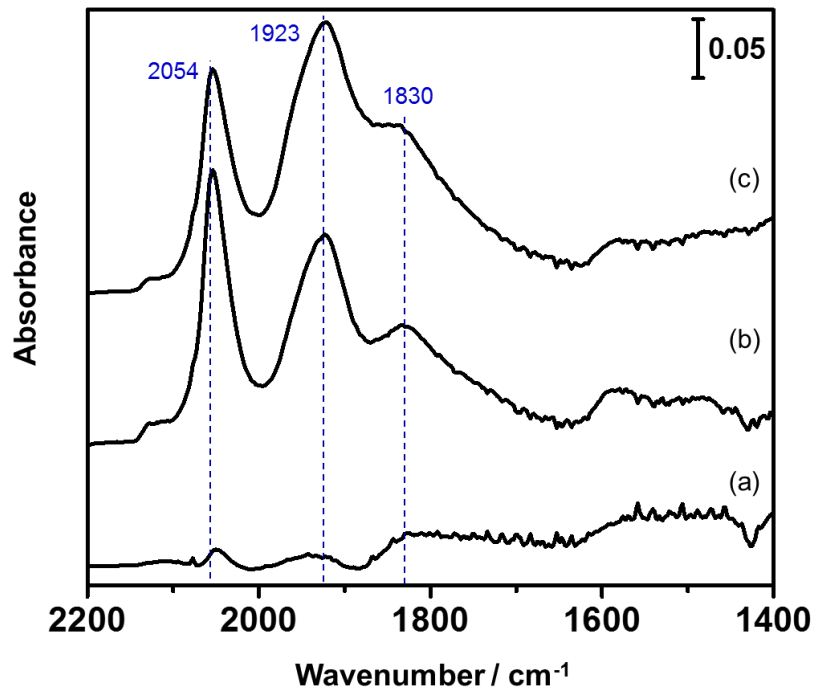


Figure 3-20 Diffuse reflectance FT-IR spectra of pre-reduced bimetallic catalysts in CO_2/H_2 at 523 K. CO_2 hydrogenation conditions: $\text{CO}_2/\text{H}_2/\text{Ar}=24/72/4$ in vol%, 0.1 MPa, ca. 30 mL min⁻¹. All spectra were processed by BG-1. (a) Pd(2.5)-Cu(10)/SiO₂; (b) Pd(8.7)-Cu(10)/SiO₂; (c) Pd(15.7)-Cu(10)/SiO₂.

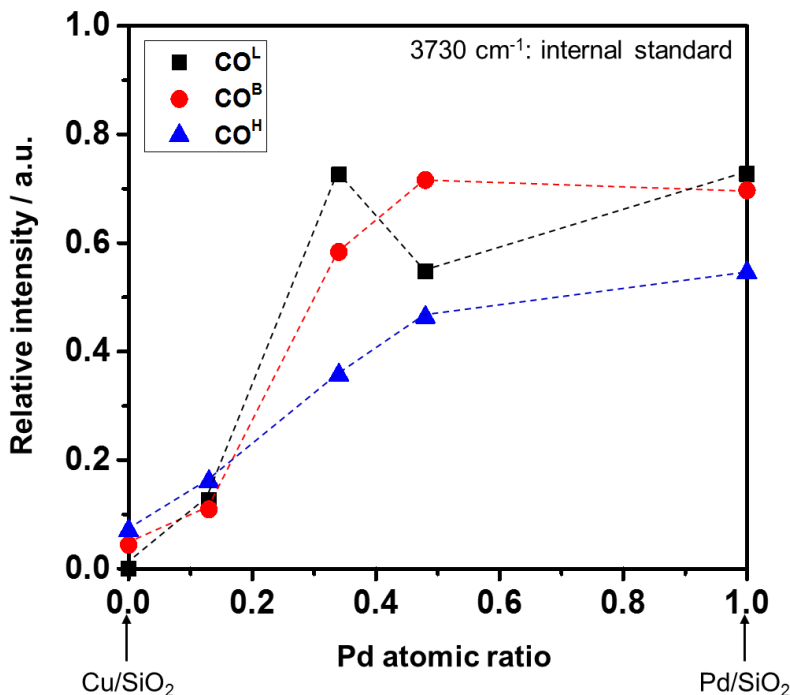


Figure 3-21 Changes of relative intensities for carious carbonyl bands over pre-reduced bimetallic catalysts in CO_2/H_2 at 523 K. The quantitative data was determined based on infrared spectra in Figs. 3-17 and 3-20, and the band at 3730 cm^{-1} was used as an internal standard in the evaluation.

3.3.4.4 CO_2 adsorption and formate formation

As discussed in the last two sections, the alloy formation and Pd content in alloy particles have significant impacts on the surface coverage of formate species. In this context, what is the adsorption site for the formate species, alloy surface and/or support? Bando *et al.* [56] investigated the CO_2 adsorption (pure CO_2) on bare support (SiO_2) and Cu/SiO_2 by FT-IR. It was found that CO_2 was able to be adsorbed as the carbonate species over the support (SiO_2); while in the flow of CO_2/H_2 , the adsorbed CO_2 (i.e., carbonate species) can be quickly hydrogenated to formate species over the metallic Cu^0 . Similar results could be seen for the Pd-based catalysts in the conditions of CO_2 alone [57] and CO_2/H_2 [25, 30, 55]. In this context, if CO_2 were largely adsorbed on the support as the carbonate species, then the corresponding bands (e.g., 1627 cm^{-1}) [56] and the

consumption of hydroxyl groups (e.g., 3747 cm^{-1}) [77] should be observed in FT-IR spectra. Apparently, these are not noticeable from respective region, as depicted in Fig. 3-20 and 3-22. Probably, the carbonate species is readily converted after the adsorption which happens too promptly to be observed from the FT-IR spectra with the present resolution. The CO_2 -TPD results demonstrate that the CO_2 uptake capacity correlates with the alloy formation. As a result, it is deduced that the Pd-Cu alloy particles play a crucial role in the adsorption of CO_2 , and the adsorption sites should be in proximity to the interface with the support. In the following step, the adsorbed CO_2 is converted to other species, such as formate species.

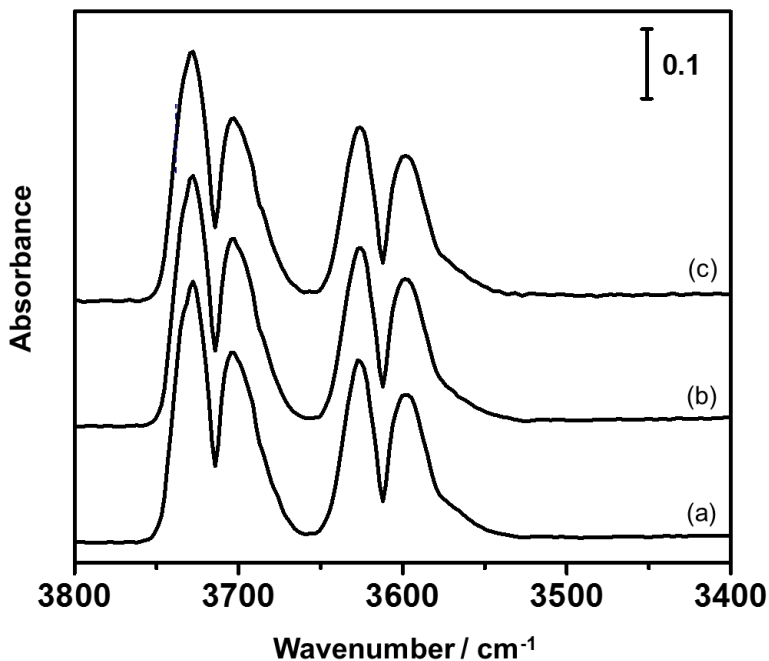


Figure 3-22 Diffuse reflectance FT-IR spectra of pre-reduced bimetallic catalysts in CO_2/H_2 at 373 K. CO_2 hydrogenation conditions: $\text{CO}_2/\text{H}_2/\text{Ar}=24/72/4$ in vol%, 0.1 MPa, ca. 30 mL min^{-1} . All spectra were processed by BG-1. (a) Pd(2.5)-Cu(10)/ SiO_2 ; (b) Pd(8.7)-Cu(10)/ SiO_2 ; (c) Pd(15.7)-Cu(10)/ SiO_2 .

3.3.4.5 H₂/N₂ purge after CO₂ hydrogenation

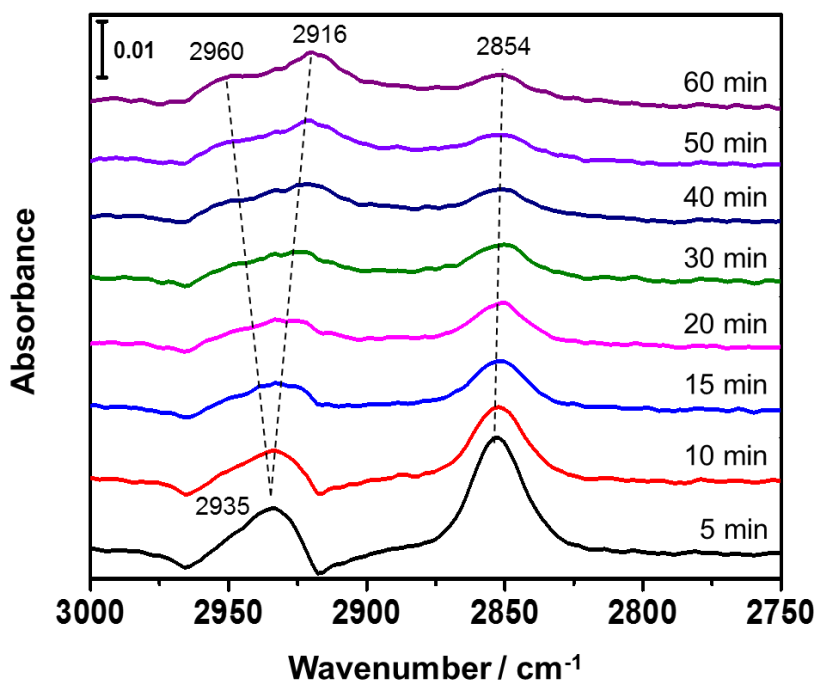


Figure 3-23 Changes of diffuse reflectance FT-IR spectra on pre-reduced Pd(8.7)-Cu(10)/SiO₂ as a function of exposing time of hydrogen purge (30 mL min⁻¹) after CO₂ hydrogenation (1 h) at 373 K. CO₂ hydrogenation conditions: CO₂/H₂/Ar=24/72/4 in vol%, 0.1 MPa, ca. 30 mL min⁻¹. All spectra were processed depending on BG-1.

A number of studies investigated the surface species formed in CO₂ hydrogenation by FT-IR technique. The formate and CO species are proposed as critical intermediates for methanol synthesis, which can undergo the hydrogenation to methoxy species and further to methanol, however, it is still in debate [48, 52, 58, 60, 66]. Since formate and carbonyl species are both observed on the bimetallic surface, it would be of great interest to verify their correlation with the methoxy species. Thus, the hydrogen purge experiments were carried out by switching from CO₂/H₂ to H₂ after 1 h CO₂ hydrogenation. Besides, the nitrogen purge experiment was employed as reference.

Fig. 3-23 depicts the changes of interferograms with the exposing time of hydrogen flow

over Pd(8.7)-Cu(10)/SiO₂ at 373 K after 1 h CO₂ hydrogenation. Clearly, the characteristic doublet of formate species reduces, and two new bands, centered at 2960 and 2916 cm⁻¹, gradually grow and eventually become distinct at ca. 60 min. In the meantime, the band, centered at 2854 cm⁻¹, decreases initially and maintains relatively stable after 30 min; it also exhibits a similar intensity as the band at 2960 cm⁻¹. These observations are particularly distinct when the spectra were reprocessed by BG-2, as shown in Fig. 3-24.

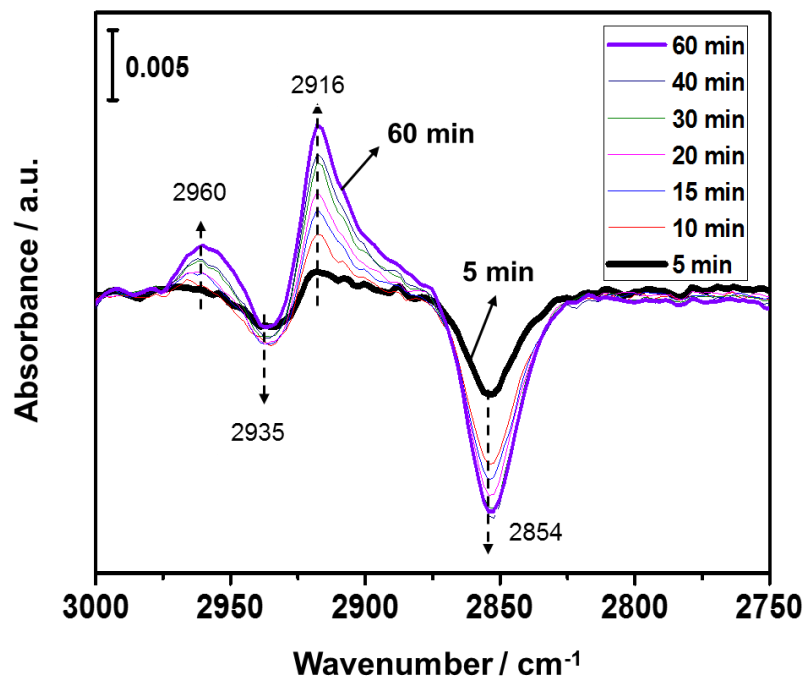


Figure 3-24 Changes of diffuse reflectance FT-IR spectra over pre-reduced Pd(8.7)-Cu(10)/SiO₂ as a function of exposing time of hydrogen purge (30 mL min⁻¹) after CO₂ hydrogenation (1 h) at 373 K. CO₂ hydrogenation conditions: CO₂/H₂/Ar=24/72/4 in vol%, 0.1 MPa, ca. 30 mL min⁻¹. The spectra were reprocessed by BG-2.

Fig. 3-25 illustrates the changes of various carbonyl species with the exposing time of hydrogen flow at 523 K after 1 h CO₂ hydrogenation. Generally, the intensities for all three forms of chemisorbed CO species gradually reduce in the flow of hydrogen. The band of CO^L decreases more promptly, while the decline of CO^B and CO^H is relatively moderate. Such difference in

desorption rate can be attributed to the bonding strength which decreases in the following order: $\text{CO}^{\text{H}} > \text{CO}^{\text{B}} > \text{CO}^{\text{L}}$ [78]. Besides, a slowly red shift is seen, which could correspond to the weakening intermolecular interactions (dipole-dipole coupling) resulting from the decline of CO surface coverage [74].

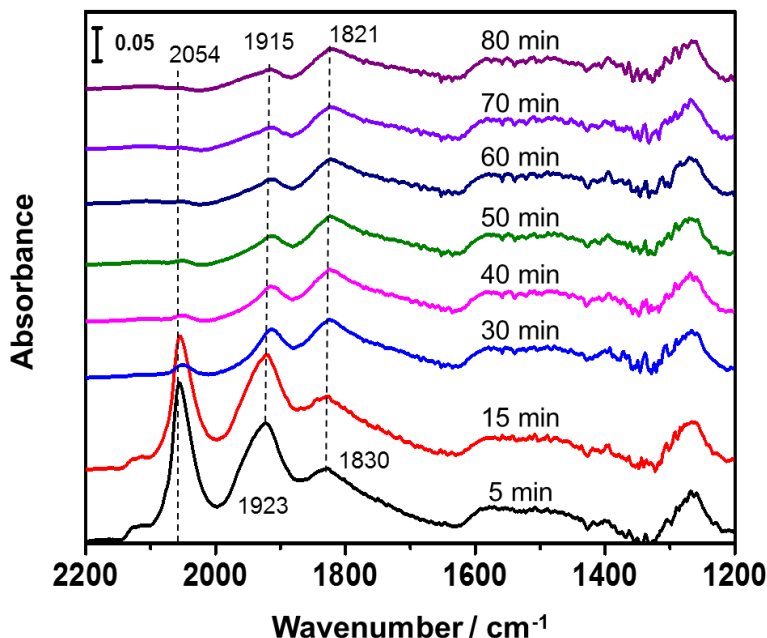


Figure 3-25 Changes of diffuse reflectance FT-IR spectra over pre-reduced $\text{Pd}(8.7)\text{-Cu}(10)/\text{SiO}_2$ as a function of exposing time of hydrogen purge (30 mL min^{-1}) after CO_2 hydrogenation (1 h) at 523 K. CO_2 hydrogenation conditions: $\text{CO}_2/\text{H}_2/\text{Ar}=24/72/4$ in vol%, 0.1 MPa, ca. 30 mL min^{-1} . All spectra were processed depending on BG-1.

From the FT-IR spectra of hydrogen purge experiment, except for the declines of known species (i.e., formate and CO species), some new bands emerge concurrently and grow intensely with the exposing time, especially in the region of $2600\text{-}3000 \text{ cm}^{-1}$ (e.g., 2960, 2916, and 2854 cm^{-1}). In order to verify their correlation with the existing surface species, the nitrogen purge experiment was carried out over the same catalyst at 373 K after 1 h CO_2 hydrogenation as well, and the resultant spectra are displayed in Fig. 3-26 by using BG-2 as background. Evidently, the

formate-related bands disappear rapidly, so does CO species (not shown here). However, no other bands emerge at all. Therefore, it is clear that these new bands develop from the existing surface species, and the identification of these hydrogen-purge-induced frequencies would be crucial to unveil their correlations with the formate and CO species in the methanol synthesis.

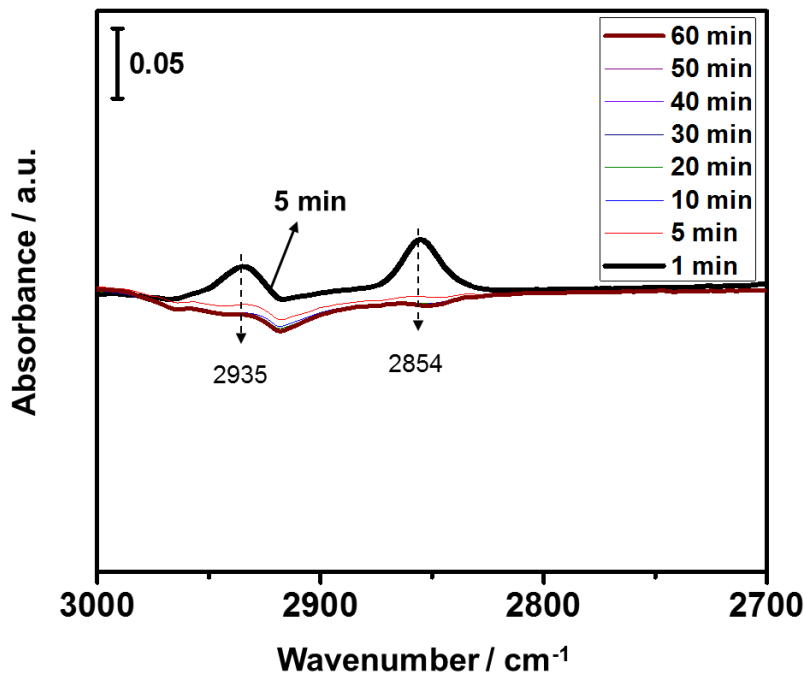


Figure 3-26 Changes of diffuse reflectance FT-IR spectra over pre-reduced Pd(8.7)-Cu(10)/SiO₂ as a function of exposing time of nitrogen purge (30 mL min⁻¹) after CO₂ hydrogenation (1 h) at 373 K. CO₂ hydrogenation conditions: CO₂/H₂/Ar=24/72/4 in vol%, 0.1 MPa, ca. 30 mL min⁻¹. All spectra were processed depending on BG-2.

Considering the frequency assignment in Table 3-5 and the CH₃OH adsorption over Pd(8.7)-Cu(10)/SiO₂ at 373 K (Fig. 3-14e), the new bands at 2960 and 2854 cm⁻¹ (Fig. 3-23) can be assigned to the asymmetric and symmetric vibrations of C-H bond of methoxy species, respectively, because both frequencies and relative intensities are in accordance with the methoxy bands. The hydrogen purge can also cause the emergence of an additional band at ca. 2916 cm⁻¹. Cabilla *et al.* [46, 49] found that the chemisorbed CO can readily react with the hydrogen flow

forming some water and methane in the process over Pd/SiO₂, leading to the C-H vibration of CH₄ at ca. 2920 cm⁻¹ and O-H vibration of H₂O at ca. 3300-3400 cm⁻¹. Moreover, this reaction is particularly favorable under the conditions with high H₂/CO ratio and low pressure. Clearly, the hydrogen purge in this work coincides with those conditions. Furthermore, the water formation can be confirmed as evidenced by the observation a plateau-like band in the fingerprint region of O-H bond, as shown in Fig. 3-27. Consequently, the band at ca. 2916 cm⁻¹ can be assigned to the C-H vibration of CH₄ which is produced from the chemisorbed CO species under a H₂-rich environment and ambient pressure. Thus, we confirm that those newly formed species develops from the existing intermediates (e.g., formate and CO species), and the formation of methoxy species is observed. However, it is difficult to correlate the origination of methoxy species with either formate species alone or CO species alone or them both at present. Although a number of studies reported the intermediate formate and CO-induced methoxy species formation via CO₂/CO hydrogenation as evidenced by FT-IR spectra at different conditions [30, 48, 55, 56, 59, 63, 64, 67, 79-85], little attention has been paid to the surface species over the Pd-Cu bimetallic catalyst. Thus, this is the area where more in-depth study is needed in future, such as the isotope labeling study.

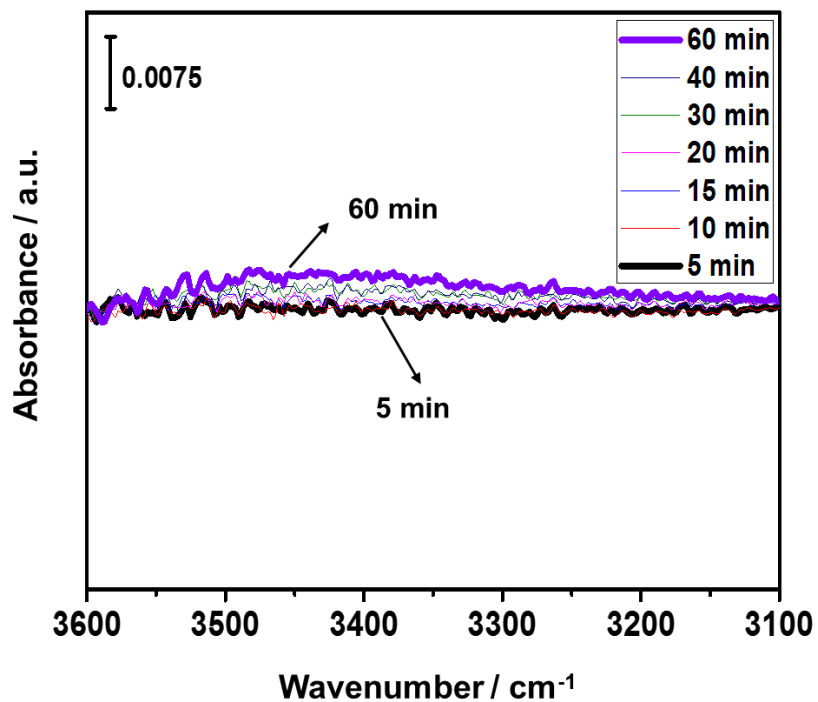


Figure 3-27 Changes of diffuse reflectance FT-IR spectra over pre-reduced Pd(8.7)-Cu(10)/SiO₂ as a function of exposing time of hydrogen purge (30 mL min⁻¹) after CO₂ hydrogenation (1 h) at 373 K. CO₂ hydrogenation conditions: CO₂/H₂/Ar=24/72/4 in vol%, 0.1 MPa, ca. 30 mL min⁻¹. Spectra range: 3100-3600 cm⁻¹. The spectra were reprocessed based on BG-2.

3.3.4.6 Reactivity of CO

In order to identify the reactivity of chemisorbed CO species produced via RWGS, the hydrogen purge measurement was also performed after 1 h CO adsorption at 523 K over the same bimetallic catalyst. The resultant FT-IR spectra are illustrated in Figs. 3-28 and 3-29 which were processed based on BG-1 and BG-3, respectively.

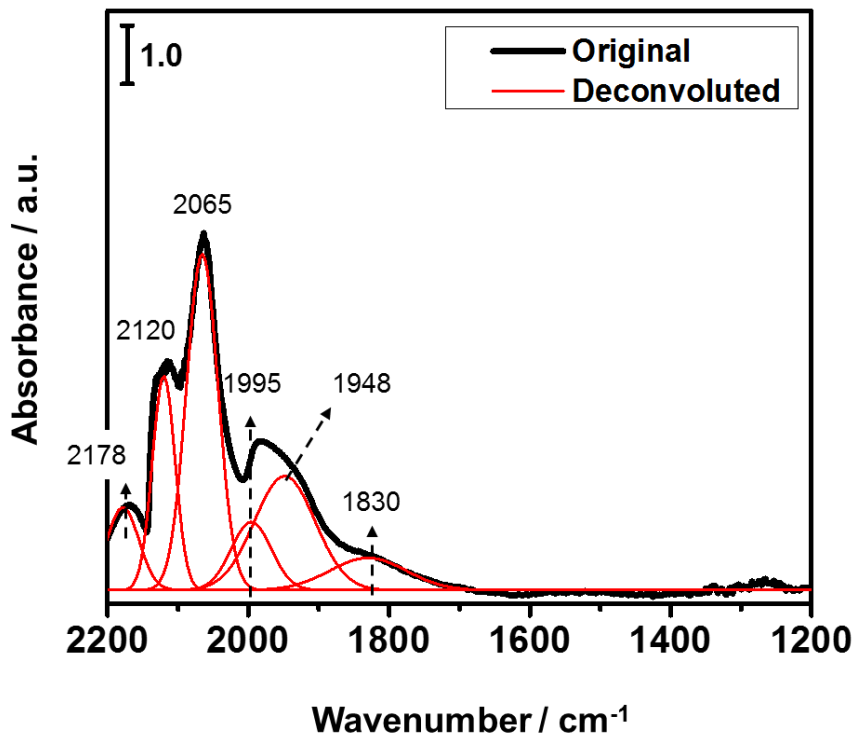


Figure 3-28 Diffuse reflectance FT-IR spectra of pre-reduced Pd(8.7)-Cu(10)/SiO₂ in CO adsorption (1 h) at 523 K. CO adsorption: CO/Ar=10/90 in vol%, 0.1 MPa, ca. 30 mL min⁻¹. The spectrum was processed by BG-1.

As shown in Fig. 3-28, multiple absorption peaks are observed from the spectrum of CO adsorption at 523 K. Evidently, 2065, 1948, and 1830 cm⁻¹ can be easily assigned to CO^L, CO^B, and CO^H, respectively, wherein the CO^B represents CO^{B2} as abbreviated above. The band, centered at 1995 cm⁻¹, lies between CO^L and CO^{B2} and corresponds to CO^{B1} [46, 51]. These are characteristic bands for the adsorbed CO species on metallic Pd⁰ sites. Additionally, two new bands are observed at 2120 and 2178 cm⁻¹, wherein the former one can be ascribed to the adsorbed CO species on Cu surface [56, 61], and the latter band corresponds to CO (g) [46, 48]. Noteworthy, it barely shows any absorption peaks within the region of 1300-1600 cm⁻¹, thereby excluding the interferences from carbonate or formate species. Fig. 3-29 displays the FT-IR spectra of hydrogen purge after CO adsorption by using BG-3 as reference. Noticeably, three bands, centered at 2963,

2857, and 2920 cm^{-1} , are observed. Similarly, the former two frequencies correspond to methoxy species, while the latter is related to methane. Clearly, the adsorbed CO species can be converted to methoxy species under the flow of hydrogen. This observation also implies that the surface intermediate CO in CO_2 hydrogenation possesses the potential to be further converted to methoxy species via CO hydrogenation over Pd(8.7)-Cu(10)/ SiO_2 .

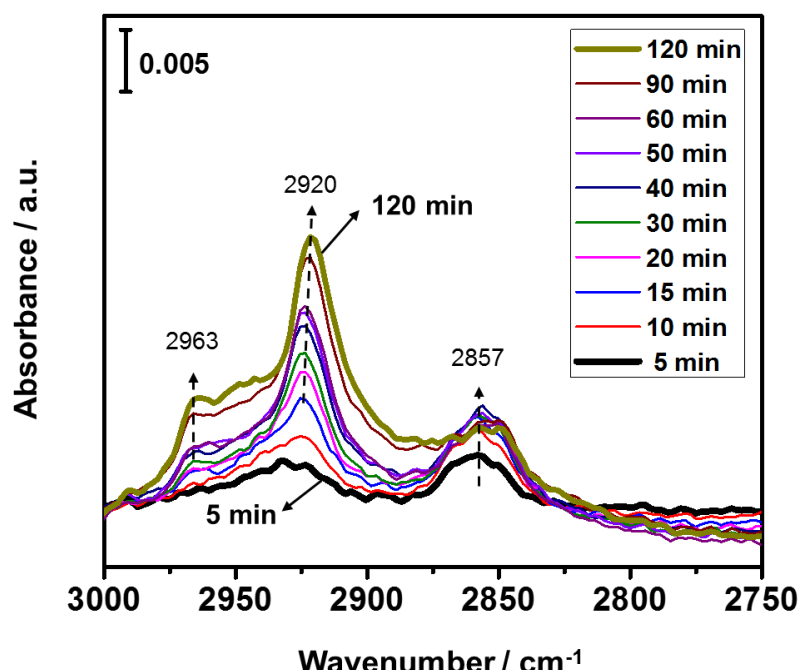


Figure 3-29 Changes of diffuse reflectance FT-IR spectra of pre-reduced Pd(8.7)-Cu(10)/ SiO_2 as a function of exposing time of hydrogen purge (30 mL min^{-1}) after CO adsorption (1 h) at 523 K. CO adsorption: $\text{CO}/\text{Ar}=10/90$ in vol%, 0.1 MPa, ca. 30 mL min^{-1} . The spectra were reprocessed by BG-3.

As an instant summary, the formate and CO species are dominant on the surface of bimetallic catalysts in CO_2 hydrogenation. In comparison to monometallic catalysts, Pd-Cu bimetallic catalysts can evidently improve the surface coverages of both formate and CO species, which particularly occurs on Pd(8.7)-Cu(10)/ SiO_2 with uniform and nano-sized alloy particles. On the other hand, the methoxy formation is evident by the H_2 purge experiment and probably

develops from the existing intermediates, namely formate and CO species.

3.3.5 CO adsorption properties of Pd-Cu catalysts

As mentioned in the last section, three forms of chemisorbed CO intermediates are observed from FT-IR spectra over pre-reduced Pd(8.7)-Cu(10)/SiO₂ in CO₂ hydrogenation, and they can potentially contribute to the methanol formation. In order to clarify the CO adsorption properties, the mono and bimetallic catalysts were measured by carbon monoxide temperature-programmed desorption (CO-TPD), and the resulting profiles are illustrated in Fig. 3-30. Note that the temperature of CO adsorption was set at 523 K which was similar to our actual reaction temperature.

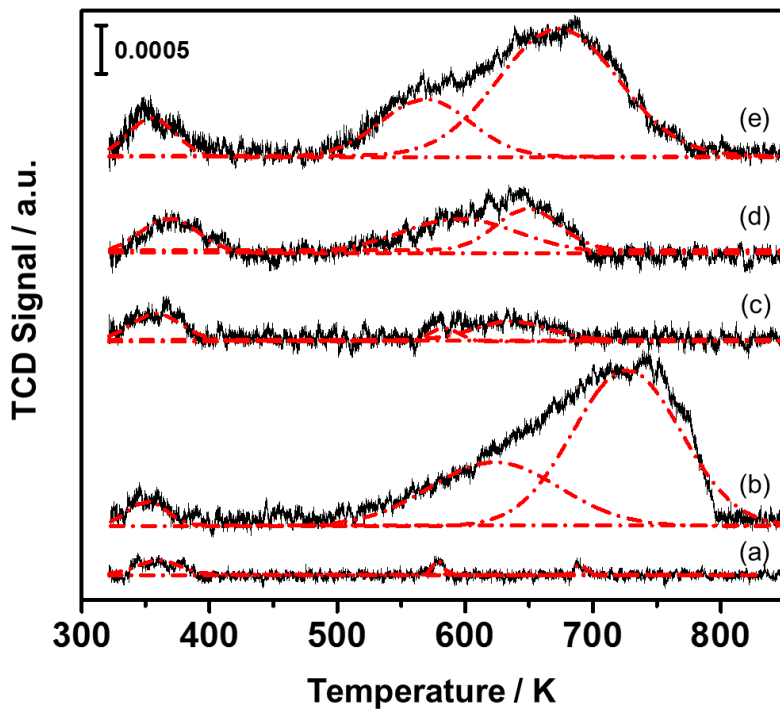


Figure 3-30 CO-TPD profiles of pre-reduced monometallic and bimetallic Pd-Cu catalysts. (a) Cu(10)/SiO₂; (b) Pd(8.7)/SiO₂; (c) Pd(2.5)-Cu(10)/SiO₂; (d) Pd(8.7)-Cu(10)/SiO₂; (e) Pd(15.7)-Cu(10)/SiO₂. CO adsorption was carried out at 523 K by using 5 vol% CO/He. TPD conditions: 5

K min⁻¹, Ar flow rate 30 mL min⁻¹. Solid lines: original desorption profiles; dash lines: fitting curves after deconvolution.

As depicted in Fig. 3-30a, the profile of Cu/SiO₂ exhibits a clear desorption peak within 350-400 K, while Pd/SiO₂ shows multiple desorption peaks (Fig. 3-30b). After deconvolution, the regions are mainly located at 350-400, 500-700, and 60-800 K. Considering the FT-IR results and the bonding strength order, these three ranges, from low to high temperature, can be assigned to CO^L, CO^B, and CO^H, respectively [86, 87]. Clearly, the surface of Pd alone is dominated by the bridging-adsorbed CO^B and CO^H species, particularly CO^H, while the Cu⁰ alone only shows a weak adsorption towards linear CO^L. Similarly, TPD profiles of bimetallic catalysts with different Pd loadings also exhibit three types of desorbed CO, and the desorption peaks for CO^B and CO^H shift towards lower temperatures in comparison to those of Pd/SiO₂, as shown in Fig. 30c-e. In the profile of Pd(8.7)-Cu(10)/SiO₂ (Fig. 3-30d), the CO^H is no longer a dominant component as evidenced by its decline in intensity compared to Pd/SiO₂. Considering the alloy features of this sample, it is suggested that the alloy formation (PdCu₃ and PdCu) greatly improves the Pd⁰ dispersion in alloy particles via the ensemble breaking, depending upon which more low-index planes and corner/edge Pd⁰ atoms would be exposed, thus restricting the adsorption towards CO^H in the lattice [49, 76]. This observation agrees with FT-IR results for the same sample (Fig. 3-20b). It is also worth stating that the CO^L has a weaker bonding strength with the metal and desorbs easily at lower temperatures in comparison to the other two species. As a result, in real reaction conditions, CO^L may readily desorb from the surface and primarily contribute to the CO formation rate as detected from the effluent gases. On the other hand, CO^B and CO^H may be relatively stable on the surface under the reaction conditions and have the potential to be converted in a further step.

Table 3-6 CO uptakes in CO-TPD of Pd(X)-Cu(10)/SiO₂ and monometallic catalysts ^{a)}

Catalyst	Tot. amt. of desorbed CO / $\mu\text{mol g}^{-1}$	Amt. of different types of desorbed CO / $\mu\text{mol g}^{-1}$		
		CO ^L	CO ^B	CO ^H
Cu ₁₀	28.5	21.1	4.4	3.0
Pd _{8.7}	663.9	24.2	215.2	424.5
Pd _{2.5} -Cu ₁₀	96.3	49.0	11.1	36.2
Pd _{8.7} -Cu ₁₀	230.3	64.2	98.9	67.2
Pd _{15.7} -Cu ₁₀	589.6	59.7	116.9	412.9

^{a)} TPD conditions: Ar (30 mL min⁻¹) with 5 K min⁻¹ as heating rate.

The desorbed amount of each form of CO species over mono and bimetallic catalysts were also quantified based on the deconvoluted Gaussian peaks, and the resultant CO uptake is tabulated in Table 3-6. For Cu/SiO₂, only a small amount of CO^L is obtained. Possibly, the CO adsorption over Cu alone is so weak that it desorbs easily under the Ar flush after the CO adsorption. For the other monometallic Pd/SiO₂, it exhibits the maximum total CO uptake, wherein CO^H accounts for almost 65 %. Thus, the CO adsorption contribution observed in the CO-TPD primarily correlates with Pd component in the bimetallic catalysts. The total CO uptake over the bimetallic samples increase as the increment of Pd content. As discussed, since the CO^L desorbs easily on the surface, CO^B and CO^H become the potential intermediates for methanol synthesis. Thus, the proportion of CO^B in the total of CO^B+CO^H calculated and plotted out in Fig. 3-31. The maximum proportion of CO^B is observed for Pd(8.7)-Cu(10)/SiO₂. Again, such advance could be attributed to the alloy formation with uniform and nano-sized alloy particles which selectively adsorbs CO^B. Noticeably, the temperature range of CO^B desorption lies in proximity to real reaction temperature (i.e., 523 K), demonstrating its great potential in methanol synthesis.

Thus, the uptake for each form of CO species varies with the Pd content in bimetallic

catalysts. More importantly, the formed alloy phases in Pd(8.7)-Cu(10)/SiO₂ lead to a substantial proportion towards CO^B adsorption which may bring an insight into the role of Pd-Cu alloy in the methanol formation via the intermediate CO on the surface.

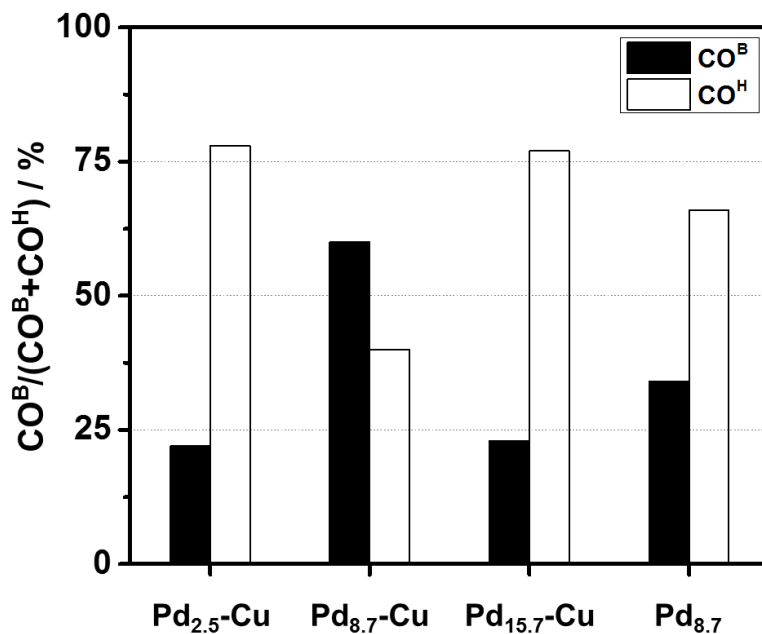
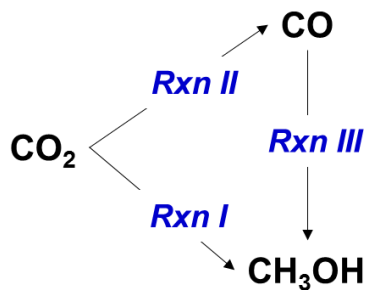


Figure 3-31 Percentage of different carbonyl species desorbed from mono and bimetallic Pd-Cu catalysts. Quantitative data was determined based on CO-TPD profiles.

3.3.6 Reaction pathway

As observed in Fig. 2-2B (Chapter 2), the maximum CH₃OH and CO formation rates appear at different Pd atomic ratios, suggesting another carbon source other than CO₂ [34]. As briefly depicted in Scheme 3-1, three reactions are possibly involved in the CO₂ hydrogenation to methanol, and the byproduct CO, from RWGS, is a potential carbon source for methanol synthesis over the alloy surface as evidenced from FT-IR and CO-TPD results. In order to clarify the existence of such reaction pathway, CO₂ hydrogenation was conducted over Pd(8.7)-Cu(10)/SiO₂ with the contact time (W/F) varying from 1.2 to 29.9 g-cat h mol⁻¹. The resulting product selectivity

was replotted as a function of CO₂ conversion, as illustrated in Fig. 3-32A. Generally, horizontal tendencies of selectivity signify a constant product distribution, thus indicating a primary involvement of Rxn I and II in Scheme 3-1; while unparallel selectivity trends indicate the involvement of Rxn III in the scheme, apart from Rxn I and II [88].



Scheme 3-1 Reactions in the methanol synthesis.

In Fig. 3-32A, the CH₃OH selectivity is approximately 20 mol% when CO₂ conversion is as low as 1.5 %. The CH₃OH selectivity increases monotonically with the increment of CO₂ conversion and reaches ca. 40 mol% at CO₂ conversion of ca. 13 %. Notably, the initial selectivity of CH₃OH is estimated to be ca. 19 mol% by extrapolating the trend line to the selectivity axis. Such significant selectivity towards methanol at zero conversion implies that CO₂ is a primary carbon source for methanol synthesis at relatively lower CO₂ conversion. On the other hand, CO selectivity declines as the increase of CO₂ conversion, indicating that the byproduct CO could also contribute to the methanol formation at relatively higher conversion, apart from CO₂. Thus, the observed different locations of the maximum CH₃OH and CO formation rates (Fig. 2-2B, Chapter 2) results from the existence of two carbon sources via different reaction pathways [34]. Yang *et al.* [58] applied density functional theory (DFT) and kinetic Monte Carlo (KMC) simulations into the examination of the CH₃OH synthesis via CO₂/H₂ over Pd-doped Cu₍₁₁₁₎ alloy surface. They

suggested that two reaction pathways are involved over Pd-Cu alloy surfaces, namely the formate species (intermediate) hydrogenation pathway and RWGS + CO hydrogenation pathway. Our experimental observations are in general agreement with theoretical simulations.

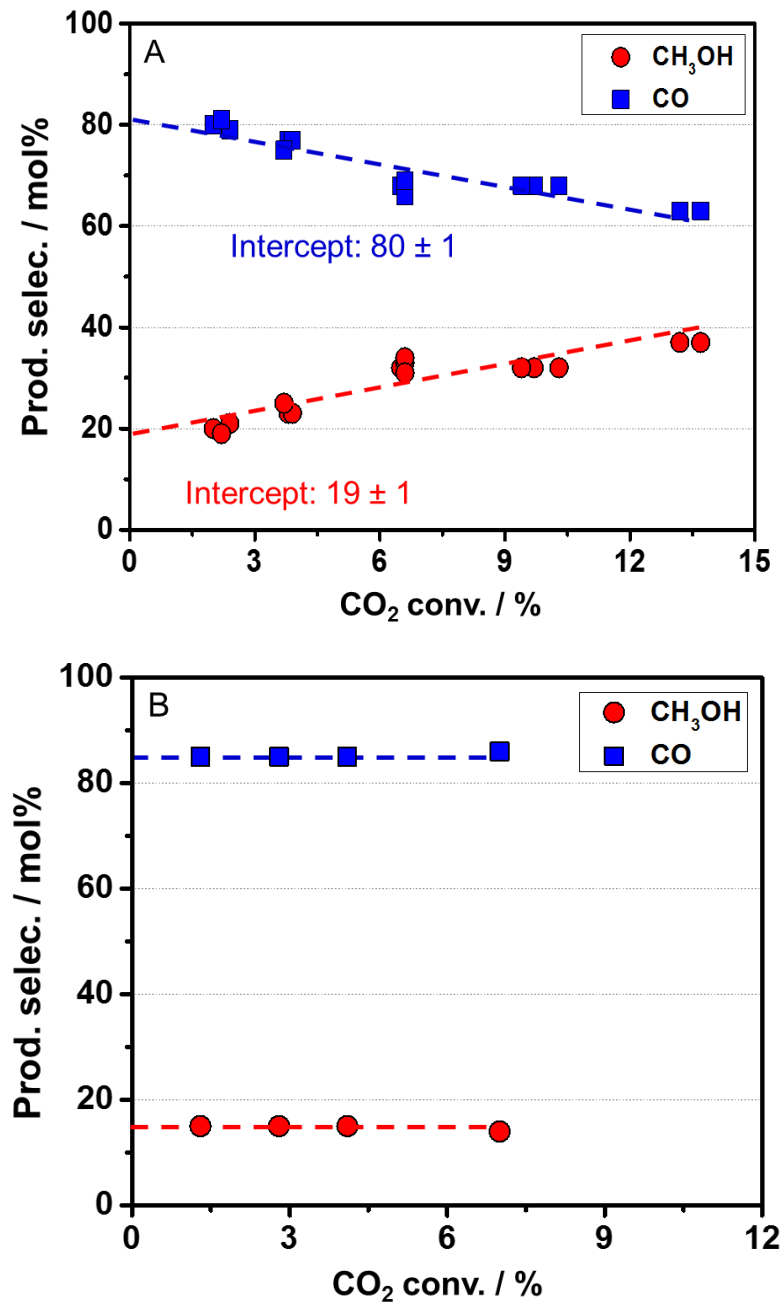


Figure 3-32 Changes in products selectivity as a function of CO₂ conversion over Pd(8.7)-Cu(10)/SiO₂ (A) and Cu(10)/SiO₂ (B). CO₂ hydrogenation conditions: 523 K, 4.1 MPa, W/F=1.2-29.9 g-cat h mol⁻¹ for (A) and 6.2-59.1 g-cat h mol⁻¹ (B).

In addition, the selectivity-conversion plot was also obtained over Cu/SiO₂ for comparison. Due to the lower activity of Cu/SiO₂, W/Fs were varied in a much larger range in order to obtain a comparable CO₂ conversion, e.g., 6.2-59.1 g-cat h mol⁻¹. The resultant plot is displayed in Fig. 3-29B. Evidently, the production selectivity is horizontal and is independent of CO₂ conversion within the range studied, indicating the involvement of only Rxn I and II in Scheme 3-1. Therefore, compared to the monometallic Cu catalyst, the alloy formation in bimetallic Pd(8.7)-Cu(10)/SiO₂ can activate the hydrogenation of chemisorbed CO species, which could also serve as a carbon source for methanol formation.

3.3.7 Discussion

The combination of Pd and Cu on the featured alloy structuring are observed from TPR profiles. Evidently, the CuO reducibility was improved significantly with the addition of Pd, which functions in ways of reducing the activation energy and providing a high-concentrated active hydrogen in reduction. In addition, the enhanced adsorption properties towards weakly-bonded H₂ and CO₂ demonstrate the enhancement of Pd dispersion in the alloy particles. Besides, in our recent work, a bimetallic Pd-Cu catalyst with a proper Pd loading dramatically decreased the metallic Cu⁰ particle size and improved its surface concentration by the formation of alloy particles after reduction [34]. Therefore, the complementary roles of Pd and Cu in the bimetallic catalysts lead to better dispersed metals in the alloy particles.

The H₂-TPD and CO₂-TPD results offered an important insight into the influence of Pd-Cu combination on the adsorption states of H₂ and CO₂, respectively. Due to the alloy formation,

the Pd-Cu bimetallic catalysts could provide more weakly-bonded H₂ and CO₂ around reaction temperatures at specific composition. In order to study the relationship between those weakly-bonded species and the catalytic performances over these bimetallic catalysts with various Pd loadings, the corresponding desorbed amounts are summarized along with the CH₃OH promotion and replotted as a function of Pd loading in Fig. 3-33. Results clearly show that the enhanced weakly-bonded H₂ (I+II) and CO₂ (I+II) around reaction temperatures appear to correlate to the CH₃OH promotion, and the values all maximize at Pd=8.7 wt%. For this particular catalyst, both metal components were found to mainly contribute to the formation of PdCu₃ and PdCu, thereby leading to the uniform and nano-sized alloy particles with well dispersed metals. Therefore, the combination of Pd and Cu promotes the adsorption of weakly-bonded H₂ and CO₂ around the reaction temperature with specific alloy compositions, which brought insights to the role of alloy in the observed synergetic effect on CH₃OH promotion.

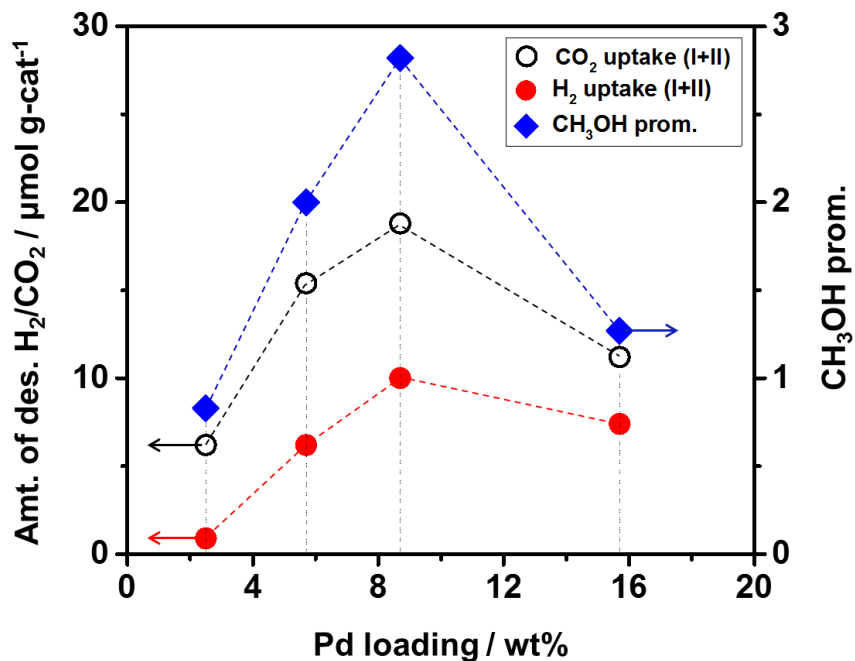


Figure 3-33 The correlations of CH₃OH promotion with the amounts of weakly-bonded H₂ (I+II) and CO₂ (I+II) for Pd(X)-Cu(10)/SiO₂. Reaction conditions: 523 K, 4.1 MPa, 6.2 g h mol⁻¹.

DRIFTS results show that formate and carbonyl species are the intermediates observed in CO₂ hydrogenation over mono and bimetallic catalysts. In comparison to monometallic catalysts, the combination of Pd and Cu greatly promotes the formation of formate species. The surface coverage of formate species varies with the Pd loadings in the bimetallic catalysts and maximizes at Pd=8.7 wt%, the trend of which appears to correlate with the CH₃OH promotion. Thus, the formate species possesses a potential to be an active intermediate species. However, this is the area which requires more in-depth studies in future.

On the other hand, FT-IR spectra also reveal that the addition of Pd greatly enhances the stabilization of CO intermediate in the bimetallic catalysts. Primarily, three forms of chemisorbed CO species are observed, and their bonding strength decreases in the following order: CO^H > CO^B > CO^L. Their reactivity towards the formation of methoxy species is confirmed by the CO adsorption-hydrogen purge experiments. Thus, the chemisorbed CO, produced via RWGS, is a potential intermediate for methanol formation over the bimetallic catalysts as well. Among these three forms of chemisorbed CO species over the alloy surface, CO^B is suggested to be more active for CO hydrogenation because of its moderate bonding strength; more importantly, CO^B desorption temperature approximates the reaction temperature (e.g., 523 K) as evidenced from corresponding CO-TPD profiles. The bonding strength of CO^L with metal is weaker than the other two and is most likely unstable at the reaction temperature. As a result, it could desorb easily from the surface and mainly consist of the product CO (g) as detected in the product stream. Quantitative analyses elucidate that the combination of Pd and Cu could promote the proportion towards CO^B adsorption and restrict the CO^H adsorption in the meanwhile at specific composition. Thus, the enhanced proportion of CO^B suggests another possibility to produce methanol over the bimetallic catalysts.

The existence of such reaction pathway, namely the hydrogenation of chemisorbed CO species, is further evidenced from the selectivity-conversion plot of Pd(8.7)-Cu(10)/SiO₂. However, the hydrogenation of CO species is not observed over monometallic Cu/SiO₂. Therefore, the combination of Pd and Cu with specific composition results in the formation of uniform and nano-sized alloy particles, which enhances the methanol formation via a strong synergetic effect by providing more weakly-bonded H₂ and CO₂ around reaction temperatures. In addition, the combination also promotes the formation of intermediate CO, which is verified evidently as another carbon source for methanol synthesis over bimetallic catalyst with specific composition.

3.4 Conclusions

The silica supported Pd-Cu bimetallic catalysts were found to have a strong synergetic effect on methanol synthesis via CO₂ hydrogenation. The superior CH₃OH promotion appeared to correlate to the alloy formation with specific composition. The effect of combining Pd and Cu on the surface chemical properties was studied by means of H₂-TPR, H₂-TPD, CO₂-TPD, CO-TPD, and DRIFTS. Important results are summarized below.

- (1) The strong interaction between Pd and Cu and its impact on the featured alloy structuring were observed from H₂-TPR profiles. The complementary roles of each metal component in the bimetallic catalysts led to the well-dispersed metals in the alloy particles.
- (2) The combination of Pd and Cu promoted the adsorption towards weakly-bonded H₂ (I+II) and CO₂ (I+II) around reaction temperatures at specific composition. The enhanced weakly-bonded H₂ and CO₂ appeared to correlate to the observed synergetic effect on CH₃OH promotion.
- (3) The formation of Pd-Cu alloy greatly improved the formation of both formate and chemisorbed CO species.
- (4) Three forms of chemisorbed adsorbed CO species were obtained over the alloy surface during

the CO₂ hydrogenation, and their bonding strengths decreased in the following order: CO^H > CO^B > CO^L (DRIFTS & CO-TPD). Among them, CO^B was suggested to be a potential intermediate for methanol synthesis because of its moderate bonding strength and proper desorption temperature range. The combination of Pd and Cu could promote the proportion towards CO^B adsorption at specific composition, which may provide the possibility to contribute the methanol synthesis via the hydrogenation of chemisorbed CO species. The existence of such reaction pathway was further evidenced by the selectivity-conversion plot over Pd(8.7)-Cu(10)/SiO₂ with featured alloy phases (e.g., coexistence of PdCu₃ and PdCu).

3.5 Acknowledgements

This work was supported in part by the Pennsylvania State University through the Penn State Institute of Energy and the Environment. The author (XJ) acknowledges the financial support from Chinese Scholarship Council (CSC). The CO-TPD measurements were performed at the Materials Characterization Laboratory of the Penn State Materials Research Institute, for which the assistance of Lymaris Ortiz Rivera is gratefully acknowledged. The author (Xiao Jiang) also acknowledges the financial support from Chinese Scholarship Council (CSC).

3.6 Reference

- [1] M.B. Ansari, S.-E. Park, Energy & Environmental Science, 5 (2012) 9419-9437.
- [2] R.W. Dorner, D.R. Hardy, F.W. Williams, H.D. Willauer, Energy & Environmental Science, 3 (2010) 884-890.
- [3] P. Markewitz, W. Kuckshinrichs, W. Leitner, J. Linssen, P. Zapp, R. Bongartz, A. Schreiber, T.E. Müller, Energy & Environmental Science, 5 (2012) 7281-7305.
- [4] W. Wang, S. Wang, X. Ma, J. Gong, Chem. Soc. Rev., 40 (2011) 3703-3727.
- [5] Z. Jiang, T. Xiao, V.L. Kuznetsov, P.P. Edwards, Philosophical transactions. Series A, Mathematical, physical, and engineering sciences, 368 (2010) 3343-3364.
- [6] C. Song, A.F. Gaffney, K. Fujimoto, in: C. Song, A.F. Gaffney, K. Fujimoto (Eds.) CO₂ Conversion and Utilization, American Chemical Society, Washington D.C., 2002, pp. 2-30.
- [7] C. Song, Catal. Today, 115 (2006) 2-32.
- [8] M. Mikkelsen, M. Jørgensen, F.C. Krebs, Energy & Environmental Science, 3 (2010) 43-81.
- [9] H. Arakawa, M. Aresta, J.N. Armor, M.A. Barreau, E.J. Beckman, A.T. Bell, J.E. Bercaw, C. Creutz, E. Dinjus, D.A. Dixon, K. Domen, D.W. Goodman, J. Keller, G.J. Kubas, H.H. Kung, J.E. Lyons, L.E. Manzer, J. Rostrup-Nielson, W.M.H. Sachtler, L.D. Schmidt, A. Sen, G.A. Somorjai, P.C. Stair, B.R. Stults, W. Tumas, Chem. Rev., 101 (2001) 953-996.
- [10] M. Aresta, A. Dibenedetto, Catal. Today, 98 (2004) 455-462.
- [11] M. Aresta, Carbon Dioxide as Chemical Feedstock, Wiley-VCH Verlag GmbH & Co. KGaA, Weinheim, 2010.
- [12] G. Centi, S. Perathoner, Z.S. Rak, Appl. Catal., B-Environ, 41 (2003) 143-155.
- [13] G. Centi, S. Perathoner, Catal. Today, 148 (2009) 191-205.

- [14] R. Raudaskoski, E. Turpeinen, R. Lenkkeri, E. Pongrácz, R.L. Keiski, *Catal. Today*, 144 (2009) 318-323.
- [15] F. Pontzen, W. Liebner, V. Gronemann, M. Rothaemel, B. Ahlers, *Catal. Today*, 171 (2011) 242-250.
- [16] J. Nakamura, I. Nakamura, T. Uchijima, Y. Kanai, T. Watanabe, M. Saito, T. Fujitani, *Catal. Lett.*, 31 (1995) 325-331.
- [17] F. Arena, G. Italiano, K. Barbera, S. Bordiga, G. Bonura, L. Spadaro, F. Frusteri, *Appl. Catal.*, A-Gen, 350 (2008) 16-23.
- [18] M. Saito, T. Fujitani, M. Takeuchi, T. Watanabe, *Appl. Catal.*, A-Gen, 138 (1996) 311-318.
- [19] M. Behrens, F. Studt, I. Kasatkin, S. Kuhl, M. Havecker, F. Abild-Pedersen, S. Zander, F. Girgsdies, P. Kurr, B. Kniep, M. Tovar, R.W. Fischer, J.K. Norskov, R. Schlogl, *Sci.*, 336 (2012) 893-897.
- [20] J. Graciani, K. Mudiyanselage, F. Xu, A.E. Baber, J. Evans, S.D. Senanayake, D.J. Stacchiola, P. Liu, J. Hrbek, J. Fernandez Sanz, J.A. Rodriguez, *Sci.*, 345 (2014) 546-550.
- [21] M.L. Poutsma, L.F. Elek, P.A. Ibarbia, A.P. Risch, J.A. Rabo, *J. Catal.*, 52 (1978) 157-168.
- [22] Y. Matsumura, W.-J. Shen, Y. Ichihashi, M. Okumura, *J. Catal.*, 197 (2001) 267-272.
- [23] Y. Kikuzono, S. Kagami, S. Naito, T. Onishi, K. Tamaru, *Faraday Discuss. Chem. Soc.*, 72 (1981) 135-143.
- [24] A. Gotti, R. Prins, *J. Catal.*, 175 (1998) 302-311.
- [25] L. Fan, K. Fujimoto, *Appl. Catal.*, A-Gen, 106 (1993) L1-L7.
- [26] T. Fujitani, M. Saito, Y. Kanai, T. Watanabe, J. Nakamura, T. Uchijima, *Appl. Catal.*, A-Gen, 125 (1995) L199-L202.
- [27] C. Shao, L. Fan, K. Fujimoto, Y. Iwasawa, *Appl. Catal.*, A-Gen, 128 (1995) L1-L6.

- [28] L. Fan, K. Fujimoto, Energy Convers. Manage., 36 (1995) 633-636.
- [29] T. Fujitani, I. Nakamura, Bull. Chem. Soc. Jpn., 75 (2002) 1393-1398.
- [30] S.E. Collins, D.L. Chiavassa, A.L. Bonivardi, M.A. Baltanas, Catal. Lett., 103 (2005) 83-88.
- [31] D.L. Chiavassa, J. Barrandeguy, A.L. Bonivardi, M.A. Baltanás, Catal. Today, 133-135 (2008) 780-786.
- [32] X.-L. Liang, X. Dong, G.-D. Lin, H.-B. Zhang, Appl. Catal., B-Environ, 88 (2009) 315-322.
- [33] N. Koizumi, X. Jiang, J. Kugai, C. Song, Catal. Today, 194 (2012) 16-24.
- [34] X. Jiang, N. Koizumi, X. Guo, C. Song, Appl. Catal., B-Environ, 170 (2015) 173-185.
- [35] J. Kugai, E.B. Fox, C. Song, Appl. Catal., A-Gen, 497 (2015) 31-41.
- [36] A. Karelovic, P. Ruiz, Catal. Sci. Technol., 5 (2015) 869-881.
- [37] M.A. Vannice, Kinetics of catalytic reactions, Springer, New York, 2005.
- [38] Z. Liu, M.D. Amiridis, Y. Chen, J. Phys. Chem. B, 109 (2005) 1251-1255.
- [39] J. Kugai, J.T. Miller, N. Guo, C. Song, Appl. Catal., B-Environ, 105 (2011) 306-316.
- [40] H.E. Kissinger, Anal. Chem., 29 (1957) 1702-1706.
- [41] D.A.M. Monti, A. Baiker, J. Catal., 83 (1983) 323-335.
- [42] I. Melian-Cabrera, M.L. Granados, J.L.G. Fierro, J. Catal., 210 (2002) 285-294.
- [43] J.T. Miller, B.L. Meyers, F.S. Modica, G.S. Lane, M. Vaarkamp, D.C. Koningsberger, J. Catal., 143 (1993) 395-408.
- [44] V. Ragagni, R. Giannantonio, P. Magni, L. Lucarelli, G. Leofanti, J. Catal., 146 (1994) 116.
- [45] A. Oancea, O. Grasset, E.L. Menn, O. Bollengier, L. Bezacier, S.L. Mouelic, G. Tobie, Icarus, 221 (2012) 900-910.
- [46] G.C. Cabilla, A.L. Bonivardi, M.A. Baltanas, Appl. Catal., A-Gen, 255 (2003) 181-195.

- [47] G.J. Millar, C.H. Rochester, K.C. Waugh, J. Chem. Soc., Faraday Trans., 87 (1991) 1491-1496.
- [48] D.B. Clarke, A.T. Bell, J. Catal., 154 (1995) 314-328.
- [49] G.C. Cabilla, A.L. Bonivardi, M.A. Baltanas, J. Catal., 201 (2001) 213-220.
- [50] R. Zhang, Y. Sun, S. Peng, Fuel, 81 (2002) 1619-1624.
- [51] G.C. Cabilla, A.L. Bonivardi, M.A. Baltanas, Catal. Lett., 55 (1998) 147-156.
- [52] Y. Yang, C.A. Mims, D.H. Mei, C.H.F. Peden, C.T. Campbell, J. Catal., 298 (2013) 10-17.
- [53] A.J. Medford, J. Sehested, J. Rossmeisl, I. Chorkendorff, F. Studt, J.K. Nørskov, P.G. Moses, J. Catal., 309 (2014) 397-407.
- [54] A. Erdohelyi, M. Pasztor, F. Solymosi, J. Catal., 98 (1986) 166-177.
- [55] S.E. Collins, M.A. Baltanas, A.L. Bonivardi, J. Catal., 226 (2004) 410-421.
- [56] K.K. Bando, K. Sayama, H. Kusama, K. Okabe, H. Arakawa, Appl. Catal., A-Gen, 165 (1997) 391-409.
- [57] L.F. Liotta, G.A. Martin, G. Deganello, J. Catal., 164 (1996) 322-333.
- [58] Y. Yang, M.G. White, P. Liu, J. Phys. Chem. C, 116 (2012) 248-256.
- [59] Y. Yang, C.A. Mims, R.S. Disselkamp, J.-H. Kwak, C.H.F. Peden, C.T. Campbell, J. Phys. Chem. C, 114 (2010) 17205-17211.
- [60] L.C. Grabow, M. Marvrikakis, ACS Catal., 1 (2011) 365-384.
- [61] K. Hadjiivanov, T. Venkov, H. Knozinger, Catal. Lett., 75 (2001) 55-59.
- [62] T. Shimanouchi, National Standards of Reference Data Services, vol. 1, National Bureau of Standards, Washington, DC, USA., (1972).
- [63] M. Bowker, H. Houghton, K.C. Waugh, Journal of chemical society, Faraday Transactions, 77 (1981) 3023-3036.

- [64] M. Bowker, R.A. Hadden, H. Houghton, J.N.K. Hyland, K.C. Waugh, *J. Catal.*, 109 (1988) 263-273.
- [65] M.A. Newton, S.M. Francis, Y. Li, D. Law, M. Bowker, *Surf. Sci.*, 259 (1991) 45-55.
- [66] Y. Yang, C.A. Mims, R.S. Disselkamp, D. Mei, J.-H. Kwak, J. Szanyi, C.H.F. Peden, C.T. Campbell, *Catal. Lett.*, 125 (2008) 201-208.
- [67] T. Fujitani, J. Nakamura, *Appl. Catal., A-Gen*, 191 (2000) 111-129.
- [68] J. Yoshihara, C.T. Campbell, *J. Catal.*, 161 (1996) 776-782.
- [69] C.-S. Chen, W.-H. Cheng, S.-S. Lin, *Appl. Catal., A-Gen*, 238 (2003) 55-67.
- [70] D.-K. Lee, D.-S. Kim, S.-W. Kim, *Appl. Organomet. Chem.*, 15 (2001) 148-150.
- [71] D.L. Chiavassa, S.E. Collins, A.L. Bonivardi, M.A. Baltanas, *Chem. Eng. J.*, 150 (2009) 204-212.
- [72] S.E. Collins, J.J. Delgado, C. Mira, J.J. Calvino, S. Bernal, D.L. Chiavassa, M.A. Baltanas, A.L. Bonivardi, *J. Catal.*, 292 (2012) 90-98.
- [73] E. Christoffersen, P. Stoltze, J.K. Norskov, *Surf. Sci.*, 505 (2002) 200-214.
- [74] A.M. Bradshaw, F.M. Hoffmann, *Surf. Sci.*, 72 (1978) 513-535.
- [75] V. Sanchez-Escribano, L. Arrighi, P. Riani, R. Marazza, G. Busca, *Langmuir*, 22 (2006) 9214-9219.
- [76] J.W. Niemantsverdriet, *Spectroscopy in catalysis: an introduction*, WILEY-VCH Verlag GmbH & KGaA, Weinheim2007.
- [77] A. Ueno, C.O. Bennett, *J. Catal.*, 54 (1978) 31-41.
- [78] M. Neurock, *Top. Catal.*, 9 (1999) 135-152.
- [79] H. Arakawa, J.-L. Dubois, K. Sayama, *Energy Convers. Manage.*, 33 (1992) 521-528.

- [80] F.L. Peltier, P. Chaumette, J. Saussey, M.M. Bettahar, J.C. Lavalley, *J. Mol. Catal. A: Chem.*, 132 (1998) 91-100.
- [81] Q. Sun, C.-W. Liu, W. Pan, Q.-M. Zhu, J.-F. Deng, *Appl. Catal., A-Gen*, 171 (1998) 301-308.
- [82] N. Koizumi, K. Murai, S. Takasaki, M. Yamada, *Prepr. Pap. - Am. Chem. Soc., Div. Fuel Chem.*, 47 (2002) 140-141.
- [83] N. Koizumi, K. Murai, S. Tamayama, H. Kato, T. Ozaki, M. Yamada, *Prepr. Pap. - Am. Chem. Soc., Div. Fuel Chem.*, 47 (2002) 519-250.
- [84] R. Yang, Y. Fu, Y. Zhang, N. Tsubaki, *J. Catal.*, 228 (2004) 23-35.
- [85] T. Fujitani, T. Matsuda, Y. Kushida, S. Ogihara, T. Uchijima, J. Nakamura, *Catal. Lett.*, 49 (1997) 175-179.
- [86] J.S. Rieck, A.T. Bell, *J. Catal.*, 103 (1987) 46-54.
- [87] J.S. Rieck, A.T. Bell, *J. Catal.*, 96 (1985) 88-105.
- [88] F. Arena, G. Mezzatesta, G. Zafarana, G. Trunfio, F. Frusteri, L. Spadaro, *J. Catal.*, 300 (2013) 141-151.

Chapter 4 Conclusions and Recommendations for Future Work

4.1 Summary

This work studied the effect of Pd-Cu combination on the catalytic properties for CO₂ hydrogenation to methanol. The work provided a fundamental understanding on composition-structure-activity relationship. The major observations from each chapter are summarized below.

In Chapter 2, the amorphous silica supported Pd-Cu bimetallic catalysts with different compositions were prepared and applied in the activity tests. Various characterizations were carried out to investigate the interaction between Pd and Cu and the effect of combining Pd and Cu on the composition-structure property relationship in the bimetallic catalysts with various Pd loadings. The correlation of Pd-Cu composition-structure property with activity performances was also examined.

The combination of Pd and Cu led to a strong synergistic promotion of CH₃OH formation rate when the Pd/(Pd+Cu) atomic ratios were within 0.25-0.34 (i.e., 5.7-8.7 wt% Pd loading) for amorphous silica supported Pd-Cu catalysts. Detailed characterization results demonstrated the strong interaction between Pd and Cu and confirmed the formation of Pd-Cu alloys. The complementary role of metal components in the bimetallic catalysts led to the formation of uniform and nano-sized alloy particles with well-dispersed metals. The observed strong synergetic effect on methanol promotion of Pd-Cu bimetallic catalysts at specific composition had been attributed to the alloy structure and the accompanying strong interaction between metal components.

In Chapter 3, for the purpose of clarifying the effect of combining Pd and Cu on the adsorption properties towards reagents and the surface chemical properties in CO₂ hydrogenation,

the monometallic catalysts and bimetallic catalysts with various Pd loadings were measured by H₂ temperature-programmed reduction (H₂-TPR), H₂/CO₂/CO temperature-programmed desorption (H₂/CO₂/CO-TPD), and diffuse reflectance FT-IR (DRIFTS).

TPR profiles of bimetallic catalysts clearly showed the structuring procedure of alloy formation which considerably improved the reducibility of CuO mainly by lowering the apparent activation energy and provide more-concentrated hydrogen in reduction. From H₂/CO₂-TPD, the combination of Pd and Cu promoted the adsorption towards weakly-bonded H₂ (I+II) and CO₂ (I+II) around reaction temperatures at specific composition, which appeared to correlate to the observed synergetic effect on the CH₃OH promotion of bimetallic catalysts. DRIFTS spectra revealed that the formation of Pd-Cu alloy greatly improved the formation of intermediates formate and CO species. CO-TPD profiles confirmed the existence of three forms of chemisorbed CO species, and the bonding strength increased in the following order: CO^L < CO^B < CO^H. Among them, the chemisorbed CO^B was suggested as a potential intermediate for methanol synthesis because of its moderate bonding strength and desorption temperature range (proximity to reaction temperature). Quantitative analyses showed that the combination of Pd and Cu could promote the proportion towards CO^B adsorption at specific composition and thus gave rise to the possibility of methanol formation via the following hydrogenation of chemisorbed CO species. Such pathway was further confirmed by the selectivity-conversion plot.

4.2 Conclusions

The key conclusions of the current study are listed in this section. Each conclusion corresponds to an objective in the same order as listed in Chapter 1.

(1) A series of Pd-Cu bimetallic catalysts with various compositions were prepared by coimpregnation method and tested in the CO₂ hydrogenation to methanol. A strong synergetic

effect was observed for CO₂ hydrogenation to methanol over Pd-Cu bimetallic catalysts supported on silica, and the optimal Pd/(Pd+Cu) atomic ratios lied in the range of 0.25-0.34.

(2) Based on the H₂-TPR and XPS measurements, the Pd and Cu were found to have a strong interaction in the bimetallic catalysts. Qualitative and quantitative analyses of XRD patterns showed that both alloy phases and content are dependent upon the Pd loading in the bimetallic catalysts. The TEM and STEM/EDS further confirmed the existence of uniform and nano-sized alloy particles, PdCu₃ and PdCu, with high dispersion. Depending upon the composition-structure-activity relationship, the observed synergetic effect on methanol promotion over Pd-Cu bimetallic catalysts at specific composition was attributed to the Pd-Cu alloy formation and the accompanying strong interaction between metal components.

(3) The combination of Pd and Cu promoted the adsorption towards weakly-bonded CO₂ and H₂ around the reaction temperatures with specific alloy compositions, which appeared to correlate to the enhanced CH₃OH promotion. In addition, combining Pd and Cu could promote the surface coverage of intermediates formate and carbonyl species. Among the observed three forms of chemisorbed CO species, CO^B was suggested to be a potential intermediate for methanol synthesis because of its moderate bonding strength and desorption temperature range (in proximity to the reaction temperatures), and the combination of Pd and Cu could promote the proportion towards CO^B adsorption at specific composition and provided the possibility to produce methanol via the following hydrogenation of chemisorbed CO species. The existence of such reaction pathway was further confirmed by the selectivity-conversion plot of Pd(8.7)-Cu(10)/SiO₂.

4.3 Recommendations for future work

This dissertation has studied the effect of combining Pd and Cu on the activity and selectivity to methanol synthesis from CO₂ hydrogenation and how bimetallic catalysts work in

the methanol formation. However, questions still remain as to the effects of alloy with lower metal loadings, different alloy structures, and additive on the methanol synthesis from CO₂. To address these questions, it is recommended that the complementary use of theory and experiment should be continued. In this context, the followings are the recommendations summarized for the actions in future.

4.3.1 Pd-Cu alloy effect with lower metal loadings

As already confirmed from both activity performances and characterization results, Pd-Cu alloys play a crucial role in the observed CH₃OH enhancement. Thus, it is of great interest to investigate the effect of alloy with lower metal loadings on the methanol synthesis while maintaining the Pd atomic ratios around 0.34, where the optimal methanol synthesis activity was obtained. Based on this idea, a series of Pd-Cu catalysts with lower metal loadings (e.g., Pd loading < 8.7 wt%) shall be prepared with an identical Pd atomic ratio. Since the metal compositions would be changed dramatically, it is suggested to normalize the space time yield (STY) based on the metal time yield (MTY) for comparison.

4.3.2 Effect of PdCu₃ and PdCu alloys on methanol synthesis

In Chapter 2 and 3, the coexistence of PdCu₃ and PdCu was found to be important for the observed methanol enhancement from CO₂ hydrogenation because it may provide more alloy content. Since these two alloy phases have different structures (FCC and BCC, respectively) and metal component stoichiometry, which might cause the difference in the ratio of CO₂/H₂ adsorbed in a local environment. Such different adsorption balance may further lead to the preference towards different reactions and the product distribution. Therefore, it would be of great interest to study the effect of different alloy structures on the methanol synthesis from CO₂. In this case, a

series of bimetallic catalysts shall be prepared, and the Pd loading shall be controlled in a range where Pd and Cu could primarily contribute to the alloy formation but with different compositions of PdCu_3 and PdCu . Theoretically, the computational simulations would be a promising and convenient tool to fundamentally study the effect of different alloy formations on the methanol synthesis. Experimentally, the composition of different alloy phases could be determined by the XRD patterns through the method of whole pattern fitting (WPF) and Rietveld method. Then, the quantitative composition could be correlated with activity performances, which could further verify the simulated results by density theory function calculation (DFT).

4.3.3 Effect of ZnO on methanol synthesis activity over Pd-Cu bimetallic catalysts

Table 4-1 Activity performances on ZnO-promoted and unpromoted Pd-Cu catalysts ^{a-c)}

Catalyst	CO_2 conv. / %	Prod. selec./ mol%		Formation rate/ $\mu\text{mol g}^{-1} \text{s}^{-1}$	
		CO	CH_3OH	CO	CH_3OH
Pd(8.7)-Cu(10)-ZnO(10)/ SiO_2	4.0	60	40	0.35	0.23
Pd(8.7)-Cu(10)/ SiO_2	6.6	66	34	0.61	0.31

^{a)} Both catalysts were prepared by the coimpregnation method in the acetone solution. $\text{Zn}(\text{NO}_3)_2 \cdot 6\text{H}_2\text{O}$ (Alfa Aesar, 99.998 %) was used as precursor source.

^{b)} All metal loadings in the parentheses were on support weight basis.

^{c)} Reaction conditions: 523 K, 4.1 MPa, W/F=6.25 g h mol⁻¹.

As reported, Zn can function to improve the CO_2 adsorption as formate species in the Cu-Zn-based catalysts, besides, it possessed the possibility to form alloy structure with Cu [1] as well as Pd [2]. Hence, it would be interesting to study the effect of ZnO on the methanol synthesis activity over Pd-Cu bimetallic catalysts. Actually, such kind of catalyst has already been prepared by the coimpregnation method and tested under the same reaction conditions, namely 523 K and 4.1 MPa, and the preliminary results are summarized in Table 4-1. Evidently, CO formation rate

decreases substantially with the addition of ZnO; however, the activity drop for CH₃OH is not as considerable as that for CO, which leads to the improvement of its selectivity in return. In order to better verify the improvement of CH₃OH selectivity, the contact time (W/F) of Pd(8.7)-Cu(10)/SiO₂ was adjusted to reach an equivalent CO₂ conversion as the Pd-Cu-Zn catalyst, and the selectivities are compared in Fig. 4-1 for clarity. Interestingly, at the similar CO₂ conversion, the Pd-Cu-Zn catalyst reveals a better CH₃OH selectivity than Pd-Cu catalysts. It is hypothesized that the active sites are affected by the addition of ZnO, which selectively inhibits the reverse water-gas shift (RWGS) and even tunes the reaction pathways. Thus, such ternary catalysts possess great potential to further improve the selectivity towards methanol synthesis while obtaining comparable methanol formation rate as Pd-Cu bimetallic catalysts. Based on these preliminary results and speculations, this course of action would be promising to continue.

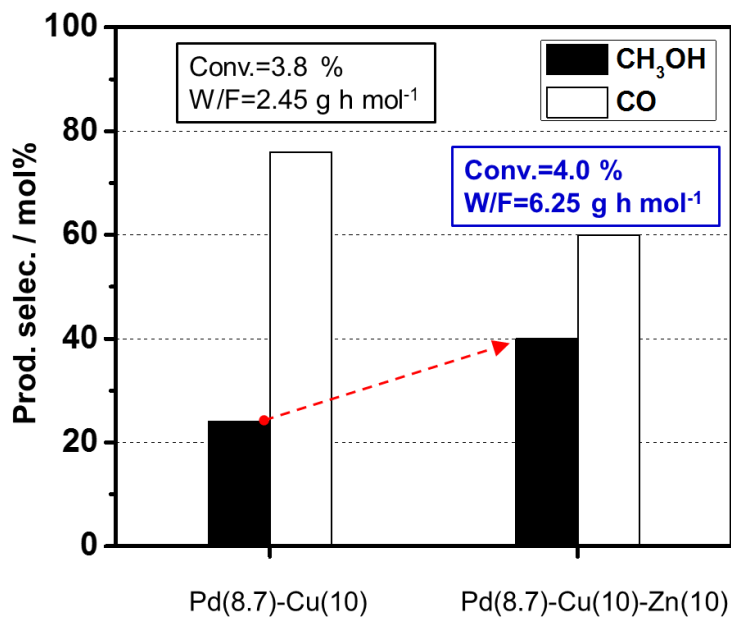


Figure 4-1 Selectivities of products over Pd(8.7)-Cu(10)/SiO₂ and Pd(8.7)-Cu(10)-ZnO(10)/SiO₂ catalysts. Reaction conditions: 523 K, 4.1 MPa. W/Fs, from left to right, were 2.45 and 6.25 g h mol⁻¹, respectively.

4.4 Reference

- [1] T. Fujitani, J. Nakamura, Appl. Catal., A-Gen, 191 (2000) 111-129.
- [2] X.-L. Liang, X. Dong, G.-D. Lin, H.-B. Zhang, Appl. Catal., B-Environ, 88 (2009) 315-322.

Appendix A Preparation of Mesoporous Silicas

MCM-48: 30 g of tetraethyl orthosilicate was weighed and dissolved in 150 g of DI-H₂O (Deionized water) under vigorous stir at 313 K for 40 min. 2.88 g of NaOH and 0.5334 g of NH₄F were added into the solution and stirred vigorously at 313 K for 1 hr. In the following step, 31.83 g of cetyltrimethylammonium bromide (CTABr, Aldrich) was added into above solution and stirred at 313 K for another 1 hr. The solution was transferred to autoclave and heated at 393 K for 24 hrs. The resultant precipitation was filtered and washed with DI-H₂O and dried in the oven at ~373 K overnight. The MCM-48 was finally obtained by calcining the sample at 823 K (temperature ramp: 1 K min⁻¹) for 6 hrs under flowing dry air (ca. 100 mL (NTP) min⁻¹).

MCM-41: 4.387 g of Cab-o-sil fumed silica (Cabot) was added step wise to 25.7 g DI-H₂O (deionized water) followed by vigorous stir for 15 min. The resultant solution was marked as Soln-A. Then, 7.73 g of tetramethylammonium silicate solution (Aldrich, 0.75 TMA/SiO₂, 10 wt%) and 5.5 g of sodium silicate (Aldrich, 14% NaOH, 27% SiO₂, weight ratio) were mixed together under strong stir for 10 min, and the resultant solution was marked as Soln-B. In the next step, Soln-A and Soln-B were mixed under vigorous stir for 15 min to form Soln-C. Soln-D was prepared by mixing cetyltrimethylammonium bromide (12.9 g, Aldrich) and DI-H₂O (87 g). The Soln-C and Soln-D were mixed under vigorous stir for 20 min, and the resultant mixture was further transferred to autoclaves and heated in the oven at ~373 K for 40 hrs (< 2 days). After hydrothermal treatment, the precipitation was filtered and washed with DI-H₂O, and the resultant light-yellowish powder was dried in the oven at 373 K overnight. Finally, the sample was calcined in an electric furnace at 823 K (temperature ramp: 1 K min⁻¹) for 6 hrs under flowing dry air (ca. 100 mL (NTP) min⁻¹).

SBA-15: 24 g of P₁₂₃ (Sigma, EO₂₀PO₇₀EO₂₀, MW=5800), 604.84 g of DI-H₂O, and 145.16 g 37% HCl were mixed together and stirred vigorously at 313 K until the solution became transparent. In the following step, 51.0 g of tetraethyl orthosilicate (Aldrich, TEOS) was added into the above solution drop wise, and the resultant solution was stirred vigorously at 313 K for 20 hrs to obtain homogenous mixture. After that, the mixture was transferred to autoclave and heated at 373 K for 24 hrs. The resultant precipitation was filtered and washed with plenty amount of DI-H₂O and then dried in the oven at 373 K overnight. Finally, the white powder was calcined in an electric furnace at 823 K (temperature ramp: 1 K min⁻¹) for 6 hrs under flowing dry air (ca. 100 mL (NTP) min⁻¹).

Appendix B Incipient Pore Volume

As mentioned in the experimental section of Appendix K, the incipient pore volume of different mesoporous silica was measured by deionized-water before the precursor impregnation. The detailed values are listed below in Table B-1.

Figure B-1 Incipient pore volumes of different mesoporous silicas used in this work

Mesoporous silica	Incipient pore volume / mL g ⁻¹
MCM-48 ^{a)}	1.2
MCM-41 ^{a)}	1.2
SBA-15 ^{a)}	0.9
SiO ₂ ^{b)}	0.9
MSU-F ^{c)}	1.6

^{a)} Prepared in the lab and detailed preparation method is described in Appendix A.

^{b)} Amorphous silica (Davisil Grade 645) was purchased from Aldrich.

^{c)} MSU-F (cellular form) was purchased from Aldrich.

Appendix C X-ray Photoelectron Spectroscopy (XPS)

Sample mounting: Sample powders were mounted on individual 7 mm x 7 mm pieces of Scotch ½ inch permanent, double-sided tape (Cat #137). Each section of tape was secured to a 10 mm x 10 mm piece of Si wafer. To mount the powders, a suitable portion of the sample powder was first poured from its vial on to food-service grade Al foil (Reynolds #624). The tape surface was repeatedly pressed into the powder until the adhesive was completely covered. The loose excess powder was then blown off the tape with a jet of dry PP grade N₂. The tape/wafer couple was subsequently secured to the sample mounting bar with a Cu spring clip. The clip applied pressure to the Si wafer, and the clip was not in contact with the sample material. Since the double-sided tape is electrically insulating, the sample powder itself is electrically floating during an analysis.

Calibration: All spectra were charge corrected to Si 2p at 103.5 eV. The positions of the Si 2p and O 1s peaks were checked after charge correction, and suitable alignment was obtained for all peaks, as shown in Figs. C-1 and C-2. The C 1s, Cu 2p, and Pd 3d peaks of the *reduced* Pd(8.7)-Cu(10)/SiO₂ sample required an additional 0.5 eV shift due to differential charging [1].

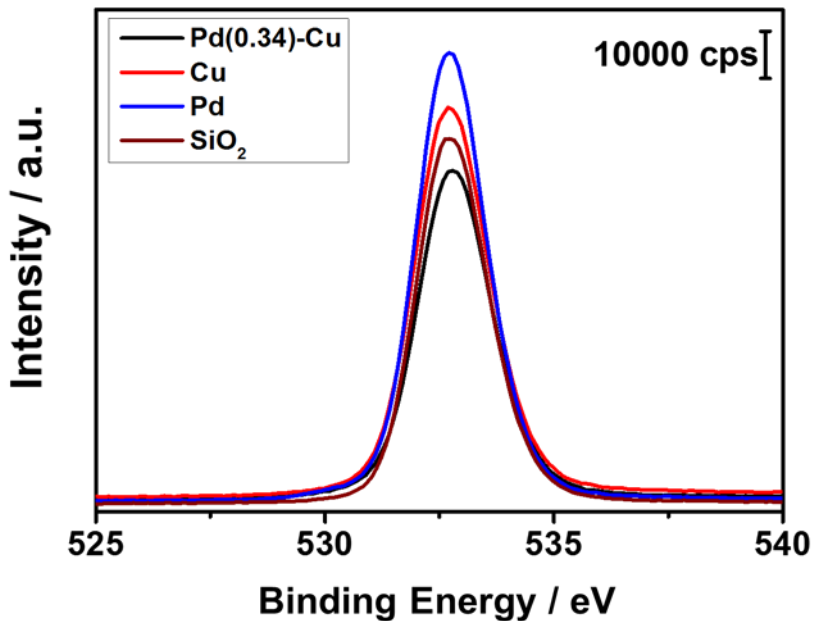


Figure C-1 O 1s XP spectra of *reduced* Pd-Cu/SiO₂ catalysts and together with support (amorphous silica). Pd loading was 8.7 wt% for Pd-containing samples and Cu loading was 10 wt% for Cu-containing samples. All samples were reduced first and then passivated.

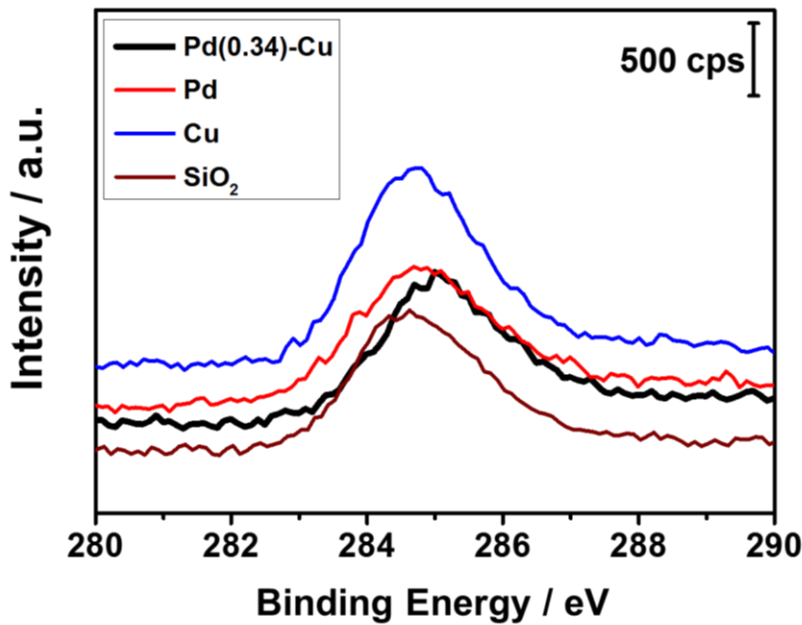


Figure C-2 C 1s XP spectra of *reduced* Pd-Cu/SiO₂ catalysts and together with support (amorphous silica). Pd loading was 8.7 wt% for Pd-containing samples and Cu loading was 10 wt% for Cu-containing samples. All samples were reduced first and then passivated.

Reference

- [1] T.L. Barr, Modern ESCA. The Principles and Practice of X-ray Photoelectron Spectroscopy, CRC Press, Boca Raton, 1994.

Appendix D X-ray Diffraction (XRD)

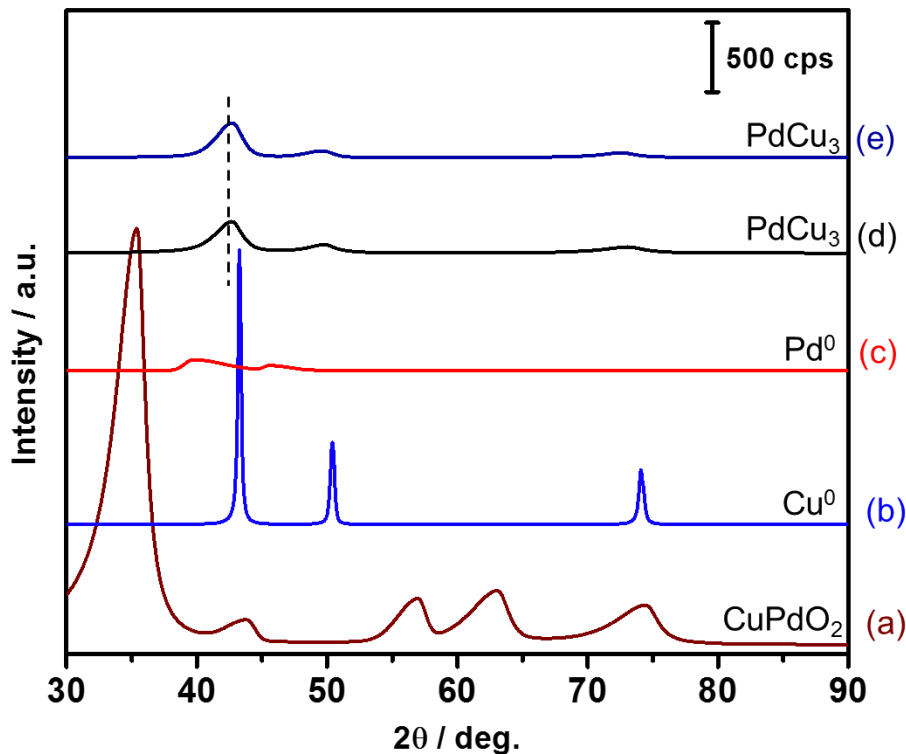


Figure D-1 XRD patterns of $\text{Pd}(X)\text{-Cu}(Y)/\text{SiO}_2$ catalysts with the thick lines indicating original patterns, while the thin lines indicating deconvoluted patterns. (a) *calcined* $\text{Pd}(5.7)\text{-Cu}(10)/\text{SiO}_2$, (b) *reduced* $\text{Cu}(10)/\text{SiO}_2$, (c) *reduced* $\text{Pd}(5.7)/\text{SiO}_2$, (d) *reduced* $\text{Pd}(5.7)\text{-Cu}(10)/\text{SiO}_2$, (e) *spent* $\text{Pd}(5.7)\text{-Cu}(10)/\text{SiO}_2$. Bimetallic catalysts were prepared by the coimpregnation method.

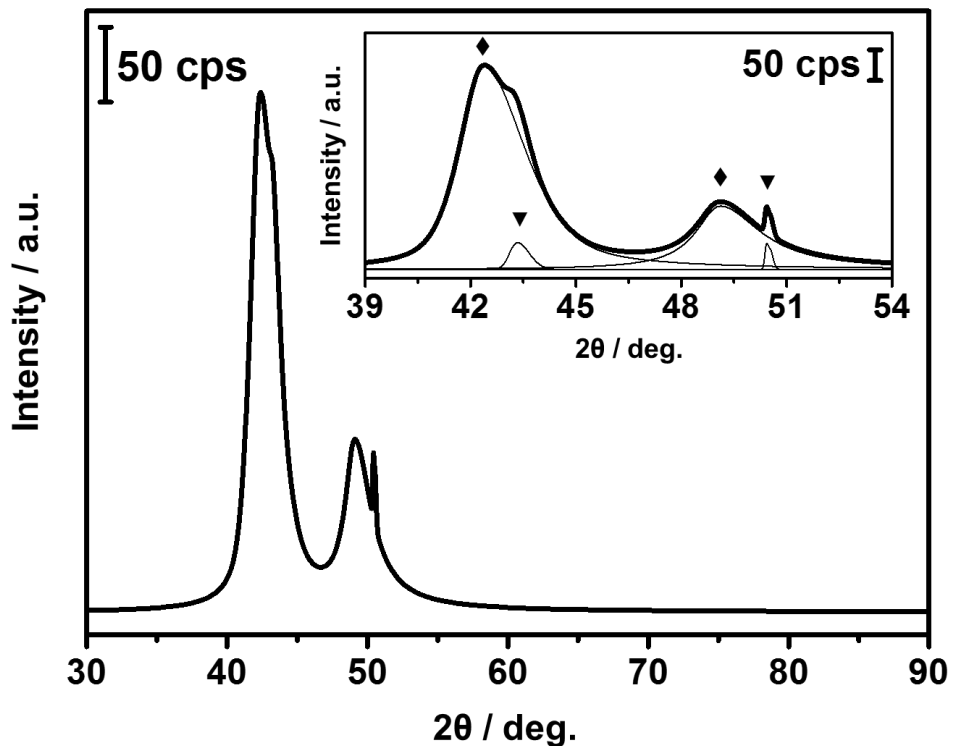


Figure D-2 XRD pattern of *reduced* Cu(10)/Pd(8.7)/SiO₂ catalyst with magnified XRD pattern in the inset (2θ: 39–45 °). Original pattern was highlighted with thick lines and patterns after deconvolution were featured with thin lines. Symbols assignment: ▼: Cu⁰ and ♦: PdCu₃.

Whole pattern fitting (WPF) refinement of X-ray diffraction patterns, using Jade 2010 from Materials Data, Inc. of Livermore, CA was used to semi-quantitatively determine the phases present in the bimetallic catalysts, Pd(8.7)-Cu(10)/SiO₂ and Pd(15.7)-Cu(10)/SiO₂. These bimetallic catalysts contain multiple alloy phases with different stoichiometries. Therefore, multiple phases must be considered during the refinement process. Two residual parameters are calculated in the fitting process which can be used to evaluate the quality of the fit; weighted-pattern residual (*R*) and expected residual (*E*). Two and three alloy models were tested to determine which model produced the best fit based on visual examination of the difference pattern, (*R*), and (*E*) values. The best fits were obtained using the two phase model - PdCu₃ and PdCu. The analysis provided semi-quantitative composition information of each alloy phase in this analysis. The

reference for each phase and fitting results are shown in Table D-1 and Figs. D-3 and D-4, respectively.

In order to improve the signal-to-noise ratio, XRD patterns for Pd(8.7)-Cu(10)/SiO₂ and Pd(15.7)-Cu(10)/SiO₂ were recollected at 45 kV and 40 mA from 36-52° (2θ) for a duration time of ~1 h. The semi-quantitative analysis was carried out in the range of 36-45° (2θ).

Table D-1 Summary of card data for potential phases

Phase	PDF card number	Source
PdCu ₃	04-004-8211	ICDD
PdCu	103082	ICSD
Pd	04-0047600	ICDD



Figure D-3 X-ray diffraction patterns observed and calculated for *reduced* Pd(8.7)-Cu(10)/SiO₂. R=1.01 % and E=0.58 %.

WPF Report

Scan ID: NK-236-1 R-P-Pd(15.7)-Cu(10)_SiO₂.xrdml

Scan Parameters: 36.02°/51.987°/0.02626°/1497.62(s), ω =18.01022°/25.99343°, φ =0.0°, I(p)=46685/24306, Cu(45kV,40mA), Monochromator

Control File: X:\XRD\2015-11-09\NK-236-1 R-P-Pd(15.7)-Cu(10)_SiO₂.wpf.xml

30-120-02_200s_mpss

<input checked="" type="checkbox"/> K _{α2} Peaks Present	Zero Offset = -0.17317 (0.02881)	X-Ray Polarization = 1.0
<input type="checkbox"/> Variable-Slit Pattern	Displacement = 0.0	K _{α2} /K _{α1} Ratio = 0.5

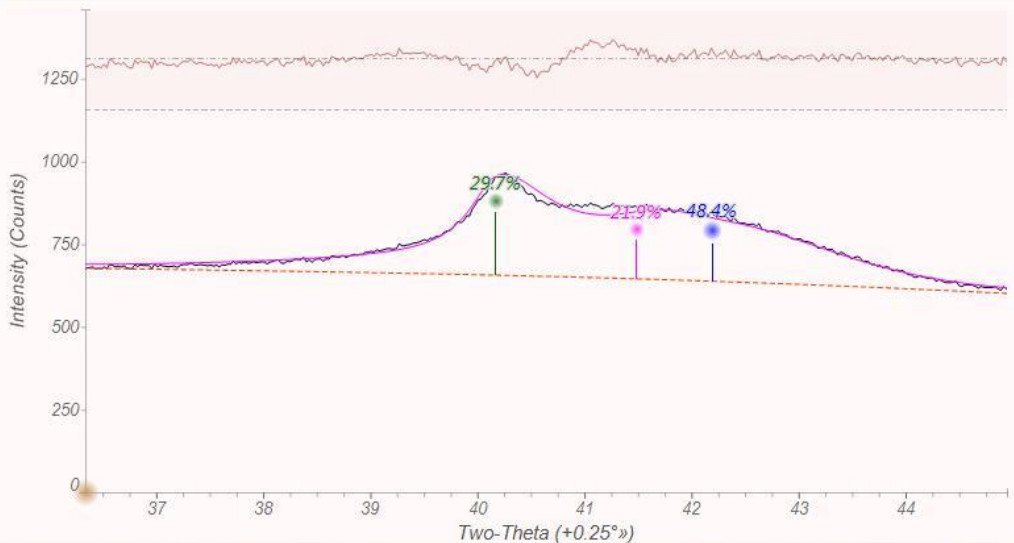
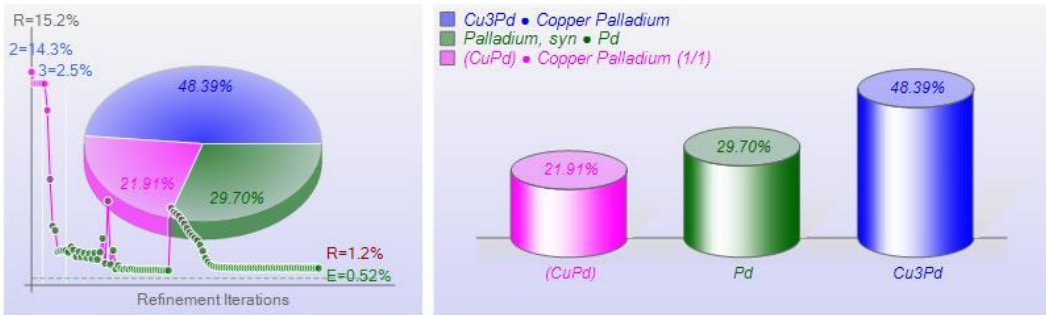
Geometry: Diffractometer Lp Fitted-Range: 36.0 - 45.0° BG-Model: Fixed-Curve (5) λ : 1.54059 Å (Cu)

PSF: pseudo-Voigt Broadening: Individual FWHM Curve Instrument: Constant FWHM = 0.1°

Phase ID (3)	Chemical Formula	PDF-#	Wt% (esd)	RIR	μ
Copper Palladium	Cu ₃ Pd	04-004-8211	48.39 (2.16)	11.54	1037.5
Copper Palladium (1/1)	(CuPd)	97-010-3082	21.91 (1.34)	13.49	1561.9
Palladium, syn	Pd	04-004-7600	29.70 (1.01)	17.38	2468.5

XRF(Wt%): Pd=60.75%, Cu=39.25%

Refinement Iterations, Ready... (E=0.52%, EPS=0.5)



X:\XRD\2015-11-09\NK-236-1 R-P-Pd(15.7)-Cu(10)_SiO₂.xrdml

Wednesday, November 11, 2015, 3:27 PM • Penn State

Figure D-4 X-ray diffraction patterns observed and calculated for *reduced* Pd(15.7)-Cu(10)/SiO₂. R=1.20 % and E=0.52 %.

Appendix E Energy Dispersive Spectroscopy Mapping (STEM/EDS)

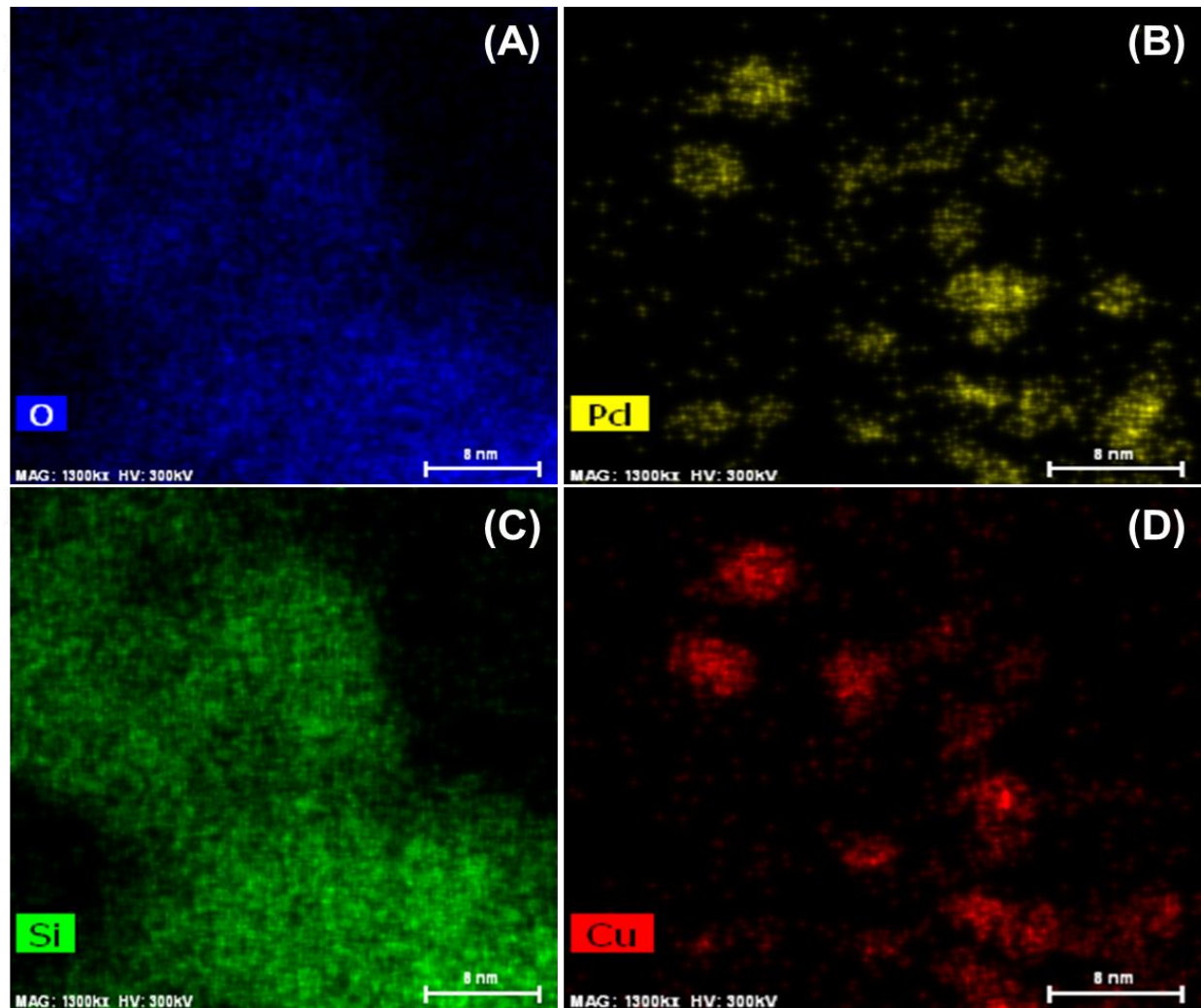


Figure E-1 STEM/EDS mapping of *reduced* Pd(8.7)-Cu(10)/SiO₂. (A): Oxygen (blue); (B): Palladium (yellow); (C): Silicon (green); (D): Copper (red).

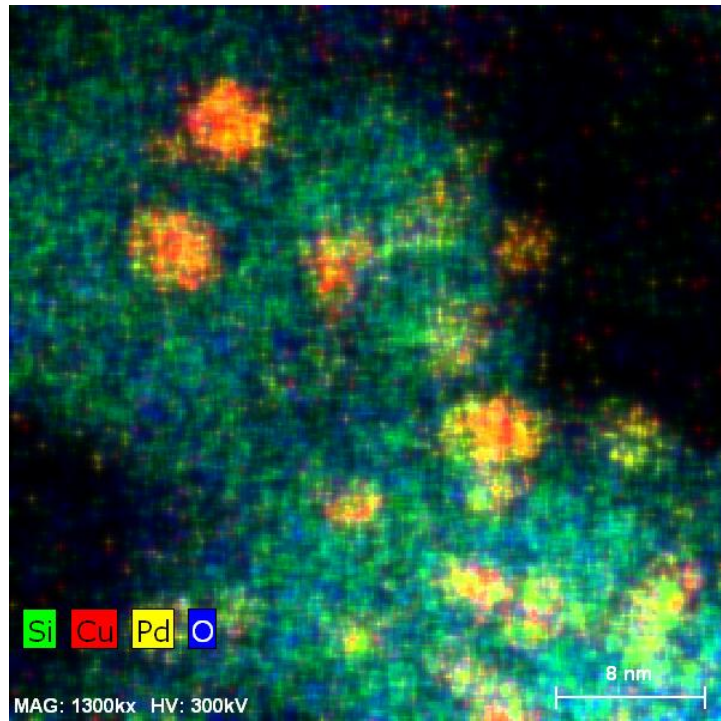


Figure E-2 STEM/EDS overlap mapping of *reduced* Pd(8.7)-Cu(10)/SiO₂. Color assignment: Oxygen (blue); Palladium (yellow); Silicon (green); Copper (red).

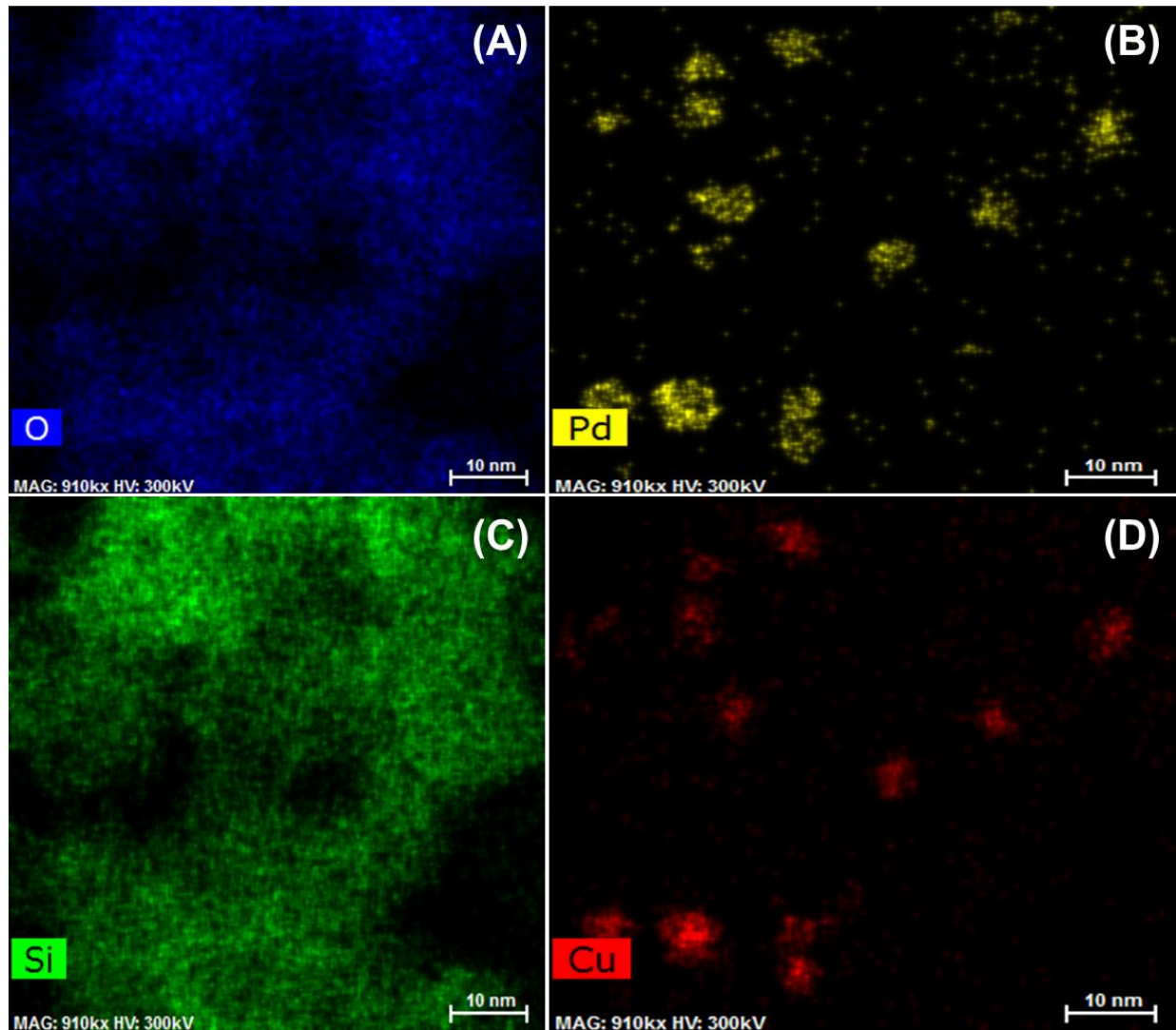


Figure E-3 STEM/EDS mapping of *reduced* Pd(2.5)-Cu(10)/SiO₂. (A): Oxygen (blue); (B): Palladium (yellow); (C): Silicon (green); (D): Copper (red).

Appendix F Temperature-Programmed Reduction (H₂-TPR)

In order to obtain the optimum reduction profiles, the effect of reduction gas flow rate, sample mass (reducible species), and temperature ramp should be considered before the experiment. Thus, a characteristic parameter P (See Eq. F-1) was introduced to determine the experimental condition and should lay below 20 K as recommended in literature [1-4]. According to the experimental condition chosen in this work, the P parameter for bimetallic Pd-Cu catalysts and monometallic catalysts are 16-18 K and 8-13 K, respectively, both of which lie within the acceptable range. One exception is the sample Pd(5.7)-Cu(40)/SiO₂ with excessive copper loading. For this particular sample, although the procedure remained unchanged for the sake of comparison, the hydrogen consumption is not quantified due to the unreliable profile.

$$P = \beta \cdot \frac{S_0}{V^* C_0} \quad \text{Eq. F-1}$$

β : Temperature ramp rate, K min⁻¹;

S_0 : Moles of reducible species in the catalyst, mol;

V^* : Total flow rate of reduction gas, mL min⁻¹;

C_0 : Concentration of hydrogen, mol mL⁻¹.

In order to quantify the hydrogen consumption, the silver oxide (II) was chosen as standard reference (Micromeritics). This standard sample has been tested twice, and the average maximum reduction peak shows at 457.7 K. The TPR profile is shown in Fig. F-1. In addition, the copper oxide (II, Sigma-Aldrich) was introduced as bench mark for comparison as well, and Dycor Dymaxion mass spectrometer DM200 M was employed (coupled with Autochem 2910 TPD/TPR) to detect hydrogen consumption.

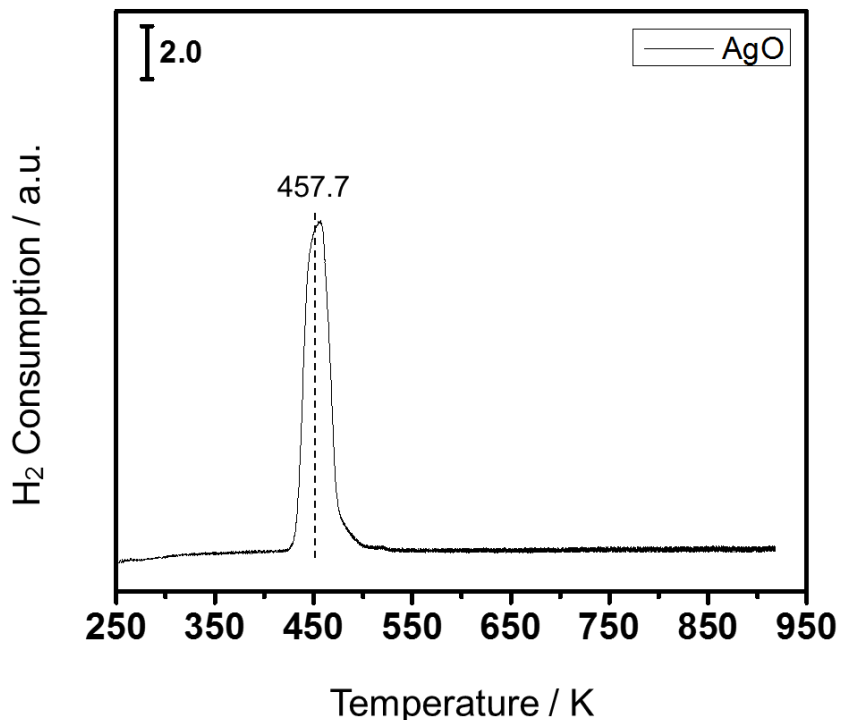


Figure F-1 TPR profile of standard sample AgO . Conditions: 20 mL min^{-1} of 5 vol% H_2/Ar with the heating rate of 10 K min^{-1} .

Before the initiation of reduction, the reduction gas was allowed to flush the catalyst bed until the baseline was stabilized; however, this step may cause the reduction of palladium oxide, because the palladium was particularly susceptible to hydrogen even at ambient temperature. Thus, the reduction peak of palladium is barely seen; instead, a negative peak appears, which is indicative of the decomposition of the β hydride [5, 6]. Fig. F-2 shows such phenomenon over the sample $\text{Pd}(8.7)/\text{SiO}_2$. In order to avoid the pre-reduction of palladium oxide before temperature elevation, the liquid nitrogen slush bath was used to cool down the temperature of the sample to as low as 223 K until the temperature elevation program was initiated.

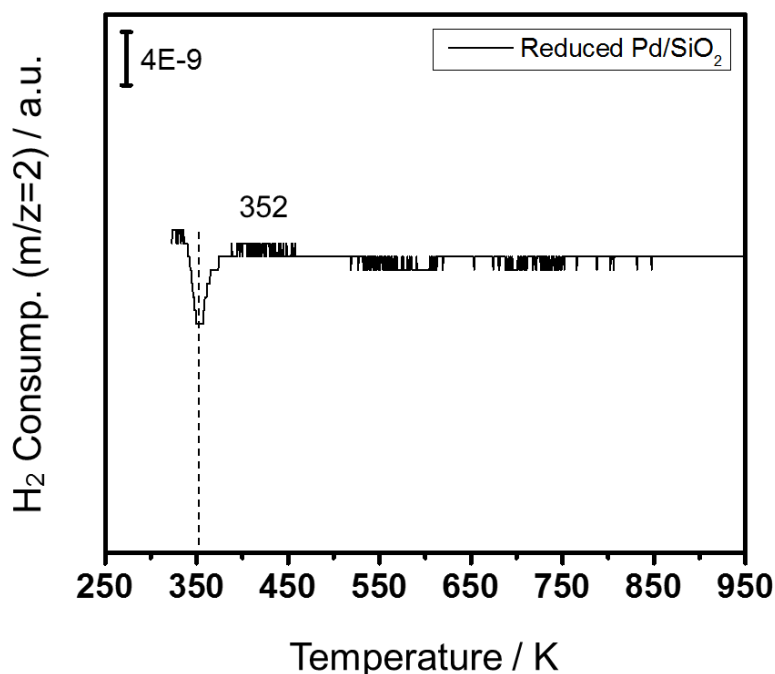


Figure F-2 TPR profile of Pd(8.7)/SiO₂. The sample was prepared by wet impregnation method in acetone solution of palladium (II) acetate. The H₂ consumption rate was recorded by mass spectroscopy. TPR conditions: 20 mL min⁻¹ of 5% H₂/Argon with a heating rate of 10 K min⁻¹.

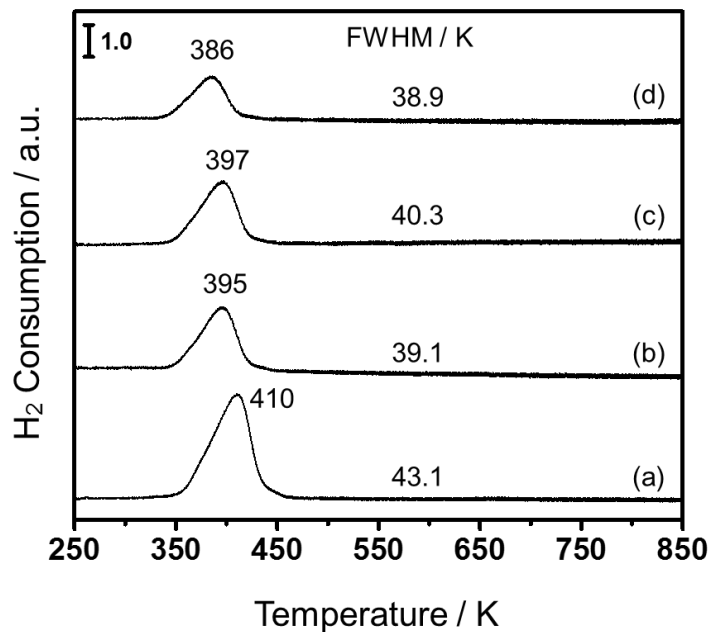


Figure F-3 TPR profiles of Pd(5.7)-Cu(10)/SiO₂ at different flow rates. TPR conditions: 5 vol% H₂/Ar flow, 10 K min⁻¹. (a) 20 mL min⁻¹; (b) 40 mL min⁻¹; (c) 40 mL min⁻¹ (repeat); (d) 60 mL min⁻¹.

Reference

- [1] G. Fierro, M.L. Jacono, M. Inversi, P. Porta, F. Cioci, R. Lavecchia, *Appl. Catal., A-Gen*, 137 (1996) 327-348.
- [2] D.A.M. Monti, A. Baiker, *J. Catal.*, 83 (1983) 323-335.
- [3] G. Fierro, M.L. Jacono, M. Inversi, P. Porta, R. Lavecchia, F. Cioci, *J. Catal.*, 148 (1994) 709-721.
- [4] I. Melian-Cabrera, M.L. Granados, J.L.G. Fierro, *J. Catal.*, 210 (2002) 285-294.
- [5] C. Amorim, M.A. Keane, *J. Colloid Interface Sci.*, 322 (2008) 196-208.
- [6] A.F. Gusovius, T.C. Watling, R. Prins, *Appl. Catal., A-Gen*, 188 (1999) 187-199.

Appendix G Hydrogen Temperature-Programmed Desorption (H₂-TPD)

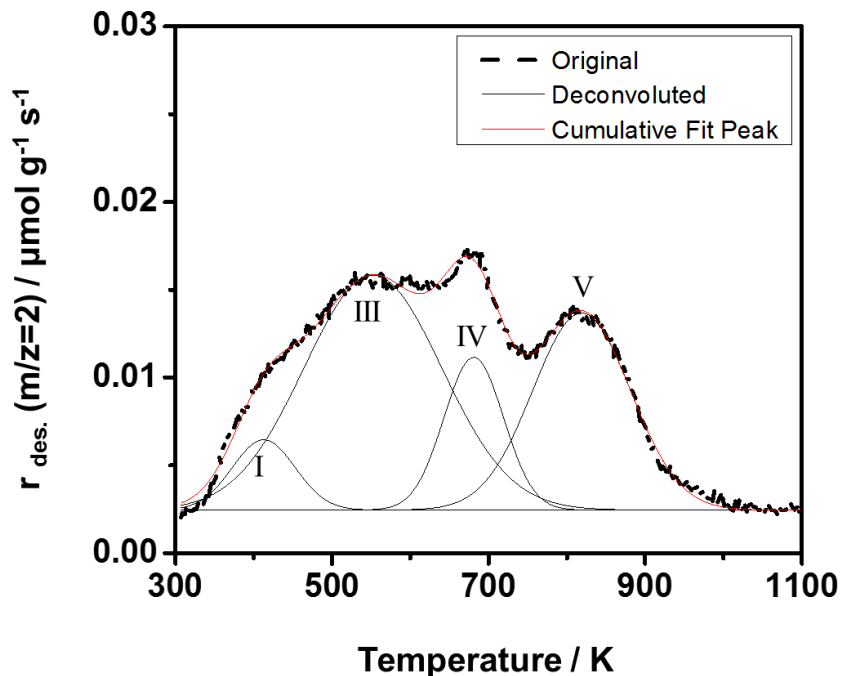


Figure G-1 Deconvolution of the H₂-TPD profile of the reduced Pd(8.7)/SiO₂. (---) measured TPD profile, (—) deconvoluted peaks, and red (—) cumulative fitting peaks.

Table G-1 Amount of adsorbed H₂ species over Pd(8.7)/SiO₂

Species	Tempt / K	Amt. / $\mu\text{mol g}^{-1}$
I	412.8	2.4
III	552.2	17.6
IV	681.1	5.0
V	818.8	10.5

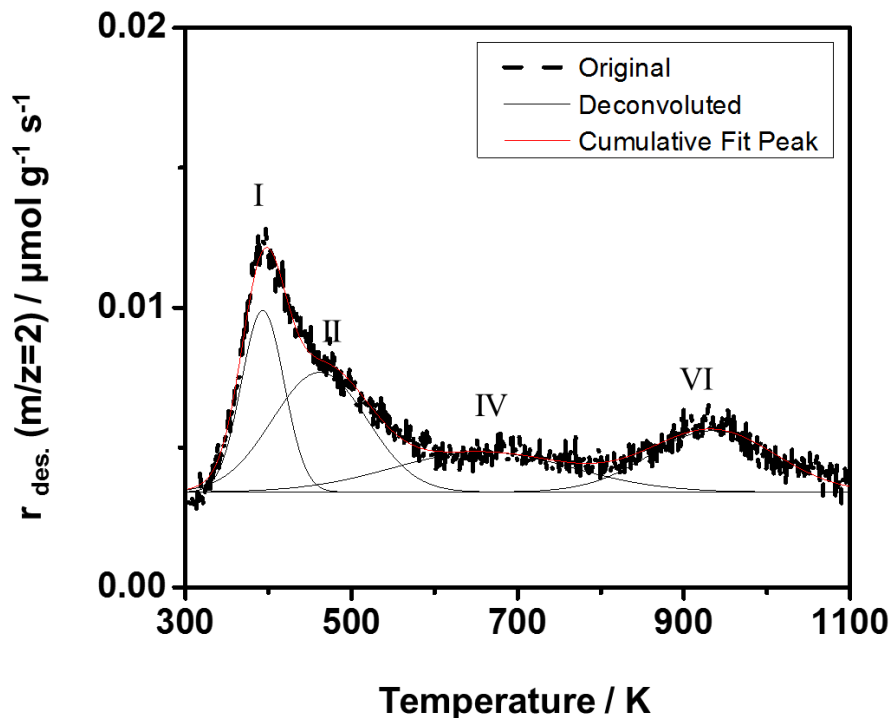


Figure G-2 Deconvolution of the H₂-TPD profile of the reduced Pd(5.7)-Cu(10)/SiO₂. (---) measured TPD profile, (—) deconvoluted peaks, and red (—) cumulative fitting peaks.

Table G-2 Amount of adsorbed H₂ species over Pd(5.7)-Cu(10)/SiO₂

Species	Tempt / K	Amt. / $\mu\text{mol g}^{-1}$
I	393.2	2.5
II	461.8	3.7
IV	658.0	2.3
VI	934.9	2.5

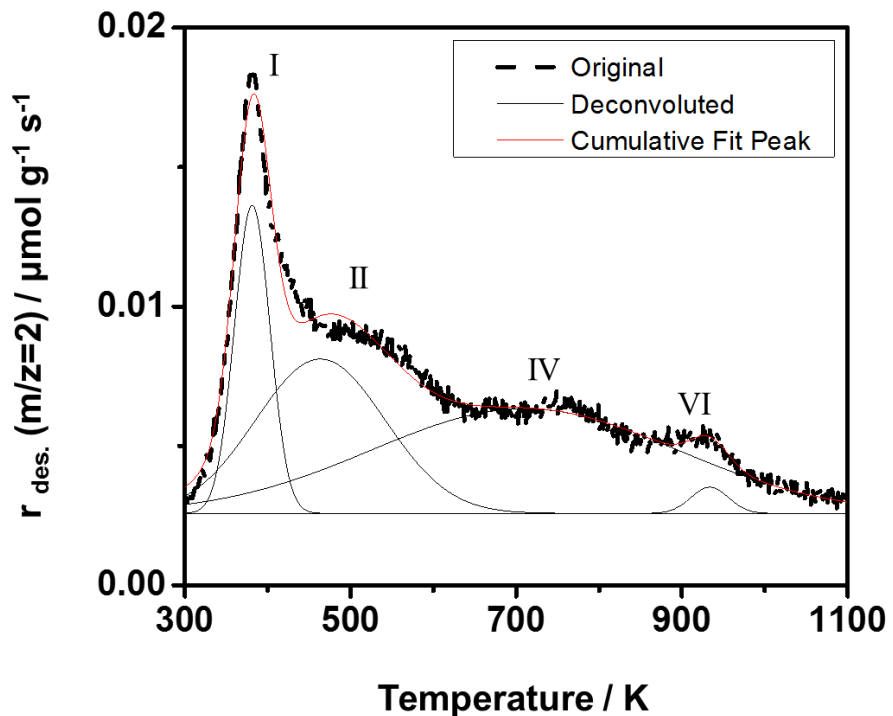


Figure G-3 Deconvolution of the H₂-TPD profile of the reduced Pd(8.7)-Cu(10)/SiO₂. (---) measured TPD profile, (—) deconvoluted peaks, and red (—) cumulative fitting peaks.

Table G-3 Amount of adsorbed H₂ species over Pd(8.7)-Cu(10)/SiO₂

Species	Tempt / K	Amt. / $\mu\text{mol g}^{-1}$
I	381.4	3.6
II	463.7	6.4
IV	710.1	9.4
VI	933.5	0.3

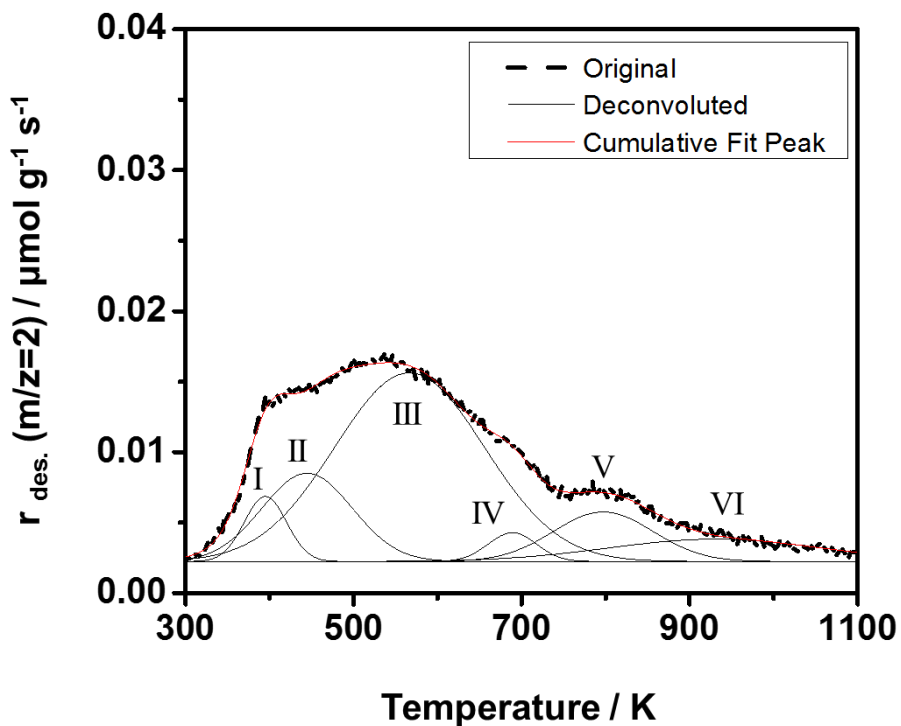


Figure G-4 Deconvolution of the H₂-TPD profile of the reduced Pd(15.7)-Cu(10)/SiO₂. (--) measured TPD profile, (—) deconvoluted peaks, and red (—) cumulative fitting peaks.

Table G-4 Amount of adsorbed H₂ species over Pd(8.7)-Cu(10)/SiO₂

Species	Tempt / K	Amt. / $\mu\text{mol g}^{-1}$
I	395.2	1.8
II	444.8	5.6
III	566.7	17.5
IV	689.0	0.8
V	791.2	3.5
VI	930.0	2.7

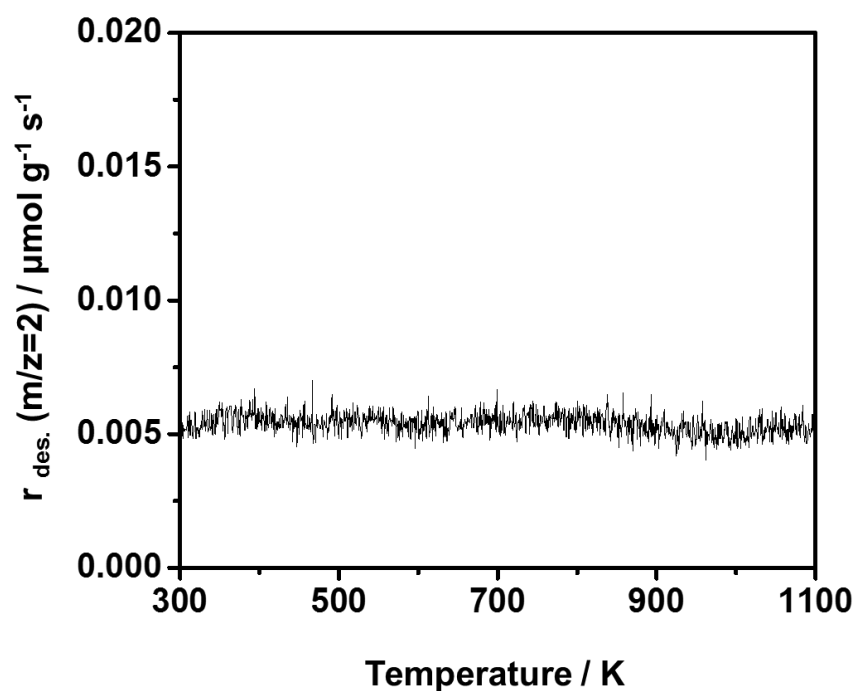


Figure G-5 H₂-TPD profile of the bare support (amorphous silica).

Appendix H Carbon Dioxide Temperature-Programmed Desorption (CO₂-TPD)

As reported, CO₂ can be adsorbed on the pre-reduced Pd/SiO₂ catalyst undergoing the reversible dissociation at T=298 K and P=1 Torr, and the dissociation process produces adsorbed CO_{ads} species and O_{ads} [1]. In order to verify this dissociation, the CO₂-TPD measurement was conducted over the pre-reduced Pd(8.7)-Cu(10)/SiO₂. The measurement was described in section 3.2.3.2 (Chapter 3). The real-time concentrations for relevant desorbed species are shown in Fig. H-1. Evidently, apart from CO₂, no desorption signals are observed for either CO (m/z=28) or O₂ (m/z=32). Thus, the dissociation of CO₂ to CO does not occur over the alloy surface during the CO₂ adsorption without the addition of hydrogen.

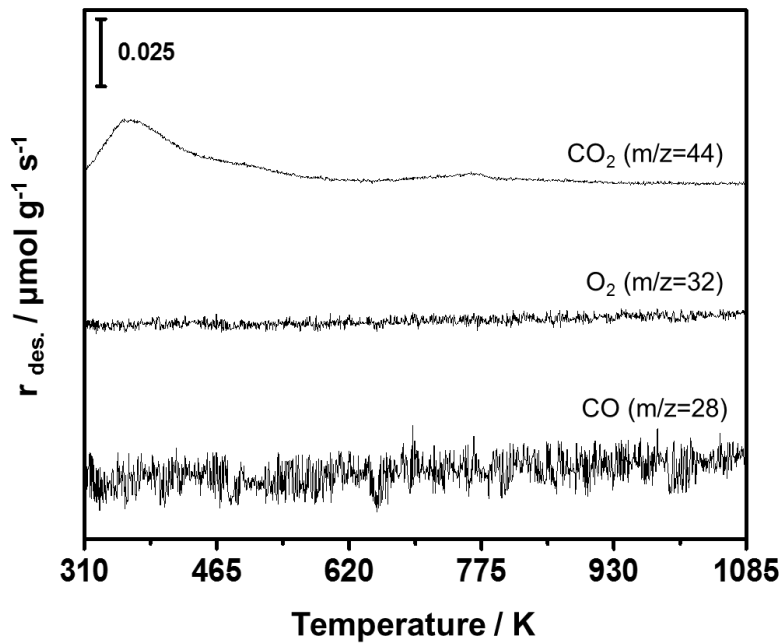


Figure H-1 CO₂-TPD profiles of pre-reduced Pd(8.7)-Cu(10)/SiO₂. CO₂-TPD condition: 1 vol% Ar/He (30 mL min⁻¹), 10 K min⁻¹ of heating rate.

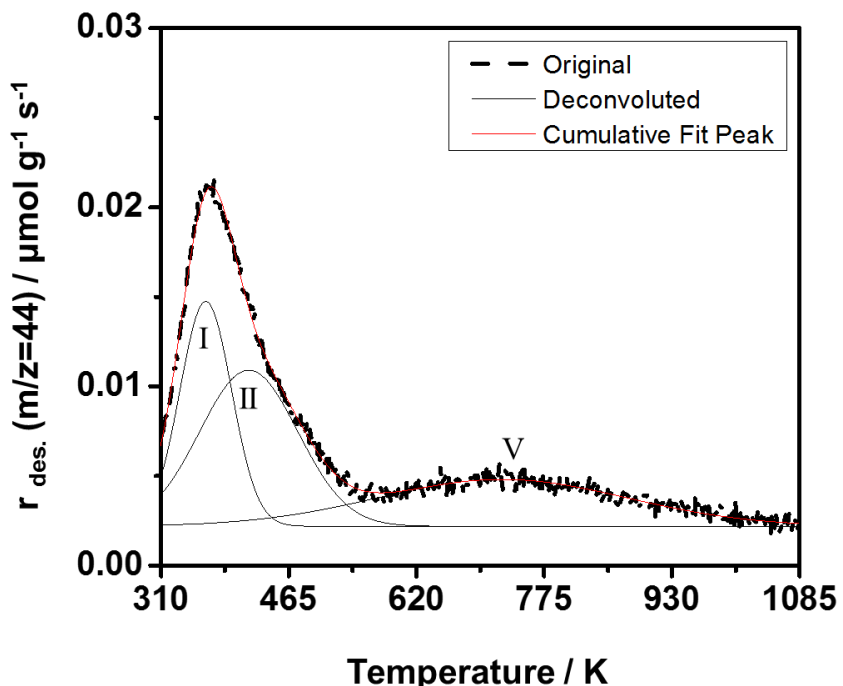


Figure H-2 Deconvolution of the CO₂-TPD profile of the reduced Pd(8.7)/SiO₂. (---) measured TPD profile, (—) deconvoluted peaks, and red (—) cumulative fitting peaks.

Table H-1 Amount of adsorbed CO₂ species over Pd(8.7)/SiO₂

Species	Tempt / K	Amt. / $\mu\text{mol g}^{-1}$
I	364.3	5.7
II	416.4	7.5
V	724.1	5.8

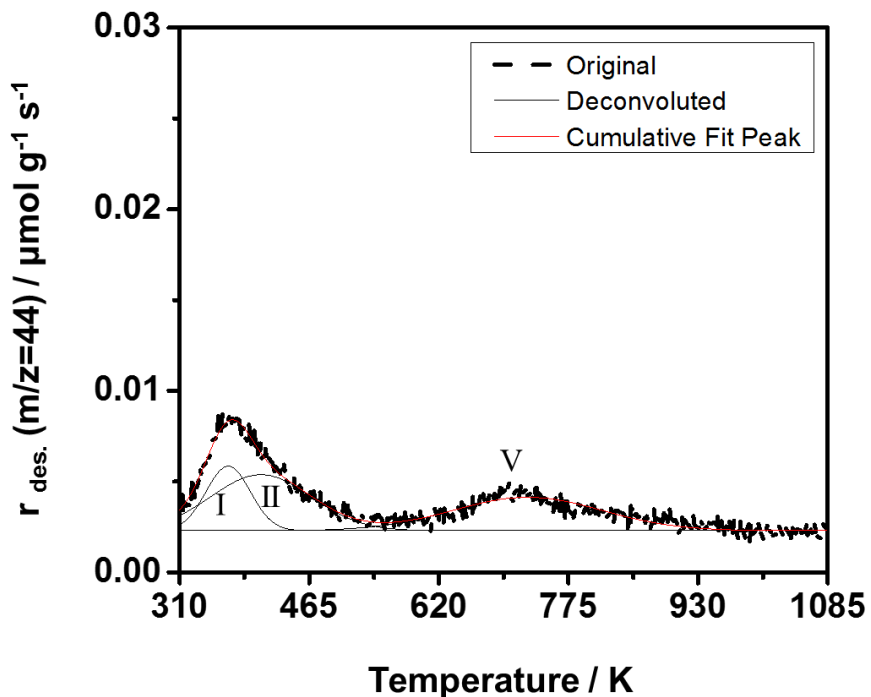


Figure H-3 Deconvolution of the CO₂-TPD profile of the reduced Cu(10)/SiO₂. (---) measured TPD profile, (—) deconvoluted peaks, and red (—) cumulative fitting peaks.

Table H-2 Amount of adsorbed CO₂ species over Cu(10)/SiO₂

Species	Tempt / K	Amt. / $\mu\text{mol g}^{-1}$
I	368.2	1.4
II	407.4	2.6
V	726.1	2.5

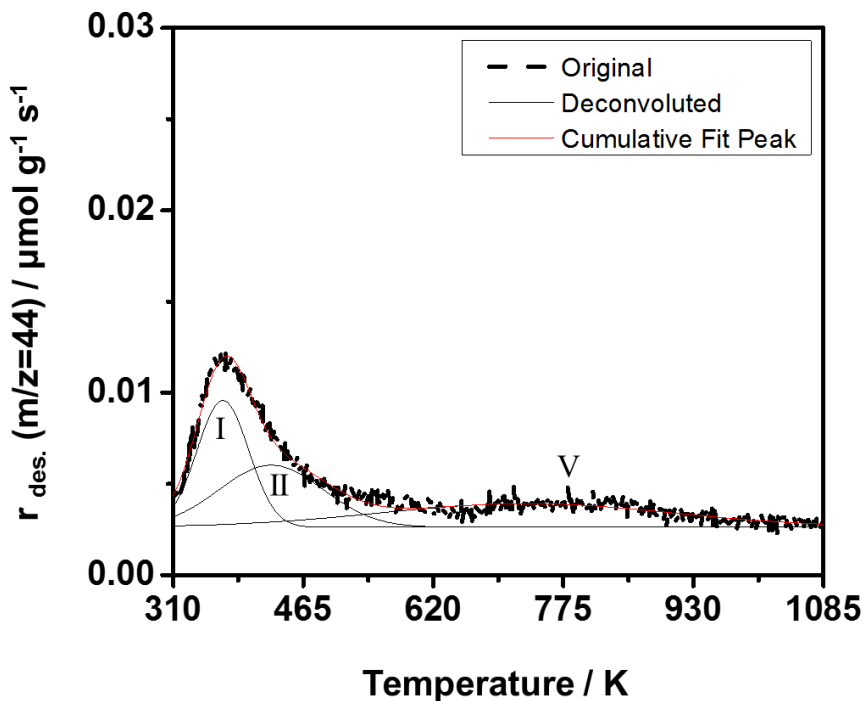


Figure H-4 Deconvolution of the CO₂-TPD profile of the reduced Pd(2.5)-Cu(10)/SiO₂. (---) measured TPD profile, (—) deconvoluted peaks, and red (—) cumulative fitting peaks.

Table H-3 Amount of adsorbed CO₂ species over Pd(2.5)-Cu(10)/SiO₂

Species	Tempt / K	Amt. / $\mu\text{mol g}^{-1}$
I	369.2	3.1
II	426.8	3.1
V	731.1	3.1

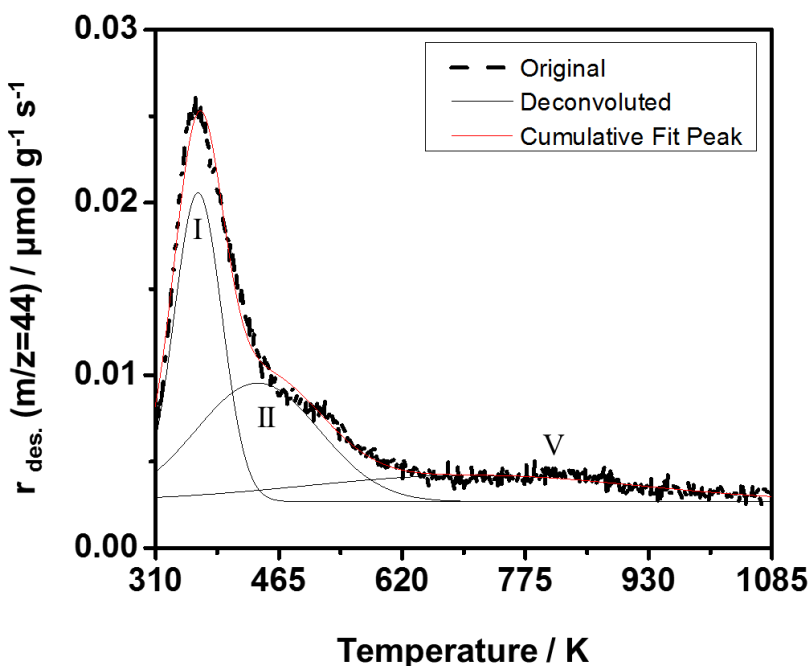


Figure H-5 Deconvolution of the CO₂-TPD profile of the reduced Pd(5.7)-Cu(10)/SiO₂. (---) measured TPD profile, (—) deconvoluted peaks, and red (—) cumulative fitting peaks.

Table H-4 Amount of adsorbed CO₂ species over Pd(5.7)-Cu(10)/SiO₂

Species	Tempt / K	Amt. / $\mu\text{mol g}^{-1}$
I	363.4	7.8
II	438.3	7.6
V	708.9	4.0

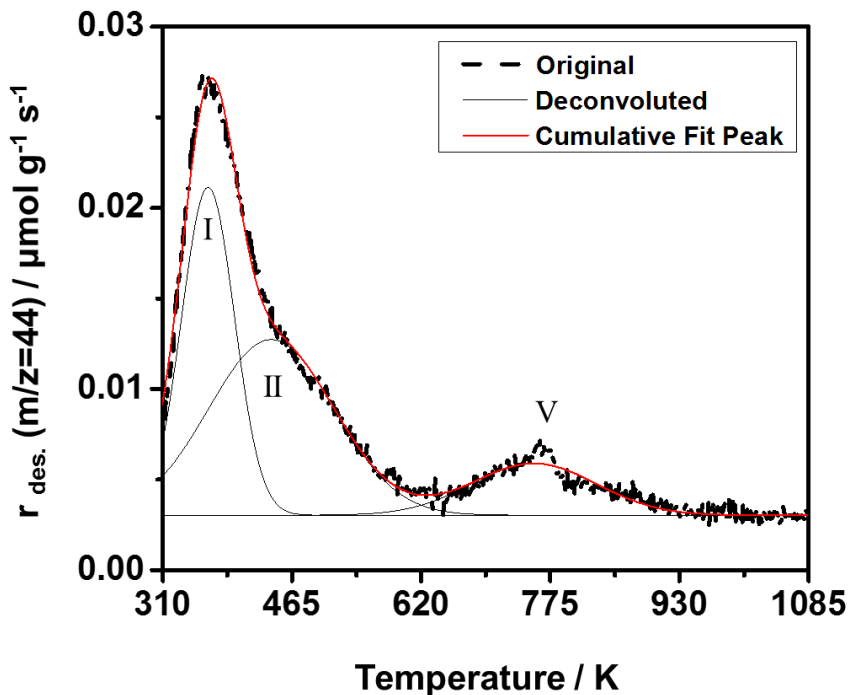


Figure H-6 Deconvolution of the CO₂-TPD profile of the reduced Pd(8.7)-Cu(10)/SiO₂. (---) measured TPD profile, (—) deconvoluted peaks, and red (—) cumulative fitting peaks.

Table H-5 Amount of adsorbed CO₂ species over Pd(8.7)-Cu(10)/SiO₂

Species	Tempt / K	Amt. / $\mu\text{mol g}^{-1}$
I	364.4	8.3
II	440.2	10.5
V	755.4	3.2

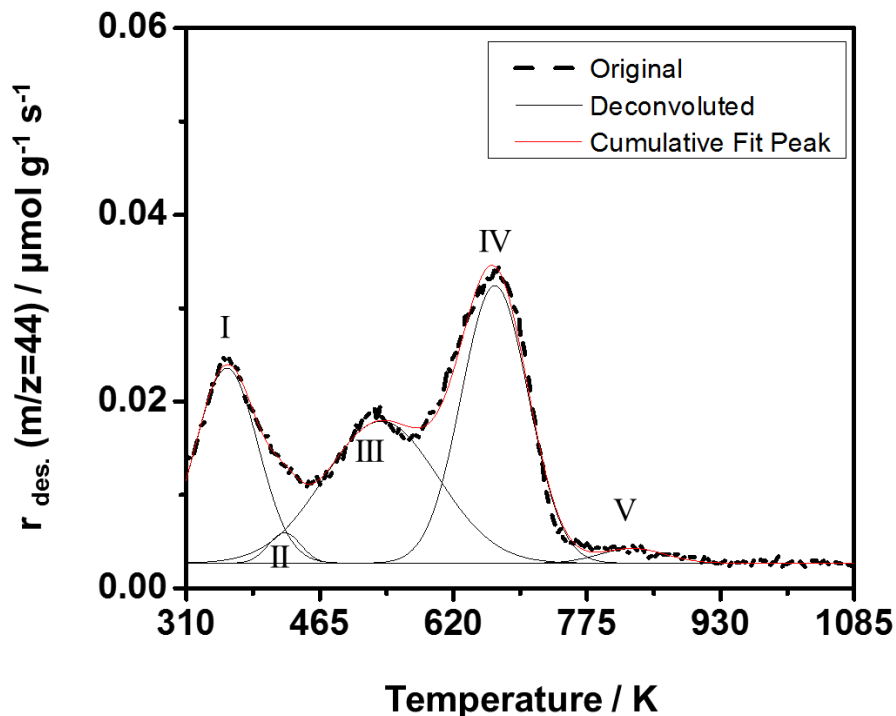


Figure H-7 Deconvolution of the CO₂-TPD profile of the reduced Pd(15.7)-Cu(10)/SiO₂. (---) measured TPD profile, (—) deconvoluted peaks, and red (—) cumulative fitting peaks.

Table H-6 Amount of adsorbed CO₂ species over Pd(15.7)-Cu(10)/SiO₂

Species	Temp / K	Amt. / μmol g ⁻¹
I	357.1	10.3
II	424.1	0.9
III	536.4	15.1
IV	668.1	17.4
V	827.7	0.9

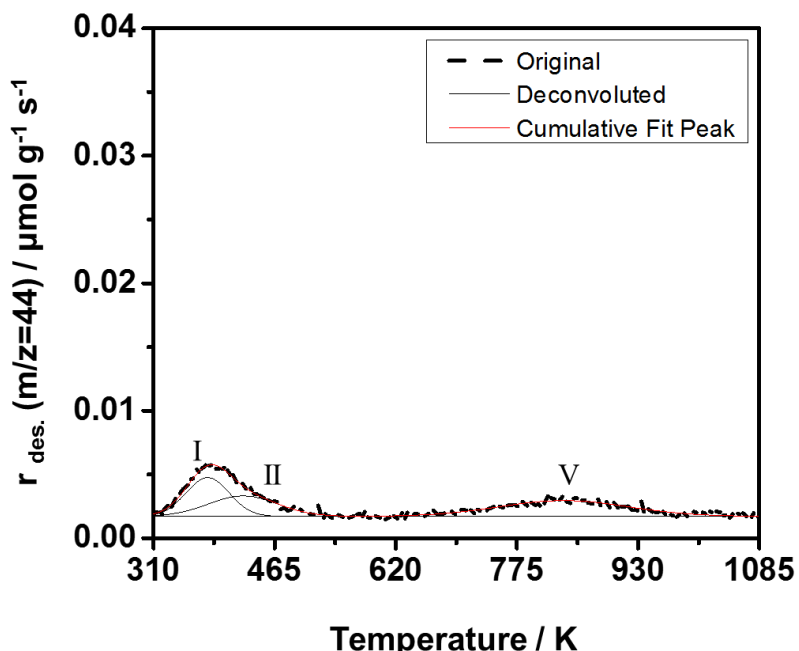


Figure H-8 Deconvolution of the CO₂-TPD profile of the bare support (amorphous silica). (---) measured TPD profile, (—) deconvoluted peaks, and red (—) cumulative fitting peaks.

Table H-7 Amount of adsorbed CO₂ species over the bare support (amorphous silica)

Species	Tempt / K	Amt. / $\mu\text{mol g}^{-1}$
I	379.3	1.3
II	424.7	1.1
V	835.1	1.5

Reference

- [1] L.F. Liotta, G.A. Martin, G. Deganello, J. Catal., 164 (1996) 322-333.

Appendix I Carbon Monoxide Temperature-Programmed Desorption (CO-TPD)

Data quantification is based upon the calibration of the TCD signal vs. the peak area of the pulse injection of a certain volume of 5 vol% CO/He in carrier gas (Ar). Before the pulse chemisorption, the system was allowed to heat up to 343 K under the flow of Ar (e.g., 30 mL min^{-1}) and maintained at this temperature for ca. 10 min. In the following step, 5 vol% CO/He was switched on to flush the system for another 10 min, then followed by the pulse chemisorption program. The pulse was controlled by the program automatically at a regular interval (e.g., 6 min). The pulses were generated by a 6-way valve connected with a 0.518 mL loop at 383 K, and the injection was operated at 343 K. The detailed procedure is depicted in Fig. I-1, and the resultant pulse signals are illustrated in Fig. I-2.

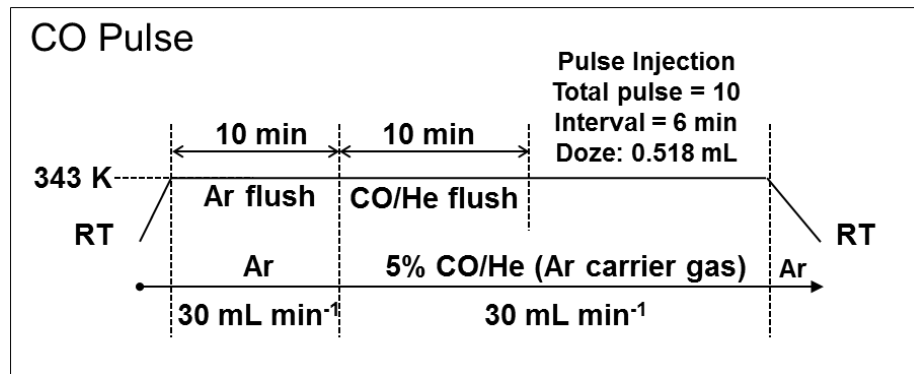


Figure I-1 A schematic illustration for the pulse injection of 5 vol% CO/He in Ar (carrier gas) at 343 K.

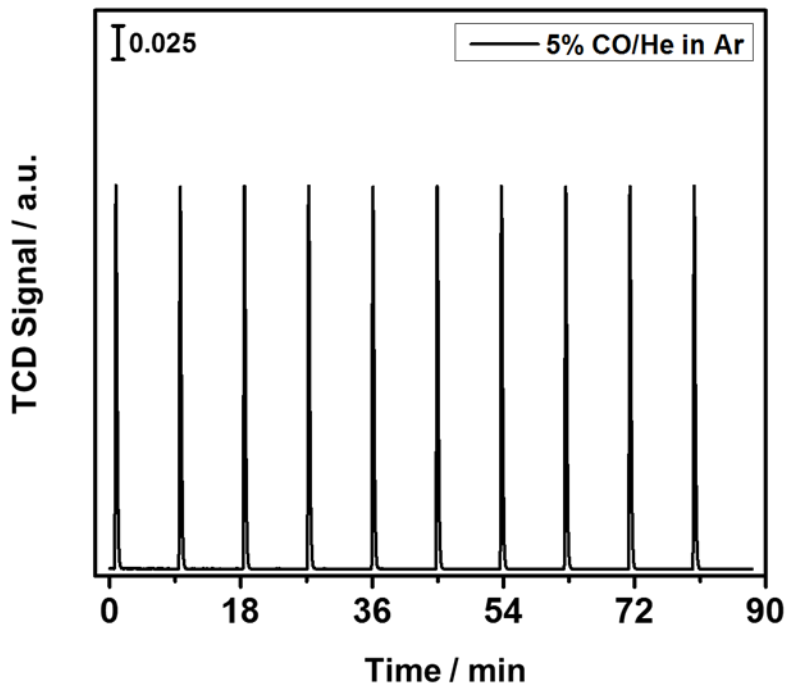


Figure I-2 Responses to 5 vol% CO/He pulses in Ar (carrier gas) at 343 K. Conditions: injection loop volume 0.518 mL (383 K), Ar flow rate 30 mL min⁻¹.

Actually, CO and He signals are indiscernible from spectrum because they merged as a single peak if the Ar was used as the carrier gas. In this case, the He pulse experiment was necessary to obtain the proportion of He superimposed with CO. The specific procedure and resultant pulse signals are depicted in Fig. I-3 and Fig. I-4, respectively. It is worth noting that the obtained average area for the He pulse signals were multiplied by 95% when it is taken back into the evaluation of its real area in the superimposed peak, because the proportion of He in the mixture gas CO/He was 95 %. As a result, in the CO pulse spectrum, the practical area for CO would be determined by subtracting the He part from the entirety.

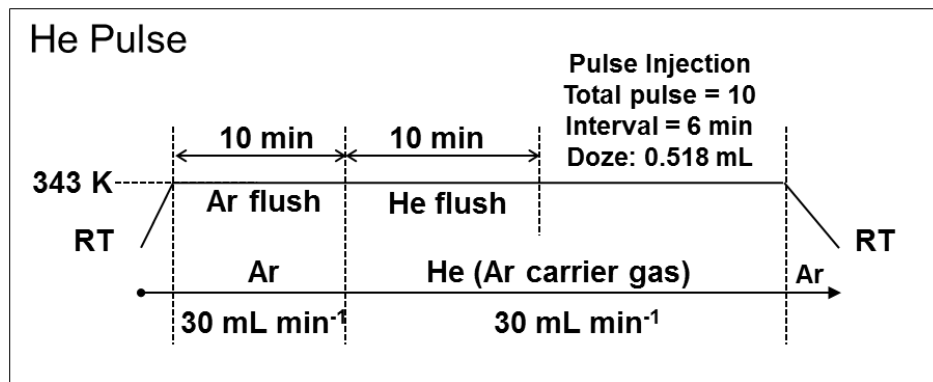


Figure I-3 A schematic illustration for the pulse injection of pure He in Ar (carrier gas) at 343 K.

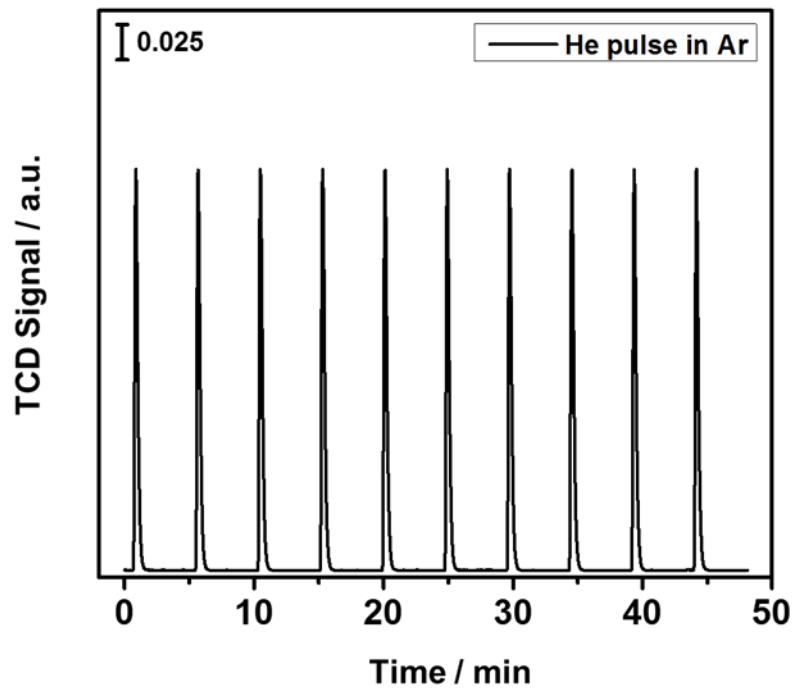


Figure I-4 Responses to pure He pulses in Ar (carrier gas) at 343 K. Conditions: injection loop volume 0.518 mL (383 K), Ar flow rate 30 mL min⁻¹.

Appendix J Mass Transfer Limitation

Before kinetic study of methanol synthesis over Pd-Cu bimetallic catalyst, it is important to confirm that the reaction takes place in a fully kinetic controlled regime and is free from mass transfer limitation. There exist experimental and theoretical methods to study the magnitude of the mass transfer processes in fixed bed reactors. In this work, the so called “Weisz-Prater criterion” is introduced for this purpose, and the relation is defined as to compare the rate of reaction to the rate of mass transfer to the active sites in the pores (see Equation J-1). The reaction can be considered as free of mass transfer limitation if the roughly estimated value is not greater 0.3. As recommended by Vannice [1], this method is particularly useful to evaluate the influence of pore diffusion on a catalytic reaction, because the dimensionless number defined hereby, N_{W-P} , only requires to obtain the parameters that can be readily measured or calculated from experiment. The detailed derivation and calculation procedure is described below.

$$N_{W-P} = \mathfrak{R} \cdot R_p^2 / (C_s \cdot D_{eff}) \quad \text{Equation J-1}$$

N_{W-P} : A dimensionless number from Weisz-Prater Criterion;

\mathfrak{R} : Conversion rate of a reaction reagent, unit: mol m⁻³ s⁻¹;

R_p : Radius of the largest particles, unit: m;

C_s : Bulk concentration of a reaction reagent, unit: mol m⁻³;

D_{eff} : Effective diffusivity of one reaction reagent, unit: m² s⁻¹.

The subsequent description only focus on the derivation and calculation of C_s and D_{eff} , because one can obtain both conversion rate and particle size from experiment directly. Specifically, parameters regarding to CO₂ is taken as an example.

J.I Bulk concentration of CO₂, C_s.

It is assumed that the bulk concentration of CO₂ equal the surface concentration, because the CO₂ conversion is low (~6.6 %), which is within the range for differential reactor. The bulk concentration of CO₂ could be calculated according to Equation J-2.

$$C_s = C_0 = N_{CO_2} / V = P_{CO_2} / RT \quad \text{Equation J-2}$$

C₀: Surface concentration of CO₂, unit: mol m⁻³;

N_{CO₂}: Mole of CO₂, unit: mol;

P_{CO₂}: Partial pressure of CO₂, unit: MPa;

R: Gas constant, unit: m³ Pa K⁻¹ mol⁻¹;

T: Reaction temperature, unit: K.

J.2 Effective diffusivity

J.2.1 Mean free path estimation

Typically, there are three different types of diffusion inside the pore based upon the governing collision between molecular species and the pore wall or molecular species itself, they are single-file diffusion, Knudsen diffusion, and molecular diffusion. In order to verify the diffusion type quantitatively, the mean free path of the reagent molecules was introduced and defined in the Equation J-3.

$$\lambda = \frac{1}{\sqrt{2}\pi \cdot \sigma^2 \cdot (N_{CO_2} / V)} = \frac{RT}{\sqrt{2}\pi \cdot \sigma^2 \cdot P_{CO_2}} \quad \text{Equation J-3}$$

λ: The mean free path, unit: m;

σ: CO₂ molecular diameter [2], nm.

J.2.2 Determine of effective diffusivity

The effective diffusivity is primarily dependent upon the comparison between the mean free path and the average pore diameter of the porous support material. In this work, the free mean path is close to the pore diameter for both CO₂ and H₂ (see Table J-2), the effective diffusivity is affected by the combinational influence of both bulk diffusion (D_b , Equation J-4) and Knudsen diffusion (D_{Kn} , Equation J-5). Therefore, the diffusivity would take the form of Equation J-6 (D_{eff}). It is worth mentioning that both bulk and Knudsen diffusivity are adjusted to take tortuosity ($\bar{\tau}$) and porosity (ε_p) into account, which are correction terms to show the “true” path of the molecular species inside the pores, especially in the case of amorphous silica with random pore structure. The corrected diffusivity is denoted as $D_{b,e}$ and $D_{Kn,e}$ for bulk and Knudsen diffusivities, respectively.

$$D_{b,e} = \frac{\varepsilon_p}{\bar{\tau}} \cdot \frac{\bar{v}\lambda}{3} \quad \text{Equation J-4}$$

$$D_{Kn,e} = \frac{\varepsilon_p}{\bar{\tau}} \cdot \frac{\bar{v}d_p}{3} \quad \text{Equation J-5}$$

$$D_{eff} = \frac{1}{\frac{1}{D_{b,e}} + \frac{1}{D_{Kn,e}}} \quad \text{Equation J-6}$$

$$\bar{v} = \sqrt{8k_B T / (\pi \cdot m)} \quad \text{Equation J-7}$$

$$m = M / N_A \quad \text{Equation J-8}$$

D_{eff} : Effective diffusivity, unit: m² s⁻¹;

$D_{b,e}$: Bulk diffusivity after correction with porosity and tortuosity, unit: m² s⁻¹;

$D_{Kn,e}$: Knudsen diffusivity after correction with porosity and tortuosity, unit: m² s⁻¹;

ε_p : Porosity, correction parameter;

$\bar{\tau}$: Tortuosity, correction parameter;

\bar{v} : Mean velocity of CO₂, unit: m s⁻¹;

d_p : Average pore diameter of support material, unit: nm;

k_B : Boltzmann's constant, unit: m² kg s⁻² K⁻¹;

m : The mass of molecular species (CO₂), unit: g

M : Formula weight (CO₂), unit: g mol⁻¹;

N_A : Avogadro constant, unit: mol⁻¹.

Since all parameters involved are either measurable or calculable, the W-P dimensionless number could be estimated according to Equation J-1. The detailed reaction conditions and values for each parameters are listed in Table J-1 and Table J-2, respectively.

Table J-1 Reaction conditions of CO₂ hydrogenation to methanol over Pd(8.7)-Cu(10)/SiO₂

Rxn cond. & conv.	Value	Catalyst	Value	Reactant	Value
Temperature / K	523	Catalyst bed height / mm	40	Total flow rate (STP) / mL min ⁻¹	12
Pressure / MPa	4.1	Catalyst load / g	0.2	CO ₂ flow rate / mol m ⁻³ s ⁻¹	1.476
CO ₂ composition	0.24	Mesh	60-200	H ₂ flow rate / mol m ⁻³ s ⁻¹	4.428
H ₂ composition ^{a)}	0.72	Max. powder size (R_p) / cm	0.0125	CO ₂ FW / g mol ⁻¹	44
Reactor diameter (ID) / mm	6.8	Pore diameter (d_p) ^{b)} / nm	12	H ₂ FW / g mol ⁻¹	2
CO ₂ conv. / %	6.6-7.0	ε_p ^{c)}	0.5	CO ₂ molecular size (σ_{CO_2}) ^{e)} / nm	0.33
		$\bar{\tau}$ ^{d)}	3	H ₂ molecular size (σ_{H_2}) ^{e)} / nm	0.29

^{a)} Ar (4 %) was introduced as an internal standard to estimate CO₂ conversion.

^{b)} The average pore diameter of pristine support was determined by N₂ physisorption analysis.

^{c)} Porosity is defined as the ratio of void volume within the pellet to the total pellet volume, and a reasonable estimate of this value is 0.5 (generally range: 0.3-0.7).

^{d)} Tortuosity accounts for the deviation in the path length of the pores, and a reasonable estimate for the amorphous silica with randomly oriented pores is approximately 3.

^{e)} Ref. [2].

After calculation, it is apparent that the dimensionless values (N_{W-P}) for CO₂ and H₂ are largely satisfied (<< 0.3), and consequently, it is concluded that the CO₂ hydrogenation to methanol over Pd(8.7)-Cu(10)/SiO₂ under current reaction condition is free from mass transfer limitation.

Table J-2 Parameter values in calculation of mass transfer effect

Parameter	CO ₂	H ₂
$C_s / \text{mol m}^{-3}$	226.30	678.90
$\lambda^{\text{a)}} / \text{nm}$	15.17 (~12)	6.55 (~12)
$\bar{v} / \text{m s}^{-1}$	501.75	2353.43
$D_{b,e} * 10^{-7} / \text{m}^2 \text{s}^{-1}$	4.23	8.56
$D_{Kn,e} * 10^{-7} / \text{m}^2 \text{s}^{-1}$	3.07	14.38
$D_{eff} * 10^{-7}^{\text{b)}} / \text{m}^2 \text{s}^{-1}$	1.78	5.37
$\mathfrak{R} / \text{mol m}^{-3} \text{s}^{-1}$	0.10	0.29
$N_{W-P} * 10^{-5}$	3.78	1.25

^{a)} The values in parentheses are the average diameters of support materials (d_p).

^{b)} The effective diffusivity is the combination of both bulk and Knudsen diffusion.

Reference

- [1] M.A. Vannice, Kinetics of catalytic reactions, Springer, New York, 2005.
- [2] D.W. Breck, Zeolite Molecular Sieves: Structure, Chemistry and Use, John Wiley & Sons, Inc., New York, London, Sydney, Toronto, 1974.

Appendix K Effects of Mesoporous Silica Supports and Alkali/Alkaline Earth Metal Promoters on the Activity of Pd-based Catalysts in CO₂ Hydrogenation for Methanol Synthesis

A major part of the text from this chapter appeared in the form of a published paper in Catalysis Today, volume 194, pages 16-24 in 2012 and was authored by Naoto Koizumi, Xiao Jiang, Junichiro Kugai, and Chunshan Song*. Most of the original version was reorganized and rephrased by the author Xiao Jiang, along with some complementary figures, tables, and discussions.

Abstract

Nano-structured Pd catalysts with enhanced CH₃OH synthesis activities for CO₂ hydrogenation were prepared by incorporation two factors, mesoporous silicas as support (MCM-41 and SBA-15) and alkali/alkaline earth metal additives as promoter. The introduction of the mesoporous silica gave rise to the confinement of small Pd nanoparticles inside nano-sized pores, while the alkali/alkaline earth metal additives were responsible for the improvement of the basicity of the catalysts, the combinational effect of which, thereby, resulted in the observed enhancement of CO₂ adsorption. Unpromoted Pd supported on these mesoporous silicas exhibited weak activities towards CH₃OH formation; in contrast, the addition of K, Mg and Ca significantly enhanced the activities. K(Ca)-promoted Pd supported on SBA-15 yielded 2-5 times more CH₃OH than the conventional amorphous silica supported Pd catalysts. Appropriate Ca/Pd molar ratio can promote the CH₃OH formation rate, however, excessive loading of CaO may lead to decline. TPR profiles indicated that the CaO was more likely to locate near the edge of Pd⁰ nanoparticles with

appropriate Ca/Pd molar ratio; however, larger Ca/Pd molar ratio may lead to the top coverage of Pd⁰ nanoparticles. The CH₃OH formation rate over the supported Ca/Pd catalysts varied as a function of the average pore diameter of the support and decreased in the order of MCM-41 > SBA-15 > MCM-48 > MSU-F ~ amorphous silica. In-situ Pd K-edge EXAFS and H₂ chemisorption measurements of the reduced catalysts demonstrated that small mesopores of MCM-41 and SBA-15 worked as a template to confine the growth of small Pd⁰ nanoparticles, leading to higher activities for CH₃OH formation compared to the amorphous silica supported counterparts. In addition, the quantitative analyses based on CO₂-TPD profiles demonstrated that the dispersion of CaO can be confined by the support SBA-15 with relatively small pore diameter, which may also have positive influences on CH₃OH formation by tuning the basicity of the catalysts. Based on detailed characterization results and their correlation with activity performances, it is suggested that the reaction may follow the bi-functional mechanism.

Key words; CO₂ hydrogenation, CH₃OH synthesis, Pd catalyst, Mesoporous silica, Alkaline promoter

K.1 Introduction

Utilization of CO₂ has become an important issue due to the significant and continuous rise of CO₂ concentration in atmosphere, which derives from both accelerated growth in the consumption of carbon-based energy worldwide and depletion of carbon-based energy resources [1]. The conversion of CO₂ would be more energy-demanding if one were to use only CO₂ as a single reactant. However, it becomes thermodynamically easier if CO₂ were used as a co-reactant with another substance such as CH₄, carbon and H₂ [2]. In this respect, the hydrogenation of CO₂ to CH₃OH is an attractive method for utilization of CO₂ as the carbon source for liquid fuels because CH₃OH can be used as a fuel for fuel cell as well as internal combustion engine.

Over the last two decades, significant efforts have been devoted to developing effective catalysts for the conversion of CO₂ to CH₃OH. These previous works mainly focused on improving the activity of Cu-ZnO-type catalysts which are widely used for CH₃OH synthesis from syngas (CO/H₂) [3]. The CH₃OH synthesis activity of this type of catalysts is enhanced by the addition of Cr₂O₃ [4-6], Ga₂O₃ [5-10] and ZrO₂ [5, 7, 10-14] as promoters. Saito *et al.* [7] reported that the multi component Cu/ZnO/ZrO₂/Al₂O₃/Ga₂O₃ catalyst yielded approximately 790 g kg-cat⁻¹ h⁻¹ of CH₃OH from CO₂ and H₂ under the reaction conditions of 523 K and 5.0 MPa. Several researchers also demonstrated that some precious metal catalysts, including Rh [15-17], Pd [18-25], Pt [26] and Au [27, 28], possessed the ability to hydrogenate CO₂ into CH₃OH as well, although productivities of CH₃OH with these catalysts are much smaller than those of the conventional Cu-ZnO based catalysts [22].

On the other hand, the formation of CH₃OH through the CO₂ hydrogenation is favorable thermodynamically at low temperatures and high pressures. The equilibrium yield of CH₃OH decreases with increasing the reaction temperature, and is only 14% under typical reaction

conditions of 523 K and 4.0 MPa for the Cu-ZnO based catalysts. Therefore, the development of a low-temperature CH₃OH synthesis catalyst, which can work at lower temperatures (e.g., ≤ 473 K), is an important issue for an efficient production of CH₃OH from CO₂. Supported Pd catalysts have been reported to be effective for CH₃OH formation from syngas at low temperatures [29]. Pd catalysts supported on La₂O₃ [30], Nd₂O₅ [30], and CeO₂ [31] can selectively hydrogenate CO into CH₃OH. Alkali and alkaline earth metals are also known as effective promoters for enhancing the CH₃OH synthesis activity of Pd/SiO₂ [32, 33]. Furthermore, Matsumura *et al.* [31] demonstrated that Pd/CeO₂ yielded 300 g kg-cat⁻¹ h⁻¹ of CH₃OH from syngas at 443 K and 3.0 MPa, whereas the Cu-ZnO catalyst required more severe reaction conditions, e.g., 503 K and 3.0 MPa, to yield comparable amounts of CH₃OH from syngas containing CO₂. Therefore, the Pd catalysts would be a potential candidate for the low-temperature CH₃OH synthesis catalyst via CO₂/H₂ as well as syngas. Thus, an improvement of their CH₃OH synthesis activity in CO₂ hydrogenation is an important challenge. So far, several researchers have reported that the CH₃OH formation rate over the supported Pd catalysts via CO₂ hydrogenation is enhanced in the presence of some metal oxide promoters, such as Ga₂O₃ [23, 24] and CaO [33], however, much less attention has been paid to the fundamental knowledge about CH₃OH synthesis over Pd-based catalysts from CO₂ hydrogenation compared to conventional Cu-ZnO based catalysts, e.g. the effects of supports, promoters, and Pd particle size.

Various kinds of mesoporous materials with unique pore structures have been synthesized recently. Due to their ordered channel structures, narrow pore size distribution, high surface area and pore volume, mesoporous materials attract great attentions as catalyst support materials. In particular, uniform pore structures of these mesoporous materials may provide nano-sized and uniform reaction environments which enable the stabilization of small metal nanoparticles inside

mesopores. In this connection, it is worth mentioning that a so-called bi-functional mechanism had been proposed for CH₃OH synthesis via CO/H₂ over the promoted Pd catalysts, where the metal oxide promoters stabilized adsorbed formate (or CO₂) species, a proposed important intermediate for methanol synthesis, and metallic Pd dissociates H₂ molecules simultaneously [23, 33]. Thus, the activity enhancement for CH₃OH formation would be expected when both small Pd and metal oxide nanoparticles are incorporated inside mesopores of the mesoporous materials. Therefore, an introduction of a nano-structured mesoporous support materials is of great interest in the view of improving the CH₃OH synthesis activity of promoted-supported Pd catalysts. On the other hand, if the size of Pd nanoparticles were able to be controlled systematically by mesoporous materials with different pore diameters, these catalysts would also become an interesting model catalyst. Although some research groups have already shown that the use of mesoporous silica enhanced the activity for hydrodesulfurization of dibenzothiophene [34], Fischer-Tropsch synthesis [35], and H₂O₂ synthesis [36] as supports, their utility in CO₂ hydrogenation to CH₃OH is still very limited.

In the present work, new Pd-based catalysts were prepared by incorporating two different promotion factors, i.e., introductions of nano-structured mesoporous silicas as supports and alkali/alkaline earth metal oxides as promoters. MCM-48, MCM-41, SBA-15 and MSU-F were used as mesoporous supports because of their typical pore structures, and K, Mg and Ca oxides were selected as promoters to improve the basicity of the catalyst. Cooperative effects of nano-structured mesoporous supports and alkali/alkaline earth metal additives on the CH₃OH synthesis activity and selectivity were studied under typical conditions (e.g., 523 K, 4.1 MPa) using a fixed bed reactor system. The effects of pore structures and Pd dispersion on CH₃OH formation from CO₂ were also investigated by various characterization techniques.

K.2 Experimental

K.2.1 Support materials

MCM-48, MCM-41, and SBA-15 were prepared in accordance with the procedures reported previously [37-39], and detailed preparation procedures for these mesoporous silicas were described in Appendix A for clarity.

Amorphous silica, Davisil Grade 645 (particle size=150-250×10⁻⁶ m), was used as a support for reference, and MSU-F (cellular form) was purchased from Aldrich. Physical properties of these support materials determined by N₂ physisorption technique are summarized in Table K-1.

K.2.2 Preparation of Pd catalysts

Supported Pd catalysts were prepared by a pore filling incipient wetness impregnation method. Aqueous solutions of Pd(NO₃)₂ (Aldrich) and Pd(NH₃)₄(NO₃)₂ (Alfa Aesar, Pd=3.162 wt%, Density=2.01 g cm⁻³) were used as Pd precursors. Herein, these precursors are simply denoted as PN and PTAN, respectively. Before preparation, incipient pore volumes of each support were measured by water, and corresponding parameters are referred to Appendix B. For comparison, concentrations of Pd in precursor solutions were adjusted according to the incipient pore volume of each mesoporous silica so that the Pd loading of the catalysts, prepared from different support materials, was maintained the same. The impregnated sample was then dried at 333 K for 2 h in a rotary evaporator followed by 393 K for 12 h in an electric oven and finally calcined in an electric furnace at 673 K for 2 h under flowing dry air (ca. 100 mL (NTP) min⁻¹). In the preparation of promoted catalysts, aqueous solutions of K, Mg and, Ca nitrate aqueous solutions (Aldrich) were impregnated on the calcined Pd catalyst followed by drying and

calcination under the same conditions. In order to study the effect of preparation sequence on methanol synthesis, some of the promoted catalysts were impregnated by a reverse order as well, namely impregnating promoter precursor solutions first followed by Pd precursor solutions. The Pd loadings of the catalysts prepared from PN and PTAN solutions were 4 and 5.7 wt% (support weight basis), respectively, while the molar ratio between promoter and Pd varied from 0 to 1.0. As bench mark, a commercial Cu-ZnO-Al₂O₃ catalyst (MDC-3, Süd-Chemie, 40 mass%-Cu) was also applied in activity tests, and the resultant activity performance was compared with the promoted Pd-based catalysts.

The catalysts are denoted as Ca(X)/Pd(Y)/support from this chapter, where X and Y represent the Ca/Pd molar ratio and Pd loading, respectively. The element, denoted next to support, was impregnated first. For those samples prepared by reverse order, the values in the parenthesis next to promoter always represented molar ratio, while the values next to palladium were active metal loading on support weight basis.

K.2.3 Activity test

The prepared catalysts were tested under pressurized conditions using a fixed bed reactor system consisting of a stainless steel tube with an internal diameter of 6 mm, which was placed in an electrically heated oven. The schematic diagram of the fixed-bed flow reactor system has been displayed in Fig. K-1.

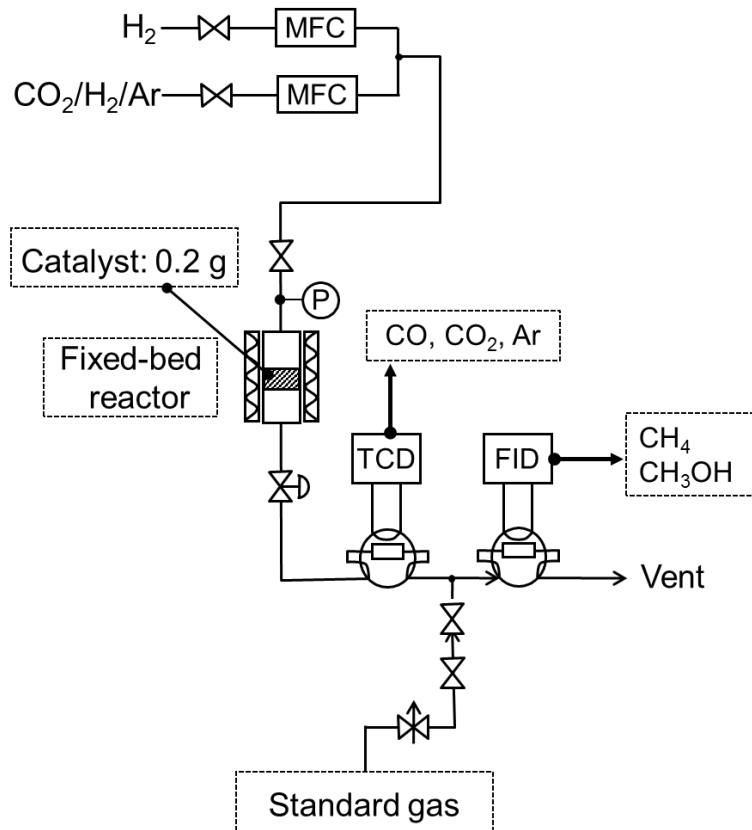


Figure K-1 Schematic diagram of the fixed-bed flow reactor system for CO_2 hydrogenation.

The gases, H_2 (99.995%) and $CO_2/H_2/Ar$ (24/72/4 in vol%, 99.995%) were used without further purification. The flow rate and pressure of these gases were regulated with mass flow controllers and a backpressure regulator, respectively. The amount of catalyst used in a typical run was 0.20 g. The amorphous silica supported catalysts were diluted by inert amorphous silica particles (~0.42 g) of the same size to attain aspect ratio of approximately 6.0; other mesoporous silica supported catalysts with lower densities (e.g., SBA-15, MCM-41, and MSU-F) were not diluted. In a typical reduction procedure, catalysts were heated up to 573 K in a stream of H_2 at a ramp rate of 2.3 K min^{-1} and then maintained under isothermal condition (573 K) for 2 h. After H_2 reduction, the temperature was reduced to ambient temperature. The feed gas $CO_2/H_2/Ar$ was then employed to pressurize the system to 4.1 MPa (GHSV=3600 mL(STP) g-cat $^{-1}$ h $^{-1}$) and the reactor

system was heated to desired temperature at a ramp rate of 1.9 K min⁻¹ for the catalytic reaction.

Gaseous products were periodically sampled with computer-controlled gas samplers and analyzed by two online GCs (SRI8610C). The online GC/TCD was used to analyze Ar, CO and CO₂, while the other online GC/FID was for CH₃OH and CH₄. Ar was an internal standard to estimate CO₂ conversion, and CH₄ was employed as an external standard for measuring methanol formation rate.

The catalysts studied in this work yielded only CO and CH₃OH as carbon containing products under the reaction conditions (i.e., 523 K and 4.1 MPa). The CO₂ conversion, as well as the formation rates of these products, decreased slightly with time on-stream, and reached fairly constant values at about 10 h on-stream. Therefore, the activity and selectivity of the catalysts were evaluated by the values obtained at about 12 h on-stream. The carbon balance was estimated according to the ratio between the simple summation of CO and CH₃OH formation rates and CO₂ conversion rate. All data published in this work lie within a reasonable range close to 100 mol%. Among all prepared Pd-based catalysts, Pd(5.7)/Ca(0.37)/SBA-15 showed a better methanol synthesis activity in the form of absolute formation rate, and the accuracy was ensured by 3 separate runs. The standard deviations for CO₂ conversion, CH₃OH formation rate, and CO formation rate over this particular sample were 0.1 %, 0.01 μmol g-cat⁻¹ s⁻¹, and 0.01 μmol g-cat⁻¹ s⁻¹.

K.2.4 N₂ physisorption

The N₂ adsorption-desorption isotherms for both prepared catalysts and pristine mesoporous materials were measured in a Micromeritics ASAP 2020 equipment. The samples (ca. 60 mg) were degassed at 523 K for nearly 12 h prior to analysis. Specific surface areas were estimated by using the B.E.T. approach. Pore size distributions were obtained by applying the

B.J.H. formalism to the desorption branches of the isotherms.

K.2.5 H₂ chemisorption

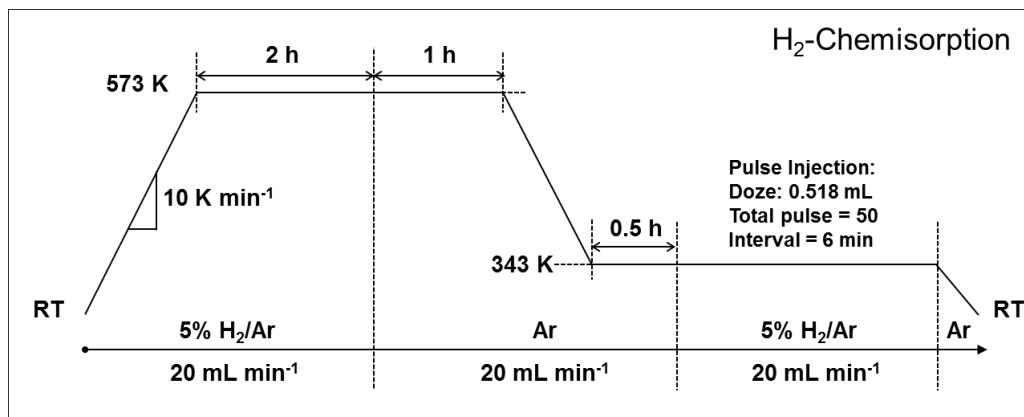


Figure K-2 A schematic illustration for hydrogen temperature-programmed reduction (H₂-TPR) over promoted and unpromoted Pd catalysts.

Dispersion of Pd was estimated by H₂ chemisorption technique and primarily acquired by using an Autochem 2910 TPD/TPR equipped with a TCD. Some of the data were also collected on Autochem 2920 TPD/TPR at the Materials Characterization Laboratory of the Penn State Materials Research Institute. Ametek Dycor Dymaxion mass spectrometer DM200M was employed for the detection of hydrogen pulse as well. Prior to the pulse injection, the calcined catalyst was reduced in situ in 5 vol% H₂/Ar at 573 K for 2 h followed by Ar flushing at the same temperature for 1 h. The catalyst was then allowed to cool down to 343 K, and 5 vol% H₂/Ar pulses were injected at regular interval. The real-time concentrations of all effluent gases were monitored by the mass spectrometer at the same time. The pulses were generated by a 6-way valve connected with a 0.518 mL loop heated at 383 K. A schematic illustration for the program is shown in Fig. K-2. Dispersion of Pd was calculated assuming H/Pd=1 chemisorption stoichiometry. Diameter of Pd particles (d_p) was then estimated from dispersion data assuming hemisphere morphology,

$$d_p = \frac{6 \cdot C_a \cdot PM \cdot 10^9}{\rho \cdot D \cdot N_{av}} \quad \text{Eq. K-1}$$

where the C_a concentration of surface metal atoms (1.27×10^{19} atoms m^{-2}), PM Pd atomic mass, ρ Pd volumetric mass (12.02×10^6 g m^{-3}), D metal dispersion, and N_{av} Avogadro number [40].

K.2.6 Temperature programmed reduction (TPR)

The temperature programmed reduction (TPR) experiments were conducted on a Micromeritics Autochem 2910 TPD/TPR equipped with a TCD. About 50 mg of sample was charged into the U-tube for every measurement. A typical temperature program process is illustrated in Fig. K-3, wherein the process used 20 mL min^{-1} of 5% H_2/Ar as reduction gas with the heating rate of 10 K min^{-1} . In order to quantify the hydrogen consumption, the silver oxide (II) was used as standard reference (Micromeritics). This standard sample has been tested twice, and the average maximum reduction peak shows at 457.7 K (see Appendix F for details).

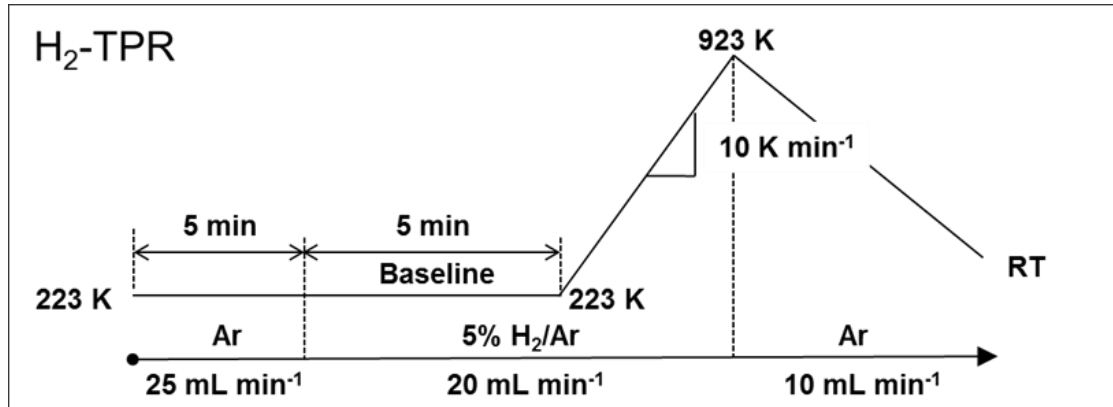


Figure K-3 A schematic illustration for hydrogen temperature-programmed reduction (H₂-TPR) promoted and unpromoted Pd catalysts.

K.2.7 *In-situ* Pd K-edge EXAFS

Pd K-edge EXAFS was measured at the insertion-device beam line of the Materials

Research Collaborative Access Team (MRCAT) at the Advanced Photon Source, Argonne National Laboratory. Details of the procedures and measurement conditions were reported elsewhere [41, 42]. Briefly, the X-rays passed through a cryogenically cooled double-crystal Si (111) monochromator in conjunction with an uncoated glass mirror to minimize the presence of higher harmonics, and focused onto the sample. The EXAFS data was collected in a transmission mode using I_0 and I ionization chambers filled with N₂/He and 20% Ar/N₂, respectively.

In-situ measurements were conducted using a continuous-flow EXAFS reactor cell (18 in. long, 0.75 in. diam.). Calcined catalyst samples were pressed into a cylindrical holder with a thickness chosen to give a total absorbance (μt) at the Pd K-edge (24.350 keV) of about 2.0 and an edge step ($\Delta \mu t$) of ca. 0.5, and then reduced in a stream of H₂ at 673 K for 2 h. After H₂ reduction, X-ray absorption spectrum at Pd K-edge was obtained at ambient temperature. The spectrum of Pd foil was acquired simultaneously with those of Pd catalysts for energy calibration. The observed Pd K-edge XAFS were analyzed in a conventional manner including background subtraction and normalization followed by Fourier filtering. Phase shift and back scattering amplitude of the Pd-Pd coordination shell were extracted from $k^3 \chi(k)$ of Pd foil, and were used for non-linear least square fitting analysis.

K.2.8 CO₂ temperature programmed desorption (CO₂-TPD)

CO₂-TPD was performed on an Autochem 2910 TPD/TPR instrument equipped with a TCD, and 10 vol% CO₂/Ar was introduced as probe molecules cylinder. Prior to CO₂ adsorption, the calcined sample was reduced in situ in 5 vol% H₂/Ar at 573 K for 1 h followed by cooling down to 523 K, where the reduced catalyst bed was flushed by He for 0.5 h to remove residual adsorbates. In the following step, CO₂ adsorption was carried out by switching to 10 vol% CO₂/Ar with the flow rate of 20 mL min⁻¹. After 1 h CO₂ adsorption, the system was allowed to cool down

to 323 K and flushed with He for another 1 h in the meantime. In the final TPD program, the system was heated up to 1173 K with the rate of 10 K min^{-1} . A representative program is illustrated in Fig. K-4.

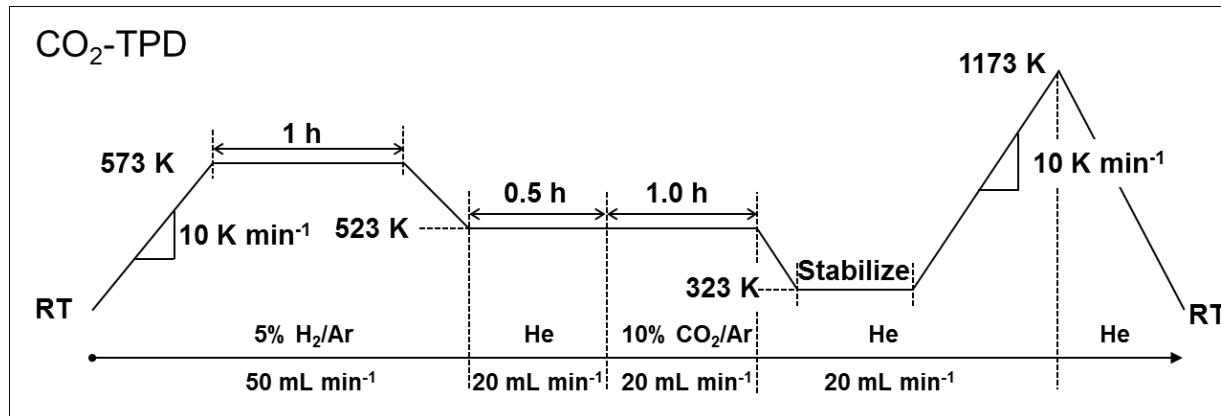


Figure K-4 A schematic illustration for carbon dioxide temperature-programmed desorption (CO_2 -TPD) over promoted and unpromoted Pd catalysts.

Data quantification is based on the calibration experiments which evaluated the peak areas of the pulse injection of 1 vol% CO_2/He in carrier gas (He). The pulse was controlled manually and injected at regular interval. The pulses were generated by a 6-way valve connected with a 1.0 mL loop at 298 K, and the injection was operated at 343 K. A detailed procedure is depicted in Fig. K-5, and corresponding pulse responses are shown in Fig. K-6. The sample, $\text{Ca}(0.37)/\text{Pd}(5.7)/\text{SBA-15}$, was tested twice, and the CO_2 uptake amounts were 104.5 and 109.6 $\mu\text{mol g}^{-1}$, respectively. Therefore, the data was repeatable with this procedure.

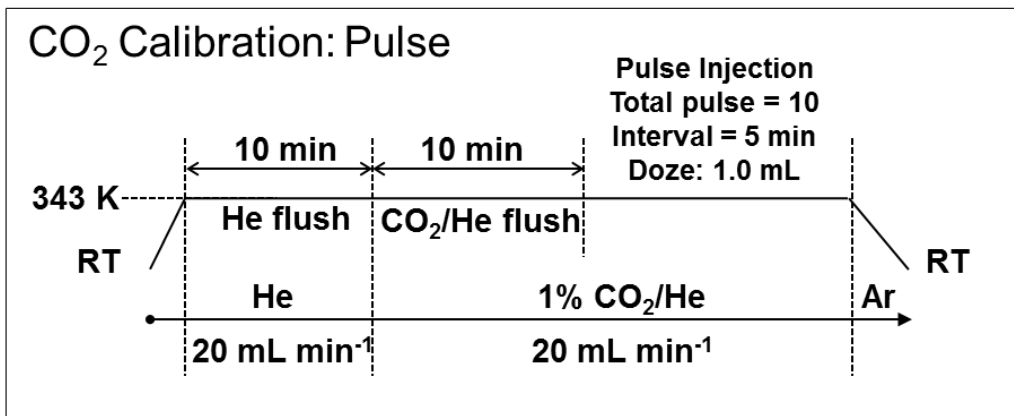


Figure K-5 A schematic illustration for the pulse injection of 1 vol% CO₂/He in He (carrier gas) at 343 K.

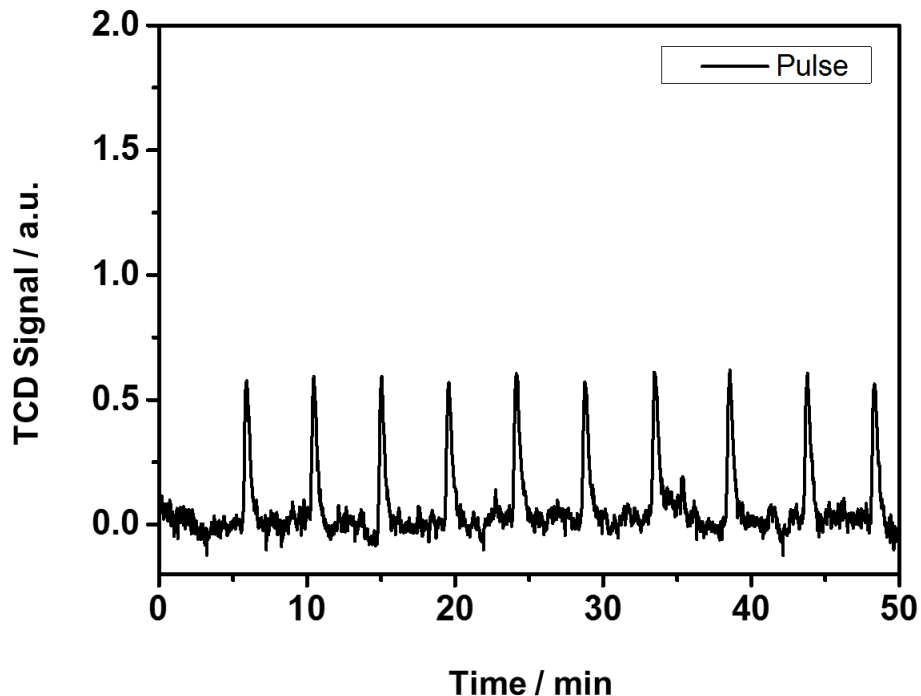


Figure K-6 Responses to 1 vol% CO₂/He pulses in He (carrier gas) at 343 K.

K.3 Results and discussions

K.3.1 Physical properties of Ca-promoted Pd catalysts

Physical properties of Pd catalysts supported on different mesoporous silica were

investigated by N₂ physisorption technique. The BET surface area, pore volume and average pore diameter of the Ca-promoted catalysts in the calcined form are summarized in Table K-1, and the BET surface area and pore volume of the calcined catalysts in the table were normalized to the weight of support because the support materials are the main component in each prepared catalyst. The values in the parentheses are the parameters for corresponding pristine support materials. All catalysts were prepared by PTAN precursor, the pH value of which is ca. 9-10 (see Table K-5). It was reported that ca. 25% of SBA-15 was found to be dissolvable in the precursor solution with pH=10 after 1 h exposure, which accompanies with the destruction of the pore structure, particularly for those mesoporous silica with relatively thin wall thickness, such as MCM-48 [43, 44]. As a result, the incipient wetness impregnation method was used to prepare the mesoporous silica supported Pd catalysts to avoid such effect.

Table K-1 Physical properties of Ca(0.37)/Pd(5.7) catalysts and support materials ^{a,b)}

Support	BET surface area / m ² g-support ⁻¹	Pore volume ^{c)} /mL g-support ⁻¹	Average pore ^{d)} diameter / nm
MCM-48	989 (1343)	0.6 (1.2)	2.7 (2.6)
MCM-41	867 (1185)	0.6 (1.4)	2.2 (3.4)
SBA-15	526 (850)	0.8 (1.1)	4.5 (5.7)
MSU-F	495 (611)	1.9 (2.5)	11 (13)
Amorphous SiO ₂	302 (313)	1.1 (1.1)	11 (11)

^{a)} Pd catalysts were prepared from aqueous Pd(NH₃)₄(NO₃)₂ solution.

^{b)} Values in parentheses are for support materials.

^{c)} BJH desorption cumulative pore volume.

^{d)} BJH desorption average pore diameter.

As listed in Table K-1, both BET surface area and pore volume of mesoporous silica reduce after impregnation of the precursor solutions. Such reductions are particularly significant when the

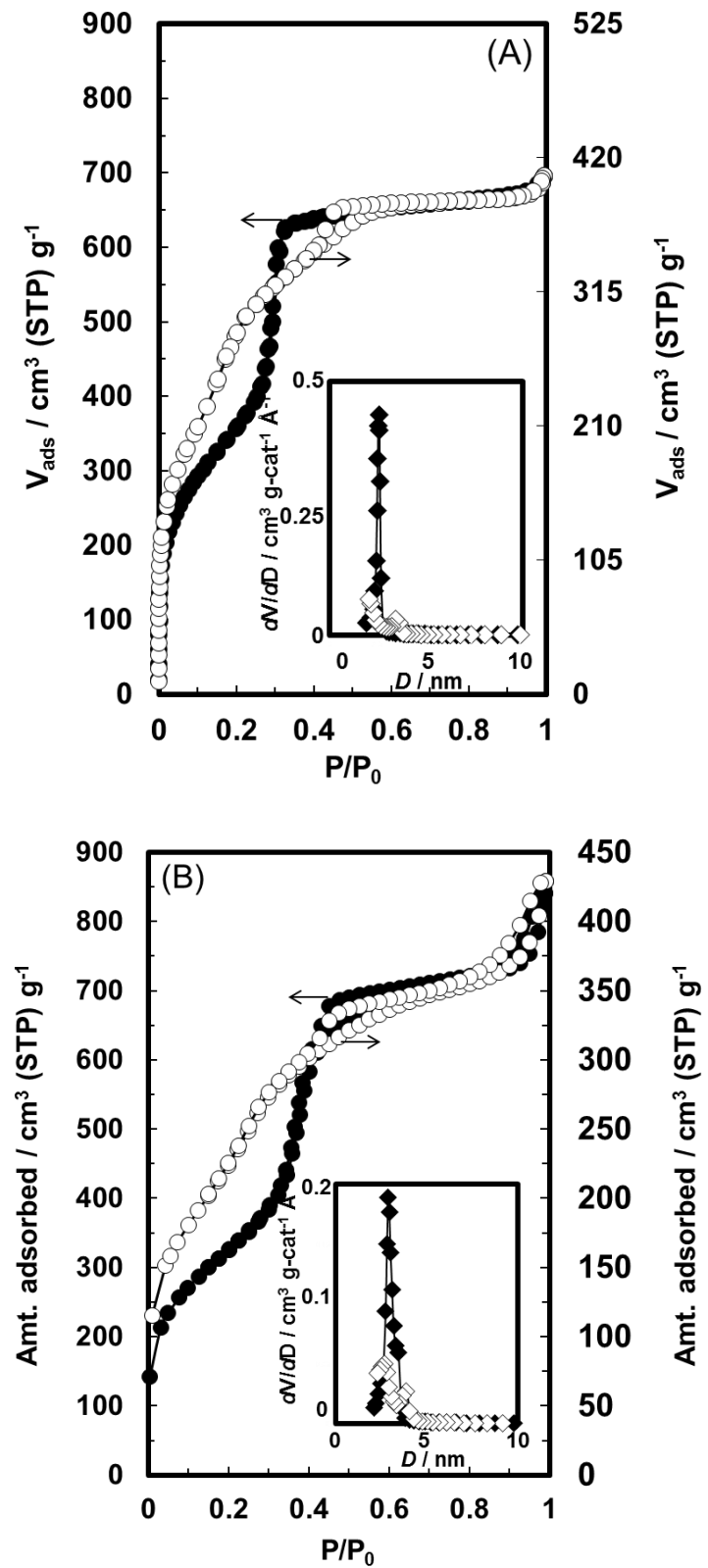
average pore diameter of mesoporous silica is smaller than 6 nm. On the other hand, the average pore diameter of these mesoporous silica, except MCM-48 and MCM-41, decreases by 1-2 nm after impregnation of the precursor solutions.

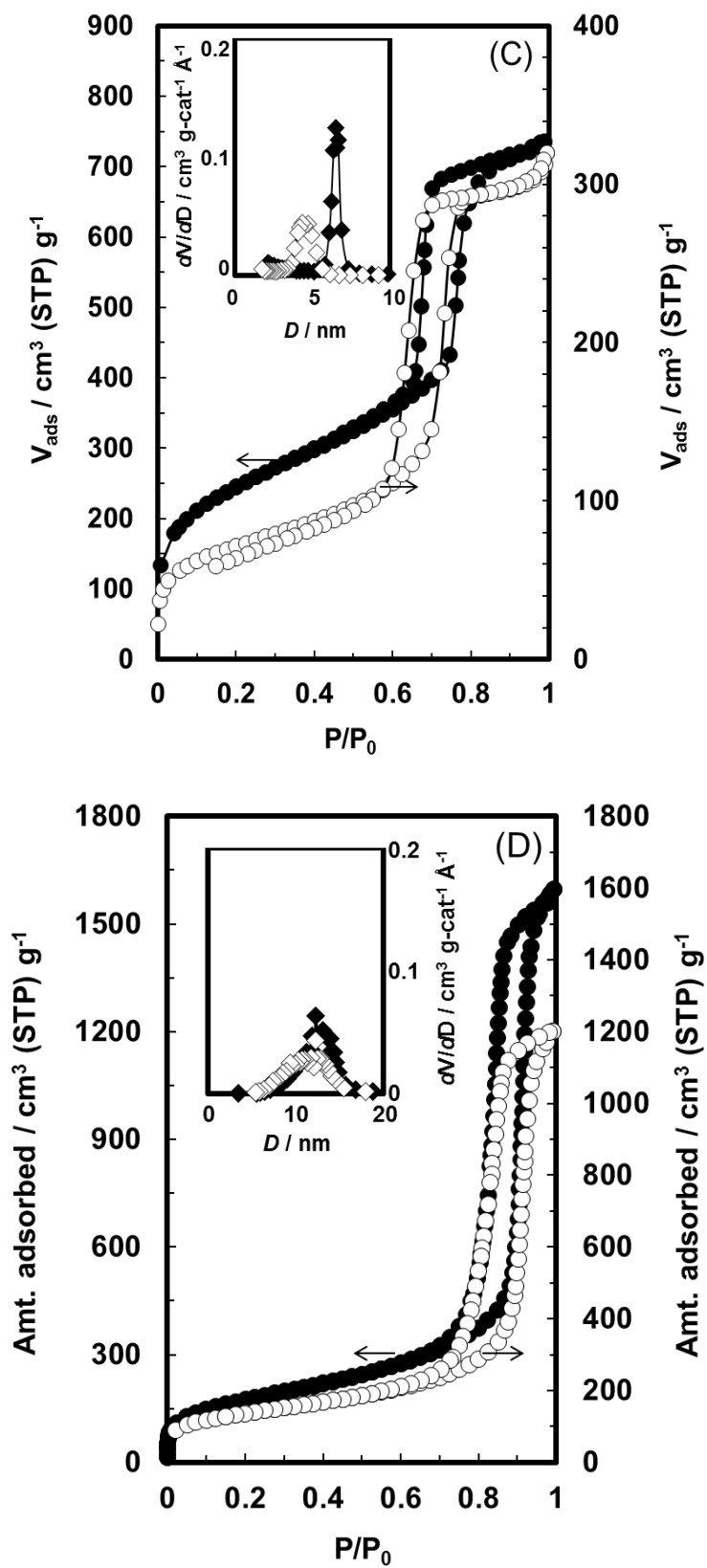
Fig. K-7A-E compares N₂ physisorption isotherms of calcined Ca(0.37)/Pd(5.7) catalysts and corresponding support materials. BJH desorption pore size distributions (PSD) of these samples are also shown in the insets of each figure. As illustrated in Fig. K-7A, the isotherm of calcined Ca(0.37)/Pd(5.7)/MCM-48 is inconsistent with that of pure MCM-48 in a wide relative pressure range. Besides, the PSD inset of this calcined sample hardly show distinct peaks compared to that of the pure MCM-48. These observations implies that the pore structure of MCM-48 has been disrupted to a large extent during the preparation, which can be ascribed to its thin thickness of the pore wall and low stability under high temperatures [43]. Similarly, the isotherm of MCM-41 supported Ca/Pd catalyst deviates from that of pristine MCM-41 (see Fig. K-7B); however, the deviation is not as severe as that observed for MCM-48 supported counterpart. The PSD inset of the MCM-41 supported catalyst exhibits a clear peak at ~2.2 nm, indicating that the destruction of the pore structure in the preparation is limited, and a large portion of the pore structure of MCM-41 is preserved after calcination. Contrarily, the isotherms of the SBA-15 (Fig. K-7C), MSU-F (Fig. K-7D), and amorphous silica (Fig. K-7E) supported Ca/Pd samples are similar to those of corresponding support materials. Moreover, their PSD figures in the insets also exhibit characteristic peaks. Thus, the pore structures of SBA-15, MSU-F, and amorphous silica are maintained during the catalyst preparation and even after calcination. In addition, from Fig. K-7B to K-7D, the peaks observed in the PSD of the promoted catalysts all shift toward lower values compared to those of corresponding pristine supports, demonstrating that the reduction of the average pore diameter probably results from the incorporation of Pd and Ca species into the

mesopores of support. In fact, EXAFS and H₂ chemisorption results reveal that the Pd particle sizes of these supported Pd catalysts are smaller than the pore diameters (except MCM-48 supported catalyst), which, thereby, indicates the incorporation of Pd species inside the mesopores. As reported, the isotherm exhibits two-step desorption branches when the hexagonal-template silica is plugged [45-47]; however, such phenomenon is not observed from the isotherms of MCM-41, SBA-15, and MSU-F supported catalysts. The absence of the two-step desorption branches is indicative of the preservation of a large portion of the pore structures after catalyst preparation, which are still accessible for N₂ adsorption. Moreover, it can also be deduced that Pd and Ca species are dispersed uniformly inside mesopores rather than agglomeration with its own species. Accordingly, compared to pristine support materials, the significant reductions of BET surface area and pore volume of the calcined catalysts are caused by the pore-mouth plugging during the preparation. Noticeably, the reductions of BET surface area and pore volume of MSU-F were less than SBA-15 and MCM-41. Probably, this can be attributed to the limited impact of pore-mouth plugging for MSU-F due to its relatively larger pore size. Unlike MCM-41, SBA-15, and MSU-F supported catalysts, amorphous silica supported Ca/Pd catalyst does not show distinct peak shift in the PSD (Fig. K-7E), even though the amorphous silica (ca. 11 nm) has a similar average pore diameter as MSU-F (ca. 13 nm). It appears that the different pore structures of MSU-F and amorphous silica cause such variation in physical properties.

N₂ physisorption measurement was also conducted on spent Ca(0.37)/Pd(5.7)/SBA-15, which was collected after CO₂ hydrogenation under pressurized conditions (523 K, 4.1 MPa, 12 h), and the corresponding isotherm is illustrated in Fig. K-7F along with the PSD in the inset. Evidently, both isotherm and PSD of the spent catalyst are practically identical to those of the fresh-calcined one, implying that the pore structure of SBA-15 is even preserved under the high-

pressure CO₂ hydrogenation conditions.





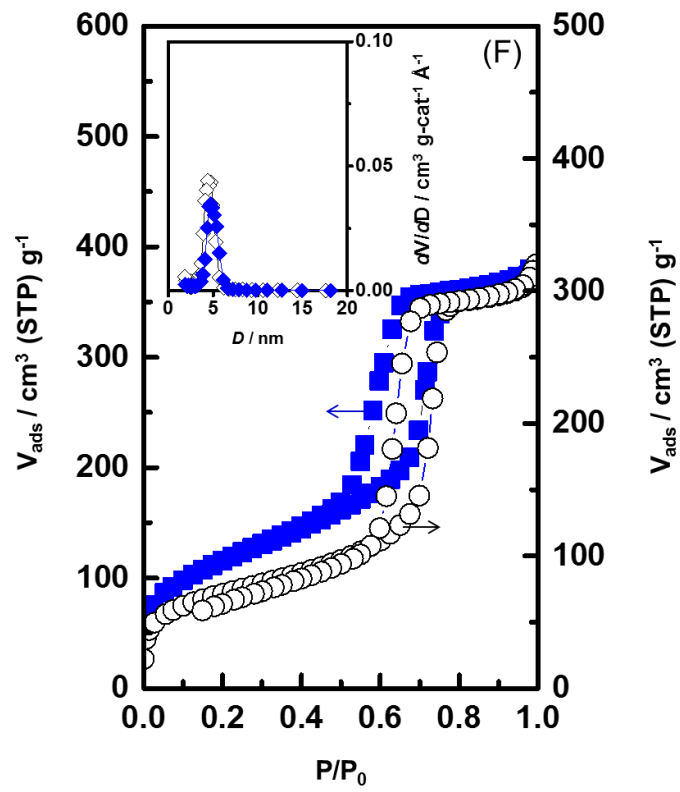
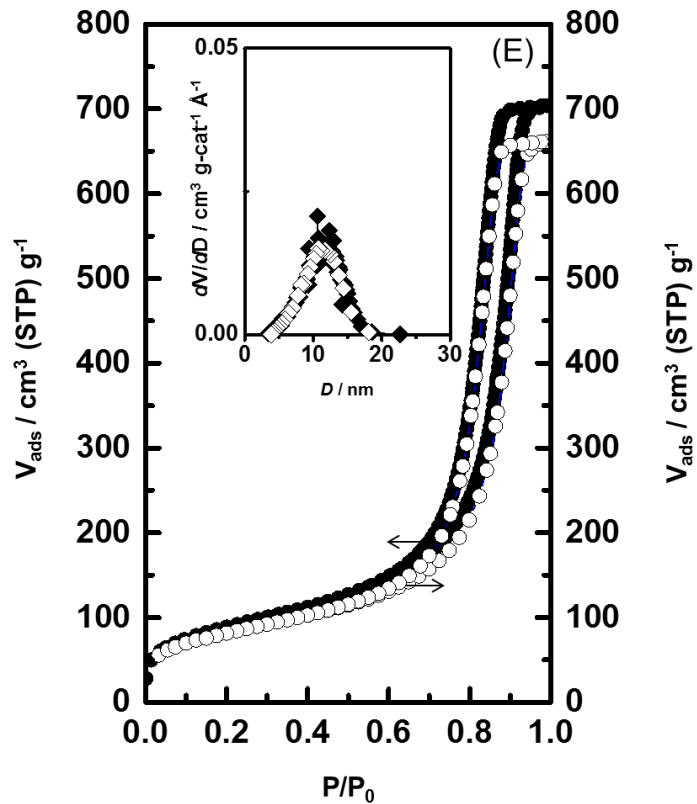


Figure K-7 N₂ adsorption isotherms (A-E) of support (solid symbol) and Ca-promoted Pd catalysts with a Ca/Pd molar ratio of 0.37 (open symbol): (A) MCM-48, (B) MCM-41, (C) SBA-15, (D) MSU-F, and (E) amorphous silica; (F) shows the isotherms of fresh (open symbol) and spent (solid symbol) Ca(0.37)/Pd(5.7)/SBA-15. Insets are BJH pore size distributions of corresponding supported Ca/Pd catalysts and pristine support materials.

K.3.2 Coordination environment

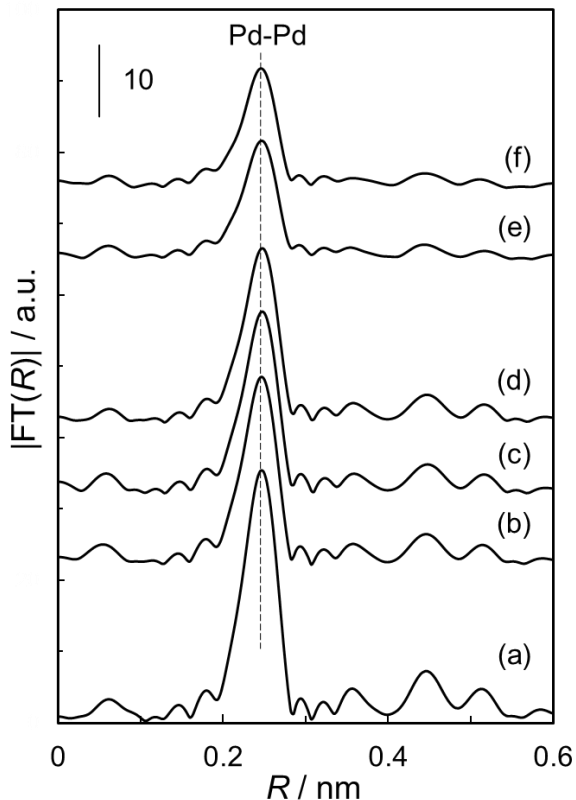


Figure K-8 In-situ Pd K-edge FT-EXAFS of promoted and unpromoted Pd catalysts prepared from PN precursor solution, showing the formation of small Pd⁰ nanoparticles on SBA-15 after H₂ reduction: (a) Pd foil, (b) Pd(4)/SiO₂, (c) Mg(0.5)/Pd(4)/SiO₂, (d) Ca(0.5)/Pd(4)/SiO₂, (e) Pd(4)/SBA-15, (f) Ca(0.5)/Pd(4)/SBA-15. H₂ reduction conditions: 673 K, 0.1 MPa.

Coordination environments of Pd species in the reduced catalysts were studied by in-situ Pd K-edge EXAFS. SBA-15 was chosen as a typical nano-structured mesoporous support, and Pd K-edge EXAFS of SBA-15 supported catalysts were compared with those of amorphous silica supported counterparts.

Fig. K-8 displays Fourier transformed $k^3\chi(k)$ (FT-EXAFS) of Pd catalysts supported on SBA-15 (e, f) and amorphous silica (b-d), respectively. As bench mark, the FT-EXAFS of Pd foil (a) is also included in the figure. The supported catalysts were prepared using the PN precursor solution, and some of these catalysts were promoted by Mg (c) and Ca (d, f) with the molar ratio (promoter/Pd) at 0.5 mol mol⁻¹. In the FT-EXAFS of Pd foil, a distinct peak is observed at about 0.24 nm (phase shift not corrected), which is ascribed to the Pd-Pd coordination shell of FCC (face cubic center) Pd. Such characteristic peak is found in the FT-EXAFS of the supported catalysts as well. Besides, no peak shift is seen regardless of the type of support or in the presence/absence of the promoters; however, the peak intensities of SBA-15 supported catalysts are not as intense as those of amorphous silica supported samples, as illustrated in Fig. K-8. Such difference may indicate that the dispersion of Pd⁰ is enhanced by the employment of SBA-15 with uniform pore structure instead of amorphous silica.

Table K-2 Structural parameters of Pd-Pd coordination shell for Pd catalysts prepared from aqueous Pd(NO₃)₂ solution

Catalyst	CN	R / nm	E ₀ / eV	DW ($\times 10^3$)	D _p / nm
Ca(0.5)/Pd(4)/SBA-15	8.2	0.273	0.0	1.0	3
Pd(4)/SBA-15	8.1	0.273	-0.2	1.0	3
Ca(0.5)/Pd(4)/SiO ₂	11	0.274	-0.1	0.5	7
Mg(0.5)/Pd(4)/SiO ₂	11	0.274	0.0	0.5	7
Pd(4)/SiO ₂	11	0.274	0.1	0.5	8
Pd ^{a)}	12	0.273	---	---	---

CN: Coordination number, R: Distance, E₀: Inner potential, DW: Debye-Waller factor, D_p: Size of Pd⁰ nanoparticles estimated from Pd-Pd coordination number

^{a)} From ref. [48]

Nonlinear least-square fitting analysis was then carried out to determine the structural

parameters of the Pd-Pd coordination shell for the supported catalysts, and the results are tabulated in Table K-2. The Pd-Pd bond distances determined are 0.274 nm and 0.273 nm for the amorphous silica supported catalysts and the SBA-15 supported ones, respectively, which are in agreement with the values from literature within the experimental error (± 0.003 nm) [48]. Moreover, note that the addition of Mg and Ca has little influence on the Pd-Pd bond distances and the coordination numbers, implying that these additives do not form alloy with Pd^0 nanoparticles after reduction. Indeed, the Ca-Pd alloy is thermodynamically unfavorable [49]. On the other hand, the Pd-Pd coordination numbers of the SBA-15 supported catalysts are evidently smaller than those of amorphous silica supported counterparts; moreover, the diameters of Pd^0 nanoparticles estimated from the Pd-Pd coordination number are 3 nm and 7 nm for the SBA-15 supported and amorphous silica supported catalysts, respectively, both of which are less than the corresponding average pore size of the support (see Table K-1). Thus, most of the Pd^0 nanoparticles can be located in the mesopores of the supports because the EXAFS results provide structural information averaged over the catalyst. In other words, the growth of Pd^0 nanoparticles can be confined by the mesopores of support, particularly in the case of SBA-15 supported catalysts, which shows even smaller particle size than amorphous silica supported counterparts. Therefore, the SBA-15 with unique and uniform pore structure exhibits better performance in the confinement of the Pd^0 nanoparticles than amorphous silica.

K.3.3 Pd^0 dispersion

The EXAFS results indicate that the Pd^0 nanoparticles can be incorporated inside the mesopores of supports; even though, it would be more convincing to be confirmed by other technique. Therefore, the H_2 chemisorption technique was carried out to estimate the particle size of Pd^0 in reduced catalysts as well as the Pd^0 dispersion which is very useful in the determination

of turnover frequency (TOF). The detailed calculation method has been described in the experimental section (see section K.2.5), and the amount of H₂ uptake and Pd⁰ dispersion are summarized in Table K-3. All samples, Pd loading=5.7 wt%, in the table were prepared by using PTAN as precursor, except the one with Pd loading=4 wt% (first line of the table), which was prepared from PN.

Table K-3 H₂ chemisorption results for Ca-promoted and unpromoted Pd catalysts

Catalyst	H ₂ uptake /μmol g-cat ⁻¹	Pd ⁰ dispersion / %	D _p ^{d)} / nm	TOF / h ⁻¹
Ca(0.5)/Pd(4)/SBA-15 ^{a)}	86.4	48	2.3	4.6
Ca(0.37)/Pd(5.7)/MCM-48 ^{b)}	99.2	42	2.6	2.5
Ca(0.37)/Pd(5.7)/MCM-41 ^{b)}	135.2	53	2.1	2.9
Ca(0.37)/Pd(5.7)/SBA-15 ^{b)}	104.4	40	2.8	3.3
Pd(5.7)/Ca(0.37)/SBA-15 ^{c)}	105.1	40	2.8	4.1
Ca(0.37)/Pd(5.7)/SiO ₂ ^{b)}	71.9	31	3.7	3.1
Ca(0.37)/Pd(5.7)/MSU-F ^{b)}	72.4	28	4.0	3.2
Pd(5.7)/SiO ₂ ^{b)}	82.0	32	3.5	1.5
Pd(5.7)/SBA-15 ^{b)}	122.5	47	2.4	0.1
Ca(0.19)/Pd(5.7)/SBA-15 ^{b)}	100.9	39	3.0	3.0
Ca(0.37)/Pd(5.7)/SBA-15 ^{b)}	104.4	40	2.8	3.3
Ca(0.50)/Pd(5.7)/SBA-15 ^{b)}	70.2	30	4.0	3.3
Ca(0.74)/Pd(5.7)/SBA-15 ^{b)}	67.9	25	4.4	4.0

^{a)} Pd(NO₃)₂ solution was used as precursor and was impregnated first.

^{b)} Pd catalysts were first prepared from aqueous Pd(NH₃)₄(NO₃)₂ solution.

^{c)} Ca(NO₃)₂ nitrate solution was impregnated first, and Pd(NH₃)₄(NO₃)₂ solution was used as precursor.

^{d)} Diameters of Pd⁰ particles were determined from Pd⁰ dispersion [40].

In order to study the confinement effect of support on Pd⁰ dispersion, the mesoporous silica with different pore structures were employed to prepare promoted Pd-based catalysts (Pd precursor: PTAN), and the corresponding H₂ chemisorption results are included in Table K-3. Clearly, the Pd⁰

dispersion changes depending upon the type of support, and the maximum Pd⁰ dispersion is obtained over the Ca/Pd catalyst supported on MCM-41 (ca. 50%) among the catalysts studied here. Table K-3 also contains chemisorption data for some unpromoted catalysts, such as SBA-15 and amorphous silica supported counterparts. Evidently, the addition of Ca promoter has a limited impact on Pd⁰ dispersion as evidenced by the observation of a slight decline. In fact, EXAFS data denies the possibility of alloy formation between Pd and Ca. Nevertheless, the TPR profiles, discussed in a later section, show that CaO is more likely to disperse beside/near Pd⁰ nanoparticles. Therefore, it is reasonable to speculate that the slight reduction of Pd⁰ dispersion can be ascribed to a slight-partial coverage on the edge regions of Pd⁰ nanoparticles due to the addition of CaO promoter. Additionally, it is also worth noting that the Pd⁰ dispersion is independent of the preparation sequence as the SBA-15 supported Ca/Pd and Pd/Ca reveal similar dispersion. Therefore, the coverage of the Pd⁰ nanoparticles in Ca/Pd catalysts is not severe.

Diameter of the Pd⁰ nanoparticles was then determined from the dispersion of Pd⁰ based on the assumption of hemispherical morphology, and the resultant values are tabulated in Table K-3 as well. Noteworthy, the sample Ca(0.5)/Pd(4)/SBA-15 was tested, and the results show that the particle size is about 2.3 nm which is in good agreement with the size estimated from in situ Pd K-edge EXAFS data (3 nm). Therefore, it is further confirmed that the Pd⁰ nanoparticle size of Ca(0.5)/Pd(4)/SBA-15, prepared from PN, is smaller than the average pore size of support SBA-15. In other words, most of the Pd⁰ particles are successfully incorporated inside the mesopores and their growth are confined by the uniform pore structure of SBA-15.

On the other hand, for those catalysts prepared from PTAN, the sizes of the Pd⁰ nanoparticles in the Ca/Pd/MCM-41 and Ca/Pd/SBA-15 are 2.9 and 4.1 nm, respectively, which approximate to the values in literature, e.g., Pd/MCM-41 (2.2 nm from Pd K-edge EXAFS) [50]

and Pd/SAB-15 (4.5 nm from TEM) [36]. Additionally, the diameters of the Pd⁰ nanoparticles in these Ca/Pd catalysts are smaller than the average pore diameters of corresponding support materials, further indicating that the Pd nanoparticles are incorporated inside the mesopores of support materials. These results are consistent with N₂ physisorption observations in section K.3.1. Furthermore, for those Ca/Pd catalysts prepared from PTAN precursor, the diameters of the Pd⁰ nanoparticles increase in the following order, Ca/Pd/MCM-41 < Ca/Pd/SBA-15 < Ca/Pd/SiO₂ < Ca/Pd/MSU-F, which increases similarly as the average pore size of the pristine support materials (Table K-1). As a result, it is deduced that smaller Pd⁰ nanoparticles are successfully obtained by introducing mesoporous silicas as support materials, particularly in the conditions with even smaller average pore diameters (e.g., < 6 nm). During the preparation, these small mesopores are filled with the Pd precursor solution, which confines the growth of Pd nanoparticles in the subsequent heat treatment and reduction. In other words, the small mesopores work as a template for the formation of small Pd⁰ nanoparticles. Unlike the other mesoporous silicas supported Ca/Pd catalysts, the Pd⁰ particle size of Ca(0.37)/Pd(5.7)/MCM-48 is similar to the average pore diameter of the MCM-48. Considering the N₂ physisorption data, it is suggested that the remaining pore structure of MCM-48 can still behave functional in the confinement of the Pd⁰ growth.

The effect of Ca/Pd molar ratio on chemisorption properties was also studied by testing a series of SBA-15 supported catalysts with the Ca/Pd molar ratio ranging from 0-0.74, and the corresponding chemisorption results are illustrated in Table K-3 as well. Clearly, higher Ca/Pd molar ratios lead to a gradual decline of both amount of H₂ uptake and Pd⁰ dispersion. Therefore, considering the fact that the promoter CaO is more likely to locate on the edge of Pd⁰ nanoparticles at Ca/Pd=0.37 (see TPR discussion), it is suggested that the addition of more CaO causes a severe coverage of large parts of Pd⁰ nanoparticles on the edge and even from the top. Such coverage may

result in the reduction of Pd⁰ dispersion.

K.3.4 Temperature-programmed reduction (TPR)

The TPR profiles for Ca-promoted and unpromoted Pd catalysts are shown in Fig. K-9. All samples were cooled down to cryogenic temperature (ca. 223 K) before the elevation of temperature program because Pd is susceptible to hydrogen even at ambient temperatures.

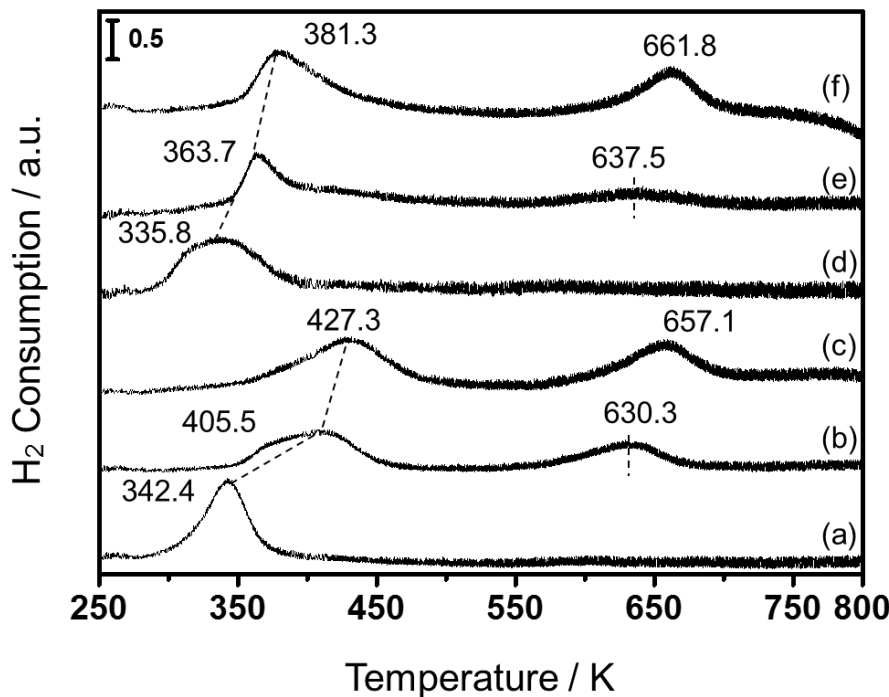


Figure K-9 TPR profiles of Ca-promoted and unpromoted Pd catalysts. The Pd loading for all samples was fixed at 5.7 wt% with PTAN as precursor, while Ca/Pd molar ratio ranged from 0.0 to 0.74 mol mol⁻¹. TPR conditions: 20 mL min⁻¹ of 5 vol% H₂/Ar flow, 10 K min⁻¹ of heating rate. (a) Pd/SiO₂; (b) Ca(0.37)/Pd/SiO₂; (c) Ca(0.74)/Pd/SiO₂; (d) Pd/SBA-15; (e) Ca(0.37)/Pd/SBA-15; (f) Ca(0.74)/Pd/SBA-15.

Fig. K-9a shows the TPR profile of the unpromoted Pd/SiO₂, and the maximum reduction peak is symmetric and centered at 342.4 K. A single-broad peak can also be observed at a similar temperature range for unpromoted Pd/SBA-15 with the same metal loading (see Fig. K-9d). These

two peaks signify the reduction of PdO. With the addition of CaO, two primary reduction peaks appear in the TPR profiles for both SiO₂ (Fig. K-9b to K-9c) and SBA-15 (Fig. K-9e to K-9f) supported catalysts. Among them, the peak at relatively lower temperature can be assigned to the PdO reduction because it shows reasonable H₂/Pd ratios (i.e., 0.9-1.1) [49]. The fact that the maximum reduction peaks of the corresponding Ca-promoted samples all shift towards higher temperature implies a retardation of PdO reduction. Furthermore, it is also noted that the higher Ca/Pd molar ratio is, the more the reduction peak shifts. These observations signify the interaction between CaO and Pd. One possibility is that the Ca-Pd alloy is formed during the reduction. Although such alloy is known to exist [51], it is thermodynamically unfavorable, because the Gibbs free energy for CaO reduction is 690 kJ mol⁻¹ at 723 K and 670 kJ mol⁻¹ at 1073 K [49]. Furthermore, as discussed in section K.3.2, the addition of Ca has little impact on neither Pd-Pd bond distance nor coordination number, which further excludes the formation of alloy. Another explanation may result from the partial coverage of PdO particles by CaO; however, this may accompany with a relevant question regarding to the location of CaO in the reduced catalysts. Prins and coworkers [49] proposed that CaO is preferentially located on and/or near Pd particles due to the affinity of CaO for Pd, such as the modification of electrons and/or reconstruction of Pd. Such conclusion may still be partially valid in this work because the reduction of PdO is evidently retarded with the addition of CaO. Besides, H₂ chemisorption data (see Table K-3) reveals that higher Ca/Pd molar ratio (i.e., > 0.37 mol mol⁻¹) clearly increases the Pd particle size compared to the unpromoted catalysts, however, such decline is limited with a lower Ca/Pd molar ratio (i.e., ≤ 0.37 mol mol⁻¹). Therefore, it is deduced that Ca prefers to locate in proximity to Pd particles, and the location is mainly dependent upon Ca/Pd molar ratio. Specifically, a lower Ca/Pd ratio primarily leads to the edge coverage of Pd particles, while a higher one may further cover more

active sites from the edge and even from the top.

Fig. K-9e shows that the peak shift of PdO (lower temperature) for SBA-15 supported Ca(0.37)/Pd sample is 27.9 K compared to the unpromoted sample. Such shift is even more considerable for the SiO₂-supported Ca(0.37)/Pd (see Fig. K-9b) than the corresponding unpromoted sample (e.g., 63.1 K). Furthermore, compared to the intense peak for Ca(X)/Pd/SBA-15, the amorphous silica supported sample exhibits a broader reduction peak. All of these observations suggest that the particle sizes of amorphous silica supported catalysts are not as uniform as those of SBA-15 supported counterparts. In Chapter 2, the TEM image of SBA-15 supported Pd-Cu bimetallic catalyst shows that the alloy particles disperse along with the 2D array of 1D channels (see Fig. 2-11A from Chapter 2), which may also occur in this chapter [52]. Additionally, recall that H₂ chemisorption results reveal a better active metal dispersion of Ca(0.37)/Pd(5.7)/SBA-15 than that of Ca(0.37)/Pd(5.7)/SiO₂. Accordingly, all of these results demonstrate that the unique 2D pore structure of SBA-15 not only confine the Pd particle growth, but also the promoter; however, the amorphous silica is in lack of such unique pore structure. In other words, within an appropriate range of Ca/Pd molar ratio (ca. $\leq 0.37 \text{ mol mol}^{-1}$), the location of promoter particles in the pores of SBA-15 may be confined sterically and more likely to locate near the active metal particles, particularly on the edge rather than on the top. As a result, the coverage of active metal over SBA-15 supported Ca/Pd catalyst is limited, thus resulting in the lower reduction temperature compared to amorphous silica supported counterparts with identical composition. Similarly, such explanation can also be applied to the observed less shift of Ca(0.74)/Pd(5.7)/SBA-15 (Fig. K-9f) than that of Ca(0.74)/Pd(5.7)/SiO₂ (Fig. K-9c).

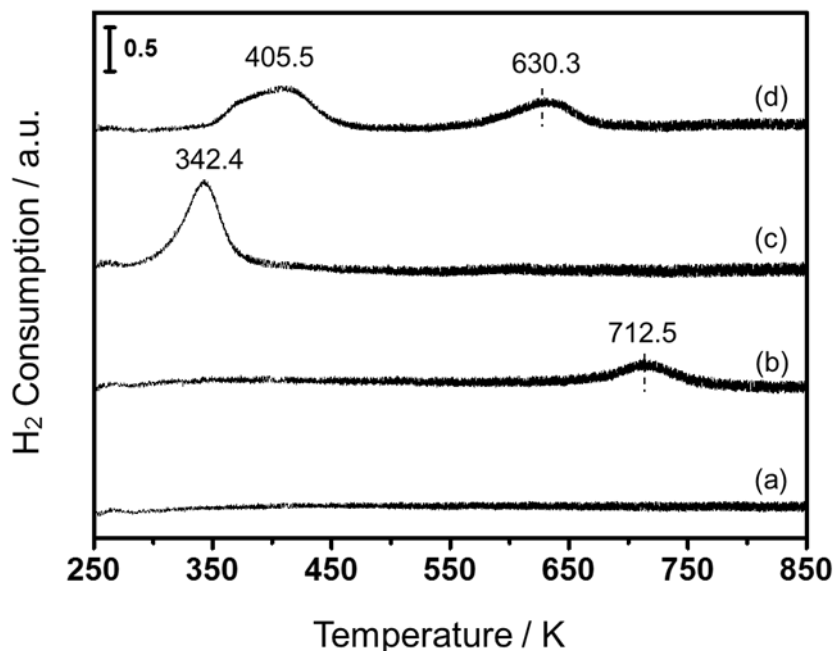


Figure K-10 TPR profiles of Ca-promoted and unpromoted Pd catalysts and bare support. (a) Amorphous SiO_2 ; (b) $\text{Ca}(0.37)/\text{SiO}_2$; (c) $\text{Pd}(5.7)/\text{SiO}_2$; (d) $\text{Ca}(0.37)/\text{Pd}(5.7)/\text{SiO}_2$. TPR conditions: 20 mL min^{-1} of 5 vol% H_2/Ar flow, 10 K min^{-1} of heating rate.

The addition of Ca also results in an additional broad peak centering at 633-653 K for both $\text{Ca}/\text{Pd}/\text{SiO}_2$ and $\text{Ca}/\text{Pd}/\text{SBA-15}$, and it is clearly sensitive to the Ca/Pd molar ratio. For clarification, the bare support (SiO_2) and Ca/SiO_2 were measured, and the resultant TPR profiles are compared in Fig. K-10. As expected, the bare support shows no reduction signals throughout the whole temperature range, while Ca/SiO_2 exhibits a single reduction peak at ca. 712.5 K. Therefore, it is suggested that the broad peak at 633-663 K over promoted samples is more likely relevant to CaO component rather than Pd. One possible explanation is that the surface basic sites of silica, such as hydroxyl group, may associate with CaO and adsorb CO_2 at ambient atmosphere to form carbonate, which, thereby, leads to the methylation at higher temperature (ca. $> 673 \text{ K}$); such hypothesis is evidently supported by the observation of CH_4 ($m/z=16$) from the mass spectrum simultaneously along with TPR program [49]. Based on this interpretation, CaO may also deposit

onto support, particularly in the condition of higher Ca/Pd molar ratio. Thus, it is suggested that only those CaO, close to PdO, can potentially promote CO₂ hydrogenation to methanol based on the proposed bi-functional mechanism [33]. This will be discussed in detail in section K.3.7.

K.3.5 CO₂ temperature programmed desorption (CO₂-TPD)

Table K-4 Quantitative data based on CO₂-TPD measurements over promoted and unpromoted Pd catalysts supported on either SBA-15 or MSU-F (Pd loading = 5.7 wt%)

Catalyst	Ca/Pd molar ratio / mol mol ⁻¹	CO ₂ uptake ^{c)} / μmol g ⁻¹	Mark
Pd/SBA-15 ^{a)}	0.00	30.9	
Ca/Pd/SBA-15 ^{a)}	0.37	104.5	
Ca/Pd/SBA-15 ^{a)}	0.37	109.6	Repeat
Pd/Ca/SBA-15 ^{b)}	0.37	219.4	
Pd/Ca/SBA-15 ^{b)}	0.37	204.9	Repeat
Pd/MSU-F ^{a)}	0.00	33.4	
Ca/Pd/MSU-F ^{a)}	0.37	71.6	

^{a)} Pd catalysts were prepared from aqueous Pd(NH₃)₄(NO₃)₂ solution which was impregnated first.

^{b)} Pd catalysts were prepared from aqueous Pd(NH₃)₄(NO₃)₂ solution, and Ca precursor was impregnated first.

^{c)} CO₂ uptake was estimated based on CO₂-TPD profiles.

As proposed, the addition of promoter is mainly responsible for the change of basicity of the catalysts, through which it assists to improve the adsorption of CO₂ during the reaction. Thus, in order to better understand the role of promoter (e.g., CaO) on CO₂ adsorption properties, the CO₂-TPD measurement was carried out over Ca-promoted Pd catalysts, and the corresponding data is summarized in Table K-4. Note that all catalysts in the table were prepared from PTAN precursor, and the Pd loading for all samples were fixed at 5.7 wt%. SBA-15 and MSU-F were selectively chosen as support materials because they possess significant differences in pore

structures, especially the average pore sizes.

Table K-4 shows that the unpromoted catalysts, Pd/SBA-15 and Pd/MSU-F, exhibit similar amounts towards the CO₂ uptake, which is helpful in excluding the interference from the support itself in the following analyses. With the addition of promoter CaO, the CO₂ uptake amounts for both SBA-15 and MSU-F supported Pd catalysts are improved substantially, particularly in the case of SBA-15 supported counterparts. The better CO₂ adsorption performance over SBA-15-supported catalyst can be attributed to the unique pore structure and smaller pore size. In fact, this is evidently consistent with the TPR results, which further confirms the pore structure and the average pore diameter of support materials may also behave as the template to confine the dispersion of the promoter particles.

Additionally, Table K-4 also includes the data for SBA-15-supported Ca/Pd catalysts but prepared in a different preparation sequence. It is noticeable that the catalyst with impregnating Ca first exhibits better CO₂ uptake than the one prepared by the reverse sequence. In other words, the preparation sequence significantly affects the dispersion of CaO and/or its interaction with the support. According to the mechanism of electrostatic adsorption, when the pH value of the precursor solution is below the point of zero charge (PZC) of the support material, the hydroxyl groups on the surface of support become protonated and thus are positively charged, thereby leading to the adsorption of anions; when the pH value of the precursor solution is above the PZC, the surface hydroxyl groups would be negatively charged and thus adsorb cations [53]. In order to further understand the effect of the preparation sequence on the CaO dispersion, the pH values of different precursors were roughly measured by the pH indicator strips (EMD Serono), and the corresponding values are summarized in Table K-5. Evidently, the pH values of both PTAN aqueous solution and calcium nitrate solution are above the PZC of the support SBA-15, wherein

the PTAN is more basic while calcium nitrate approaches neutral area. Besides, it was reported that the addition of nitrate precursor has limited impact on the PZC of silica [54]; however, the basic tetraammine-based metal complex leads to an increase of the PZC of silica from 4.0 to even higher than 7.0 [55]. Thus, it is deduced that the impregnation of Ca precursor first has little impact on the total PZC of support, which hardly affects the adsorption of $[Pd(NH_3)_4]^{2+}$ in the subsequent impregnation. Such postulation is evidently supported by the resemblance of both Pd dispersion and nanoparticle size over SBA-15 supported Ca/Pd and Pd/Ca catalysts (see Table K-3). On the other hand, the PZC of support can be dramatically changed with the first impregnation of PTAN precursor, which influences the adsorption of Ca^{2+} cations negatively during the subsequent impregnation. Therefore, the higher amount of CO_2 adsorption would be expected over the catalyst by impregnating Ca precursor at the beginning of the preparation.

Table K-5 Point of zero charge (PZC) of SBA-15 and pH values for precursors

Precursor solution ^{a)}	pH ^{d)}	pH _{PZC} value
$Ca(NO_3)_2$ ^{b)}	6-7	---
$Pd(NO_3)_2$ ^{b)}	1-2	---
$Pd(NH_3)_4(NO_3)_2$ ^{c)}	9-10	---
SBA-15	---	4.0 ^{e)}

^{a)} All precursor solutions used from this chapter were aqueous.

^{b)} Purchased from Sigma Aldrich.

^{c)} Purchased from Alfa Aesar (Pd=3.162 wt%, Density=2.01 g cm⁻³).

^{d)} pH values were roughly measured by pH indicator strips from EMD Serono.

^{e)} See reference [56].

K.3.6 Effects of support (SBA-15 & amorphous SiO_2) and promoters

N_2 physisorption and Pd K-edge EXAFS results indicate that Pd species are incorporated inside the mesopores of supports; moreover, SBA-15 supported catalyst exhibits better stability

during catalyst preparation and pressurized reaction than MCM-type supported Ca/Pd catalysts. Therefore, SBA-15 supported catalysts were chosen to study the effects of support and promoter in the CO₂ hydrogenation to methanol. As bench mark, the amorphous silica supported catalysts were also employed as reference. On the other hand, the influence of promoter was also investigated in this section. In the screening tests, the alkali/alkaline earth metals, such as K, Mg, and Ca, were employed as promoters because they were representative promoters in the CO/CO₂ hydrogenation, which function to change the basicity of the catalysts [33, 57-59]. Noteworthy, the sodium was excluded from the screening test because of its negative impact on methanol formation as reported elsewhere [60].

Table K-6 summarizes the CO₂ conversions, product selectivities, and product formation rates over the promoted and unpromoted catalysts, and PN solution was used as the precursor exclusively for all samples in the table. The maximum CH₃OH formation rate is observed over Ca(0.5)/Pd(4)/SBA-15 ($0.22\text{-}0.23 \mu\text{mol g-cat}^{-1} \text{s}^{-1}$), which is still less than the equilibrium value ($1.5 \mu\text{mol g-cat}^{-1} \text{s}^{-1}$). When the amorphous silica was used as the support, the CO₂ conversion over the unpromoted Pd(4)/SiO₂ is only 3%, and this catalyst yields $0.04 \mu\text{mol g-cat}^{-1} \text{s}^{-1}$ of CH₃OH with the selectivity of 12 mol%. It is noted that neither conversion nor products formation rates is changed by the addition of Mg into Pd(4)/SiO₂ based catalyst. Contrarily, the addition of K to Pd(4)/SiO₂ enhances the conversion by 1.7 fold, wherein the CO formation contributes exclusively. Unlike K's single promoting effect on CO formation, when Ca was introduced as the promoter, the formation rates of both CO and CH₃OH are enhanced simultaneously. Compared to Pd(4)/SiO₂, the promotion degrees of CH₃OH and CO formation rates over Ca/Pd/SiO₂ are ~ 50 % and ~ 60%, respectively. Thus, Pd(4)/SiO₂ exhibits a higher CH₃OH selectivity in the presence of Ca. On the other hand, Pd(4)/SBA-15 reveals weak activity towards CH₃OH formation in the absence of

promoters, and the formation rate of CH₃OH over Pd(4)/SBA-15 is less than 0.01 μmol g-cat⁻¹ s⁻¹. In contrast, K, Mg, and Ca-promoted Pd(4)/SBA-15 catalysts yield 16-24 times more CH₃OH than the unpromoted Pd(4)/SBA-15. Furthermore, the CH₃OH formation rates over these promoted catalysts are 2-5 times greater than those over the amorphous silica supported counterparts. Clearly, SBA-15, with the uniform pore structure, shows a great potential to benefit CH₃OH synthesis via CO₂/H₂ compare to amorphous silica under the same reaction conditions. In addition, the K and Ca-promoted catalysts were also prepared by a reverse order. As summarized in Table K-6, the CH₃OH formation rates are identical regardless of the order of impregnation. It is also worth mentioning that the maximum methanol formation rate is obtained in the case of Ca-promoted Pd/SBA-15 catalyst, thus, Ca nitrate precursor is used to prepare the promoted catalysts in the following studies exclusively.

Table K-6 Support effect of SBA-15 on CO₂ hydrogenation activity and selectivity over Pd and Cu-ZnO catalysts ^{a,b)}

Active metals	Support	CO ₂ conv. /%	Selec. / mol%		Formation rate / μmol g-cat ⁻¹ s ⁻¹	
			CO	CH ₃ OH	CO	CH ₃ OH
Pd(4)	SiO ₂	3	88	12	0.26	0.04
	SBA-15	< 1	86	14	0.03	< 0.01
K(0.5)/Pd(4)	SiO ₂	8	97	3	0.87	0.03
	SBA-15	14	89	11	1.44	0.19
Pd(4)/K(0.5)	SBA-15	13	89	11	1.46	0.18
Mg(0.5)/Pd(4)	SiO ₂	3	86	14	0.29	0.05
	SBA-15	3	60	40	0.24	0.16
Ca(0.5)/Pd(4)	SiO ₂	5	84	16	0.42	0.08
	SBA-15	7	31	69	0.54	0.22
Pd(4)/Ca(0.5)	SBA-15	6	63	37	0.39	0.23
40%Cu/ZnO/Al ₂ O ₃	—	18	73	27	1.26	0.48

^{a)} Pd catalysts were prepared from aqueous Pd(NO₃)₂ solution

^{b)} Reaction conditions: 523 K, 4.1 MPa

The methanol synthesis from CO₂/CO hydrogenation over Cu/ZnO-based catalysts were extensively studied in the last two decades [7, 61-65]. Thus, for the sake of comparison, the activity test was also conducted on a commercial catalyst Cu/ZnO/Al₂O₃ (MDC-3, Cu=40 wt%), and the activity performances are tabulated in Table K-6. Noticeably, the formation rates of CH₃OH over Ca(0.5)/Pd(4)/SBA-15 and Pd(4)/Ca(0.5)/SBA-15 were about 45% of that over the Cu/ZnO/Al₂O₃ catalyst, and such significant variation may result from the differences in metal loadings. Thus, the metal efficiency (metal time yield, MTY) is more appropriate to evaluate their real performances based on the metal loadings, where the real-time CH₃OH space time yield (STY) was normalized by the total amounts of active metal in each catalyst. After reprocessing, the MTYs are ca. 0.55 mmol mol-Pd⁻¹ s⁻¹ and 0.08 mmol mol-Cu⁻¹ s⁻¹ for Ca/Pd based catalyst and Cu/ZnO commercial catalyst, respectively. Therefore, the SBA-15 supported Ca/Pd catalyst exhibits higher metal efficiency for CH₃OH formation than the commercial Cu/ZnO/Al₂O₃ catalyst, even without taking the ZnO loading into consideration.

K.3.7 Effect of Ca/Pd molar ratio on CH₃OH formation

As discussed in section K.3.6, the incorporation of Ca promoter and SBA-15 with uniform pore structure is crucial for the observed enhancement of CH₃OH formation. In order to better understand the effects of the support and the additive, the activity tests were also conducted over Ca/Pd/SBA-15 catalysts with the Ca/Pd molar ratio ranging from 0-1.0 mol mol⁻¹. Amorphous silica supported Ca/Pd catalysts were also tested for reference. Two different Pd precursors, Pd(NO₃)₂ (PN) and ammine-based Pd(NH₃)₄(NO₃)₂ (PTAN), were used to prepare the catalysts. For comparison, the activity results were normalized by the mole of Pd loading which was maintained the same for every catalyst tested. The change of the Pd-time yield was plotted as a function Ca/Pd molar ratio, and the resultant figures are illustrated in Fig. K-11.

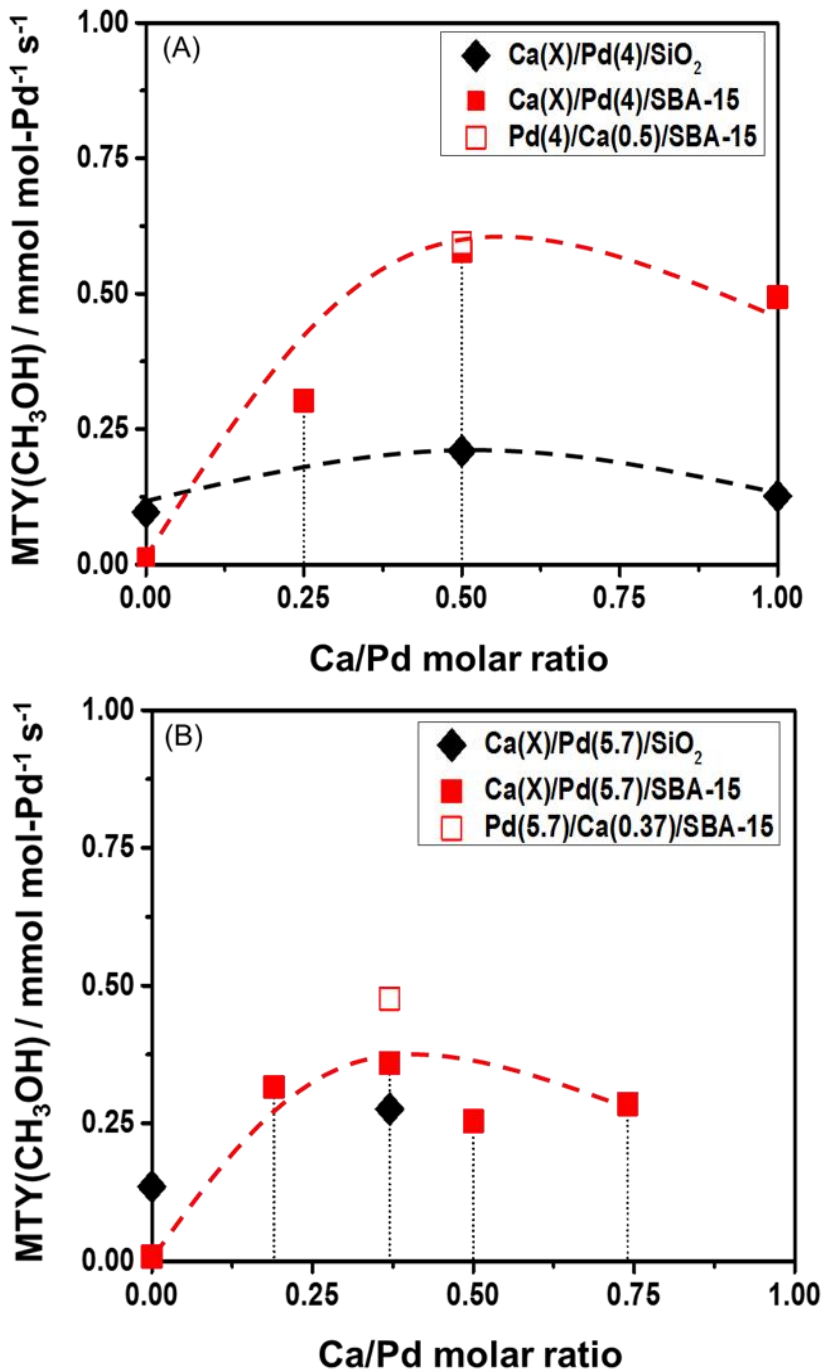


Figure K-11 Promoting effect of Ca on CH₃OH synthesis activity (Pd-time yield) for Pd catalysts supported on SiO₂ and SBA-15. All catalysts in (A) were prepared by PN precursor, and the Pd loading was fixed at 4 wt%; all samples in (B) were prepared by PTAN precursor with a fixed Pd loading of 5.7 wt%. CO₂ hydrogenation conditions: 523 K, 4.1 MPa, W/F=6.2-6.3 g h mol⁻¹.

Fig. K-11A illustrates the Pd-time yields of CH₃OH over Ca(X)/Pd(4)/SiO₂ and

$\text{Ca}(\text{X})/\text{Pd}(4)/\text{SBA-15}$ as a function of the Ca/Pd molar ratio. These catalysts were prepared by the PN precursor. The Ca/Pd molar ratio was varied by changing the Ca loading, whereas the Pd loading was fixed at 4 wt%. The Pd-time yield for SiO_2 supported Ca/Pd(4) catalysts maximizes at the Ca/Pd molar ratio of 0.5 and then declines with a continuous addition of Ca. The Pd-time yield for SBA-15 supported Ca/Pd(4) catalysts exhibits a similar tendency and maximizes at the Ca/Pd molar ratio of 0.4-0.5. Moreover, the best performance of Ca/Pd/SBA-15 catalyst yields 2-3 folds more CH_3OH than the Ca/Pd/ SiO_2 with identical compositions under the same reaction conditions. Thus, such promoter-induced activity enhancement is more remarkable for SBA-15 supported Ca/Pd catalysts than the amorphous silica supported counterparts. Noteworthy, the methanol formation rate over SBA-15 supported Ca/Pd catalyst is independent of the preparation sequence.

Similarly, such large activity enhancement is also observed for $\text{Ca}(\text{X})/\text{Pd}(5.7)/\text{SBA-15}$ from PTAN solution, as illustrated in Fig. K-11B. As reported, a significant activity enhancement was also observed in the CO hydrogenation to CH_3OH over the Ca-promoted Pd/ SiO_2 , and a so-called bi-functional mechanism had been proposed for this catalytic system: the promoter oxide is responsible for the CO_2 adsorption, while Pd could provide more active hydrogen for the subsequent hydrogenation [33]. Recall that EXAFS spectra show the existence of isolated Pd^0 nanoparticles, and TPR profiles suggest the proximity of CaO towards Pd^0 particles when the Ca/Pd lies within an appropriate range. These observations demonstrate that the promoter CaO and active metal Pd^0 may behave their own role towards the adsorption of reagents CO_2 and H_2 , respectively, and the close distribution of CaO and Pd^0 may further facilitate the subsequent hydrogenation. Accordingly, correlating the dependency upon Ca/Pd molar ratios observed from Fig. K-11 and detailed characterization results, it is suggested that the bi-functional mechanism is

still valid for the CO₂ hydrogenation to CH₃OH over Ca-promoted Pd catalysts in this work. Furthermore, compared to the amorphous silica supported Ca/Pd catalysts, the superior activity enhancement of SBA-15 supported counterparts indicates that the bi-functional mechanism works more effectively. This can be ascribed to the unique pore structure of SBA-15, which leads to the improvement of CaO dispersion as evidenced by the quantitative analyses based on CO₂-TPD profiles.

Additionally, it can also be noticed from Fig. K-11 that the maximum MTY(CH₃OH) of PTAN-based Ca(0.37)/Pd(5.7)/SBA-15 does not yield as much as that of PN-based Ca(0.50)/Pd(4)/SBA-15. Since the Pd⁰ dispersion of these two catalysts is similar as tabulated in Table K-3, the lower Pd-time yield form PTAN based catalyst may result from the lower dispersion of Ca species. As discussed in the section of CO₂-TPD, the pH values for PTAN and PN differ significantly (see Table K-5). On the other hand, the regular preparation sequence in this work begins with the impregnation of PN and PTAN precursor solutions, the variance of which may further reflect on the Ca-support interaction during the subsequent impregnation. Thus, a PTAN-based catalyst with a reverse impregnation order was prepared and also tested under the same reaction conditions. As depicted in Fig. K-11B, the Pd-time yield of this catalyst is clearly higher than that of Ca(0.37)/Pd(5.7)/SBA-15, but still slightly less than that of PN-based Ca(0.5)/Pd(4)/SBA-15 as shown in Fig. K-11A. Actually, such small difference may derive from different metal loadings because the STY of CH₃OH formed over PTAN-based Pd(5.7)/Ca(0.37)/SBA-15 is slightly higher than that over PN-based Ca(0.5)/Pd(4)/SBA-15 (i.e., $0.25 > 0.22 \mu\text{mol g}^{-1} \text{s}^{-1}$). Thus, Pd(5.7)/Ca(0.37)/SBA-15 actually exhibits the maximum absolute CH₃OH formation rates among the catalysts tested in Fig. K-11. Note that Pd(5.7)/Ca(0.37)/SBA-15 yields approximately $30 \text{ g kg-cat}^{-1} \text{ h}^{-1}$ of CH₃OH under the reaction conditions of 523 K and

4.1 MPa, which approximates the values reported for the Pd based catalysts under similar reaction conditions, ca. $35 \text{ g kg-cat}^{-1} \text{ h}^{-1}$ for Pd/CeO₂ [21, 22] and $37 \text{ g kg-cat}^{-1} \text{ h}^{-1}$ Pd-ZnO/CNT [25].

It is also worth mentioning that SBA-15 used in this work was prepared using alkali/alkaline earth metals-free conditions [36-38], while commercially available amorphous silica usually contains some impurities in ppm levels, such as alkali/alkaline earth metals [33, 66]. Therefore, the observed higher CH₃OH synthesis activity for unpromoted Pd(4)/SiO₂ compared to Pd(4)/SBA-15 can be attributed to the presence of such ppm-level impurities in amorphous silica.

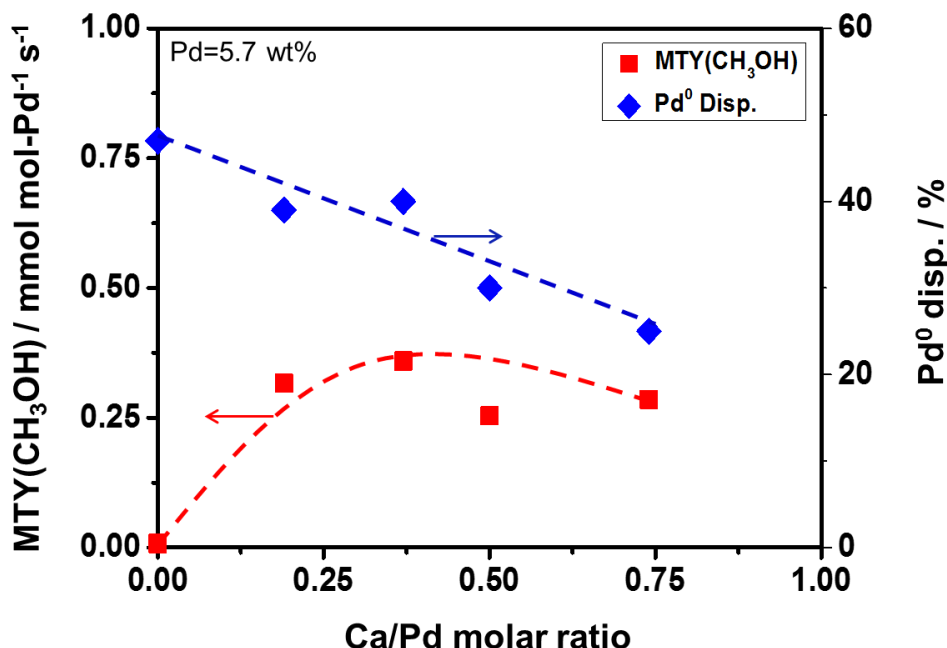


Figure K-12 Changes of CH₃OH formation rate in Pd-time yield and corresponding Pd⁰ dispersion as a function of Ca/Pd molar ratios. Reaction conditions: 523 K, 4.1 MPa, W/F=6.2 g h mol⁻¹.

In order to correlate the CH₃OH Pd-time yield with corresponding Pd⁰ dispersion, the H₂ chemisorption data over PTAN-based Ca(X)/Pd(5.7)/SBA-15 (see Table K-2) was also merged into Fig. K-11B, and the updated figure is replotted in Fig. K-12. Clearly, an addition of amount of Ca gradually causes a monotonic reduction of Pd⁰ dispersion, while the MTY reveals a volcano-

like curve with the addition of CaO. Therefore, considering the dispersion of CaO in proximity to Pd⁰ particles and its positive effect on CO₂ uptake, it is reasonable to deduce that the observed maximum CH₃OH formation rate is based on a tradeoff between the active sites for CO₂ adsorption and hydrogen chemisorption. In other words, a proper Ca/Pd molar ratio may provide optimal active sites for the adsorption of both reagents, which plays a critical role in the methanol promotion.

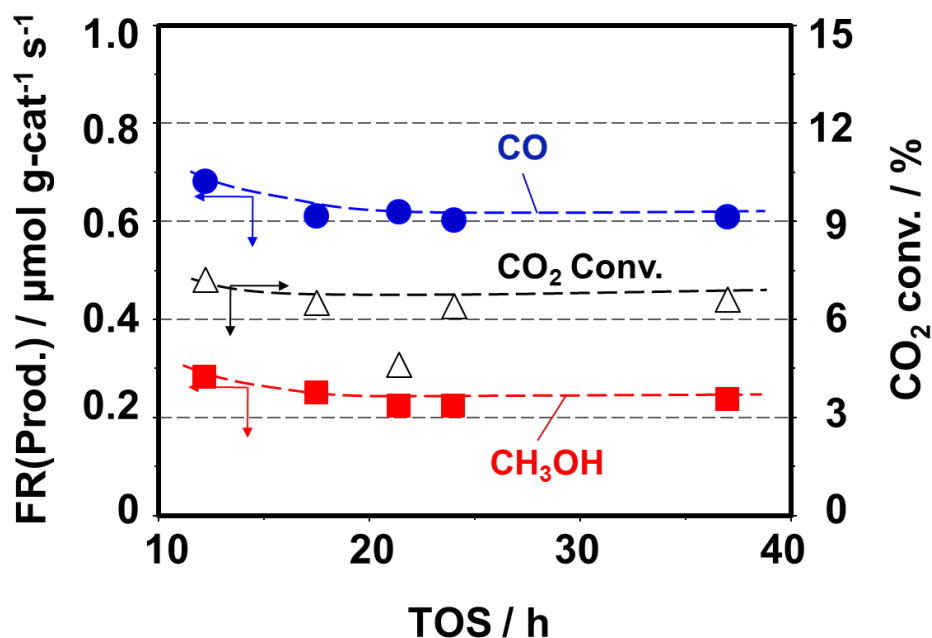


Figure K-13 The stability test of CO₂ conversion (open triangle) and formation rates of CO (closed circle) and CH₃OH (closed square) over PTAN-based Pd(5.7)/Ca(0.37)/SBA-15. CO₂ hydrogenation conditions: 523 K, 4.1 MPa, 6.2 g h mol⁻¹.

Fig. K-13 demonstrates the stability test of the CO₂ hydrogenation over PTAN-based Pd(5.7)/Ca(0.37)/SBA-15. Evidently, both CO₂ conversion and product formation rates are practically stable within the time on stream studied. Thus, no apparent deactivation of the CH₃OH synthesis activity is observed.

K.3.8 Impact of pore diameter

Table K-7 CO₂ hydrogenation activity and selectivity of Pd catalysts supported on mesoporous silica with different pore diameters ^{a-c)}

Support	Active metal	CO ₂ conv. /%	Selec. / mol%		Formation rate / $\mu\text{mol g-cat}^{-1} \text{s}^{-1}$	
			CO	CH ₃ OH	CO	CH ₃ OH
MCM-48	Pd	< 1	85	15	0.04	< 0.01
	Ca/Pd	4	72	28	0.44	0.17
MCM-41	Pd ^{d)}	—	—	—	—	< 0.01
	Ca/Pd	5	72	28	0.56	0.22
SBA-15	Pd	< 1	85	15	0.08	< 0.01
	Ca/Pd	4	69	31	0.44	0.19
MSU-F	Pd	1	81	19	0.11	0.03
	Ca/Pd	3	74	26	0.37	0.13
SiO ₂	Pd	3	82	18	0.31	0.07
	Ca/Pd	6	82	18	0.67	0.14

^{a)} Pd catalysts were prepared from Pd(NH₃)₄(NO₃)₂ aqueous solution.

^{b)} Reaction conditions: 523 K, 4.1 MPa, W/F=6.2 g h mol⁻¹.

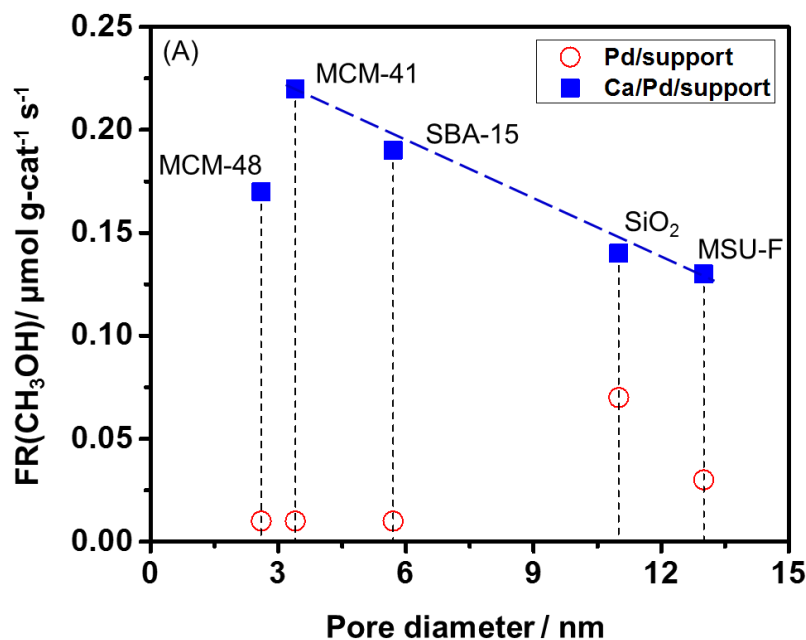
^{c)} General errors: Conversion: ~0.1%; CH₃OH formation rate: 0.01 $\mu\text{mol g-cat}^{-1} \text{s}^{-1}$; CO formation rate: 0.01 $\mu\text{mol g-cat}^{-1} \text{s}^{-1}$.

^{d)} TCD not measured due to low activity.

As discussed in a previous section, the SBA-15 supported Ca/Pd catalysts exhibits a more prominent activity toward CH₃OH synthesis than the amorphous silica supported catalysts, and such superior performance can be ascribed to the unique pore structure of the SBA-15 which can confine the dispersions of Pd⁰ particles and CaO. In this respect, it would be of great interest to investigate the influence of other mesoporous silicas on the methanol synthesis activity and its correlations with the average pore diameters. Thus, MCM-41, MCM-48, and MSU-F, were introduced to prepare Pd-based catalysts. MCM-41 has a hexagonal array of unidirectional pores, while MCM-48 has a cubic pore system (3D) [67]. More importantly, they possess even smaller pore diameters than SBA-15. On the other hand, MSU-F has a worm-like pore structure with even

larger pore diameter than the amorphous silica [68, 69]. For the sake of comparison, the PTAN precursor solution was used exclusively in this section because the catalyst Pd(5.7)/Ca(0.37)/SBA-15 exhibits a better absolute CH₃OH formation rate than other catalysts. Moreover, the Ca/Pd molar ratio and Pd loading were fixed at 0.37 mol mol⁻¹ and 5.7 wt%, respectively.

Table K-7 summarizes the activity performances over promoted and unpromoted catalysts. The formation rates of CH₃OH over the unpromoted catalysts, except Pd(5.7)/SiO₂, are extremely low regardless of the types of support materials. Contrarily, the CH₃OH formation rates over the promoted catalysts are enhanced significantly and decrease in the following order: MCM-41 > SBA-15 > MCM-48 > MSU-F ~ amorphous SiO₂. Besides, the CH₃OH selectivity of the promoted catalysts presents similarities (26-31%), implying that both CO and CH₃OH formation rates are improved simultaneously with the addition of promoter.



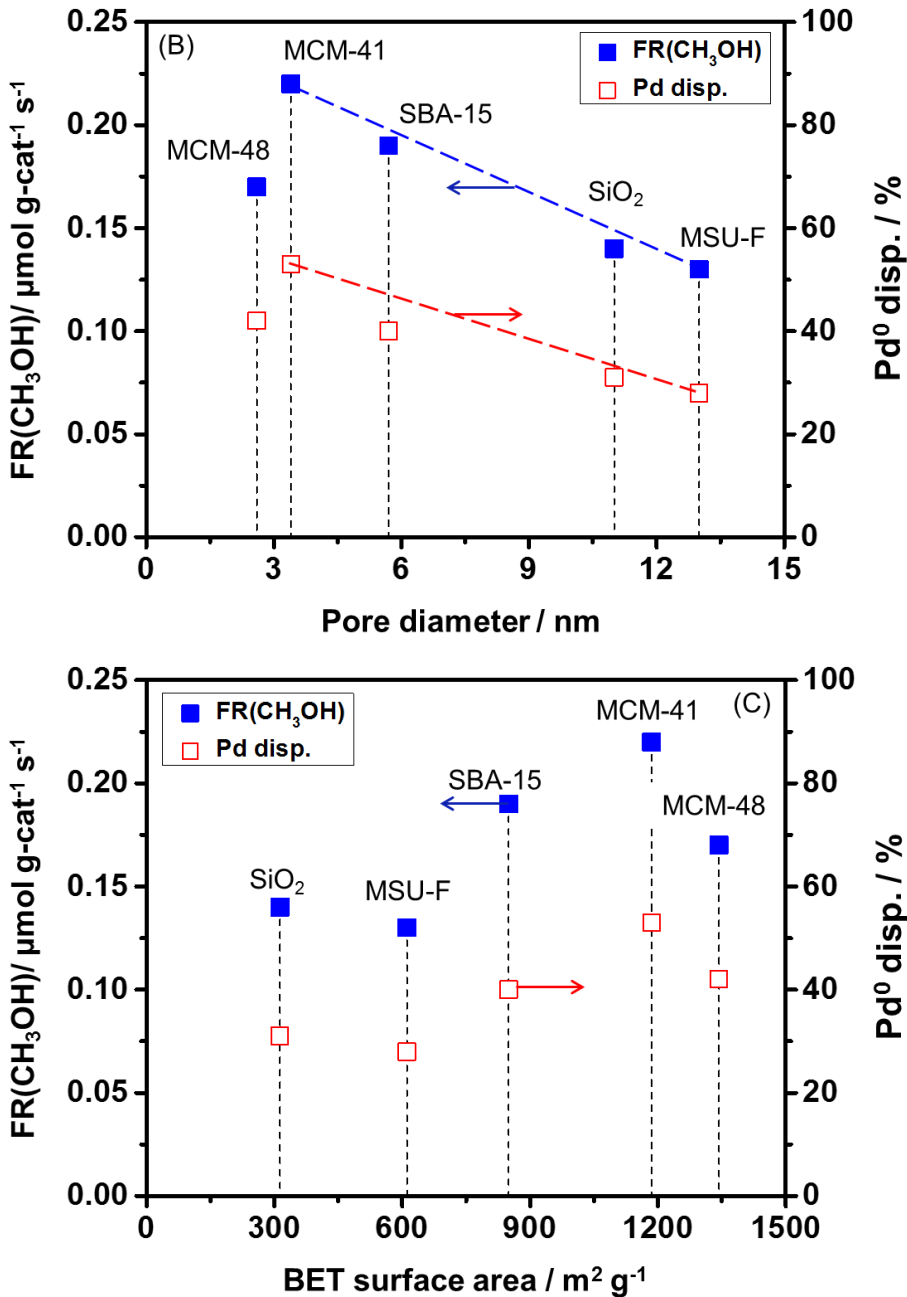


Figure K-14 (A) Changes of CH₃OH formation rate over promoted and unpromoted Pd catalysts as a function of the average pore diameter of the support materials. (B) Dependencies of CH₃OH formation rate over Ca(0.37)/Pd(5.7) catalysts on averages pore diameter of the support materials. (C) Dependencies of CH₃OH formation rate over Ca(0.37)/Pd(5.7) catalysts on BET surface areas of the support materials. PTAN solution was used exclusively the preparation of catalysts. CO₂ hydrogenation conditions: 523 K, 4.1 MPa, 6.2-6.3 g h mol⁻¹.

In Fig. K-14A, the changes of CH₃OH formation rates for promoted and unpromoted

catalysts are plotted as a function of the average pore diameter of corresponding support materials. Evidently, the formation rate of CH₃OH for the promoted catalysts maximizes at about 3 nm and then decreases distinctly with increasing the average pore diameter (i.e., 3-13 nm). In order to establish the correlation between physical properties of catalysts and activity performances, the changes of the absolute CH₃OH formation rates over these catalysts were replotted as functions of the average pore diameter and BET surface area of each support along with corresponding Pd⁰ dispersions, as illustrated in Fig. K-14B and K-14C, respectively. In Fig. K-14B, superior CH₃OH synthesis activities are obtained over those Ca/Pd catalysts with MCM-41 and SBA-15 as support materials with relatively smaller pore diameter. Interestingly, the trend of Pd⁰ dispersion resembles the activity performances. On the other hand, the dependency of the CH₃OH formation rate on the BET surface area scatters irregularly, as shown in Fig. K-14C. Considering the prominent effect of small and regular pore structure on Pd⁰ dispersion and CO₂ uptake as mentioned in characterization discussions, it is clear that the pore diameter plays a more crucial role in the observed activity enhancement of CH₃OH formation.

Since the mesoporous silicas used in this section possess various pore structures, the TOFs for CH₃OH formation were calculated based on Pd⁰ dispersions as well, as tabulated in Table K-3. Clearly, TOFs are approximately the same and independent of the average pore diameters of the support materials. Therefore, the higher CH₃OH formation rates over the Ca/Pd catalysts supported on MCM-41 and SBA-15 can be mainly attributed to the higher dispersion of Pd⁰ nanoparticles formed inside their mesopores. In other words, small mesopores of MCM-41 and SBA-15 would work as a template for the formation of the small Pd⁰ nanoparticles via confinement, further leading to the higher activity for CH₃OH formation compared to the amorphous silica supported counterparts.

It is worth pointing out that the formation rates of CH₃OH over the Ca/Pd catalysts are simply dependent upon the size of Pd⁰ nanoparticles regardless of pore structures of mesoporous supports, e.g., 1D unidirectional channel (SBA-15) and 3D pore system (MCM-48). This suggests that the overall reaction for CH₃OH formation is more likely governed by the surface reaction rather than the diffusion of the reactants, probably due to the low reaction temperature in this work. In other words, the effect of pore structure of support would be significant at higher reaction temperatures. The results obtained in this work also reveal that TOFs for CH₃OH formation over the supported Ca/Pd catalyst are close to each other and independent of the size of Pd⁰ nanoparticles within the mesoporous silicas studied here, which suggests that further activity enhancement is expected if smaller nanoparticles (e.g., < 2 nm) are incorporated inside mesopores or even micropores of support materials.

K.4 Conclusions

In this work, the Pd-based catalysts for CH₃OH synthesis via CO₂/H₂ were prepared by incorporating two different factors, i.e., nano-structured mesoporous silicas with different pore diameters (MCM-48, MCM-41, SBA-15, amorphous silica, and MSU-F) as support materials and alkali/alkaline earth metal additives as promoters. Their CH₃OH synthesis activities and selectivities were investigated under the reaction conditions of 523 K and 4.1 MPa using a fixed-bed reactor system. The effect of pore diameter on coordination environment, Pd⁰ dispersion, CO₂ adsorption property, and active metal reduction were studied. Important results are summarized as follows.

- (1) The introduction of nano-structured mesoporous silica, such as MCM-41 and SBA-15, successfully improved the CH₃OH synthesis activity of the Pd-based catalyst in the presence of alkali/alkaline metal promoters. K(Ca)-promoted Pd supported on SBA-15 yielded 2-5 times more

CH_3OH than the conventional amorphous silica supported catalysts.

(2) The methanol formation could be improved within an appropriate Ca/Pd molar ratio over supported Pd catalysts (e.g., 0.37), while an excessive CaO loading caused a decline in activity.

(3) The formation rate of CH_3OH over the supported Ca/Pd varied as a function of the average pore diameter of support materials and decreased in the following order: MCM-41 > SBA-15 > MCM-48 > MSU-F ~ amorphous SiO_2 .

(4) The PTAN-based Pd(5.7)/Ca(0.37)/SBA-15 was active for CO_2 hydrogenation to CH_3OH over 40 h on stream, and no apparent deactivation was observed within the time on stream studied in this work.

(5) In-situ Pd K-edge EXAFS and H_2 chemisorption measurements of the reduced catalysts demonstrated that small mesopores of MCM-41 and SBA-15 worked as a template to confine the growth of small Pd^0 nanoparticles, thereby leading to the enhancement of Pd^0 dispersion. Such promoted Pd^0 dispersion was responsible for the observed superior activity toward CH_3OH formation compared to the amorphous silica supported counterparts.

(6) TPR profiles indicated that the CaO was more likely to locate on the edge of Pd^0 nanoparticles with an appropriate Ca/Pd molar ratio (e.g., ≤ 0.37), while a higher Ca/Pd molar ratio may lead to a severe coverage of Pd^0 nanoparticles even from the top.

(7) Quantitative analyses of CO_2 -TPD profiles demonstrated that the dispersion of CaO can also be tuned by the average pore diameter of support, and SBA-15, with a uniform pore structure and smaller pore diameter, (e.g., $< 6 \text{ nm}$), could improve the CaO dispersion compared to a mesoporous silica with a larger pore diameter (e.g., MSU-F). Such difference could further reflect on the CH_3OH synthesis activity.

(8) The correlation between the activity performances over Ca-promoted and unpromoted Pd

catalysts and their corresponding H₂ and CO₂ adsorption properties suggested that the reaction may also follow the bi-functional mechanism proposed for CO hydrogenation.

K.5 Acknowledgements

This work was supported by the Pennsylvania State University through the Penn State Institute of Energy and the Environment. EXAFS measurements were performed at the Argonne National Laboratory APS Beam Line. We gratefully acknowledge the help from Dr. Jeffrey Miller of the Argonne National Laboratory and Dr. Junichiro Kugai with the EXAFS spectra measurements and analyses. Parts of the H₂ pulses experiments were conducted at the Materials Characterization Laboratory of the Penn State Materials Research Institute, for which the assistance of Lymaris Ortiz Rivera is acknowledged. The author also would like to show sincere gratitude to Dr. Xiaoxing Wang for helpful discussions and suggestions.

K.6 Reference

- [1] C.D. Keeling, T.P. Whorf, Atmospheric CO₂ records from sites in the SiO air sampling network, in: Trends: A Compendium of Data on Global Change. Carbon Doxide Information Anlysis Center, Oak Ridge National Laboratory, U.S. Department of Energy, Oak Rdge, TN, USA, 2005.
- [2] C. Song, Catal. Today, 115 (2006) 2-32.
- [3] G. Centi, S. Perathoner, Catal. Today, 148 (2009) 191-205.
- [4] H. Arakawa, J.-L. Dubois, K. Sayama, Energy Convers. Manage., 33 (1992) 521-528.
- [5] M. Saito, T. Fujitani, I. Takahara, T. Watanabe, M. Takeuchi, Y. Kanai, K. Moriya, T. Kakumoto, Energy Convers. Manage., 36 (1995) 577-580.
- [6] T. Inui, H. Hara, T. Takeguchi, J.-B. Kim, Catal. Today, 36 (1997) 25-32.
- [7] M. Saito, T. Fujitani, M. Takeuchi, T. Watanabe, Appl. Catal., A-Gen, 138 (1996) 311-318.
- [8] J. Toyir, P.R.d.l. Piscina, J.L.G. Fierro, N. Homs, Appl. Catal., B-Environ, 29 (2001) 207-215.
- [9] J. Toyir, P.R.d.l. Piscina, J.L.G. Fierro, N. Homs, Appl. Catal., B-Environ, 34 (2001) 255-266.
- [10] J. Słoczyński, R. Grabowski, P. Olszewski, A. Kozłowska, J. Stoch, M. Lachowska, J. Skrzypek, Appl. Catal., A-Gen, 310 (2006) 127-137.
- [11] Y. Ma, Q. Sun, D. Wu, W.-H. Fan, Y.-L. Zhang, J.-F. Deng, Appl. Catal., A-Gen, 171 (1998) 45-55.
- [12] J. Słoczyński, R. Grabowski, A. Kozłowska, P. Olszewski, J. Stoch, J. Skrzypek, M. Lachowska, Appl. Catal., A-Gen, 278 (2004) 11-23.

- [13] F. Arena, K. Barbera, G. Italiano, G. Bonura, L. Spadaro, F. Frusteri, *J. Catal.*, 249 (2007) 185-194.
- [14] J. Toyir, R. Miloua, N.E. Elkadri, M. Nawdali, H. Toufik, F. Miloua, M. Saito, *Phys. Procedia*, 2 (2009) 1075-1079.
- [15] T. Inoue, T. Iizuka, K. Tanabe, *Appl. Catal.*, 46 (1989) 1-9.
- [16] K.K. Bando, K. Soga, K. Kunimori, H. Arakawa, *Appl. Catal., A-Gen*, 175 (1998) 67-81.
- [17] H. Kusama, K.K. Bando, K. Okabe, H. Arakawa, *Appl. Catal., A-Gen*, 205 (2001) 285-294.
- [18] L. Fan, K. Fujimoto, *Appl. Catal., A-Gen*, 106 (1993) L1-L7.
- [19] T. Fujitani, M. Saito, Y. Kanai, T. Watanabe, J. Nakamura, T. Uchijima, *Appl. Catal., A-Gen*, 125 (1995) L199-L202.
- [20] C. Shao, L. Fan, K. Fujimoto, Y. Iwasawa, *Appl. Catal., A-Gen*, 128 (1995) L1-L6.
- [21] L. Fan, K. Fujimoto, *Energy Convers. Manage.*, 36 (1995) 633-636.
- [22] T. Fujitani, I. Nakamura, *Bull. Chem. Soc. Jpn.*, 75 (2002) 1393-1398.
- [23] S.E. Collins, D.L. Chiavassa, A.L. Bonivardi, M.A. Baltanas, *Catal. Lett.*, 103 (2005) 83-88.
- [24] D.L. Chiavassa, J. Barrandeguy, A.L. Bonivardi, M.A. Baltanás, *Catal. Today*, 133-135 (2008) 780-786.
- [25] X.-L. Liang, X. Dong, G.-D. Lin, H.-B. Zhang, *Appl. Catal., B-Environ.*, 88 (2009) 315-322.
- [26] M.C. Roman-Martinez, D. Cazorla-Amoros, A. Linares-Solano, C.S.-M.d. Lecea, *Appl. Catal., A-Gen*, 134 (1996) 159-167.
- [27] H. Sakurai, S. Tsubota, M. Haruta, *Appl. Catal., A-Gen*, 102 (1993) 125-136.
- [28] H. Sakurai, M. Haruta, *Catal. Today*, 29 (1996) 361-365.
- [29] M.L. Poutsma, L.F. Elek, P.A. Ibarbia, A.P. Risch, J.A. Rabo, *J. Catal.*, 52 (1978) 157-168.
- [30] M. Ichikawa, K. Shikakura, *Shokubai*, 21 (1979) 253-255.

- [31] Y. Matsumura, W.-J. Shen, Y. Ichihashi, M. Okumura, *J. Catal.*, 197 (2001) 267-272.
- [32] Y. Kikuzono, S. Kagami, S. Naito, T. Onishi, K. Tamaru, *Faraday Discuss. Chem. Soc.*, 72 (1981) 135-143.
- [33] A. Gotti, R. Prins, *J. Catal.*, 175 (1998) 302-311.
- [34] C. Song, K.M. Reddy, *Appl. Catal., A-Gen*, 176 (1999) 1-10.
- [35] Y. Ohtsuka, T. Arai, S. Takasaki, N. Tsubouchi, *Energy Fuels*, 17 (2003) 804-809.
- [36] E. Ghedini, F. Menegazzo, M. Signoretto, M. Manzoli, F. Pinna, G. Strukul, *J. Catal.*, 273 (2010) 266-273.
- [37] X. Xu, C. Song, J.M. Andresen, B.G. Miller, A.W. Scaroni, *Energy Fuels*, 16 (2002) 1463-1469.
- [38] X. Wang, V. Schwartz, J.C. Clark, X. Ma, S.H. Overbury, X. Xu, C. Song, *J. Phys. Chem. C*, 113 (2009) 7260-7268.
- [39] X. Ma, X. Wang, C. Song, *J. Am. Chem. Soc.*, 131 (2009) 5777-5783.
- [40] D. Roth, P. Gélin, A. Kaddouri, E. Garbowski, M. Primet, E. Tena, *Catal. Today*, 112 (2006) 134-138.
- [41] E.B. Fox, S. Velu, M.H. Engelhard, Y.-H. Chin, J.T. Miller, J. Kropf, C. Song, *J. Catal.*, 260 (2008) 358-370.
- [42] J. Kugai, J.T. Miller, N. Guo, C. Song, *Appl. Catal., B-Environ.*, 105 (2011) 306-316.
- [43] S. Jun, J.M. Kim, R. Ryoo, Y.-S. Ahn, M.-H. Han, *Microporous Mesoporous Mater.*, 41 (2000) 119-127.
- [44] P. Munnik, P.E. de Jongh, K.P. de Jong, *Chem. Rev.*, (2015).
- [45] M. Kruk, M. Jaroniec, S.H. Joo, R. Ryoo, *J. Phys. Chem. B*, 107 (2003) 2205-2213.

- [46] P.V.D. Voort, P.I. Ravikovitch, K.P.D. Jong, M. Benjelloun, E.V. Bavel, A.H. Janssen, A.V. Neimark, B.M. Weckhuysen, E.F. Vansant, *J. Phys. Chem. B*, 106 (2002) 5873-5877.
- [47] E.V. Bavel, P. Cool, K. Aerts, E.F. Vansant, *J. Phys. Chem. B*, 108 (2004) 5263-5268.
- [48] M. Harada, K. Asakura, Y. Ueki, N. Toshima, *J. Phys. Chem.*, 96 (1992) 9730-9738.
- [49] A.F. Gusovius, T.C. Watling, R. Prins, *Appl. Catal., A-Gen*, 188 (1999) 187-199.
- [50] L.-C. Wang, C.-Y. Huang, C.-Y. Chang, W.-C. Lin, K.-J. Chao, *Microporous Mesoporous Mater.*, 110 (2008) 451-460.
- [51] A. Palenzona, P. Manfrinetti, *J. Alloy Compd.*, 85 (1982) 307-312.
- [52] D. Zhao, J. Feng, Q. Huo, N. Melosh, G.H. Fredrickson, B.F. Chmelka, G.D. Stucky, *Sci.*, 279 (1998) 548-552.
- [53] L. Jiao, J.R. Regalbuto, *J. Catal.*, 260 (2008) 329-341.
- [54] M. Kosmulski, *J. Colloid Interface Sci.*, 253 (2002) 77-87.
- [55] J.T. Miller, M. Schreier, A.J. Kropf, J.R. Regalbuto, *J. Catal.*, 225 (2004) 203-212.
- [56] L. Jiao, J.R. Regalbuto, *J. Catal.*, 260 (2008) 342-350.
- [57] J. Słoczyński, R. Grabowski, A. Kozłowska, P. Olszewski, M. Lachowska, J. Skrzypek, J. Stoch, *Appl. Catal., A-Gen*, 249 (2003) 129-138.
- [58] R. Yang, Y. Zhang, Y. Iwama, N. Tsubaki, *Appl. Catal., A-Gen*, 288 (2005) 126-133.
- [59] H. Zhan, F. Li, P. Gao, N. Zhao, F. Xiao, W. Wei, L. Zhong, Y. Sun, *J. Power Sources*, 251 (2014) 113-121.
- [60] K.-W. Jun, W.-J. Shen, K.S.R. Rao, K.-W. Lee, *Appl. Catal., A-Gen*, 174 (1998) 231-238.
- [61] R.G. Herman, K. Klier, G.W. Simmons, B.P. Finn, J.B. Bulko, *J. Catal.*, 56 (1979) 407-429.
- [62] J. Wu, M. Saito, M. Takeuchi, T. Watanabe, *Appl. Catal., A-Gen*, 218 (2001) 235-240.
- [63] J. Nakamura, T. Uchijima, Y. Kanai, T. Fujitani, *Catal. Today*, 28 (1996) 223-230.

- [64] T. Fujitani, I. Nakamura, T. Uchijima, J. Nakamura, *Surf. Sci.*, 383 (1997) 285-298.
- [65] M. Behrens, F. Studt, I. Kasatkin, S. Kuhl, M. Havecker, F. Abild-Pedersen, S. Zander, F. Girgsdies, P. Kurr, B. Kniep, M. Tovar, R.W. Fischer, J.K. Norskov, R. Schlogl, *Sci.*, 336 (2012) 893-897.
- [66] S. Irusta, A.J. Marchi, E.A. Lombardo, E.E. Miro, *Catal. Lett.*, 40 (1996) 9-16.
- [67] K. Schumacher, P.I. Ravikovitch, A.D. Chesne, A.V. Neimark, K.K. Unger, *Langmuir*, 16 (2000) 4648-4654.
- [68] A. Taguchi, F. Schüth, *Microporous Mesoporous Mater.*, 77 (2005) 1-45.
- [69] N. Linares, E. Serrano, M. Rico, A.M. Balu, E. Losada, R. Luque, J. Garcia-Martinez, *Chem. Commun.*, 47 (2011) 9024-9035.

VITA

Xiao Jiang

EDUCATION

Doctor of Philosophy (Ph.D.) in John and Willie Leone Family Department of Energy & Mineral Engineering, The Pennsylvania State University, USA (Aug. 2010 ~ Dec. 2015).
Thesis advisor: Dr. Chunshan Song.

Master of Science (M.S.) in School of Chemical Engineering with the Option in Industrial Catalysis, Dalian University of Technology, CHINA (Sep. 2007 ~ Jul. 2010).
Thesis advisor: Dr. Xinwen Guo.

Bachelor of Science (B.S.) in School of Chemical Engineering with the Option in Industrial Catalysis, Dalian University of Technology, CHINA (Sep. 2003 ~ Jul. 2007).

PUBLICATIONS

1. **X. Jiang**, X.X. Wang, N. Koizumi, C. Song, Role of the Alloy in Pd-Cu/SiO₂ Bimetallic Catalysts for CO₂ Hydrogenation to Methanol, in preparation.
2. **X. Jiang**, N. Koizumi, X.W. Guo, C. Song, Bimetallic Pd-Cu Catalysts for Selective CO₂ Hydrogenation to Methanol, *Applied Catalysis B: Environment*. 170 (2015), 173-185.
3. N. Koizumi, **X. Jiang**, J. Kugai, C. Song, Effects of Mesoporous Silica Supports and Alkaline Promoters on Activity of Pd Catalysts in CO₂ Hydrogenation for Methanol Synthesis, *Catalysis Today*, 194 (2012), 16-24.
4. **X. Jiang**, P.P. Li, X.M. Liu, X.W. Guo, L. Liu, One-pot Synthesis-assembly-separation of cucurbit[6]uril via SO₃H-functionalized Ionic Liquids, *Journal of Inclusion Phenomena and Macrocyclic Chemistry*, 80 (2014), 457-461.
5. L. Liu, **X. Jiang**, J. Zhang, Anion-linked cucurbit[6]uril frameworks formed by microwave-assisted synthesis in ionic liquids, *Crystal Engineering Communications*, 12 (2010), 3445-3447.
6. X.M. Liu, **X. Jiang**, C. Wang, L. Gao, X.W. Guo, Tert-butylation of Hydroquinone over Trimethylammonium-based SO₃H-functionalized Ionic Liquids, *ACTA PETROL EI SINICA*, 24 (2008), 533-539.

AWARDS

1. 2015: Frank and Lucy Rusinko Graduate Fellowship award, John and Willie Leone Family Department of Energy and Mineral Engineering, The Pennsylvania State University.
2. 2015: Kokes award for the 24th North American Meeting of the Catalysis Society in Pittsburgh.